

Study of black holes in standard and modified gravity

Thesis submitted for the award of
Doctor of Philosophy in Science (Physics)
of
The University of Burdwan



Submitted by

SOHAN KUMAR JHA

(R-Ph.D./Regn./sc/physics/43) dated 24.06.2022

Under the Supervision of Dr. Anisur Rahaman (WBES)

Durgapur Govt. College, Durgapur, Burdwan

Work done in

Hooghly Mohsin College, Chinsurah, Hooghly

And

Durgapur Govt. College, Durgapur, Burdwan

Department of Physics
DURGAPUR GOVERNMENT COLLEGE
Accredited by NAAC with "A" Grade (2017)
J.N. Avenue, Durgapur, Paschim Bardhaman 713214

=====

To whom it may concern

Certified that this thesis entitled '**Study of black holes in standard and modified gravity**' submitted by Sohan kumar Jha who has got his name registered on with registration No. **R-Ph.D./Regn./sc/physics/43** dated **24.06.2022** for the award of Ph. D. (Science) degree of the University of Burdwan is based on his own work done under my supervision and that nether this thesis nor any part of it has been submitted for any degree /diploma or any other academic award before.

ANISUR RAHAMAN
Associate Professor, W.B.E.S
Durgapur Government College

Certificate from the Candidate

I do hereby declare that the subject matter embodied in the thesis '**Study of black holes in standard and modified gravity**' is solely based on my own work done under the supervision of Dr. Anisur Rahaman, Associate professor (W.B.E.S.) presently posted at Durgapur Government College. This thesis or any part of it has not been submitted or will not be submitted for any other academic award. I have made an effort to present it without errors. Instead, I am assuming responsibility for any mistakes if found on me.

Sohan Kumar Jha

Date

Registration No.: R-Ph.D./Regn./sc/physics/43

Dated: 24.06.2022

Acknowledgement

First, I want to thank my supervisor Dr. Anisur Rahaman, for all the time and the patience invested in me throughout all my research, giving. He was able to transmit me the passion for research with supervision and long discussions where fantastic ideas emerged. I think that I could not find a better person to guide me through this experience. He taught me how to deal with new physical problems. Then, I want to thank my family for supporting me throughout this journey. It is not an easy path as those who have already walked it know. But with the guidance of my supervisor and with the support of my family, the journey was made easy.

Sohan Kumar Jha
Ph.D. scholar
Department of Physics
University of Burdwan

List of Pulications

Thesis is based on following works:

S. K. Jha, H. barman, A. Rahaman:: JCAP04 (2021) 036

S. K. Jha, A. Rahaman: Eur. Phys. J. C (2021) 81:345

S. K. Jha, S. Aziz, A. Rahaman: Eur. Phys. J. C (2022) 82:106

S. K. Jha, A. Rahaman: Eur. Phys. J. C (2022) 82:411

S. K. Jha, A. Rahaman: Eur. Phys. J. C (2022) 82:728

S. K. Jha, A. Rahaman: Eur. Phys. J. Plus 138, 86 (2023)

Additional Works done:

H. Barman, A. Rahaman and S.K.Jha: Modern Physics Letter A Vol. 36, No. 19, 2150130 (2021)

S. Aziz, S. K. Jha and A. Rahaman: Class. Grav. 38(2021) 22,225008

H. Barman, A. Rahaman and S.K.Jha: Eur. Phys. J. Plus (2022) 137: 1270

List of Symbols

Notation	Description	Notation	Description
c	velocity of light	D_X	axial ratio
G	gravitational constant	ℓ_0	hair parameter
α, β	celestial coordinates	α_h	deviation parameter of hairy Schwarzschild metric
τ	proper time	b_h	impact parameter
t	coordinate time	α_D	angle of deflection for strong gravitational lensing
λ	affine parameter	γ_D	angle of deflection for weak gravitational lensing
λ_r	wavelength at distance r	\tilde{a}, \tilde{b}	lensing coefficients
λ_{inf}	wavelength measured at infinity	θ_n^E	position of the nth Einstein ring
Ω_h	angular velocity of black hole	μ_n	magnification of the image
T_H	Hawking temperature	a	specific angular velocity of black hole
b	charge parameter of black hole	M	mass of black hole
ϑ_n	non-commutative parameter	ℓ	Lorentz violating parameter
k	plasma parameter	V_{eff}	effective potential
λ_s	Snyder parameter	R_s	size of the black hole
δ_s	deviation from circular form	κ	surface gravity
h	Planck constant	r_{eh}, r_+	position of event horizon
r_{ch}, r_-	position of Cauchy horizon	A_h	area of horizon
Z_{jm}	amplification factor	ΔC	deviation from circularity
θ_d	angular diameter	a_p	proper acceleration

Contents

Introduction	1
1 Theory of general relativity in brief in the eyes of Einstein	3
1.1 Solutions of Einstein's field equation	4
1.1.1 Schwarzschild solution	4
1.1.2 Motion of a particle in circular orbit	5
1.2 Experimental test of general theory of relativity	6
1.2.1 The perihelion shift of Mercury	6
1.2.2 Bending of light	7
1.2.3 Radar echo delay	7
1.2.4 Gravitational Redshift	7
1.2.5 Proper acceleration and surface gravity	7
1.3 Kerr solution	8
1.3.1 Event horizon and Cauchy horizon	8
1.3.2 Static limit surface and ergosphere	9
1.3.3 Surface gravity and Hawking temperature	10
1.3.4 Constants of motion and differential equations of motion	10
1.3.5 Frame-dragging	12
1.3.6 Effective potential, critical radii, and conserved parameters	12
1.3.7 Black hole shadow	13
1.4 Kerr-Sen black hole	14
1.4.1 Event horizon and ergosphere	15
1.4.2 Surface gravity and Hawking temperature	16
1.4.3 Basic equations	16
1.4.4 Spherical orbit and Black hole shadow	16
1.4.5 The deviation from the circular form (δ_s) and the size (R_s) of the shadow	17
1.4.6 Rate of Energy Emission	18
2 Spontaneous Lorentz symmetry breaking and the Bumblebee model	20
2.1 Schwarzschild-like Lorentz violating black hole solution	22
2.1.1 Hawking temperature	22
2.1.2 Redshift for both static and free-falling source.	23
2.1.3 Surface Gravity	24
2.1.4 Circular orbit in bumblebee background	24
2.1.5 A discussion of Snyder algebra	26
2.2 Motion of Particle in bumblebee background in the Snyder orbit	27
2.3 Constraining the Snyder parameter λ_s and the LV parameter ℓ	29
3 Non-commutative Kerr-like black hole	31
3.1 Non-commutative Kerr-like black hole	32
3.2 Combining non-commutative and Lorentz violation effect	32
3.3 Geometry concerning Horizon and ergosphere	33
3.4 Photon orbit and black hole shadow	35

3.5	Deviation from the circularity δ_s and the size R_s of black hole shadow	37
3.6	Computation of energy emission rate	38
4	Kerr-Sen-like black hole	40
4.1	Hawking temperature	45
4.2	Photon orbit and black-hole shadow	45
4.3	Energy emission rate	50
4.4	Comparison between Schwarzschild-like, Kerr-like and Kerr-Sen-like Black holes	52
4.5	Bending of light	53
5	Kerr-Sen-like black hole in the presence of a dispersive medium	55
5.1	Effective potential and Critical radius	56
5.2	Photon orbit and black hole shadow	58
5.3	The deviation from the circular form of the shadow (δ_s) and the size (R_s) of the shadow	61
5.4	The rate of energy emission	63
6	Superradiance	65
6.1	Superradiance scattering of the scalar field off non-commutative Kerr-like black hole	66
6.2	Amplification factor Z_{jm} for superradiance	68
6.3	Superradiant instability for Lorentz violating and non-commutative Kerr-like black hole	72
6.4	Superradiance scattering of the scalar field off Kerr-Sen-like black hole	74
6.5	Calculation of the amplification factor Z_{jm} for superradiance	75
6.6	Superradiant instability for Kerr-Sen-like black hole	80
7	Constraining parameters involved in modified gravity using observational data for M87* black hole	83
7.1	Constraining LV parameter ℓ for the Kerr-Sen-like black hole surrounded by plasma	84
7.2	Constraining the charge parameter b in Kerr-Sen-like black hole in vacuum from the observed data for M87*	88
7.3	Constraining the non-commutative parameter ϑ_n from the observed data for M87*	89
8	Strong gravitational lensing in hairy Schwarzschild background	92
8.1	Strong and weak gravitational lensing	93
8.2	Observables in the strong field limit	98
8.3	Time delay	101
8.4	Weak gravitational lensing	102
9	Summary and Conclusions	106
10	References	111

I. INTRODUCTION

Our present description of nature is based on 2 enormously successful theories: General Relativity (GR), a classical theory describing all gravitational phenomena, and the Standard Model (SM) of particle physics, which provides a quantum description of all other interactions. General relativity has emerged as a highly successful model of gravitation and cosmology, which has so far passed many unambiguous observational and experimental tests. However, there are strong indications that the theory is incomplete. The problem of quantum gravity and the question of the reality of spacetime singularities remain open. Observational data that is taken as evidence for dark energy and dark matter could indicate the need for new physics. It is widely expected that these theories are merely the low-energy limit of some more fundamental theory that would take over as the characteristic energies involved in experiments approach the Planck scale, 10^{19} GeV. Experimental information to guide the development of a Planck-scale theory would, by conventional thinking, come from Planck-energy experiments, which are likely to remain infeasible far into the future. An alternative approach is to search for small deviations from known physics (the SM and GR) in present-day experiments, with the hope that small deviations, if found, would encode information about the underlying theory. Lorentz symmetry, the idea that physical results are unchanged under rotations and boosts of the system is the pillar of both the SM and GR. Hence violation of the symmetry, if found, would provide a novel signal of new physics. Moreover, the possibility of violation of this symmetry has been demonstrated in candidates for the underlying theory, like strings. Here, we consider a special class of theory, called Bumblebee model, where Lorentz symmetry is spontaneously broken. The Lorentz violation arises from the dynamics of a single vector B_μ , that assumes vacuum expectation value, b_μ , which is unequal to zero. The vacuum value b_μ acts as a fixed background field that spontaneously breaks Lorentz symmetry.

II. THEORY OF GENERAL RELATIVITY:EINSTEIN'S EQUATION

In 1905 Einstein published his special theory of relativity. While this theory has been able to predict many observed phenomena, it was not complete in true sense. To explain matter and energy Changing the geometry of spacetime, Einstein proposed a new theory Gravity known as general theory relativity. This theory is characterized by a set of dynamic equations expressed as: Einstein Field Equations showing basics gravitational interaction as a result of spacetime curvature in mass and energy. Albert Einstein published this new theory Gravity as a tensor equation 1915. Movement of the body under gravitational field is almost completely described by geodetic equation. Einstein used three principles in his development of general theory of relativity namely Mach Principle, Equality Principle and Co-variance principle. Einstein's field equations are given by

$$\begin{aligned} R_{ij} - \frac{1}{2}g_{ij}R &= -\kappa T_{ij} \\ \Rightarrow G_{ij} &= -\kappa T_{ij} \end{aligned} \quad (1)$$

Trace inverted form of the above equation is

$$R_{ij} = -\kappa(T_{ij} - \frac{1}{2}g_{ij}T) \quad (2)$$

Here $G_{ij} = R_{ij} - \frac{1}{2}g_{ij}R$ are the components of Einstein tensor, and T is defined by $T = g^{ij}T_{ij}$, g_{ij} being components of metric tensor. If the space-time has signature $(-, +, +, +)$ then, equation (1) becomes

$$\begin{aligned} R_{ij} - \frac{1}{2}g_{ij}R &= \kappa T_{ij} \\ \Rightarrow G_{ij} &= \kappa T_{ij} \end{aligned} \quad (3)$$

whose trace inverted form is

$$R_{ij} = \kappa(T_{ij} - \frac{1}{2}g_{ij}T) \quad (4)$$

On solving Einstein's equations, one obtains the Schwarzschild metric:

$$ds^2 = -\left(1 - \frac{2M}{r}\right)dt^2 + \left(1 - \frac{2M}{r}\right)^{-1} + r^2(d\theta^2 + \sin^2\theta d\phi^2), \quad (5)$$

where M is the mass of the black hole in unit of length and $G = c = 1$ for the entire thesis. Since the coefficients of the metric do not depend on t , and the metric does not have any cross term involving space-like and time-like increments, it is a static metric. The metric has two singularities, one at $r = 0$ and another at $r = 2M$. The first one cannot be removed using a change of coordinates, but the second one can be removed using a different choice of coordinates. It is called event horizon. Since the metric is static and spherically symmetric, E , the relativistic energy per unit mass of the particle and L , the angular momentum per unit mass, both with respect to an observer stationary at infinity, are constants of motion. Here, we study circular motion of a particle around the black hole and the proper period of the particle in the circular orbit is found out to be

$$\tau = \frac{r^2}{L} = 2\pi \frac{r^{\frac{3}{2}}}{\sqrt{M}} \sqrt{1 - \frac{3M}{r}}. \quad (6)$$

Perihelion shift also studied for Schwarzschild black hole. For small eccentricity, the perihelion rotates through $\frac{6\pi M^2}{L^2}$. Gravitational redshift and Surface Gravity for Schwarzschild black hole are also studied.

The Kerr solution, which describes a rotating black hole in 4D spacetime, is actually the solution of Einstein's equations in vacuum. In other words, the metric is exterior of an axially rotating body. The Kerr metric, in Boyer-Lindquist coordinates reads [1]

$$ds^2 = - \left(1 - \frac{2Mr}{\rho^2}\right) dt^2 - \frac{4Mr a \sin^2 \theta}{\rho^2} dt d\phi + \frac{\rho^2}{\Delta} dr^2 + \rho^2 d\theta^2 + \frac{A \sin^2 \theta}{\rho^2} d\phi^2. \quad (7)$$

where $a = \frac{J}{M}$, J being the angular momentum of the black hole and

$$\begin{aligned} \rho^2 &= r^2 + a^2 \cos^2 \theta, \\ \Delta &= r^2 - 2Mr + a^2, \\ A &= (r^2 + a^2)^2 - \Delta a^2 \sin^2 \theta. \end{aligned} \quad (8)$$

The equation $\Delta = 0$ has two real solutions when $a \leq M$. The larger of the two solutions gives the Event horizon (r_+) and the smaller one gives the Cauchy horizon (r_-). The surface given by $g_{00} = 0$ is called static limit surface as no particle, even photon, can remain static within this surface. The region between Event horizon and the static limit surface is called ergosphere. We also study surface gravity and Hawking temperature for the Kerr black hole. Frame dragging which is unique to rotating black holes are also studied here. Black hole shadows for Kerr black hole are studied here.

In ([6]) Sen obtained a charged rotating BH solution which came to be known as the Kerr-Sen (KS) solution. The rotating charged metric in Boyer-Lindquist coordinates (t, r, θ, ϕ) is [6]

$$ds^2 = - \left(1 - \frac{2Mr}{\rho^2}\right) dt^2 - \frac{4Mr a \sin^2 \theta}{\rho^2} dt d\phi + \frac{\rho^2}{\Delta} dr^2 + \rho^2 d\theta^2 + \frac{A \sin^2 \theta}{\rho^2} d\phi^2. \quad (9)$$

where

$$\rho^2 = r(r + b) + a^2 \cos^2 \theta, \Delta = r(r + b) - 2Mr + a^2, \text{ and } A = [r(r + b) + a^2]^2 - \Delta a^2 \sin^2 \theta. \quad (10)$$

where $b = Q/M^2$, Q being the charge of the black hole. Here we also study Hawking temperature and other effects for the Kerr-Sen black hole.

III. SPONTANEOUS LORENTZ SYMMETRY BREAKING AND THE BUMBLEBEE MODEL

General relativity and the standard model of particle physics are two very successful field theoretical models that assist us to describe our Universe. The formulation of both these theories is based on the well celebrated Lorentz symmetry. However, the regime of applicability and the nature of service towards describing the Universe by these two theories are profoundly different. The general relativity describes the gravitational interaction and it is a classical field theory in the curved spacetime and there is no direct way to include the quantum effect. On the contrary, the standard model describes the other fundamental interactions and it is the quantum field theory in the flat spacetime that neglects all gravitational effects, but to study the physical system in the vicinity of the Planck scale (10^{-19} GeV), the effect due to gravity cannot be ignored, since the gravitational interaction is strong enough in that energy scale. Therefore, the study of physics in the vicinity of the Planck scale necessarily entails the unification of general relativity

and standard model of particle physics. Motivated by this, in recent times theorists have started to doubt whether the Lorentz symmetry is an exact symmetry of nature. Indeed, the central point of recent research in quantum-gravity phenomenology is the search for Lorentz violation.

Einstein-bumblebee model is essentially a simple model that contains Lorentz symmetry breaking scenario in a significant manner in which the physical Lorentz symmetry breaks down through an axial vector field known as the bumblebee field. It is described by the action [20]

$$\mathcal{S} = \int d^4x \sqrt{-g} \left[\frac{1}{16\pi G_N} (\mathcal{R} + \varrho B^\mu B^\nu \mathcal{R}_{\mu\nu}) - \frac{1}{4} B^{\mu\nu} B_{\mu\nu} - V(B^\mu) \right]. \quad (11)$$

where ϱ^2 is a real coupling constant (with mass dimension -1) which controls the non-minimal gravity interaction to bumblebee field B_μ which has the mass dimension 1. The field strength tensor corresponding to the bumblebee field reads

$$B_{\mu\nu} = \partial_\mu B_\nu - \partial_\nu B_\mu. \quad (12)$$

Einstein-Bumblebee field equations acquire a generalized form:

$$\begin{aligned} \mathcal{R}_{\mu\nu} - \kappa b_{\mu\alpha} b_\nu^\alpha + \frac{\kappa}{4} g_{\mu\nu} b^{\alpha\beta} b_{\alpha\beta} + \varrho b_\mu b^\alpha \mathcal{R}_{\alpha\nu} + \varrho b_\nu b^\alpha \mathcal{R}_{\alpha\mu} \\ - \frac{\varrho}{2} g_{\mu\nu} b^\alpha b^\beta \mathcal{R}_{\alpha\beta} - \frac{\varrho}{2} [\nabla_\alpha \nabla_\mu (b^\alpha b_\nu) + \nabla_\alpha \nabla_\nu (b^\alpha b_\mu) - \nabla^2 (b_\mu b_\nu)] = 0 \\ \Rightarrow \bar{R}_{\mu\nu} = 0 \end{aligned} \quad (13)$$

with

$$\begin{aligned} \bar{R}_{\mu\nu} &= \mathcal{R}_{\mu\nu} - \kappa b_{\mu\alpha} b_\nu^\alpha + \frac{\kappa}{4} g_{\mu\nu} b^{\alpha\beta} b_{\alpha\beta} + \varrho b_\mu b^\alpha \mathcal{R}_{\alpha\nu} + \varrho b_\nu b^\alpha \mathcal{R}_{\alpha\mu} - \frac{\varrho}{2} g_{\mu\nu} b^\alpha b^\beta \mathcal{R}_{\alpha\beta} + \bar{B}_{\mu\nu} \\ \bar{B}_{\mu\nu} &= -\frac{\varrho}{2} [\nabla_\alpha \nabla_\mu (b^\alpha b_\nu) + \nabla_\alpha \nabla_\nu (b^\alpha b_\mu) - \nabla^2 (b_\mu b_\nu)] \end{aligned} \quad (14)$$

The static, spherically symmetric vacuum solution of modified equations [13] is found to be [20]

$$ds^2 = - \left(1 - \frac{2M}{r} \right) dt^2 + (1 + \ell) \left(1 - \frac{2M}{r} \right)^{-1} dr^2 + r^2 (d\theta^2 + \sin^2 \theta d\phi^2), \quad (15)$$

where the parameter ℓ is defined by $\ell = \varrho b^2$ is termed as Lorentz violating (LV) parameter. In the limit $\ell \rightarrow 0$, the metric [15] yields the well known Schwarzschild solution. Hawking temperature for the metric [15] is

$$T_H = \frac{1}{2\pi\sqrt{1+\ell}} \frac{M}{r^2} \Big|_{r=r_h} = \frac{1}{8\pi M\sqrt{1+\ell}} \quad (16)$$

It is clear from the above expression that as the LV parameter increases, the Hawking temperature decreases. In the limit $\ell \rightarrow 0$ we obtain $T_H = \frac{1}{8\pi M}$ which is the Hawking temperature for the Schwarzschild black hole. For both static and free-falling emitter, the redshift scenarios remain unaffected by the Lorentz violating effect associated with the bumblebee gravity. The expression of surface gravity turns into

$$\chi_{BB} = \frac{M}{r^2\sqrt{1+\ell}}. \quad (17)$$

For Schwarzschild radius $r = 2M$ that becomes $\frac{1}{4M\sqrt{1+\ell}}$. It shows that the surface gravity for the bumblebee background depends on the LV factor ℓ in an explicit manner. The circular motion around the black hole remain unaffected by the Lorentz violating effect, but the effect does affect non-circular motion.

Here we discuss the general Snyder algebra. The algebra reads [22]

$$\{x_\mu, p_\nu\} = \eta_{\mu\nu} + \lambda p_\mu p_\nu, \quad \{x_\mu, x_\nu\} = \lambda J_{\mu\nu}, \quad \{p_\mu, p_\nu\} = 0. \quad (18)$$

In ordinary units, this corresponds to $\lambda^2 \sim \sqrt{\hbar}/cM_{Pl} \sim 10^{-17}(\text{s/kg})^{1/2}$. The Poisson bracket [18] preserves the Lorentz invariance. Next we consider the motion of a particle in bumblebee background in the Snyder orbit. The generalized expression for the perihelion shift:

$$\begin{aligned} d\theta &= \pi\epsilon [6 + 10\lambda m^2 + (-3q + 1 + \frac{3e^2}{4} + 3e)\lambda m^2 l] + \pi\lambda m^2 \ell + 5l\pi\epsilon\lambda m^2 + \ell\pi \\ &= \ell\pi + 6\pi\epsilon + 10\pi\epsilon\lambda m^2 + \pi\epsilon(-3q + 1 + \frac{3e^2}{4} + 3e) + \pi(1 + 5\epsilon)\lambda m^2 \ell. \end{aligned} \quad (19)$$

Note that the expression of time period agrees with the time period obtained in the article [20] since if we set $\lambda = 0$, ω will reduce to $\omega \approx \frac{1-\epsilon}{\sqrt{1+\ell}}$. The first term represents the shift due to the curvature of the spacetime. The term containing only λ appears due to the use of Snyder noncommutative dynamics and the term containing only ℓ emerges because of the replacement of the Schwarzschild background by the bumblebee. These two can be considered as pure corrections due to the use of noncommutative dynamics and the use of bumblebee gravity respectively. We have given a table with possible constraint values of ℓ and λ .

IV. NON-COMMUTATIVE KERR-LIKE BLACK HOLE

In this chapter we discuss non-commutative Kerr-like black hole. Kerr-like black hole is the rotating, axisymmetric stationary vacuum solution of modified Einstein equations [13]. Ding et al. obtained a Kerr-like solution in [24] keeping in view of the development of Koltz to reproduce the Kerr solution [25]. Kerr-like metric which in the Boyer-Lindquist coordinates reads [24]

$$ds^2 = - \left(1 - \frac{2Mr}{\rho^2} \right) dt^2 - \frac{4Mra\sqrt{1+\ell}\sin^2\theta}{\rho^2} dt d\varphi + \frac{\rho^2}{\Delta} dr^2 + \rho^2 d\theta^2 + \frac{A\sin^2\theta}{\rho^2} d\varphi^2. \quad (20)$$

where

$$\Delta = \frac{r^2 - 2Mr}{1+\ell} + a^2, \rho^2 = r^2 + a^2 \cos^2\theta, A = [r^2 + (1+\ell)a^2]^2 - \Delta(1+\ell)^2 a^2 \sin^2\theta, \text{ and } \phi = \varphi/\sqrt{1+\ell}$$

To incorporate the non-commutativity effect we consider that the mass density of the black hole has a Lorentzian distribution as it was found in article [32, 33]. For the smeared matter distribution, it can be shown that [33]

$$\mathcal{M}_{\vartheta_n} = \int_0^r \rho_{\vartheta_n}(r) 4\pi r^2 dr = \frac{2M}{\pi} \left(\tan^{-1} \left(\frac{r}{\sqrt{\pi\vartheta_n}} \right) - \frac{\sqrt{\pi\vartheta_n}r}{\pi\vartheta_n + r^2} \right) \approx -\frac{4\sqrt{\vartheta_n}M}{\sqrt{\pi}r} + M + \mathcal{O}(\vartheta_n^{3/2}). \quad (21)$$

Here ϑ_n is the strength of non-commutativity of spacetime and M is the total mass distributed throughout a region with a linear size $\sqrt{\vartheta_n}$. Therefore, the generalized spacetime metric, where both the LV and non-commutating effects are bestowed simultaneously, takes the form

$$ds^2 = - \left(1 - \frac{2M_{\vartheta_n}r}{\rho^2} \right) dt^2 - \frac{4M_{\vartheta_n}ra\sqrt{1+\ell}\sin^2\theta}{\rho^2} dt d\varphi + \frac{\rho^2}{\hat{\Delta}} dr^2 + \rho^2 d\theta^2 + \frac{A\sin^2\theta}{\rho^2} d\varphi^2, \quad (22)$$

where

$$\rho^2 = r^2 + (1+\ell)a^2 \cos^2\theta, \quad \hat{\Delta} = \frac{r^2 - 2M_{\vartheta_n}r}{1+\ell} + a^2, \quad \text{and} \quad A = [r^2 + (1+\ell)a^2]^2 - \hat{\Delta}(1+\ell)^2 a^2 \sin^2\theta.$$

We study Event and Cauchy horizons, ergosphere, and shadows for the black hole. We observe that all of them depend on both ℓ and ϑ_n . Using the parameters which are introduced by Hioki and Maeda in [7], we analyze the deviation from the circularity form δ_s and the size R_s of the shadow cast by the black hole. For calculating these parameters, we consider five points, $(\alpha_t, \beta_t), (\alpha_b, \beta_b), (\alpha_r, 0), (\alpha_p, 0)$, and $(\bar{\alpha}_p, 0)$, which are top, bottom, rightmost, leftmost of the shadow and leftmost of the reference circle respectively. So, we have

$$R_s = \frac{(\alpha_t - \alpha_r)^2 + \beta_t^2}{2|\alpha_t - \alpha_r|}$$

and

$$\delta_s = \frac{|\bar{\alpha}_p - \alpha_p|}{R_s}.$$

We observe that both ℓ and ϑ_n have significant impact on R_s and δ_s . We also study the impact of ℓ and ϑ_n on the energy emission rate.

V. KERR-SEN LIKE BLACK HOLE

In this chapter we will derive the metric for Kerr-Sen like black hole and study various aspects of it. We find out the exact Kerr-Sen-like solution from Einstein-bumblebee equations [13] in a similar way the Ding et al. offered the exact Kerr-like solution in [24] following the development of Koltz to reproduce the Kerr solution [25, 42]. Following the procedure we obtain the rotating metric in the bumblebee gravity as

$$ds^2 = - \left(1 - \frac{2Mr}{\rho^2} \right) dt^2 - \frac{4Mr a \sqrt{1+\ell} \sin^2 \theta}{\rho^2} dt d\varphi + \frac{\rho^2}{\Delta} dr^2 + \rho^2 d\theta^2 + \frac{A \sin^2 \theta}{\rho^2} d\varphi^2. \quad (23)$$

where

$$\Delta = \frac{r(r+b) - 2Mr}{1+\ell} + a^2 \quad \text{and} \quad A = [r(r+b) + (1+\ell)a^2]^2 - \Delta(1+\ell)^2 a^2 \sin^2 \theta. \quad (24)$$

If $\ell \rightarrow 0$, it recovers the usual Kerr-Sen metric. We will have a black hole when the condition given below is satisfied $|b - 2M| \geq 2a\sqrt{1+\ell}$. We see that the parameter space for which we have black hole is shrinking with increase in ℓ . We study the black hole shadow and observe that the left end of the shadow shifts towards right for positive values of ℓ for a particular b and reverse is the case when ℓ is negative. However, irrespective of the sign of ℓ the shifting of the left end of the shadow is towards right for increasing b . Using the parameters which are introduced by Hioki and Maeda [7], we analyze deviation from circular form (δ_s) and the size (R_s) of the shadow image of the black hole. We observe that as we increase b for a fixed value ℓ and a , R_s decreases and δ_s increases. For fixed values of b and a , both R_s and δ_s increases but the nature of variation differ for different values of a . The emission rate decreases with the increase in b for any set of fixed values of a and ℓ . It also decreases when ℓ increases for any set of fixed values of a and b . However, there is a crucial difference in the situation when ℓ increases. It is true that the emission rate decreases with the increase in ℓ like the case when b increases, but unlike the situation when b increases, the pick of the curve gets shifted when ℓ increases. We also made comparison between Schwarzschild-like, Kerr-like and Kerr-Sen like Black holes. We obtain an expression for bending of light.

VI. KERR-SEN LIKE BLACK HOLE IN THE PRESENCE OF A DISPERSIVE MEDIUM

In General Relativity, light is attributed to the null geodesic of the spacetime metric and the in-medium effect, which is negligible for most of the frequency ranges, is significant for the radio frequency range. In this context, it is worth mentioning the impact of Solar corona on the time of travel and on the deflection angle of radio signals that come close to the Sun. Since 1960s, this influence has been routinely observed. In this case, one may assume that the medium is a non-magnetized pressureless plasma. The black hole metric [23] associated with Kerr-Sen-like spacetime contains an LV parameter as both the Swarczschild-like and Kerr-like spacetime contain [20, 24]. This Kerr-Sen-like spacetime will enable us to study the LV effect in presence of plasma.. We consider a static inhomogeneous plasma in the gravitational field with a refractive index n . We consider [55]

$$n = \sqrt{1 - \frac{k}{r}}. \quad (25)$$

where k is the plasma parameter. We see that with the increase in the value of b , keeping k and ℓ fixed, the size of the shadow decreases and the left end of the shadow moves a little to the right. We also observe the change of shape of the shadow with a variation of the plasma parameter k , keeping b and ℓ fixed. Figures show that the size of the shadow increases with the increase in the value of k . Using the parameters, which are introduced by Hioki and Maeda in [7], we analyze the deviation from the circular form of the shadow (δ_s) and the size (R_s) of the shadow image of the black hole. It is observed that the rate of emission is higher for smaller values of b . However, the reverse is the case when k increases. It is evident from the spectrum that in the absence of plasma, the minimum energy will be released from the black hole, which indeed agrees with the Kerr-Newman black hole [56]. From the plots, we see that for negative ℓ , there is an enhancement of emission whereas, for increasing positive value of ℓ , there is a reduction in the emission of radiation. The dependence of the angle of deflection $\hat{\alpha}_p$ on the impact parameter p for various charge and plasma parameters are studied. It is found that as the value of b increases, the angle of deflection decreases and it is seen that $\hat{\alpha}_p$ is maximum when $b = 0$. We also observe that the deflection angle $\hat{\alpha}_p$ increases with the increase in the plasma parameter.

VII. SUPERRADIANCE

Superradiance is a radiation enhancement process. The concept of superradiance was introduced by Dicke in 1954 in his work [62]. In a gravitational system, the scattering of radiation off absorbing rotating objects produce waves with amplitude larger than incident one under certain conditions which is known as rotational superradiance [63, 64]. It was showed by Zel'dovich in 1971 that, under certain conditions, scattering of radiation off rotating absorbing surfaces results in waves with a larger amplitude [64, 65]. The black hole superradiance can be explained using the thermodynamic laws of black hole [65]. According to first law of black hole thermodynamics, the changes in mass M , angular momentum J , horizon area A_h and charge Q of a stationary black hole in the vacuum, are related to each other by

$$\delta M = \frac{\kappa}{8\pi} \delta A_h + \Omega_h \delta J + \phi_h \delta Q \quad (26)$$

where κ is the surface gravity, Ω_h is the angular velocity of the black hole and Φ_h is the electrostatic potential at the horizon. Now, we consider a neutral black hole for which we have $\Phi_h = 0$. The ratio of angular momentum flux L to energy E of a wave is given by $L/E = m/\omega$, where m is the azimuthal number and ω is the frequency of the wave. Putting this in Eq. (26) yields

$$\delta M = \frac{\omega \kappa}{8\pi} \frac{\delta A_h}{\Omega - m\omega_h} \quad (27)$$

The second law of black hole thermodynamics states that $\delta A_h \geq 0$. It implies that for $\omega < m\Omega_h$, waves can extract energy from black holes. This result applies to all stationary black holes in vacuum.

We bring the Klein-Gordon equation in curved spacetime into action to study the superradiance scattering of a scalar field Φ .

$$(\nabla_\alpha \nabla^\alpha + \mu^2) \Phi(t, r, \theta, \phi) = \left[\frac{-1}{\sqrt{-g}} \partial_\sigma (g^{\sigma\tau} \sqrt{-g} \partial_\tau) + \mu^2 \right] \Phi(t, r, \theta, \phi) = 0. \quad (28)$$

Here μ represents the mass of the scalar field Φ . We now adopt the standard separation of variables method to the equation Eq.(28) in order to separate it into radial and angular part using the following ansatz. With the standard Boyer-Lindquist coordinates (t, r, θ, ϕ) we can write

$$\Phi(t, r, \theta, \phi) = R_{\omega jm}(r) \Theta(\theta) e^{-i\omega t} e^{im\phi}, \quad j \geq 0, \quad -j \leq m \leq j, \quad \omega > 0, \quad (29)$$

where $R_{\omega jm}(r)$ represents the radial function and $\Theta(\theta)$ refers to the oblate spheroidal wave function. The symbols j , m , and ω respectively stand for the angular eigenfunction, angular quantum number, and the positive frequency of the field under investigation as viewed by a far away observer. Using the ansatz (29), the differential equation (28) for the metric (22), is found to get separated into the following two ordinary differential equations. For the radial part, the equation reads

$$\begin{aligned} \frac{d}{dr} \left(\hat{\Delta} \frac{dR_{\omega jm}(r)}{dr} \right) + \left(\frac{((r^2 + a^2(1 + \ell))\omega - am\sqrt{1 + \ell})^2}{\hat{\Delta}(1 + \ell)} \right) R_{\omega jm}(r) \\ - (\mu^2 r^2 + j(j + 1) + a^2(1 + \ell)\omega^2 - 2m\omega a\sqrt{1 + \ell}) R_{\omega jm}(r) = 0, \end{aligned} \quad (30)$$

and the angular part of it is

$$\begin{aligned} \sin \theta \frac{d}{d\theta} \left(\sin \theta \frac{d\Theta_{\omega jm}(\theta)}{d\theta} \right) + \left(j(j + 1) \sin^2 \theta - \left((a\sqrt{1 + \ell}\omega \sin^2 \theta - m)^2 \right) \right) \Theta_{\omega jm}(\theta) \\ + a^2(1 + \ell)\mu^2 \sin^2 \theta \cos^2 \theta \Theta_{\omega jm}(\theta) = 0. \end{aligned} \quad (31)$$

where $\hat{\Delta} = \frac{r^2 - 2M_{\vartheta_n} r}{1 + \ell} + a^2$, $M_{\vartheta_n} = -\frac{4\sqrt{\vartheta_n} M}{\sqrt{\pi} r} + M$. Using asymptotic matching procedure used in [46, 47, 68, 78, 79] the amplification factor ultimately results out to be

$$Z_{jm} \equiv \frac{|\mathcal{D}_{ref}^\infty|^2}{|\mathcal{D}_{in}^\infty|^2} - 1. \quad (32)$$

where

$$\begin{aligned} \mathcal{D}_{in}^{\infty} = & \frac{d(-2i)^{-\frac{1+\sqrt{1+4(\ell+1)j(j+1)}}{2}}}{\sqrt{(1+\ell)(\omega^2-\mu^2)}} \cdot \frac{\Gamma(\sqrt{1+4(\ell+1)j(j+1)})\Gamma(1+\sqrt{1+4(\ell+1)j(j+1)})}{\Gamma\left(\frac{1+\sqrt{1+4(\ell+1)j(j+1)}}{2}-2i\sqrt{\ell+1}B\right)\left(\Gamma\left(\frac{1+\sqrt{1+4(\ell+1)j(j+1)}}{2}\right)\right)^2} \times \\ & \Gamma(1-2i\sqrt{\ell+1}B)k_{\ell}^{\frac{1-\sqrt{1+4(\ell+1)j(j+1)}}{2}} + \frac{d(-2i)^{\frac{\sqrt{1+4(\ell+1)j(j+1)}-1}{2}}}{\sqrt{(1+\ell)(\omega^2-\hat{\mu}^2)}} \times \\ & \frac{\Gamma(1-\sqrt{1+4(\ell+1)j(j+1)})\Gamma(-\sqrt{1+4(\ell+1)j(j+1)})}{\left(\Gamma\left(\frac{1-\sqrt{1+4(\ell+1)j(j+1)}}{2}\right)\right)^2\Gamma\left(\frac{1-\sqrt{1+4(\ell+1)j(j+1)}}{2}-2i\sqrt{\ell+1}B\right)} \Gamma(1-2i\sqrt{\ell+1}B)k_{\ell}^{\frac{1+\sqrt{1+4(\ell+1)j(j+1)}}{2}}, \end{aligned} \quad (33)$$

and

$$\begin{aligned} \mathcal{D}_{ref}^{\infty} = & \frac{d(2i)^{-\frac{1+\sqrt{1+4(\ell+1)j(j+1)}}{2}}}{\sqrt{(1+\ell)(\omega^2-\mu^2)}} \cdot \frac{\Gamma(\sqrt{1+4(\ell+1)j(j+1)})\Gamma(1+\sqrt{1+4(\ell+1)j(j+1)})}{\Gamma\left(\frac{1+\sqrt{1+4(\ell+1)j(j+1)}}{2}-2i\sqrt{\ell+1}B\right)\left(\Gamma\left(\frac{1+\sqrt{1+4(\ell+1)j(j+1)}}{2}\right)\right)^2} \times \\ & \Gamma(1-2i\sqrt{\ell+1}B)k_{\ell}^{\frac{1-\sqrt{1+4(\ell+1)j(j+1)}}{2}} + \frac{d(2i)^{\frac{\sqrt{1+4(\ell+1)j(j+1)}-1}{2}}}{\sqrt{(1+\ell)(\omega^2-\hat{\mu}^2)}} \times \\ & \frac{\Gamma(1-\sqrt{1+4(\ell+1)j(j+1)})\Gamma(-\sqrt{1+4(\ell+1)j(j+1)})}{\left(\Gamma\left(\frac{1-\sqrt{1+4(\ell+1)j(j+1)}}{2}\right)\right)^2\Gamma\left(\frac{1-\sqrt{1+4(\ell+1)j(j+1)}}{2}-2i\sqrt{\ell+1}B\right)} \Gamma(1-2i\sqrt{\ell+1}B)k_{\ell}^{\frac{1+\sqrt{1+4(\ell+1)j(j+1)}}{2}}. \end{aligned} \quad (34)$$

For negative m , amplification factor takes negative value which refers to the nonoccurrence of superradiance. The plots also show transparently that with the decrease in the value of the Lorentz violation parameters the superradiance process enhances and the reverse is the case when the value of the Lorentz violation parameter decreases. We have also studied the effect of the parameter ϑ_n on the superradiance scenario. It shows that the superradiance scenario gets diminished with the increase in the value of the parameter ϑ_n . However, with the increase in \hat{a} , the superradiance effect increases. The dynamics of the massive scalar field in noncommutative Kerr like black hole will remain stable when $\mu \geq \sqrt{2}m\hat{\Omega}_h$, where $\hat{\Omega}_h = \frac{\hat{a}}{r_{eh}^2 + \hat{a}^2}$ and μ represents the mass of the scalar field Φ . For the Kerr-Sen like black hole given by metric (23), radial part of the equation reads

$$\begin{aligned} & \frac{d}{dr} \left(\Delta \frac{dR_{\omega jm}(r)}{dr} \right) + \left(\frac{((r(r+b) + a^2(1+\ell))\omega - am\sqrt{1+\ell})^2}{\Delta(1+\ell)} \right) R_{\omega lm}(r) \\ & - (\mu^2 r(r+b) + j(j+1) + a^2(1+\ell)\omega^2 - 2m\omega a\sqrt{1+\ell}) R_{\omega lm}(r) = 0, \end{aligned} \quad (35)$$

and for the angular part it is

$$\begin{aligned} & \sin\theta \frac{d}{d\theta} \left(\sin\theta \frac{d\Theta_{\omega jm}(\theta)}{d\theta} \right) + \left(j(j+1)\sin^2\theta - \left((a\sqrt{1+\ell}\omega\sin^2\theta - m)^2 \right) \right) \Theta_{\omega jm}(\theta) \\ & + a^2(1+\ell)\mu^2\sin^2\theta\cos^2\theta\Theta_{\omega jm}(\theta) = 0. \end{aligned} \quad (36)$$

where $\Delta = \frac{r(r+b)-2Mr}{1+\ell} + a^2$. Following the asymptotic matching process we obtain amplification factor given by

$$Z_{jm} \equiv \frac{|\mathcal{A}_{ref}^{\infty}|^2}{|\mathcal{A}_{in}^{\infty}|^2} - 1 \quad (37)$$

where

$$\begin{aligned} \mathcal{A}_{in}^{\infty} = & \frac{c(-2i)^{-\frac{1+\sqrt{1+4(\ell+1)j(j+1)}}{2}}}{\sqrt{(1+\ell)(\omega^2-\mu^2)}} \cdot \frac{\Gamma(\sqrt{1+4(\ell+1)j(j+1)})\Gamma(1+\sqrt{1+4(\ell+1)j(j+1)})}{\Gamma\left(\frac{1+\sqrt{1+4(\ell+1)j(j+1)}}{2}-2i\sqrt{\ell+1}B\right)\left(\Gamma\left(\frac{1+\sqrt{1+4(\ell+1)j(j+1)}}{2}\right)\right)^2} \times \\ & \Gamma(1-2i\sqrt{\ell+1}B)k_l^{\frac{1-\sqrt{1+4(\ell+1)j(j+1)}}{2}} + \frac{c(-2i)^{\frac{\sqrt{1+4(\ell+1)j(j+1)}-1}{2}}}{\sqrt{(1+\ell)(\omega^2-\hat{\mu}^2)}} \times \\ & \frac{\Gamma(1-\sqrt{1+4(\ell+1)j(j+1)})\Gamma(-\sqrt{1+4(\ell+1)j(j+1)})}{\left(\Gamma\left(\frac{1-\sqrt{1+4(\ell+1)j(j+1)}}{2}\right)\right)^2\Gamma\left(\frac{1-\sqrt{1+4(\ell+1)j(j+1)}}{2}-2i\sqrt{\ell+1}B\right)} \Gamma(1-2i\sqrt{\ell+1}B)k_l^{\frac{1+\sqrt{1+4(\ell+1)j(j+1)}}{2}} \end{aligned} \quad (38)$$

and

$$\begin{aligned} \mathcal{A}_{ref}^{\infty} = & \frac{c(2i)^{-\frac{1+\sqrt{1+4(\ell+1)j(j+1)}}{2}}}{\sqrt{(1+\ell)(\omega^2-\mu^2)}} \cdot \frac{\Gamma(\sqrt{1+4(\ell+1)j(j+1)})\Gamma(1+\sqrt{1+4(\ell+1)j(j+1)})}{\Gamma\left(\frac{1+\sqrt{1+4(\ell+1)j(j+1)}}{2}-2i\sqrt{\ell+1}B\right)\left(\Gamma\left(\frac{1+\sqrt{1+4(\ell+1)j(j+1)}}{2}\right)\right)^2} \times \\ & \Gamma(1-2i\sqrt{\ell+1}B)k_l^{\frac{1-\sqrt{1+4(\ell+1)j(j+1)}}{2}} + \frac{c(2i)^{\frac{\sqrt{1+4(\ell+1)j(j+1)}-1}{2}}}{\sqrt{(1+\ell)(\omega^2-\hat{\mu}^2)}} \times \\ & \frac{\Gamma(1-\sqrt{1+4(\ell+1)j(j+1)})\Gamma(-\sqrt{1+4(\ell+1)j(j+1)})}{\left(\Gamma\left(\frac{1-\sqrt{1+4(\ell+1)j(j+1)}}{2}\right)\right)^2\Gamma\left(\frac{1-\sqrt{1+4(\ell+1)j(j+1)}}{2}-2i\sqrt{\ell+1}B\right)} \Gamma(1-2i\sqrt{\ell+1}B)k_l^{\frac{1+\sqrt{1+4(\ell+1)j(j+1)}}{2}} \end{aligned} \quad (39)$$

We observe that superradiance for a particular j occurs when the allowed values of m are restricted to $m > 0$. For negative m amplification factor takes negative value indicating the nonoccurrence of superradiance. The plots also show transparently that with the decrease in LV parameter the superradiance process is getting enhanced and the reverse is the case when the LV parameter decreases. We have also studied the effect of the parameter $b = \frac{Q^2}{M}$ on the superradiance scenario. It shows that the superradiance scenario gets diminished with the increase in the value of the parameter b . We also observe that as we increase ℓ , the parameter space over which the dynamics of the massive scalar field in Kerr-Sen like black hole shrinks.

VIII. CONSTRAINING PARAMETERS INVOLVED IN MODIFIED GRAVITY USING OBSERVATIONAL DATA FOR M87* BLACK HOLE

We compare the shadows produced, from numerical calculations, by the noncommutative Kerr-like black hole in vacuum, the Kerr-Sen-like black hole in vacuum and when surrounded by plasma with the observed one for the M87* black hole. For comparison, we consider the following experimentally obtained astronomical data [84]:

$$\Delta C \leq 0.10 \quad \text{and} \quad \theta_d = 42 \pm 3 \mu\text{as} \quad (40)$$

where ΔC is the circularity deviation and θ_d is the angular diameter. The boundary of the shadow is described by the polar coordinates $(R(\phi), \phi)$ with the origin at the center of the shadow (α_C, β_C) where $\alpha_C = \frac{|\alpha_{max} + \alpha_{min}|}{2}$ and $\beta_C = 0$.

If a point (α, β) over the boundary of the image subtends an angle ϕ on the α axis at the geometric center, $(\alpha_C, 0)$ and $R(\phi)$ be the distance between the point (α, β) and $(\alpha_C, 0)$, then the average radius R_{avg} of the image is given by [90]

$$R_{\text{avg}}^2 \equiv \frac{1}{2\pi} \int_0^{2\pi} d\phi R^2(\phi), \quad (41)$$

where $R(\phi) \equiv \sqrt{(\alpha(\phi) - \alpha_C)^2 + \beta(\phi)^2}$, and $\phi = \tan^{-1} \frac{\beta(\phi)}{\alpha(\phi) - \alpha_C}$.

With the above inputs, the deviation from circularity ΔC is defined by [91],

$$\Delta C \equiv 2 \sqrt{\frac{1}{2\pi} \int_0^{2\pi} d\phi (R(\phi) - R_{\text{avg}})^2}. \quad (42)$$

We also consider the angular diameter of shadow, which is define by

$$\theta_d = \frac{2}{d} \sqrt{\frac{A}{\pi}} \quad (43)$$

where $A = 2 \int_{r_-}^{r_+} \beta d\alpha$ is the shadow area and $d = 16.8 Mpc$ is the distance of M87* from the earth. In case of M87*, the mass has been estimated to be $M = (6.6 \pm 0.4) \times 10^9 M_\odot$, M_\odot being the mass of Sun [92]. We Consider $M = 6.5 \times 10^9 M_\odot$ for the M87* black hole. These relations will enable us to accomplish a comparison between the theoretical predictions and the experimental findings of the Event Horizon Telescope collaboration. By modelling M87* black hole as Kerr black hole, the author in the article [93] has found a lower limit of a for the M87* black hole. If we bring this result under consideration in the present situation, the interval of interest for a becomes $[0.50M, 0.99M]$ with $b = k = 0$. Now, if we combine the constraints (40) and the knowledge that $a \in [0.50M, 0.99M]$, we observe that $\ell \in (-1, 0.621031]$. Here, we find an upper bound of ℓ , which comes out to be 0.621031. To constrain the charge parameter b of Ker-Sen like black hole, we consider $a \in [0.50M, 0.99M]$ [93] and $\ell \in (-1, 0.621031]$ [95]. With these findings along with the constrains (40), we find that $b \in [0, 0.10242M]$. Here, the upper bound of b is found out to be $0.10242M$. In a similar way taking into account the bounds $a \in [0.50M, 0.99M]$ and $\ell \in (-1, 0.621031]$ and the experimental constraints $\Delta C \leq 0.1$ and $\theta_d = 39 \pm 3 \mu as$, we get a bound on the parameter ϑ_n which is linked with the noncommutativity of spacetime. We find that the parameter $\vartheta_n \in [0, 0.000505973M^2]$. It is intriguing to have an upper bound of ϑ_n which is found out to be $0.000505973M^2$.

IX. STRONG GRAVITATIONAL LENSING IN HAIRY SCHWARZSCHILD BACKGROUND

In the article [222], Ovalle et al. considered Schwarzschild black hole surrounded by spherically symmetric matter. The ansatz for the hairy Schwarzschild black used there was

$$\begin{aligned} ds^2 &= - \left(1 - \frac{2M}{r} + \alpha_h e^{-r/(M - \frac{\ell_0}{2})} \right) dt^2 + \left(1 - \frac{2M}{r} + \alpha_h e^{-r/(M - \frac{\ell_0}{2})} \right)^{-1} dr^2 + r^2 (d\theta^2 + \sin^2 \theta d\phi^2) \\ &= -f(r)dt^2 + f(r)^{-1}dr^2 + r^2 (d\theta^2 + \sin^2 \theta d\phi^2). \end{aligned} \quad (44)$$

were $f(r) = \left(1 - \frac{2M}{r} + \alpha_h e^{-r/(M - \frac{\ell_0}{2})} \right)$, M represents the mass of the black hole and α_h refers to a parameter that induces deformation due to additional sources. Here $\ell_0 = \alpha_h \hat{\ell}$ represents the increase in entropy caused by the hair and to ensure asymptotic flatness, it must satisfy the condition $\ell_0 \leq 2M = \ell_K$. It is evident from our study that the event horizon $r_{eh} = 2Mx_{eh}$ increases with ℓ_0 where $r = 2Mx$. As r_{eh} increases with ℓ_0 , the horizon area A increases and hence the entropy of black hole increases with an increase in ℓ_0 . In the limit $\alpha_h \rightarrow 0$, the (44) reduces to the standard metric corresponding to the Schwarzschild black hole. We observe that the horizon radius decreases with α_h , but it increases with ℓ_0 . Note that for $\alpha_h = 0$ that corresponds to $\ell_0 = 1$ we have $x_{eh} = 1$ which resembles the Schwarzschild metric. However when ℓ_0 is kept constant the horizontal radius decreases with an increase in α_h , but the radius increases with an increase in ℓ_0 when α_h remains constant. It reflects that the horizontal radius for the hairy Schwarzschild black hole is smaller than that for the Schwarzschild black hole. Therefore the presence of hair has a reducing effect on the Schwarzschild radius. We observe that the lensing coefficient \bar{a} increases with α_h but the lensing coefficient \bar{b} and the impact parameter b_m decrease with the increase of α_h . However, with the increase of ℓ_0 , although \bar{a} decrease \bar{b} gets enhanced. The impact parameter b_m increases with the increase of ℓ_0 . The values of the parameters resemble Schwarzschild black hole whenever we put $\alpha_h = 0$.

-
- [1] R. P. Kerr, Phys. Rev. Lett. 11, 237 (1963).
 - [2] R. Penrose: Riv. Nuovo Cim. 1, 252 (1969).
 - [3] R. M. Wald, Phys. Rev. D 48, R3427 (1993).
 - [4] P. J. Young, Phys. Rev. D 14, 3281 (1976).
 - [5] J. M. Bardeen, W. H. Press and S. A. Teukolsky, Astro-phys. J. 178, 347 (1972).
 - [6] A. Sen. Phys.Rev.Lett.69 1006 (1992)
 - [7] K. Hioki and K. I. Maeda, Phys. Rev. D 80, 024042 (2009)
 - [8] S. Hawking, Commun.Math.Phys. 43 (1975) 199
 - [9] S.-W. Wei and Y.-X. Liu, J. Cosmol. Astropart. Phys. 11 063 (2013).
 - [10] U. Papnoi, F. Atamurotov, S. G. Ghosh, B. Ahmedov: Phys. Rev. D 90, 024073 (2014).

Introduction

Our universe presents an amazing variety of physical objects and phenomena. The empty cold intergalactic space, the regions around black holes, the stars, and planets within the arms of galaxies are the main components of the universe. The characters of the stars and planets within one arm of the galaxies are very different in terms of average density, temperature, and gravitational field. It is without a doubt very interesting and important to examine these objects and their features.

The general theory of relativity (GTR) has been found to render a remarkable service in describing gravity and cosmology. The gravitational redshift, the gravitational lensing of light from distant background stars, the anomalous perihelion precession of Mercury, the Shapiro time delay effect, etc. have all demonstrated striking agreement with GTR. The aforementioned hypotheses are also true in areas with weak gravitational fields, such as those found near the Sun [1]. It has been established that binary pulsar orbital shifts caused by gravitational-wave emission and black-hole mergers occur outside of the solar system where we belong [2–4]. But a disastrous event involving strong gravity is the merging of two black holes [4]. In this regime, it is debatable whether GR can accurately represent gravity.

Both theory and experimental results suggest that the strong gravity domain of GTR may still experience significant classical and quantum corrections. By directly observing gravitational waves in ground-based detectors from such events, theories of gravity in the strong-gravity domain should be put to test. Every discovery offers a new viewpoint on the universe, as is always the case, and serves as a catalyst for other discoveries. The future gravitational wave detectors, such as Cosmic Explorer and the Einstein telescope will have a signal-to-noise ratio (SNR) that is at least 50 times greater than the current laser interferometer [7]. These detectors have the potential to confirm or deny general relativity. The biggest surprise from observational cosmology is the rapid expansion of the universe on a large scale [8–11]. The presence of an exotic source called dark energy, or changes in GR on the largest length scales [11] can explain this. Therefore, testing GR in space and GW observations is of great importance in understanding the universe. In the upcoming new missions, we will be able to answer the above questions.

Modified theories of gravity primarily try to address some of the current problems through the observation of contemporary advanced tools, either partially or completely. General relativity can be altered in a variety of ways. This can be accomplished by selecting at least one of the adjustments listed below: 1) by substituting other fields for the metric tensor (and giving it a mass), 2) by using higher-order derivatives of the metric, 3) by using more dimensions than four, 4) Ignoring Lorentz invariance, and 5) Ignoring locality. The spin 2 field of GR can have additional fields added to it in expanded theories of gravity. Scalar, vector, and tensor fields may be included in this. The theory must revert to general relativity at scales where experiments can be performed for it to be true.

From the theoretical point of view, the background spacetime metric is expected to exhibit quantum fluctuations that make it appear ‘foamy’ at close ranges [12]. As a result, models have been put forth in a number of theoretical contexts, including non-critical string theory [13], loop quantum gravity [14], string theory [15], double special relativity [16], and an effective field theory approach [17]. The propagation of light in this spacetime foam has also been theorized to have a non-trivial dispersion relation in vacuum [18] that correlates to Lorentz violation via an energy-dependent light velocity. Additionally, it was mentioned that one potent technique to investigate this possibility could be made possible by far-off astronomical sources of intense photons that show significant and rapid temporal variations, such as gamma-ray bursts (GRBs) [18], which have been studied and constrained by numerous phenomenological analyses using pulsars and active galactic nuclei (AGNs) in addition

to GRBs, has also been raised as a potent way to investigate this possibility. There have been several reported limits in the $M > 10^{15} - 10^{17}$ GeV range [19–23]. Both the significance of Lorentz violation for high-energy cosmic rays and laboratory probes of various types of Lorentz violations have been studied [24, 25].

We consider mainly two types of modification. One type of modification involves Lorentz violation by the incorporation of the bumblebee field. The other type of modification involves the amendment of non-commutative spacetime structure in order to take into account the quantum gravity correction. Our analysis takes into account the effect of the surrounding medium like the presence of plasma and other types of exotic matter in both situations. Special emphasis has been given to the study of the shadow of black hole and attempts has been made to constrain the parameter involved in the model from the recent observation of the Event Horizon (EHT) collaboration concerning the capturing of the shadow of $M87^*$ and $SgrA^*$ supermassive black hole in the center of $M87$ and Milky-Way galaxy respectively. Superradiance phenomena for rotating black holes have also been taken into consideration. The impact of Lorentz violation and non-commutative spacetime on superradiance has been studied. Besides, a special type of modification connected with scalar hair is also considered here. The strong and weak lensing in hairy Schwarzschild background has been studied.

This thesis is organized as follows. In Chapter-I, we discuss the general theory of relativity in brief and the different aspects of it that follows from Einstein's equation. Chapter-II contains an introduction to the Bumblebee model and different aspects of the Schwarzschild-like black hole which is a non-rotating, static, and spherically symmetric solution of Einstein-bumblebee field equations in vacuum. In Chapter III, we modify the Kerr-like black hole taking into account the non-commutative effect, and discuss different aspects of the modified black hole metric. Chapter IV contains detailed calculations of Kerr-Sen-like black hole metric and different aspects of it. In Chapter V, we extend our discussion of Kerr-Sen-like black holes but this time in presence of a dispersive medium. Chapter VI contains a study of the superradiance effect in the background of non-commutative Kerr-like black holes and Kerr-Sen-like black holes. In chapter-VII, we constrain Lorentz violating parameter ℓ , charge parameter b , and non-commutative parameter ϑ_n using observational data for $M87^*$. Chapter VIII is devoted to describing the Strong and weak gravitational lensing in hairy Schwarzschild background. With a succinct summary and conclusions, Chapter IX wraps up the thesis.

Chapter 1

Theory of general relativity in brief in the eyes of Einstein

In 1905 Einstein published his special theory of relativity. While this theory has been able to predict many observed phenomena, it was not complete in true sense. Einstein proposed a new theory of gravity known as general theory of relativity. This theory is characterized by a set of dynamic equations expressed as Einstein field equations showing gravitational interaction as a result of space-time curvature in mass and energy. Albert Einstein published this new theory of gravity as a tensor equation in 1915. Movement of the body under gravitational field is almost completely described by geodesic equation. Einstein used three principles in his development of general theory of relativity.

1. Mach Principle: Ernest Mach suggested some ideas with proof which is known as the Mach principle. There are various forms of the Mach principle: Some forms are used in General relativity some are not. (i). Geometry is determined by distribution of matter. ii. if matter does not exist, no geometry will be displayed. These statements are not absolutely true since there is a vacuum solution of the Einstein field equations. (iii). The local inertial system is persistent through the dynamical fields of the universe. In fact, this form of the Mach principle is key in the idea of Einstein.

2. Equality Principle: The laws of physics are the same for all inertial system. No preferential inertial system is required. According to this principle, locally, it is not possible to differentiate between accelerated and un-accelerated frame. It is also referred to as strong equivalence principle. Following this theory, Einstein derived field equations of general theory of relativity. After these equations were given by Einstein, Hilbert derived the same equations through analogical approach using the action principle.

3. Co-variance principle: Gravity should be independent of the coordinate system. This means that the gravitational field equation is invariant under any coordinate transformation. In other words, the field equations should have a tensor form.

To have covariance, the gravitational Lagrangian density, L^g , cannot have R_{ijkl} or R_{ij} as components. Since scalars are form invariant, L^g can contain scalars like R , R^2 , $R^{ij}R_{ij}$ etc. The simplest choice is R , the Ricci scalar. The Einstein-Hilbert Lagrangian density is given by $R/2\kappa$ where $\kappa = \frac{8\pi G}{c^4}$ is a coupling constant having dimension $[ML^{-1}]$. The action, thus, is given by

$$S^g = \int_{\Omega} d^4x \sqrt{-g} \frac{R}{2\kappa}, \quad (1.1)$$

where Ω and g are 4-volume of the spacetime and determinant of the metric tensor respectively. The above action is for empty spacetime. For spacetime having some source of energy and momentum, the total action is given by

$$S = S^g + S^m \quad (1.2)$$

where S^m is the action for matter having Lagrangian density L^m given by

$$S^m = \int_{\Omega} d^4x \sqrt{-g} L^m. \quad (1.3)$$

1.1. SOLUTIONS OF EINSTEIN'S FIELD EQUATION

Here, spacetime has signature $(+, -, -, -, -)$. If we vary S^m with respect to g^{ij} we get

$$\delta S^m = \frac{1}{2} \int_{\Omega} d^4x \sqrt{-g} T_{ij} \delta g^{ij}. \quad (1.4)$$

Here, T_{ij} are components of energy-momentum tensor. On varying S^g with respect to g^{ij} , we obtain

$$\delta S^g = \frac{1}{2\kappa} \int_{\Omega} d^4x \sqrt{-g} \left[R_{ij} - \frac{1}{2} g_{ij} R \right] \delta g^{ij}. \quad (1.5)$$

Combining above two equations we get

$$\delta S = \int_{\Omega} \left[\frac{1}{2\kappa} (R_{ij} - \frac{1}{2} g_{ij} R) + \frac{1}{2} T_{ij} \right] \delta g^{ij}, \quad (1.6)$$

which in turn gives

$$\frac{2}{\sqrt{-g}} \frac{\delta S}{\delta g^{ij}} = \frac{1}{\kappa} (R_{ij} - \frac{1}{2} g_{ij} R) + T_{ij}. \quad (1.7)$$

According to the action principle

$$\frac{\delta S}{\delta g^{ij}} = 0. \quad (1.8)$$

Thus, we get

$$\begin{aligned} R_{ij} - \frac{1}{2} g_{ij} R &= -\kappa T_{ij} \\ \Rightarrow G_{ij} &= -\kappa T_{ij}. \end{aligned} \quad (1.9)$$

Trace inverted form of the above equation is

$$R_{ij} = -\kappa (T_{ij} - \frac{1}{2} g_{ij} T). \quad (1.10)$$

Here, $G_{ij} = R_{ij} - \frac{1}{2} g_{ij} R$ are the components of the Einstein tensor and T is defined by $T = g^{ij} T_{ij}$. If the spacetime has signature $(-, +, +, +)$, equation (1.9) becomes

$$\begin{aligned} R_{ij} - \frac{1}{2} g_{ij} R &= \kappa T_{ij} \\ \Rightarrow G_{ij} &= \kappa T_{ij}, \end{aligned} \quad (1.11)$$

whose trace inverted form is

$$R_{ij} = \kappa (T_{ij} - \frac{1}{2} g_{ij} T). \quad (1.12)$$

Equations (1.9) and (1.11) are known as Einstein's field equations.

1.1 Solutions of Einstein's field equation

Einstein's field equation was not so straightforward to have a solution. However, endeavours of scientists led to different solution of Einstein's field equations for different physical environment. Let us first consider spherically symmetric vacuum solution.

1.1.1 Schwarzschild solution

The first exact solution of Einstein's equations was found by Karl Schwarzschild in 1916. He obtained the solution for vacuum gravitational field produced by a non-rotating spherical mass. For such a distribution of matter, general metric can be written as

$$g_{\mu\nu} = -e^{2\gamma} dt^2 + e^{2\rho} dr^2 + r^2 (d\theta^2 + \sin^2 \theta d\phi^2), \quad (1.13)$$

1.1. SOLUTIONS OF EINSTEIN'S FIELD EQUATION

where γ and ρ are functions of r . On solving Einstein's equations, one obtains the Schwarzschild metric:

$$ds^2 = - \left(1 - \frac{2M}{r}\right) dt^2 + \left(1 - \frac{2M}{r}\right)^{-1} dr^2 + r^2(d\theta^2 + \sin^2\theta d\phi^2), \quad (1.14)$$

where M is the mass of the black hole in unit of length and $G = c = 1$ for the entire thesis. Since the coefficients of the metric do not depend on t , and the metric does not have any cross term involving space-like and time-like increments, it is a static metric.

Event Horizon

The metric has two singularities, one at $r = 0$ and another at $r = 2M$. The first one cannot be removed using a change of coordinates, but the second one can be removed using a different choice of coordinates. Within the surface $r = 2M$, all future directions point towards decreasing r . Since real bodies travel in time-like or null directions, it is impossible to escape from the region $r < 2M$. The surface $r = 2M$ acts as a one-way membrane. It is called event horizon and the space within this is known as black hole.

Constants of motion

Now, we consider constants of motion in the background of spherical non-rotating mass. Since Schwarzschild metric is a static metric, it has symmetry along time direction. Therefore, we can write $k^\mu = (1, 0, 0, 0)$. Thus, we have

$$\begin{aligned} -g_{\mu\nu}k^\mu u^\nu &= -g_{00}u^0 = -E = \text{Constant} \\ \Rightarrow \left(1 - \frac{2M}{r}\right) \frac{dt}{d\tau} &= E. \end{aligned}$$

Here, $u^\mu = \frac{dx^\mu}{d\tau}$ is the tangent vector to a geodesic and E is the relativistic energy per unit mass of the particle with respect to a stationary observer at infinity. For spherically symmetric mass, we have symmetry along ϕ -direction. For this, we consider $k^\mu = (0, 0, 0, 1)$ and thus, we have

$$g_{\mu\nu}k^\mu u^\nu = g_{33}u^3 = u_3 = L = \text{Constant}, \quad (1.15)$$

which, in turn, gives

$$r^2 \frac{d\phi}{d\tau} = L = \text{Constant} \quad (1.16)$$

Here, L is the angular momentum per unit mass with respect to an observer stationary at infinity.

1.1.2 Motion of a particle in circular orbit

Now, we study the motion of a particle in circular orbit. For this, we consider the equation

$$-1 = -\left(1 - \frac{2M}{r}\right)\left(\frac{dt}{d\tau}\right)^2 + \left(1 - \frac{2M}{r}\right)^{-1}\left(\frac{dr}{d\tau}\right)^2 + r^2\left(\frac{d\phi}{d\tau}\right)^2. \quad (1.17)$$

Using the equations (1.15) and (1.16), we obtain

$$\left(\frac{dr}{d\tau}\right)^2 = E^2 - \left(1 + \frac{L^2}{r^2}\right)\left(1 - \frac{2M}{r}\right). \quad (1.18)$$

For a circular orbit, we have the following two conditions

$$\frac{dr}{d\tau} = 0 \quad \frac{d^2r}{d\tau^2} = 0. \quad (1.19)$$

The first condition gives

$$E = \sqrt{\left(1 + \frac{L^2}{r^2}\right)\left(1 - \frac{2M}{r}\right)}, \quad (1.20)$$

and the second condition yields

$$Mr^2 - L^2r + 3ML^2 = 0. \quad (1.21)$$

The quadratic equation (1.21) yields

$$r = \frac{L^2}{2M} \pm \frac{1}{2} \sqrt{\frac{L^4}{M^2} - 12L^2}. \quad (1.22)$$

For $L^2 > 12M^2$, there are two solutions. The negative sign corresponds to an unstable orbit and the positive sign corresponds to a stable orbit. At $L^2 = 12M^2$, we have one circular orbit which is the innermost (marginally) stable orbit. The condition $L^2 = 12M^2$ gives $r = 6M$. Since it is marginally stable, particle, if perturbed inward, will fall towards $r = 2M$. From equation (1.21), we also get

$$L = \sqrt{\frac{Mr}{1 - 3Mr}}. \quad (1.23)$$

We get the following expression of E using equations (8.1) and (1.23)

$$E = (1 - \frac{2M}{r})(1 - \frac{3M}{r})^{-\frac{1}{2}}. \quad (1.24)$$

The above information leads us to compute the time period of revolution in a circular path as follows:

$$\frac{d\tau}{d\phi} = \frac{r^2}{L} = \frac{r^{\frac{3}{2}}}{\sqrt{M}} \sqrt{1 - \frac{3M}{r}}. \quad (1.25)$$

Thus, the proper period of the particle in the circular orbit is found out to be

$$\tau = \frac{r^2}{L} = 2\pi \frac{r^{\frac{3}{2}}}{\sqrt{M}} \sqrt{1 - \frac{3M}{r}}. \quad (1.26)$$

1.2 Experimental test of general theory of relativity

Using the trajectory in the gravitational field of sun (i.e., in the Schwarzschild spacetime), attempts are usually made to verify the theory of general relativity. In the weak field limit, general theory of relativity necessarily approaches to Newtonian gravity. Therefore, the observation which is consistent with Newtonian theory should have an indirect support to general theory of relativity. However, some phenomena that Newtonian theory cannot explain, those can be explained by general theory of relativity.

1.2.1 The perihelion shift of Mercury

Now, the differential equation of motion of a test mass in the equatorial plane is given by

$$\frac{du^2}{d\phi^2} + u - \frac{M}{L^2} - 3Mu^2 = 0, \quad (1.27)$$

where $u = r^{-1}$. We can write the general solution of the above equation as

$$u \simeq \frac{M}{L^2} [1 + e \cos(\phi(1 - \epsilon))]. \quad (1.28)$$

Here $\epsilon = \frac{3M^2}{L^2} \ll 1$ and e is the eccentricity of the orbit. Thus, for small eccentricity, the perihelion rotates through $\frac{6\pi M^2}{L^2}$.

1.2.2 Bending of light

One of the astonishing results given by general theory of relativity is the bending of light by gravity. In the absence of mass, light rays travel in a straight line. But in the presence of massive objects such as stars and galaxies, light rays coming from left are bent inwards in such a way that their direction viewed from right differs by an angle α which is inversely proportional to the closest distance d of those rays from the center of the object. As d increases, α decreases and as d decreases, α increases. It is this phenomena that is used in gravitational lensing process. Gravitational lensing process has in the past helped us find objects that were hiding behind brighter and closer objects.

1.2.3 Radar echo delay

Radar echo delay is one of the classical tests of general relativity. To explain it, we consider two planets A and B with a massive object S in between them. Now, if we send a radar signal from planet A to B then in the absence of S the signal would travel in a straight line and hence, would take less time to come back to A. But in the presence of the massive object S, due to gravitational time dilation, the signal will take longer time to come back to the planet A after getting reflected from the planet B. This delay in reaching the signal due to gravitational field of the massive object is known as radar echo delay.

1.2.4 Gravitational Redshift

Now, we consider the case of redshift. The proper time, in the Schwarzschild background, is give by

$$d\tau = \left(1 - \frac{2M}{r}\right)^{\frac{1}{2}} dt. \quad (1.29)$$

Since the wavelength of radiation is proportional to the period of vibration, we can write

$$\lambda_r = \left(1 - \frac{2M}{r}\right)^{\frac{1}{2}} \lambda_{\text{inf}}, \quad (1.30)$$

for the relation between the wavelength λ_r of radiation emitted at r and the wavelength λ_{inf} received at infinity. The redshift z is defined by

$$z = \frac{\lambda_{\text{inf}} - \lambda_r}{\lambda_r}, \quad (1.31)$$

and we get

$$1 + z = \left(1 - \frac{2M}{r}\right)^{-\frac{1}{2}}. \quad (1.32)$$

1.2.5 Proper acceleration and surface gravity

From the standard definition, the proper acceleration is given by

$$a^\mu a_\mu = -a^2, \quad (1.33)$$

where 4-acceleration a^μ is defined by

$$a^\mu = \frac{du^\mu}{d\tau} + \Gamma_{\rho\sigma}^\mu u^\rho u^\sigma. \quad (1.34)$$

The components of the 4-velocity of a hovering observer are given by

$$u^\mu = \left(\left(1 - \frac{2M}{r}\right)^{-\frac{1}{2}}, 0, 0, 0\right). \quad (1.35)$$

The non-zero component of the 4-acceleration is given by

$$a^1 = \frac{du^1}{d\tau} + \Gamma_{00}^1 (u^0)^2. \quad (1.36)$$

1.3. KERR SOLUTION

where $\Gamma_{00}^1 = \frac{M}{r^2}(1 - \frac{2M}{r})$. Since $u^1 = 0$, we obtain

$$a^1 = \frac{M}{r^2}, \quad a_1 = g_{11}a^1. \quad (1.37)$$

Finally, we get

$$a^\mu a_\mu = -(\frac{M}{r^2})^2(1 - \frac{2M}{r})^{-1}, \quad (1.38)$$

which ultimately gives $a_p = \frac{M}{r^2}(1 - \frac{2M}{r})^{-\frac{1}{2}}$. The time dilation factor, in this situation, is $(1 - \frac{2M}{r})^{\frac{1}{2}}$. Thus, the expression of surface gravity turns into $\frac{1}{4M}$. This, in short, few aspects of Schwarzschild solution. Let us now turn towards rotating situation.

1.3 Kerr solution

In our universe there are billions of stars and they are not spherical but axisymmetric about an axis of rotation and Schwarzschild's solution is inadequate to study these rotating bodies. However, the exact vacuum solution of Einstein's equations compatible to rotating situation was not known until 1963. It was discovered in 1963 by the ingenious effort of Roy Kerr. The Kerr solution, which describes a rotating black hole in 4D spacetime, is actually the solution of Einstein's equations in vacuum. In other words, the metric is exterior of an axially rotating body. This black hole has a curvature singularity similar to that of Schwarzschild spacetime and is encircled by a horizon. The Kerr metric, in Boyer-Lindquist coordinates, reads [26]

$$ds^2 = -\left(1 - \frac{2Mr}{\rho^2}\right)dt^2 - \frac{4Mra \sin^2 \theta}{\rho^2} dt d\phi + \frac{\rho^2}{\Delta} dr^2 + \rho^2 d\theta^2 + \frac{A \sin^2 \theta}{\rho^2} d\phi^2, \quad (1.39)$$

where $a = \frac{J}{M}$, J being the angular momentum of the black hole and

$$\begin{aligned} \rho^2 &= r^2 + a^2 \cos^2 \theta, \\ \Delta &= r^2 - 2Mr + a^2, \\ A &= (r^2 + a^2)^2 - \Delta a^2 \sin^2 \theta. \end{aligned} \quad (1.40)$$

This black hole does not have explicit variation with time. Therefore, it is stationary. Also it is independent of ϕ and as a result, it is axisymmetric. The specified transformation $(t, \phi) \rightarrow (-t, -\phi)$ keeps it unchanged. This implies that angular velocity gets reversed under time reversal. The time reversal of a rotating object, therefore, suggests the rotation of an object in the reverse direction. The Kerr metric becomes Minkowski's flat metric in the limit $r \rightarrow \infty$. This signifies that the Kerr spacetime is asymptotically flat. Kerr metric is basically a solution having dependence on two parameters. Those parameters are mass M and angular momentum $J = Ma$. For $a = 0$, we recover the Schwarzschild solution. The parameter a has units of length.

1.3.1 Event horizon and Cauchy horizon

From the metric (1.39) we observe that when $\Delta \rightarrow 0$, $g_{11} \rightarrow \infty$. The equation $\Delta = 0$ has two solutions. The solution

$$r_+ = M + \sqrt{M^2 - a^2}, \quad (1.41)$$

is called the event horizon and the solution

$$r_- = M - \sqrt{M^2 - a^2}, \quad (1.42)$$

is called the Cauchy horizon. The equation $\Delta = 0$ has real solution only when $a \leq M$. The case $a = M$ is referred to as extremal Kerr black hole. The figure below exhibits the above mentioned geometrical features of the Kerr metric.

1.3. KERR SOLUTION

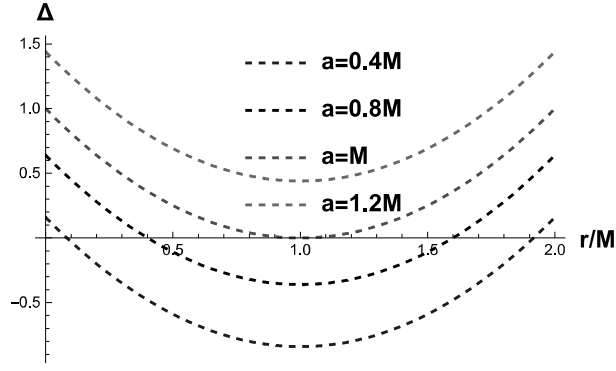


Figure 1.1: Variation of Δ with a . It shows that for $a > M$, $\Delta = 0$ does not have any real solution.

We can see from the plot that the equation $\Delta = 0$ has no solution for $a > M$. So, there will be no black hole for $a > M$.

1.3.2 Static limit surface and ergosphere

We describe here the importance of the surface described by $g_{00} = 0$. For a stationary particle, we have $r = \theta = \phi = \text{Constant}$. Thus

$$1 = -g_{00} \left(\frac{dt}{d\tau} \right)^2. \quad (1.43)$$

For $g_{00} \geq 0$, the above condition cannot be satisfied and hence, within the surface $g_{00} = 0$, no massive particle can be stationary. The surface defined by $g_{00} = 0$ is called static limit surface.

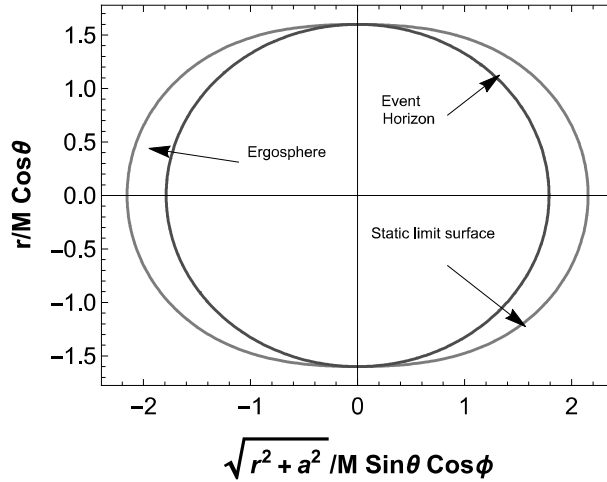


Figure 1.2: Event horizon, ergosphere and static limit surface of a Kerr black hole

The radius of the static limit surface is given by

$$r_{st} = M + \sqrt{M^2 - a^2 \cos^2 \theta}. \quad (1.44)$$

The static limit surface lies outside the event horizon except at poles where two surfaces coincide. The region between the static limit surface and the event horizon is called ergosphere. Since negative energy orbits are possible in the ergosphere, it is possible to extract energy from black hole through Penrose process [27]. In the Fig. below we show variation of ergosphere with a . It shows that the size of the ergosphere is increasing with a .

1.3. KERR SOLUTION

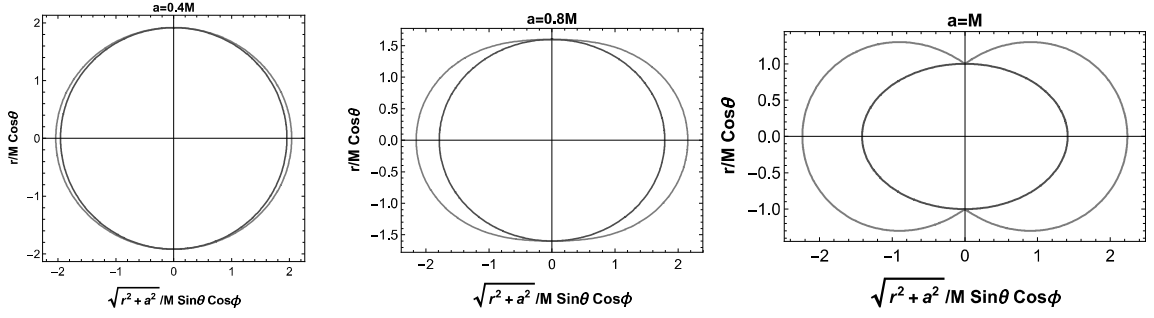


Figure 1.3: Variation of ergosphere with a .

1.3.3 Surface gravity and Hawking temperature

The surface gravity is given by [28]

$$\kappa = -\frac{1}{2} \lim_{r \rightarrow r_+} \sqrt{\frac{-1}{X}} \frac{dX}{dr}, \quad (1.45)$$

where $X \equiv g_{00} - \frac{g_{03}^2}{g_{33}}$. Inserting corresponding metric components we get

$$\kappa = \frac{\Delta'(r_+)}{2[r_+^2 + a^2]} = \frac{r_+ - M}{[r_+^2 + a^2]}. \quad (1.46)$$

The Hawking temperature can be obtained from surface gravity using the relation

$$T_H = \frac{\kappa}{2\pi}. \quad (1.47)$$

Thus, the Hawking temperature is

$$T_H = \frac{r_+ - M}{2\pi[r_+^2 + a^2]}. \quad (1.48)$$

1.3.4 Constants of motion and differential equations of motion

Covariant components of velocity u_0 and u_3 are constants, but it is the contravariant components that are related to the coordinate differentials. We now employ the metric to connect the two sets of components. For the energy equation, we have

$$\frac{dt}{d\lambda} = u^0 = g^{00}u_0 + g^{03}u_3. \quad (1.49)$$

Substituting the metric coefficients we get

$$\rho^2 \frac{dt}{d\lambda} = a(L_z - aE \sin^2 \theta) + \frac{r^2 + a^2}{\Delta} [E(r^2 + a^2) - aL_z], \quad (1.50)$$

where L_z gives the component of the angular momentum of the particle normal to the equatorial plane per unit mass. It is positive for rotation of the particle in the same sense as that of the black hole and negative in the opposite sense, and E is the energy of the particle per unit mass.

For the angular momentum equation, we have

$$\frac{d\phi}{d\lambda} = u^3 = g^{30}u_0 + g^{33}u_3, \quad (1.51)$$

from which we obtain

$$\rho^2 \frac{d\phi}{d\lambda} = \frac{L_z}{\sin^2 \theta} - aE + \frac{a}{\Delta} [E(r^2 + a^2) - L_z a]. \quad (1.52)$$

1.3. KERR SOLUTION

Another constant of motion was discovered by Carter by demonstrating the separability of the Hamilton-Jacobi equation. Let us now study the null geodesics in background of Kerr metric. The Hamilton-Jacobi equation for the geodesic motion is given by

$$2 \frac{\partial S}{\partial \lambda} = g^{ij} \frac{\partial S}{\partial x^i} \frac{\partial S}{\partial x^j}, \quad (1.53)$$

where S denotes Hamilton's principal function. With g^{ij} for the Kerr geometry we have

$$2 \frac{\partial S}{\partial \lambda} = -\frac{1}{\rho^2 \Delta} \left[(r^2 + a^2) \frac{\partial S}{\partial t} + a \frac{\partial S}{\partial \phi} \right]^2 + \frac{1}{\rho^2 \sin^2 \theta} \left[(a \sin^2 \theta) \frac{\partial S}{\partial t} + \frac{\partial S}{\partial \phi} \right]^2 \quad (1.54)$$

$$+ \frac{\Delta}{\rho^2} \left(\frac{\partial S}{\partial r} \right)^2 + \frac{1}{\rho^2} \left(\frac{\partial S}{\partial \theta} \right)^2. \quad (1.55)$$

With the assumption that the variables can be separated, we seek for a solution of the last equation of the form

$$S = \frac{1}{2} \delta_1 \lambda - Et + L_z \phi + S_r(r) + S_\theta(\theta), \quad (1.56)$$

where S_r and S_θ are functions only of the variable specified. For the chosen form of S , we can write

$$\left\{ \Delta \left(\frac{dS_r}{dr} \right)^2 - \frac{1}{\Delta} [(r^2 + a^2) E - a L_z]^2 + (L_z - a E)^2 - \delta_1 r^2 \right\} \quad (1.57)$$

$$+ \left\{ \left(\frac{dS_\theta}{d\theta} \right)^2 + (L_z^2 \operatorname{cosec}^2 \theta - a^2 E^2) \cos^2 \theta - \delta_1 a^2 \cos^2 \theta \right\} = 0. \quad (1.58)$$

The above equation yields

$$\Delta \left(\frac{dS_r}{dr} \right)^2 = \frac{1}{\Delta} [(r^2 + a^2) E - a L_z]^2 - [Q + (L_z - a E)^2 - \delta_1 r^2]. \quad (1.59)$$

and

$$\left(\frac{dS_\theta}{d\theta} \right)^2 = Q - (L_z^2 \operatorname{cosec}^2 \theta - a^2 E^2 - \delta_1 a^2) \cos^2 \theta, \quad (1.60)$$

where Q is a separation constant usually called the Carter constant. Now, we introduce two conserved parameters

$$\xi = \frac{L_z}{E} \quad \text{and} \quad \eta = \frac{Q}{E^2}. \quad (1.61)$$

Equations (1.50) and (1.52) along with equations (1.59) and (1.60), in terms of above conserved quantities, for null geodesics ($\delta_1 = 0$), can be written as

$$\begin{aligned} \rho^2 \frac{dr}{d\lambda} &= \pm \sqrt{R}, & \rho^2 \frac{d\theta}{d\lambda} &= \pm \sqrt{\Theta} \\ \Delta \rho^2 \frac{dt}{d\lambda} &= A - 2Mr a \xi \\ \Delta \rho^2 \frac{d\phi}{d\lambda} &= 2Mr a + \frac{\xi}{\sin^2 \theta} (\rho^2 - 2Mr), \end{aligned} \quad (1.62)$$

where λ is the affine parameter and

$$R(r) = [r^2 + a^2 - a\xi]^2 - \Delta [\eta + (\xi - a)^2], \quad \Theta(\theta) = \eta + a^2 \cos^2 \theta - \xi^2 \cot^2 \theta. \quad (1.63)$$

1.3.5 Frame-dragging

Next, we introduce frame-dragging which is a unique feature of rotating black holes. For a particle falling from infinity with $L_z = 0$, equation (1.50) becomes

$$\rho^2 \frac{dt}{d\lambda} = \frac{[(r^2 + a^2)^2 - a^2 \Delta \sin^2 \theta]}{\Delta} E, \quad (1.64)$$

and the equation (1.52) becomes

$$\rho^2 \frac{d\phi}{d\lambda} = \frac{2Mar}{\Delta} E. \quad (1.65)$$

The angular velocity of the particle, as seen by a distant observer, is

$$\omega(r, \theta) = \frac{d\phi}{dt} = \frac{2Mar}{(r^2 + a^2)^2 - a^2 \Delta \sin^2 \theta}, \quad (1.66)$$

which is clearly non-zero at finite radii. It shows that, though the particle was falling radially without any angular momentum, it acquired angular motion during infall. Since positive a gives positive Ω , the particle obtains angular velocity in the direction of the spin of the black hole. This can be interpreted as a dragging round of the local inertial frames by the rotating hole. The angular velocity of the black hole, Ω_h , is given by putting $\Delta = 0$ and $r = r_+$ in the above equation. Thus

$$\Omega_h = \frac{a}{2Mr_+}. \quad (1.67)$$

1.3.6 Effective potential, critical radii, and conserved parameters

The radial equation of motion (1.62) can be written down in the form

$$\left(\rho^2 \frac{dr}{d\lambda} \right)^2 + V_{eff} = 0. \quad (1.68)$$

The effective potential V_{eff} reads

$$V_{eff} = -[r^2 + a^2 - a\xi]^2 + \Delta[\eta + (\xi - a)^2]. \quad (1.69)$$

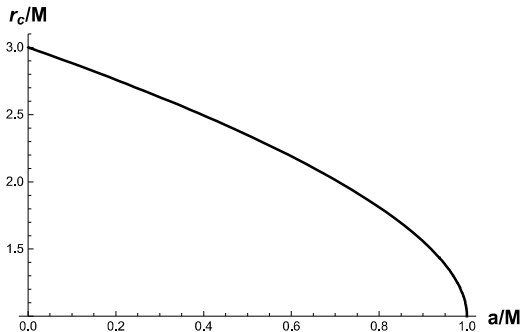
Note that $V_{eff}(0) = 0$ and $V_{eff}(r \rightarrow \infty) \rightarrow \infty$. On the equatorial plane, the unstable spherical orbit is given by the following equations

$$\theta = \frac{\pi}{2}, \quad R(r) = 0, \quad \frac{dR}{dr} = 0, \quad \frac{d^2 R}{dr^2} > 0, \quad \text{and} \quad \eta = 0, \quad (1.70)$$

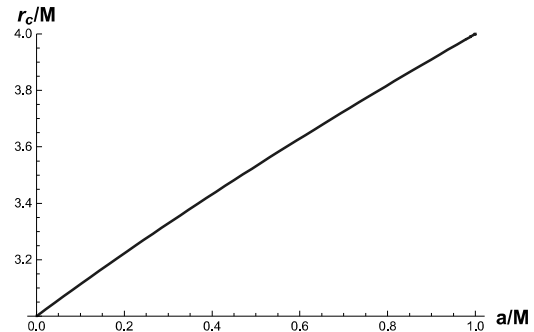
which gives the radius of the unstable orbit as

$$r_c = 2M \left\{ 1 + \cos \left[\frac{2}{3} \cos^{-1} \left(\pm \frac{a}{M} \right) \right] \right\}, \quad (1.71)$$

where the upper sign corresponds to retrograde orbits and the lower sign corresponds to prograde orbits. In case of prograde orbit, particle rotates about the axis of symmetry in the same sense as that of the black hole and in case of retrograde orbit, particle rotates about the axis of symmetry in the opposite sense as that of black hole.



(a) Variation of radius of prograde orbit.



(b) Variation of radius of retrograde orbit.

1.3. KERR SOLUTION

As we can see from the above figures that the radius of prograde orbit decreases with increase in a and the radius of retrograde orbit increases with increase in a .

We have $\theta \neq \pi/2$ for more generic orbits and $\eta \neq 0$ and the solution of Eq. (1.70) for such orbits, $r = r_s$, gives the r - constant orbit, which is also called spherical orbit. For spherical orbits the conserved parameters are given by

$$\begin{aligned}\xi_s &= \frac{a^2 (M + r_s) + r_s (r_s^2 - 3Mr_s)}{a (M - r_s)} \\ \eta_s &= -\frac{r_s^2 \left(-4a^2 Mr_s + (r_s^2 - 3Mr_s)^2 \right)}{a^2 (M - r_s)^2}.\end{aligned}\tag{1.72}$$

1.3.7 Black hole shadow

Next, we discuss the black hole shadow which has become the center of great research after publication of image of the black hole, $M87^*$, by EHT. The black hole shadow is not like the shadows we encounter everyday life. Whereas the shadows we encounter everyday are cast by preventing light from passing objects, a black hole creates effect of a shadow by siphoning light towards itself. The shadow of the black hole is created as follows: Suppose some light rays are emitted at infinity ($r = +\infty$) and propagate near the black hole. If they can reach the observer at infinity after scattering, then its direction is not dark. On the other hand, the observer will never see light rays that fall into the event horizon of a black hole. Such a direction becomes dark. It makes a shadow.

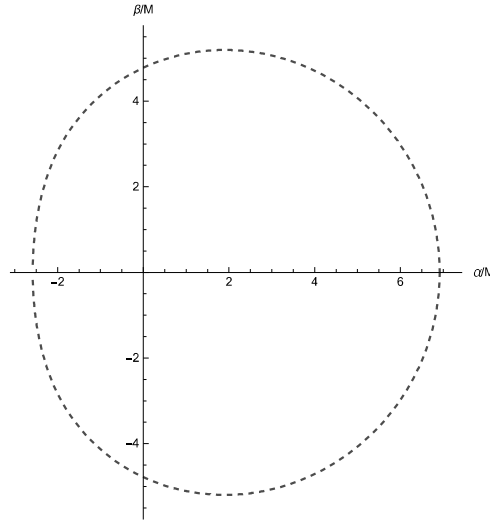
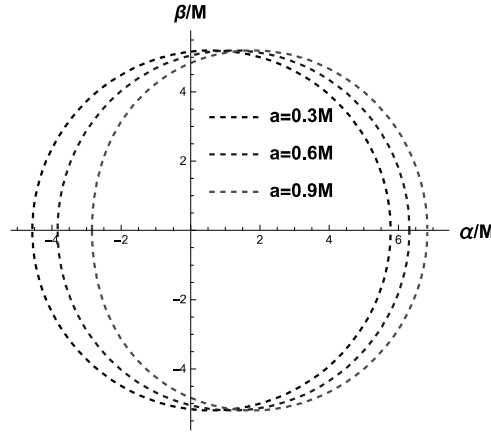


Figure 1.5: Shadow of a Kerr black hole on the equatorial plane.

We define the apparent shape of a black hole by the boundary of the shadow [29]. The shape of the shadow that is seen by an observer in the sky is described by the following celestial coordinates

$$\begin{aligned}\alpha(\xi, \eta; \theta) &= \lim_{r \rightarrow \infty} \frac{-rp^{(\phi)}}{p^{(t)}} = -\xi_s \csc \theta, \\ \beta(\xi, \eta; \theta) &= \lim_{r \rightarrow \infty} \frac{rp^{(\theta)}}{p^{(t)}} = \sqrt{\eta_s + a^2 \cos^2 \theta - \xi_s^2 \cot^2 \theta}.\end{aligned}\tag{1.73}$$

Here, with respect to locally non-rotating reference frames, the tetrad components of the photon momentum are $(p^{(t)}, p^{(r)}, p^{(\theta)}, p^{(\phi)})$ [30]. We show the shape of the shadow below. The shape and size of black hole shadow depends on a as demonstrated below.


 Figure 1.6: Variation of black hole shadow with spin parameter a .

As we can see from the plot, the shadow shifts toward right as a increases.

1.4 Kerr-Sen black hole

In [31], a four dimensional metric is given that describes a rotating and electrically charged black hole in the low energy heterotic string theory. In the low-energy heterotic string theory, action is given by:

$$S = \int d^4x \sqrt{-g} e^{-\Phi} \left(R - \frac{1}{8} F_{\mu\nu} F^{\mu\nu} + g^{\mu\nu} \partial_\mu \tilde{\Phi} \partial_\nu \tilde{\Phi} - \frac{1}{12} H_{k\lambda\mu} H^{k\lambda\mu} \right), \quad (1.74)$$

where Φ is the dilaton field and $H_{k\lambda\mu}$ is a third-rank tensor field defined as

$$H_{k\mu\nu} \equiv \partial_k B_{\mu\nu} + \partial_\nu B_{k\mu} + \partial_\mu B_{\nu k} - \frac{1}{4} (A_k F_{\mu\nu} + A_\nu F_{k\mu} + A_\mu F_{\nu k}), \quad (1.75)$$

where $F_{\mu\nu}$ is the electromagnetic tensor given by

$$F_{\mu\nu} = \partial_\mu A_\nu - \partial_\nu A_\mu \quad (1.76)$$

Here, $B_{\mu\nu}$ is a second-rank antisymmetric tensor gauge field and A_μ is the electromagnetic vector potential. In ([31]), Sen obtained a charged rotating BH solution which came to be known as the Kerr-Sen (KS) solution. The rotating charged metric in Boyer-Lindquist coordinates (t, r, θ, ϕ) is [31]

$$ds^2 = - \left(1 - \frac{2Mr}{\rho^2} \right) dt^2 - \frac{4Mra \sin^2 \theta}{\rho^2} dt d\phi + \frac{\rho^2}{\Delta} dr^2 + \rho^2 d\theta^2 + \frac{A \sin^2 \theta}{\rho^2} d\phi^2. \quad (1.77)$$

where

$$\rho^2 = r(r+b) + a^2 \cos^2 \theta, \Delta = r(r+b) - 2Mr + a^2, \text{ and } A = [r(r+b) + a^2]^2 - \Delta a^2 \sin^2 \theta. \quad (1.78)$$

For $a \rightarrow 0$ and $b \rightarrow 0$, it becomes

$$ds^2 = - \left(1 - \frac{2M}{r} \right) dt^2 + \frac{1}{1 - 2M/r} dr^2 + r^2 d\theta^2 + r^2 \sin^2 \theta d\phi^2, \quad (1.79)$$

The metric (1.77) represents a purely radial black hole solution with specific angular momentum equals to a and charge equals to \sqrt{bM} .

1.4. KERR-SEN BLACK HOLE

1.4.1 Event horizon and ergosphere

The event horizon and the Cauchy horizon are given by the solution of $\Delta = 0$ which are

$$r_{\pm} = M - \frac{b}{2} \pm \frac{\sqrt{(-b + 2M)^2 - 4a^2}}{2}. \quad (1.80)$$

and the location of the static limit surface is

$$r^{ergo} = M - \frac{b}{2} + \frac{\sqrt{(-b + 2M)^2 - 4a^2 \cos^2 \theta}}{2}. \quad (1.81)$$

The variation of size and shape of ergosphere of the Kerr-Sen black hole is shown below.

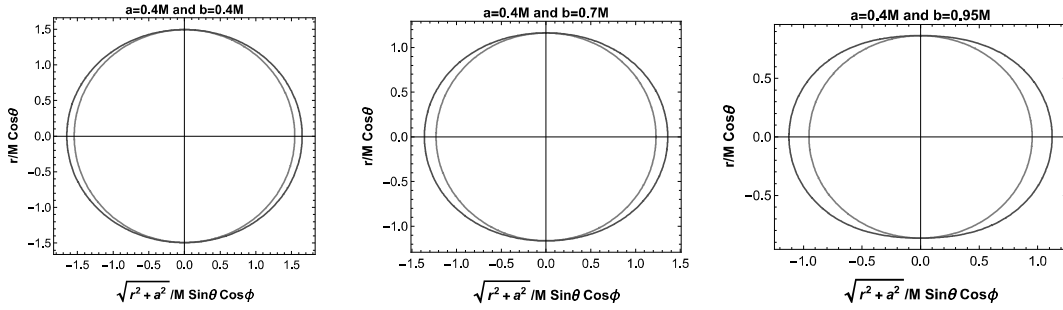


Figure 1.7: Variation of ergosphere with b .

The size of the ergosphere, as we can observe from above, increases with b . There exists a black hole if and only if

$$(-b + 2M) \geq 2a. \quad (1.82)$$

The parameter space for the Kerr-Sen black hole is shown below.

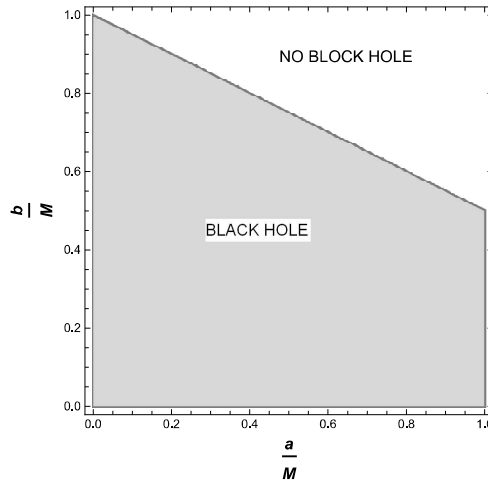


Figure 1.8: Parameter space for the Kerr-Sen black hole.

The blue region is where we will get black hole and the white region is where there will be no black hole. The condition $-b + 2M = 2a$ corresponds to extremal Kerr-Sen black hole where Cauchy and event horizons coincide.

1.4.2 Surface gravity and Hawking temperature

The surface gravity for the Kerr-Sen black hole, using equation (1.45), is given by

$$\kappa = \frac{\sqrt{(2M-b)^2 - 4a^2}}{2M \left(2M - b + \sqrt{(2M-b)^2 - 4a^2} \right)}. \quad (1.83)$$

Thus, the Hawking temperature, using the relation

$$T_H = \frac{\kappa}{2\pi}, \quad (1.84)$$

is given by

$$T_H = \frac{\sqrt{(2M-b)^2 - 4a^2}}{4\pi M \left(2M - b + \sqrt{(2M-b)^2 - 4a^2} \right)}. \quad (1.85)$$

1.4.3 Basic equations

Following the same procedure as that was followed for Kerr black hole, equations for null geodesics in case of Kerr-Sen black hole are given by

$$\begin{aligned} \rho^2 \frac{dr}{d\lambda} &= \pm \sqrt{R}, & \rho^2 \frac{d\theta}{d\lambda} &= \pm \sqrt{\Theta} \\ \Delta \rho^2 \frac{dt}{d\lambda} &= A - 2Mra\xi \\ \Delta \rho^2 \frac{d\phi}{d\lambda} &= 2Mra + \frac{\xi}{\sin^2 \theta} (\rho^2 - 2Mr), \end{aligned} \quad (1.86)$$

where λ is the affine parameter and

$$R(r) = [r(r+b) + a^2 - a\xi]^2 - \Delta [\eta + (\xi - a)^2], \quad \Theta(\theta) = \eta + a^2 \cos^2 \theta - \xi^2 \cot^2 \theta. \quad (1.87)$$

1.4.4 Spherical orbit and Black hole shadow

On the equatorial plane, the unstable spherical orbit is given by the equations (1.70). For more generic orbits, we have $\theta \neq \pi/2$ and $\eta \neq 0$. For such orbits, the solution of Eq. (1.70), $r = r_s$, gives the r -constant orbit. The conserved parameters of the spherical orbits, for the Kerr-Sen black hole, are given by

$$\begin{aligned} \xi_s &= \frac{a^2 (2M + 2r_s + b) + r_s (2r_s^2 + 3br_s + b^2 - 2M (3r_s + b))}{a (2M - 2r_s - b)} \\ \eta_s &= - \frac{r_s^2 \left(-8a^2 M (2r_s + b) + (2r_s^2 + 3br_s + b^2 - 2M (3r_s + b))^2 \right)}{a^2 (2M - 2r_s - b)^2}. \end{aligned}$$

The two celestial coordinates are

$$\begin{aligned} \alpha(\xi, \eta; \theta) &= -\xi_s \csc \theta, \\ \beta(\xi, \eta; \theta) &= \sqrt{(\eta_s + a^2 \cos^2 \theta - \xi_s^2 \cot^2 \theta)}. \end{aligned} \quad (1.88)$$

We show below the variation of black hole shadow with b .

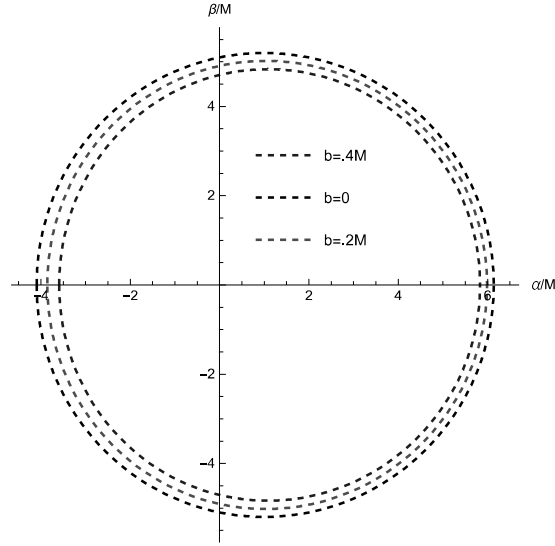


Figure 1.9: The shapes of the shadow for various values of b with $a = 0.5M$ and $\theta = \pi/2$

As we can see, the size of the shadow decreases with an increase in b . This result will be reinforced in the next section.

1.4.5 The deviation from the circular form (δ_s) and the size (R_s) of the shadow

Hioki and Maeda in [32] introduced two parameters, the deviation from the circular form of the shadow (δ_s) and the size (R_s) of the shadow image of the black hole, to study black hole shadow. For calculating these parameters, five points are considered. The four points (α_t, β_t) , (α_b, β_b) , $(\alpha_r, 0)$ and $(\alpha_p, 0)$ are, respectively, the top, bottom, rightmost, and the leftmost point of the shadow, and $(\bar{\alpha}_p, 0)$ is the leftmost point of the reference circle.

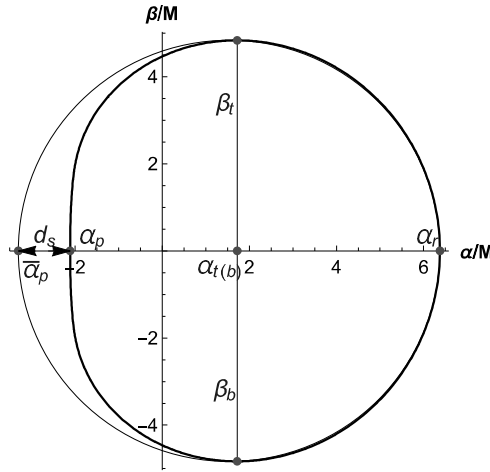


Figure 1.10: A sketch of the black hole shadow and the reference circle. Here, d_s represents the distance between the extreme left point of the shadow and the reference circle.

The expression for the radius R_s is given by

$$R_s = \frac{(\alpha_t - \alpha_r)^2 + \beta_t^2}{2(-\alpha_t + \alpha_r)}. \quad (1.89)$$

Below, we show variation of R_s for Kerr and Kerr-Sen black holes. From plots above we can conclude that size of the shadow, R_s , increases with a but decreases with b . These conclusions are also evident

1.4. KERR-SEN BLACK HOLE

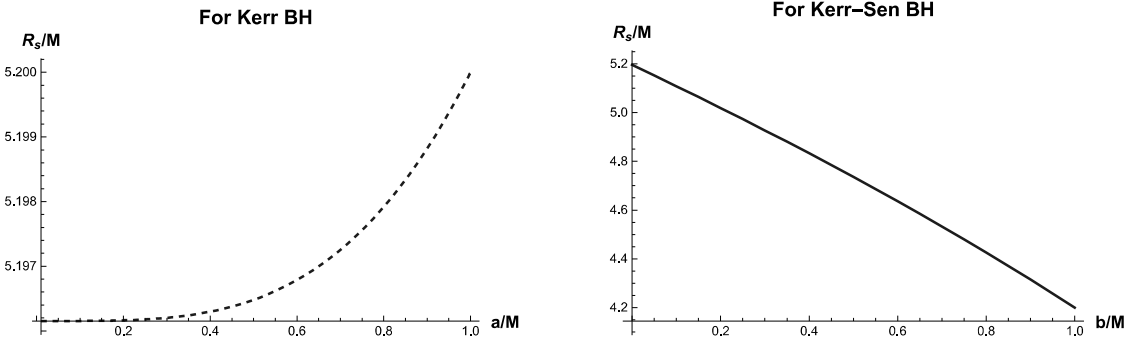


Figure 1.11: The figure at the left side represents the variation of shadow radius R_s with a/M . The figure at the right side represents the variation of R_s with b/M for $a = 0.3M$. For both of them $\theta = \pi/2$.

from Fig. (1.5) and Fig. (1.9).

The deviation from circularity, δ_s , is

$$\delta_s = \frac{(-\bar{\alpha}_p + \alpha_p)}{R_s}. \quad (1.90)$$

Below, we show the variation of δ_s for Kerr and Kerr-Sen black holes.

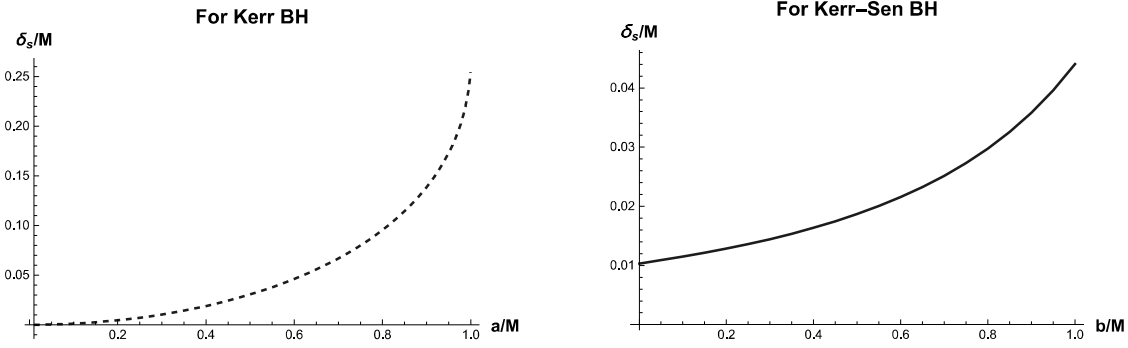


Figure 1.12: The figure at the left side represents the variation of δ_s with a/M . The figure at the right side represents the variation of δ_s with b/M for $a = 0.3M$. For both of them $\theta = \pi/2$.

As we can conclude from above plots, the shadow deviates more and more from circular form as we increase a or b .

1.4.6 Rate of Energy Emission

We know that black holes emit radiation and the mass of the black hole, as a result, decreases and the process continues until it collapses down completely [33]. For various black holes, authors have studied this emission rate [34–36]. In [34], it was conjectured that the black hole shadow corresponds to the high energy absorption cross-section of the black hole for the observer located at infinity. In general, the absorption cross-section oscillates around a limiting constant value σ_{lim} for a spherically symmetric black hole. In [34, 195, 203], it was found that the limiting value is equal to the geometrical cross section of its photon sphere. As we can see from Fig. (1.5) and Fig. (1.9), shadows are almost a circle. Therefore, we can write

$$\sigma_{lim} \approx \pi R_s^2. \quad (1.91)$$

Hence, the rate of emission is given by

$$\frac{d^2 E}{d\omega dt} = \frac{2\pi^3 R_s^2}{e^{\frac{\omega}{T_H}} - 1} \omega^3. \quad (1.92)$$

where ω is the frequency and T_H is the Hawking temperature which given by Eq. (1.48) and Eq. (1.85) for Kerr black holes and Kerr-Sen black holes respectively. Next, we plot emission rate for Kerr

1.4. KERR-SEN BLACK HOLE

and Kerr-Sen black holes. For Kerr-Sen black hole, we have taken $a = 0.3M$. We have considered equatorial plane i.e. $\theta = \pi/2$ for both of them.

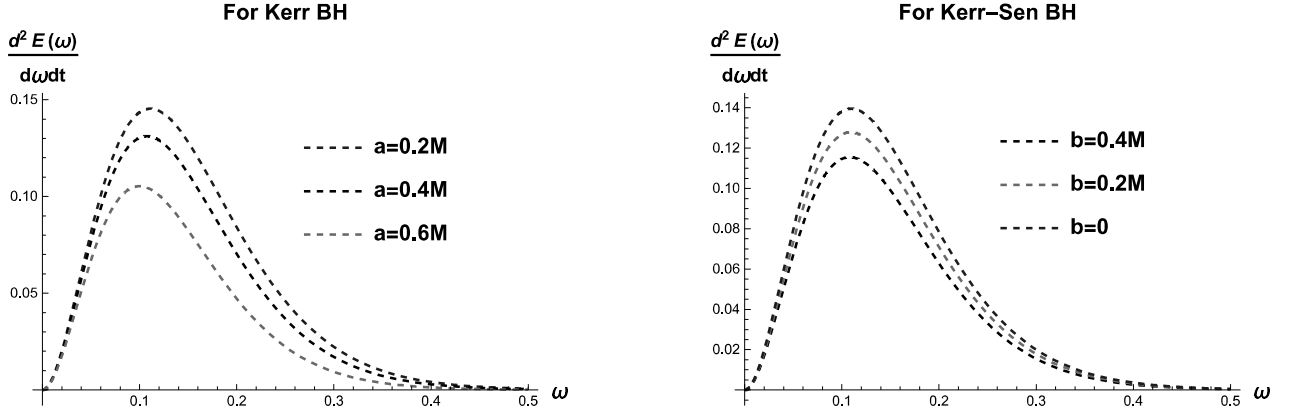


Figure 1.13: The figure at the left side represents the variation of emission rate with ω for Kerr black hole for different values of a . The figure at the right side shows the variation of emission rate with ω for Kerr-Sen black hole for different values of b .

It is evident from above plots that the rate of emission increases with an increase in a , whereas it decreases with an increase in b .

Chapter 2

Spontaneous Lorentz symmetry breaking and the Bumblebee model

General relativity and the standard model of particle physics are two very successful field theoretical models that assist us to describe our Universe. The formulation of both these theories is based on the well celebrated Lorentz symmetry. However, the regime of applicability and the nature of service towards describing the Universe by these two theories are profoundly different. The general relativity describes the gravitational interaction and it is a classical field theory in the curved spacetime and there is no direct way to include the quantum effect. On the contrary, the standard model describes the other fundamental interactions and it is the quantum field theory in the flat spacetime that neglects all gravitational effects, but to study the physical system in the vicinity of the Plank scale ($10^{-19} GeV$), the effect due to gravity cannot be ignored, since the gravitational interaction is strong enough in that energy scale. Therefore, the study of physics in the vicinity of the Planck scale necessarily entails the unification of general relativity and standard model of particle physics. Motivated by this, in recent times theorists have started to doubt whether the Lorentz symmetry is an exact symmetry of nature. Indeed, the central point of recent research in quantum-gravity phenomenology is the search for Lorentz violation.

According to string theory, Lorentz invariance should not be an exact principle at all energy scales [15,37–39]. If Lorentz violation (LV) is considered to be a probe for the foundation of theoretical physics, then a suitable model is needed, which contains LV adopted from the standard physical principle. The LV has been introduced through the formulation of an effective field theory known as standard model extension(SME), where particle standard model along with GR has been attempted to bring together in one framework and every operator is expected to break the Lorentz symmetry [40–43]. Standard model extension provides essential inputs to probe LV, both in high energy particle physics and astrophysics. The SME can be used in analysis of most modern experimental results indeed. Einstein-bumblebee model is essentially a simple model that contains Lorentz symmetry breaking scenario in a significant manner in which the physical Lorentz symmetry breaks down through an axial vector field known as the bumblebee field. The breaking of the Lorentz symmetry in a local Lorentz frame takes place when at least one quantity carrying local Lorentz indices receives non-vanishing vacuum expectation value. In the Einstein-bumblebee model, it is the bumblebee field that receives it. The violation of Lorentz symmetry arises from the dynamics of the bumblebee field vector B_μ , that assumes vacuum expectation value, b_μ , which is unequal to zero. It is the vacuum value b_μ that acts as a fixed background field and is responsible for the spontaneous breaking of Lorentz symmetry. The spontaneous LV is triggered by a potential whose functional form has a minimum, ensuring $U(1)$ symmetry breaking. It is described by the action [44]

$$S = \int d^4x \sqrt{-g} \left[\frac{1}{16\pi G_N} (\mathcal{R} + \varrho B^\mu B^\nu \mathcal{R}_{\mu\nu}) - \frac{1}{4} B^{\mu\nu} B_{\mu\nu} - V(B^\mu) \right], \quad (2.1)$$

where ϱ^2 is a real coupling constant (with mass dimension -1) which controls the non-minimal gravity interaction to bumblebee field B_μ which has the mass dimension 1. The field strength tensor corre-

sponding to the bumblebee field reads

$$B_{\mu\nu} = \partial_\mu B_\nu - \partial_\nu B_\mu. \quad (2.2)$$

A suitable potential gives rise to a spontaneous Lorentz symmetry rendering a vacuum expectation value to the field B_μ . The conventional functional form of the potential $V(B^\mu)$ that induces Lorentz symmetry breaking is

$$V = V(B_\mu B^\mu \pm b^2), \quad (2.3)$$

in which b^2 is a real positive constant. It donates a non-vanishing vacuum expectation value (VEV) for the field B_μ . This potential is assumed to have a minimum through the condition

$$B_\mu B^\mu \pm b^2 = 0. \quad (2.4)$$

The Eq. (2.4) ensures that a nonzero VEV,

$$\langle B^\mu \rangle = b^\mu, \quad (2.5)$$

will be supplied to the field B_μ by the potential V . The vector b^μ is a function of the spacetime coordinates having constant magnitude $b_\mu b^\mu = \mp b^2$. Here \pm signs indicates that b^μ may have time-like as well as space-like nature depending upon the choice of sign. The gravitational field equation in vacuum that follows from the action (2.1) reads

$$\mathcal{R}_{\mu\nu} - \frac{1}{2}g_{\mu\nu}\mathcal{R} = \kappa T_{\mu\nu}^B, \quad (2.6)$$

where $\kappa = 8\pi G_N$ is the gravitational coupling constant and the bumblebee energy momentum tensor $T_{\mu\nu}^B$ has the following expression

$$\begin{aligned} T_{\mu\nu}^B &= B_{\mu\alpha}B_\nu^\alpha - \frac{1}{4}g_{\mu\nu}B^{\alpha\beta}B_{\alpha\beta} - g_{\mu\nu}V + 2B_\mu B_\nu V' \\ &+ \frac{\varrho}{\kappa} \left[\frac{1}{2}g_{\mu\nu}B^\alpha B^\beta R_{\alpha\beta} - B_\mu B^\alpha R_{\alpha\nu} - B_\nu B^\alpha R_{\alpha\mu} \right. \\ &+ \left. \frac{1}{2}\nabla_\alpha \nabla_\mu (B^\alpha B_\nu) + \frac{1}{2}\nabla_\alpha \nabla_\nu (B^\alpha B_\mu) - \frac{1}{2}\nabla^2 (B^\mu B_\nu) - \frac{1}{2}g_{\mu\nu}\nabla_\alpha \nabla_\beta (B^\alpha B^\beta) \right]. \end{aligned} \quad (2.7)$$

Here prime (') denotes differentiation with respect to the argument,

$$V' = \left. \frac{\partial V(x)}{\partial x} \right|_{x=B^\mu B_\mu \pm b^2}. \quad (2.8)$$

Using the trace of Eq. (2.7) we obtain the trace-reversed version

$$\mathcal{R}_{\mu\nu} = \kappa T_{\mu\nu}^B + 2\kappa g_{\mu\nu}V - \kappa g_{\mu\nu}B^\alpha B_\alpha V' + \frac{\varrho}{4}g_{\mu\nu}\nabla^2 (B^\alpha B_\alpha) + \frac{\varrho}{2}g_{\mu\nu}\nabla_\alpha \nabla_\beta (B^\alpha B^\beta). \quad (2.9)$$

One can immediately see that when the bumblebee field B_μ vanishes, we recover the ordinary Einstein equations. The equation of motion for the bumblebee field is

$$\nabla^\mu B_{\mu\nu} = 2V' B_\nu - \frac{\varrho}{\kappa} B^\mu R_{\mu\nu}. \quad (2.10)$$

When the bumblebee field remains frozen in its vacuum expectation value (VEV) we are allowed to write

$$\begin{aligned} B_\mu &= b_\mu \\ b_{\mu\nu} &= \partial_\mu b_\nu - \partial_\nu b_\mu. \end{aligned} \quad (2.11)$$

Under this condition, form of the potential is irrelevant. We have

$$V = 0 \quad \text{and} \quad V' = 0. \quad (2.12)$$

In this situation, Einstein equations acquire a generalized form:

$$\begin{aligned} & \mathcal{R}_{\mu\nu} - \kappa b_{\mu\alpha} b_{\nu}^{\alpha} + \frac{\kappa}{4} g_{\mu\nu} b^{\alpha\beta} b_{\alpha\beta} + \varrho b_{\mu} b^{\alpha} \mathcal{R}_{\alpha\nu} + \varrho b_{\nu} b^{\alpha} \mathcal{R}_{\alpha\mu} \\ & - \frac{\varrho}{2} g_{\mu\nu} b^{\alpha} b^{\beta} \mathcal{R}_{\alpha\beta} - \frac{\varrho}{2} [\nabla_{\alpha} \nabla_{\mu} (b^{\alpha} b_{\nu}) + \nabla_{\alpha} \nabla_{\nu} (b^{\alpha} b_{\mu}) - \nabla^2 (b_{\mu} b_{\nu})] = 0 \\ & \Rightarrow \bar{R}_{\mu\nu} = 0, \end{aligned} \quad (2.13)$$

with

$$\begin{aligned} \bar{R}_{\mu\nu} &= \mathcal{R}_{\mu\nu} - \kappa b_{\mu\alpha} b_{\nu}^{\alpha} + \frac{\kappa}{4} g_{\mu\nu} b^{\alpha\beta} b_{\alpha\beta} + \varrho b_{\mu} b^{\alpha} \mathcal{R}_{\alpha\nu} + \varrho b_{\nu} b^{\alpha} \mathcal{R}_{\alpha\mu} - \frac{\varrho}{2} g_{\mu\nu} b^{\alpha} b^{\beta} \mathcal{R}_{\alpha\beta} + \bar{B}_{\mu\nu} \\ \bar{B}_{\mu\nu} &= -\frac{\varrho}{2} [\nabla_{\alpha} \nabla_{\mu} (b^{\alpha} b_{\nu}) + \nabla_{\alpha} \nabla_{\nu} (b^{\alpha} b_{\mu}) - \nabla^2 (b_{\mu} b_{\nu})]. \end{aligned} \quad (2.14)$$

2.1 Schwarzschild-like Lorentz violating black hole solution

In this chapter we discuss some of the salient features of the Schwarzschild-like black hole which is a static, spherically symmetric vacuum solution of the modified Einstein equations (2.13). The solution was obtained by Casana et al. in [44] by assuming that the spacetime is governed by the metric of the form

$$g_{\mu\nu} = -e^{2\gamma} dt^2 + e^{2\rho} dr^2 + r^2 (d\theta^2 + \sin^2 \theta d\phi^2), \quad (2.15)$$

where γ and ρ are functions of r . Moreover, $b_{\mu} = [0, b_r(r), 0, 0]$ is set as space like background for the bumblebee field b_{μ} which satisfies the condition $b^{\mu} b_{\mu} = b^2 = \text{Constant}$. With these assumptions, the static, spherically symmetric vacuum solution of modified equations (2.13) is found out to be [44]

$$ds^2 = -\left(1 - \frac{2M}{r}\right) dt^2 + (1 + \ell) \left(1 - \frac{2M}{r}\right)^{-1} dr^2 + r^2 (d\theta^2 + \sin^2 \theta d\phi^2), \quad (2.16)$$

where the parameter ℓ is defined by $\ell = \varrho b^2$, termed as Lorentz violating(LV) parameter. In the limit $\ell \rightarrow 0$, the metric (2.16) yields the well-known Schwarzschild solution. Although the metric has a structural similarity with the Schwarzschild metric, it is known to be very different from that since this metric renders the following Kretschmann scalar

$$\mathcal{K} = \frac{4(12M^2 + 4LMr + \ell^2 r^2)}{r^6 (1 + \ell)^2}. \quad (2.17)$$

2.1.1 Hawking temperature

The Hawking temperature is given by

$$T_H = \frac{1}{4\pi \sqrt{-g_{tt} g_{rr}}} \left. \frac{dg_{tt}}{dr} \right|_{r=r_h}. \quad (2.18)$$

Here $g_{tt} = -\left(1 - \frac{2M}{r}\right)$, $g_{rr} = (1 + \ell) \left(1 - \frac{2M}{r}\right)^{-1}$, and the event horizon $r_h = 2M$. Putting these values in the above equation, we obtain the Hawking temperature for the metric (2.16) as

$$T_H = \frac{1}{2\pi \sqrt{1 + \ell}} \left. \frac{M}{r^2} \right|_{r=r_h} = \frac{1}{8\pi M \sqrt{1 + \ell}}. \quad (2.19)$$

It is clear from the above expression that as the LV parameter increases, the Hawking temperature decreases. In the limit $\ell \rightarrow 0$, we obtain $T_H = \frac{1}{8\pi M}$, which is the Hawking temperature for the Schwarzschild black hole.

2.1.2 Redshift for both static and free-falling source.

Let us first consider the redshift scenario in the bumblebee gravity. To this end, we compute the redshift due to bumblebee gravity for both static and free-falling emitting sources. For static source, it can be easily understandable that the redshift will remain unaffected by bumblebee gravity background since we have the same expression of proper time as we find in Schwarzschild background i.e.

$$d\tau = \left(1 - \frac{2M}{r}\right)^{\frac{1}{2}} dt. \quad (2.20)$$

Since the wavelength of radiation is proportional to the period of vibration, the above equation gives us

$$\lambda_r = \left(1 - \frac{2M}{r}\right)^{\frac{1}{2}} \lambda_\infty, \quad (2.21)$$

for the relation between the wavelength λ_r of radiation emitted at r and the wavelength λ_∞ received at infinity. For the redshift z , defined by

$$z = \frac{\lambda_\infty - \lambda_r}{\lambda_r}, \quad (2.22)$$

we get

$$1 + z = \left(1 - \frac{2M}{r}\right)^{-\frac{1}{2}}, \quad (2.23)$$

which is the same as that for Schwarzschild background. Thus, amount of redshift does not depend on LV factor ℓ . Let us now consider a free falling source and see what does it results.

Consider the case of a probe in radial free-fall emitting signals back to a spaceship at infinity. To find out the relationship between the received and transmitted wavelengths, we have to compute the scalar product $u^\mu p_\mu$, where u^μ is the 4-velocity of the probe and p^μ is the 4-momentum of the emitted photon. A straightforward calculation enables us to evaluate the scalar product in a local freely falling frame in which the probe is stationary which is given by

$$u^\mu p_\mu = h\nu,$$

where ν is the frequency of the signal in the rest frame of the probe. Now, we calculate the scalar product in the Schwarzschild-like frame generated from Einstein-bumblebee background. The components of the 4-velocity of the probe in this Schwarzschild-like modified frame, assuming it has dropped from rest at infinity, are

$$(u^\mu) = \left(\left(1 - \frac{2M}{r}\right)^{-1}, -\left(\frac{2M}{r(1+\ell)}\right)^{\frac{1}{2}}, 0, 0 \right),$$

with $E = 1$. The u^1 component is obtained from $g_{\mu\nu} u^\mu u^\nu = 1$ with the assumption that the probe falls from rest at infinity. The covariant components of the outwardly propagating photon are

$$(p_\mu) = \left(h\nu_\infty, -\frac{h\nu_\infty \sqrt{(1+\ell)}}{\left(1 - \frac{2M}{r}\right)}, 0, 0 \right).$$

So,

$$\begin{aligned} u^\mu p_\mu &= \frac{h\nu_\infty}{\left(1 - \frac{2M}{r}\right)} + \left(\frac{2M}{r}\right)^{\frac{1}{2}} \frac{h\nu_\infty}{\left(1 - \frac{2M}{r}\right)} \\ &= h\nu_\infty \frac{\left[1 + \left(\frac{2M}{r}\right)^{\frac{1}{2}}\right]}{\left(1 - \frac{2M}{r}\right)} \\ &= h\nu_\infty \left(1 - \left(\frac{2M}{r}\right)^{\frac{1}{2}}\right)^{-1} = h\nu, \end{aligned}$$

where the final expression follows from the invariance of the scalar product. Therefore, the wavelength at infinity results out to be $\lambda_\infty = \lambda_r \left(1 - \left(\frac{2M}{r}\right)^{1/2}\right)^{-1}$. Note that it is also ℓ independent like the static case. So, for both static and free-falling emitter, the redshift scenarios remain unaffected by the Lorentz violating effect associated with the bumblebee gravity. However, the other features do not remain the same which will be revealed in the following sections.

2.1.3 Surface Gravity

We now proceed to calculate the surface gravity in this new background. It is known that the surface gravity is the local proper acceleration multiplied by the gravitational time dilation factor. From the standard definition, the proper acceleration is given by

$$a^\mu a_\mu = -a^2, \quad (2.24)$$

where 4-acceleration a^μ is given by

$$a^\mu = \frac{du^\mu}{d\tau} + \Gamma_{\rho\sigma}^\mu u^\rho u^\sigma. \quad (2.25)$$

Let us now write down the component of the 4-velocity of a hovering observer:

$$u^\mu = \left(\left(1 - \frac{2M}{r}\right)^{-\frac{1}{2}}, 0, 0, 0\right). \quad (2.26)$$

The only non-zero component that the 4-acceleration contains is

$$a^1 = \frac{du^1}{d\tau} + \Gamma_{00}^1 (u^0)^2, \quad (2.27)$$

where $\Gamma_{00}^1 = \frac{M}{r^2(1+\ell)}\left(1 - \frac{2M}{r}\right)$. Since $u^1 = 0$, we obtain

$$a^1 = \frac{M}{r^2(1+\ell)}, \quad a_1 = g_{11}a^1. \quad (2.28)$$

We, therefore, have

$$a^\mu a_\mu = -\frac{1}{1+\ell} \left(\frac{M}{r^2}\right)^2 \left(1 - \frac{2M}{r}\right)^{-1}, \quad (2.29)$$

which ultimately gives $a_p = \frac{1}{\sqrt{1+\ell}} \frac{M}{r^2} \left(1 - \frac{2M}{r}\right)^{-\frac{1}{2}}$. The time dilation factor in this situation is $\left(1 - \frac{2M}{r}\right)^{\frac{1}{2}}$. Thus the expression of surface gravity turns into

$$\chi_{BB} = \frac{M}{r^2 \sqrt{1+\ell}} \Big|_{r \rightarrow 2M} = \frac{1}{4M \sqrt{1+\ell}}. \quad (2.30)$$

It shows that the surface gravity for the bumblebee background depends on the LV factor ℓ in an explicit manner. While the redshift scenario does remain unaffected by the LV factor, the surface gravity does not remain so. One more surprise is laid in the study of particle motion under this background to which we now turn.

2.1.4 Circular orbit in bumblebee background

To see the dependence of circular motion of a particle on LV factor ℓ , let us study the motion of a particle in a circular orbit in the bumblebee background. For bumblebee background, we have

$$1 = \left(1 - \frac{2M}{r}\right) \left(\frac{dt}{d\tau}\right)^2 - (1+\ell) \left(1 - \frac{2M}{r}\right)^{-1} \left(\frac{dr}{d\tau}\right)^2 - r^2 \left(\frac{d\phi}{d\tau}\right)^2. \quad (2.31)$$

Along any geodesic in the presence of bumblebee background we can, therefore, obtain

$$\left(1 - \frac{2M}{r}\right) \frac{dt}{d\tau} = E = \text{constant}. \quad (2.32)$$

Here, E is the relativistic energy per unit mass of the particle relative to a stationary observer at infinity. We have one more information regarding this motion given by

$$r^2 \frac{d\phi}{d\tau} = L = \text{constant}, \quad (2.33)$$

where L is the angular momentum per unit mass relative to an observer at infinity. Using the above two equations we obtain

$$\left(\frac{dr}{d\tau}\right)^2 = \frac{E^2}{1+\ell} - \frac{1}{1+\ell} \left(1 + \frac{L^2}{r^2}\right) \left(1 - \frac{2M}{r}\right). \quad (2.34)$$

For a circular orbit, the following two conditions

$$\frac{dr}{d\tau} = 0 \quad \text{and} \quad \frac{d^2r}{d\tau^2} = 0, \quad (2.35)$$

must be satisfied. The first condition gives us the same result as that obtained in Eq. (8.1) and the second condition, after some simplification, turns out to be

$$Mr^2 - L^2r + 3ML^2 = 0. \quad (2.36)$$

The quadratic equation (2.36) yields the following solution for r ,

$$r = \frac{L^2}{2M} \pm \frac{1}{2} \sqrt{\frac{L^4}{M^2} - 12L^2}. \quad (2.37)$$

With this r , the expression of L comes out to be same as that given in Eq. (1.23). We get the following expression of E using equations (8.1) and (1.23).

$$E = \left(1 - \frac{2M}{r}\right) \left(1 - \frac{3M}{r}\right)^{-\frac{1}{2}}. \quad (2.38)$$

Note that for circular orbit the equation (2.38) has no LV factor but the energy of a particle in non-circular orbit does not remain independent of LV factor as it is known in the article [44]. The above information leads us to compute the time period of revolution in a circular path as follows:

$$\frac{d\tau}{d\phi} = \frac{r^2}{L} = \frac{r^{\frac{3}{2}}}{\sqrt{M}} \sqrt{1 - \frac{3M}{r}}. \quad (2.39)$$

Thus, proper period of the particle in the circular orbit is found out to be

$$\tau = \frac{r^2}{L} = 2\pi \frac{r^{\frac{3}{2}}}{\sqrt{M}} \sqrt{1 - \frac{3M}{r}}. \quad (2.40)$$

We observe that the proper period of a circular orbit in the bumblebee background is identical with the time period for Schwarzschild background and it does not depend on LV factor ℓ . If we look at the expression of a general non-circular orbit, we find that the time period in that situation for bumblebee background was exclusively dependent on the LV factor. So, the LV factor has no influence on the symmetric circular orbit! We would like to mention that this result may follow from the general discussion of the article [44]. A careful look reveals that the expression for the energy (8.1) coincides with the equation (47) of the article [44], since the only ℓ independent contribution comes from the \dot{r} term which vanishes for the circular orbit. So, the result obtained here in this regard is in agreement with the article [44]. What follows next is much involved: the study of a particle motion in the bumblebee gravity where the canonical variable satisfies non-commutative but Lorentz Symmetric Snyder algebra. This problem in the Schwarzschild background was studied in [45]. The motivation of generalization of it in bumblebee gravity is, therefore, automatic after the work of Mignemi et al. [45]. Besides, both the Lorentz effect and the effect due to the non-commutative setting are supposed to appear in the vicinity of the Planck scale. So, the study of the unified effect is instructive. Before going to study the motion of a particle in the bumblebee gravity with Snyder non-commutative framework, it will be beneficial to give a brief discussion of Snyder formulation.

2.1.5 A discussion of Snyder algebra

Here we discuss the general Snyder algebra. The non-canonical generalization of the canonical Poisson brackets that follow from [46] is

$$\{x_\mu, p_\nu\} = \eta_{\mu\nu} + \lambda_s p_\mu p_\nu + \alpha x_\mu x_\nu + \alpha \lambda_s p_\mu x_\nu, \quad \{x_\mu, x_\nu\} = \lambda_s J_{\mu\nu}, \quad \{p_\mu, p_\nu\} = 0, \quad (2.41)$$

where $J_{\mu\nu} = x_\nu p_\mu - x_\mu p_\nu$, $\eta_{\mu\nu}$ is the flat metric with signature $(-1, 1, 1, 1)$ and λ_s and α are two coupling constants and the square of these two are having the dimension of inverse Planck length and inverse Planck mass respectively. For $\alpha \rightarrow 0$, the algebra (2.41) reduces to the ordinary Snyder non-relativistic model with which we are interested in our present article. So, precisely the algebra reads

$$\{x_\mu, p_\nu\} = \eta_{\mu\nu} + \lambda_s p_\mu p_\nu, \quad \{x_\mu, x_\nu\} = \lambda_s J_{\mu\nu}, \quad \{p_\mu, p_\nu\} = 0. \quad (2.42)$$

In ordinary units, this corresponds to $\lambda_s^2 \sim \sqrt{\hbar}/cM_{Pl} \sim 10^{-17}(\text{s/kg})^{1/2}$. The Poisson bracket (2.42) preserves the Lorentz invariance. In order to study the free particle in a bumblebee gravity background with the non-canonical framework of Snyder, it would be beneficial to work with polar coordinates. The spatial sections with polar coordinates are parameterized in terms of Cartesian coordinates as follows

$$t = x_0 = -x^0, \quad \rho = \sqrt{(x^1)^2 + (x^2)^2}, \quad \theta = \tan^{-1} \frac{x^2}{x^1}. \quad (2.43)$$

Therefore, the momenta corresponding to the polar coordinates can be written down as

$$p_t = p_0, \quad p_\rho = \frac{x^1 p_1 + x^2 p_2}{\sqrt{(x^1)^2 + (x^2)^2}}, \quad p_\theta \equiv J_{12} = x_1 p_2 - x_2 p_1, \quad (2.44)$$

in order to satisfy the canonical Poisson bracket. Using the Snyder algebra (2.42) it is straightforward to see that the phase space in the polar coordinate in the Snyder space lose the symplectic structure and acquire the following modified form

$$\begin{aligned} \{t, p_t\} &= -1 + \lambda_s p_t^2, & \{\rho, p_\rho\} &= 1 + \lambda_s \left(p_\rho^2 + \frac{p_\theta^2}{\rho^2} \right), & \{\theta, p_\theta\} &= 1, \\ \{\rho, \theta\} &= \lambda_s \frac{p_\theta}{\rho}, & \{t, \rho\} &= \lambda_s (t p_\rho - \rho p_t), & \{t, \theta\} &= \lambda_s \frac{t p_\theta}{\rho^2}, \\ \{p_t, p_\rho\} &= -\lambda_s \frac{p_t p_\theta^2}{\rho^3}, & \{p_t, p_\theta\} &= \{p_\rho, p_\theta\} = \{t, p_\theta\} = \{\rho, p_\theta\} = 0, \\ \{t, p_\rho\} &= \lambda_s \left(p_t p_\rho + \frac{t p_\theta^2}{\rho^3} \right), & \{\rho, p_t\} &= \lambda_s p_t p_\rho, \\ \{\theta, p_t\} &= \lambda_s \frac{p_t p_\theta}{\rho^2}, & \{\theta, p_\rho\} &= \lambda_s \frac{p_\rho p_\theta}{\rho^2}. \end{aligned} \quad (2.45)$$

The above information will be useful to study the motion of a particle in a bumblebee background.

2.2 Motion of Particle in bumblebee background in the Snyder orbit

The motion of a particle in bumblebee background in the Snyder orbit is an extension of the work done in the article [44] with the inclusion of non-commutative spacetime through the Snyder formalism. It can also be thought of as an extension of the work presented in the article [45] where bumblebee background replaces the Schwarzschild background. The necessary inputs for this extension are all given in the previous sections. The extension is done by us in [118]. In [118], we have studied the motion of a planet (particle) with the metric consistent with the bumblebee gravity model. Precisely, the metric is

$$ds^2 = -f(\rho) dt^2 + (1 + \ell)f^{-1}(\rho) d\rho^2 + \rho^2 d\Omega^2, \quad (2.46)$$

where $f(\rho) = A = 1 - \frac{2M}{\rho}$ and M is the mass of the Sun. It is a system defined in $(3 + 1)$ dimension, however, the azimuthal symmetry leads to the conservation of angular momentum that offers a simplification which helps to reduce it into a problem of $(2 + 1)$ dimension like its special relativistic counterpart.

The dynamics of a massive body with mass m in the presence of bumblebee gravity background is given by the Hamiltonian

$$H = \frac{k}{2} \left[-\frac{p_t^2}{f(\rho)} + \frac{f(\rho)}{1 + \ell} p_\rho^2 + \frac{p_\theta^2}{\rho^2} + m^2 \right] = 0. \quad (2.47)$$

Now we are in a position to study the perihelion shift of a planet of mass m under the active influence of the bumblebee gravity with Snyder like Lorentz invariant non-commutative framework. The equations of motion of the planet under investigation with Snyder-like non-commutative framework in presence bumblebee background can be calculated using the equation (2.47) in a straightforward manner.

$$\dot{t} = k \left[p_t (A^{-1} - \lambda_s m^2 - \lambda_s \frac{M}{\rho} (p_\rho^2 + \frac{p_t^2}{A^2})) + \lambda_s \frac{M t p_\rho}{\rho^2} (p_\rho^2 + \frac{p_t^2}{A^2} - 2 \frac{p_\theta^2}{\rho^2 (1 + \ell)}) - \lambda_s \frac{p_\theta^2 \ell t p_\rho}{\rho^3} \right], \quad (2.48)$$

$$\dot{\rho} = k \left[\frac{A}{1 + \ell} - \lambda_s m^2 - \frac{2 \lambda_s M p_\theta^2}{\rho^3 (1 + \ell)} - \lambda_s \frac{p_\theta^2 \ell}{\rho^2 (1 + \ell)} \right] p_\rho, \quad (2.49)$$

$$\dot{\theta} = k \frac{p_\theta}{\rho^2} \left[1 - \lambda_s m^2 - \frac{\lambda_s M}{\rho} \left(\frac{p_\rho^2}{1 + \ell} + \frac{p_t^2}{A^2} \right) \right], \quad (2.50)$$

$$\dot{p}_t = -k \left[\frac{\lambda_s M p_t p_\rho}{\rho^2} \left(\frac{p_\rho^2}{1 + \ell} - \frac{2 p_\theta^2}{\rho^2 (1 + \ell)} + \frac{p_t^2}{A^2} - \frac{p_\theta^2 \ell}{\rho^2 M (1 + \ell)} \right) \right], \quad \dot{p}_\theta = 0, \quad (2.51)$$

$$\dot{p}_\rho = k \left[(1 - \lambda_s m^2) \frac{p_\theta^2}{\rho^3} + \frac{\lambda_s p_\theta^2 p_\rho^2 \ell}{\rho^3 (1 + \ell)} - \frac{M}{\rho^2} \left(\left(\frac{p_\rho^2}{1 + \ell} + \frac{p_t^2}{A^2} \right) (1 + \lambda_s (p_\rho^2 + \frac{p_\theta^2}{\rho^2})) - 2 \lambda_s \frac{p_\rho^2 p_\theta^2}{\rho^2} \right) \right]. \quad (2.52)$$

To find out the perihelion shift with this altered scenario is our principal objective. To get it, we indeed require the equation of the orbits. Note that p_t is no longer conserved but p_θ is. So, if we look at the expression

$$E = \frac{p_t}{\sqrt{1 + \lambda_s (-p_t^2 + p_\rho^2 + p_\theta^2 / \rho^2)}}, \quad (2.53)$$

we find that it is a conserved quantity and it denotes the energy of the particle revolving under bumblebee gravity in Snyder framework. Equation (2.53) gives

$$p_t^2 = \frac{E^2}{1 + \lambda_s E^2} [1 + \lambda_s (p_\rho^2 + p_\theta^2 / \rho^2)]. \quad (2.54)$$

Equations (2.47) and (2.54) yield

$$p_\rho^2 = (1 + \ell) \frac{E^2(1 + \lambda_s m^2 h^2 / \rho^2) - m^2(1 + \lambda_s E^2)(1 + h^2 / \rho^2)A}{(1 + \lambda_s E^2)A^2 - \lambda_s E^2(1 + \ell)}, \quad (2.55)$$

where $h = p_\theta / m$ is set for convenience.

It would be beneficial to get the equation of the orbits in terms of the variable u which is defined by $u = 1/\rho$. In terms of u , the equation looks

$$\frac{du}{d\theta} = -\frac{1}{\rho^2} \frac{\dot{\rho}}{\dot{\theta}} = -\frac{\frac{A}{1+\ell} - \lambda_s m^2 (1 + \frac{2Mh^2 u^3}{1+\ell} + \frac{h^2 u^2 \ell}{1+\ell})}{1 - \lambda_s m^2 - \lambda_s M u (\frac{p_\rho^2}{1+\ell} + \frac{p_t^2}{A^2})} \frac{p_\rho}{mh}. \quad (2.56)$$

If we use the expression for p_ρ and p_t from equations (2.55) and (2.54) respectively in equation (2.56), it will enable us to get a decoupled equation for the single dimensionless variable v , which is defined as $v = \frac{h^2}{M} u$. It will also be helpful if we define another dimensionless parameter $\epsilon = \frac{M^2}{h^2}$. The parameter ϵ is small for planetary orbits and it can be taken as an expansion parameter. We also assume that $\lambda_s m^2 \ll \epsilon$ since the Snyder corrections are expected to be small with respect to the correction appears from general relativity. Besides, by the virial theorem, and the definition of E standing in equation (2.53) reveals that $(E^2 - m^2 \sim m^2 (\epsilon q + \lambda_s E^2))$, where q is a parameter of order unity. After a bit of algebra with the first-order expansion of both $\lambda_s m^2$ and ϵ results the following first-order second-degree equation for v

$$\begin{aligned} v'^2 = & \frac{q}{1+\ell} + \frac{2v}{1+\ell} - \frac{v^2}{1+\ell} + \frac{2\epsilon v^3}{1+\ell} + \lambda_s m^2 \left[-q\ell \frac{1+2\ell}{1+\ell} + \frac{2v}{1+\ell} - \ell v \frac{2+4\ell}{1+\ell} \right. \\ & + \ell v^2 \frac{1+2\ell}{1+\ell} + \epsilon \left(\frac{q^2 \ell}{1+\ell} + qv \frac{4-2\ell}{1+\ell} - q\ell v \frac{6+4\ell}{1+\ell} + v^2 \frac{(4-4\ell)}{1+\ell} - q\ell v^2 \frac{3+2\ell}{1+\ell} \right. \\ & \left. \left. - 8\ell v^2 \frac{2+\ell}{1+\ell} + \ell v^3 \frac{4-4\ell}{1+\ell} + 2\ell v^4 \right) \right]. \end{aligned} \quad (2.57)$$

To obtain a solution of the second degree equation it is convenient to take the derivative of equation (2.57) to convert it into a second order differential equation:

$$\begin{aligned} v'' = & \frac{1 - \lambda_s m^2 \ell - 2\lambda_s m^2 \ell^2 + \lambda_s m^2}{1+\ell} + \frac{\lambda_s m^2 \ell + 2\lambda_s m^2 \ell^2 - 1}{1+\ell} v \\ & + \epsilon (k_0 + k_1 v + k_2 v^2 + k_3 v^3), \end{aligned} \quad (2.58)$$

where $k_0 = \lambda_s m^2 \frac{-4q\ell + 2q - 2q\ell^2}{1+\ell}$, $k_1 = \lambda m^2 \frac{-3q\ell - 2q\ell^2 - 20\ell - 8\ell^2 + 4}{1+\ell}$, $k_2 = \frac{3+6\lambda_s m^2 \ell - 6\lambda_s m^2 \ell^2}{1+\ell}$, and $k_3 = \lambda_s m^2 \ell$. If an expansion of v up to first order in ϵ is made as $v = v_0 + \epsilon v_1 + \dots$, where

$$v_0 = 1 + \lambda_s m^2 + e \cos \gamma \theta, \quad e = 1 + \frac{q}{\epsilon} = 1 + \frac{h^2(E^2 - m^2)}{M^2 m^2},$$

then the zeroth order, i.e., v_0 will render the result that corresponds to the Newtonian limit as usual, where v_1 will satisfy the differential equation

$$v_1'' + \gamma^2 v_1 = k_0 + k_1 v_0 + k_2 v_0^2 + k_3 v_0^3, \quad (2.59)$$

where

$$\gamma^2 = \frac{1}{1+\ell} - \lambda_s m^2 \ell \frac{1+2\ell}{1+\ell}. \quad (2.60)$$

The solution of this second-order differential equation is found out to be

$$\begin{aligned} v_1 = & \frac{1}{\gamma^2} \left[k_0 + k_1(1 + \lambda_s m^2) + k_2(1 + 2\lambda_s m^2 + \frac{e^2}{2}) + k_3(1 + 3\lambda_s m^2 + \frac{3e^2}{2}) \right] + e[k_1 \\ & + 2k_2(1 + \lambda_s m^2) + k_3(\frac{3e^2}{4} + 3e)] \frac{\theta \sin \gamma \theta}{2w} - [k_2 + 3k_3] \frac{e^2}{6\gamma^2} \cos 2\gamma \theta - \frac{k_3 e^3}{32\gamma^2} \cos 3\gamma \theta. \end{aligned} \quad (2.61)$$

2.3. CONSTRAINING THE SNYDER PARAMETER λ_s AND THE LV PARAMETER ℓ

In the solution (2.61), terms that oscillate around zero are neglected and hence, with the lowest order it reads

$$\begin{aligned}
v &\sim (1 + \lambda_s m^2) + \frac{\epsilon}{\gamma^2} [k_0 + k_1(1 + \lambda_s m^2) + k_2(1 + 2\lambda_s m^2 + \frac{e^2}{2}) + k_3(1 + 3\lambda_s m^2 + \frac{3e^2}{2})] \\
&+ e \cos[1 - \frac{\epsilon}{\gamma^2} (\frac{k_1}{2} + k_2(1 + \lambda_s m^2) + \frac{k_3}{2} (\frac{3e^2}{4} + 3e))] \gamma \theta \\
&= (1 + \lambda_s m^2) + \frac{\epsilon}{\gamma^2} [k_0 + k_1(1 + \lambda_s m^2) + k_2(1 + 2\lambda_s m^2 + \frac{e^2}{2}) + k_3(1 + 3\lambda_s m^2 + \frac{3e^2}{2})] \\
&+ e \cos \omega \theta,
\end{aligned} \tag{2.62}$$

where $\omega = [1 - \frac{\epsilon}{\gamma^2} (\frac{k_1}{2} + k_2(1 + \lambda_s m^2) + \frac{k_3}{2} (\frac{3e^2}{4} + 3e))] \gamma$. From the above expression one obtains the generalized expression for the perihelion shift:

$$\begin{aligned}
d\theta &= \pi \epsilon [6 + 10\lambda_s m^2 + (-3q + 1 + \frac{3e^2}{4} + 3e)\lambda_s m^2 l] + \pi \lambda_s m^2 \ell + 5l\pi \epsilon \lambda_s m^2 + \ell \pi \\
&= \ell \pi + 6\pi \epsilon + 10\pi \epsilon \lambda_s m^2 + \pi \epsilon (-3q + 1 + \frac{3e^2}{4} + 3e) + \pi (1 + 5\epsilon) \lambda_s m^2 \ell.
\end{aligned} \tag{2.63}$$

Note that the expression of time period agrees with the time period obtained in the article [44] since if we set $\lambda_s = 0$, ω will reduce to $\omega \approx \frac{1-\epsilon}{\sqrt{1+\ell}}$. The first term represents the shift due to the curvature of the spacetime. The term containing only λ_s appears due to the use of Snyder non-commutative dynamics and the term containing only ℓ emerges because of the replacement of the Schwarzschild background by the bumblebee. These two can be considered as pure corrections due to the use of non-commutative dynamics and the use of bumblebee gravity respectively.

2.3 Constraining the Snyder parameter λ_s and the LV parameter ℓ

To constrain the parameters λ_s and ℓ , we use the conjecture that the correction due to non-commutativity and Lorentz violation would individually be of the order of general relativistic correction.

Table 2.1: Estimates of upper bounds for various planets

Planet	GR prediction	Observed	Uncertainty in arcseconds per century	LV Parameter	Snyder parameter
Mercury	42.9814	42.9794 ± 0.0030	-0.0020 ± 0.0030	1.1×10^{-11}	2.0×10^{-89}
Venus	8.6247	8.6273 ± 0.0016	0.0026 ± 0.0016	1.5×10^{-11}	2.2×10^{-91}
Earth	3.83877	3.83896 ± 0.00019	0.00019 ± 0.00019	2.9×10^{-12}	4.3×10^{-92}
Mars	1.350938	1.350918 ± 0.000037	-0.000020 ± 0.000037	1.1×10^{-12}	2.0×10^{-90}
Jupiter	0.0623	0.121 ± 0.0283	0.0587 ± 0.0283	5.2×10^{-9}	3.7×10^{-93}
Saturn	0.01370	0.01338 ± 0.00047	-0.00032 ± 0.00047	2.1×10^{-10}	3.2×10^{-93}

Here, we have neglected terms that contain both λ_s and ℓ as these terms are very very small. We have inserted here a table containing the upper bound of the individual correction parameters of each effect. The upper bound of λ_s is in agreement with the prediction made in [47], where it was predicted that it should be less than 10^{-18} for the Mercury. Of course, few terms are there which may be considered as an interfering (mixed) term containing the product of $\lambda_s \ell$. These terms are indeed

small compared to the pure term but for this setting, we cannot avoid the presence of it. It has some interesting consequences too. If we would like to have the contribution of the order of the first term as it has been conjectured in [45] and [44] to constrain λ_s and ℓ , it will impose a new constraint on λ_s which shows that these two corrections have an inverse effect with each other so far magnitude of the correction is concerned. The enhancement of one will be demised by the other since the product is put under constraint. Note that if we would like to constrain λ_s with the consideration that $\pi\lambda_s\mu^2\lambda_s$ will give the same type of contribution as the other two pure terms then the parameter λ_s will come out approximately to be 9.4×10^{-48} for Mercury. From the interfering terms, a single term $\pi\lambda_s\mu^2\lambda_s$ is considered here for computation to get the approximated value since the order of magnitude will not change if all the interfering terms are considered. It can be constrained for other planets as well in this manner. It also agrees with the prediction made in the article [45].

Chapter 3

Non-commutative Kerr-like black hole

In this chapter we discuss non-commutative Kerr-like black hole which we have studied in [121]. Kerr-like black hole is the rotating, axisymmetric stationary vacuum solution of modified Einstein equations (2.13). Ding et al. obtained a Kerr-like solution in [48] keeping in view of the development of Koltz to reproduce the Kerr solution [49]. According to the development of Koltz, the generalized form of rotating stationary axially symmetric black hole metric can be written down as [48, 49]

$$ds^2 = -\gamma(\zeta, \theta)d\tau^2 + a[p(\zeta) - q(\theta)] \left(d\zeta^2 + d\theta^2 + \frac{q}{a}d\phi^2 \right) - 2q(\theta)d\tau d\phi. \quad (3.1)$$

where a is a constant which is introduced matching the dimension. The time t and τ have the relation

$$d\tau = dt - qd\phi. \quad (3.2)$$

In terms of t , Eq. (3.1) turns into

$$\begin{aligned} ds^2 &= -\gamma(\zeta, \theta)dt^2 + a[p(\zeta) - q(\theta)] (d\zeta^2 + d\theta^2) \\ &+ \{ [1 - \gamma(\zeta, \theta)]q^2(\theta) + p(\zeta)q(\theta) \} d\phi^2 - 2q(\theta)[1 - \gamma(\zeta, \theta)]dt d\phi. \end{aligned} \quad (3.3)$$

The metric ansatz (3.3) is then used to compute the gravitational field equations considering space-like nature of the field b_μ :

$$b_\mu = (0, b(\zeta, \theta), 0, 0). \quad (3.4)$$

The space-like nature of the bumblebee field was chosen since in this situation spacetime curvature showed up great radial variation compared to its temporal variation. The condition

$$b_\mu b^\mu = b_0^2,$$

where b_0 is a constant, leads to find out b_μ in the form

$$b_\mu = (0, b_0\sqrt{a(p-q)}, 0, 0), \quad (3.5)$$

in a straightforward manner. With this set up, they established that Einstein-bumblebee modified theory permitted to write the bumblebee field as $b_\mu = (0, b_0\ell, 0, 0)$ that contained the LV parameter ℓ and landed onto a Kerr-like metric which, in the Boyer-Lindquist coordinates, reads

$$ds^2 = -\left(1 - \frac{2Mr}{\rho^2}\right)dt^2 - \frac{4Mra\sqrt{1+\ell}\sin^2\theta}{\rho^2}dt d\varphi + \frac{\rho^2}{\Delta}dr^2 + \rho^2 d\theta^2 + \frac{A\sin^2\theta}{\rho^2}d\varphi^2, \quad (3.6)$$

where

$$\Delta = \frac{r^2 - 2Mr}{1 + \ell} + a^2, \rho^2 = r^2 + a^2 \cos^2\theta, A = [r^2 + (1 + \ell)a^2]^2 - \Delta(1 + \ell)^2 a^2 \sin^2\theta, \text{ and } \phi = \varphi/\sqrt{1 + \ell}.$$

In the slow rotating [50] case, i.e. for $a^2 \rightarrow 0$, the metric has the form

$$ds^2 \approx - \left(1 - \frac{2M}{r}\right) dt^2 - \frac{4Ma\sqrt{1+\ell}\sin^2\theta}{r} d\theta d\varphi + \frac{1+\ell}{1-2M/r} dr^2 + r^2(d\theta^2 + \sin^2\theta)d\varphi^2. \quad (3.7)$$

If $\ell \rightarrow 0$ it recovers the usual Kerr metric and for $a \rightarrow 0$ it becomes

$$ds^2 = - \left(1 - \frac{2M}{r}\right) dt^2 + \frac{1+\ell}{1-2M/r} dr^2 + r^2(d\theta^2 + \sin^2\theta)d\varphi^2, \quad (3.8)$$

which is the metric (2.16) for Schwarzschild-like black hole.

3.1 Non-commutative Kerr-like black hole

Let us now describe, in brief, the incorporation of the effect of non-commutativity. It has been done in [121]. Like the Lorentz violation effect, the non-commutativity is also believed to have the potential that leads to significant effects on the properties of black holes. Therefore, non-commutative spacetime in the theories of gravity have been the subject of several interest [51, 52]. In particular, the study considering the effects of non-commutativity on black hole physics has been an area of huge interest. The generalization of quantum field theory by non-commutativity based on coordinate coherent state formalism is of interest in this respect which cures the short distance singular behavior of point-like structures [53–55]. In this approach, the black hole mass M is considered to be distributed throughout a region of linear size instead of being localized at a point. Therefore, non-commutativity is introduced by modifying the mass density so that the Dirac delta function is replaced by a Gaussian distribution [54] or alternatively by a Lorentzian distribution [55]. The implementation of these arguments leads to the replacement of the position Dirac-delta function that describes a point-like structure, with suitable function, e.g. Gaussian distribution function or Lorentzian distribution describing smeared structures.

To incorporate the non-commutativity effect we consider that the mass density of the black hole has a Lorentzian distribution as it was found in article [56, 57]. Precisely, the distribution is given by

$$\rho_{\vartheta_n} = \frac{\sqrt{\vartheta_n} M}{\pi^{3/2} (\pi\vartheta_n + r^2)^2}. \quad (3.9)$$

Here, ϑ_n is the strength of non-commutativity of spacetime and M is the total mass distributed throughout a region with a linear size $\sqrt{\vartheta_n}$. For the smeared matter distribution, it can be shown that [57]

$$\mathcal{M}_{\vartheta_n} = \int_0^r \rho_{\vartheta_n}(r) 4\pi r^2 dr = \frac{2M}{\pi} \left(\tan^{-1} \left(\frac{r}{\sqrt{\pi\vartheta_n}} \right) - \frac{\sqrt{\pi\vartheta_n} r}{\pi\vartheta_n + r^2} \right) \approx -\frac{4\sqrt{\vartheta_n} M}{\sqrt{\pi} r} + M + \mathcal{O}(\vartheta_n^{3/2}). \quad (3.10)$$

It indicates that the Mass is point-like when the spread of the distribution approaches towards a vanishing value since $\lim_{\vartheta_n \rightarrow 0} \mathcal{M}_{\vartheta_n} = M$.

3.2 Combining non-commutative and Lorentz violation effect

To combine these two effects we need a suitable framework where these two can fit suitably. Now, these two can be amalgamated if we replace M by M_{ϑ_n} in the expression of the spacetime metric given in equation (3.6), which is already endowed with the LV effect. Therefore, the generalized spacetime metric, where both the LV and non-commutating effects are bestowed simultaneously, takes the form

$$ds^2 = - \left(1 - \frac{2M_{\vartheta_n} r}{\rho^2}\right) dt^2 - \frac{4M_{\vartheta_n} r a \sqrt{1+\ell} \sin^2\theta}{\rho^2} dt d\varphi + \frac{\rho^2}{\hat{\Delta}} dr^2 + \rho^2 d\theta^2 + \frac{A \sin^2\theta}{\rho^2} d\varphi^2, \quad (3.11)$$

where

$$\rho^2 = r^2 + (1+\ell)a^2 \cos^2\theta, \quad \hat{\Delta} = \frac{r^2 - 2M_{\vartheta_n} r}{1+\ell} + a^2, \quad \text{and} \quad A = [r^2 + (1+\ell)a^2]^2 - \hat{\Delta}(1+\ell)a^2 \sin^2\theta.$$

The metric (3.11) carries the information of two significant effects which have already been found needful to be taken into account in the perspective of black hole physics. Although these two are supposed to show a prominent role in the vicinity of Planck scale, it is believed that these two have the ability to lead to significant effects on the properties of the black holes at an observable scale. The parameter ϑ_n is connected with the non-commutativity of spacetime and the parameter ℓ is associated with the Lorentz violation scenario. If the LV effect is switched off, i.e. $\ell = 0$, it will render only the non-commutative effect and the reverse will be the case if the non-commutating effect will be switched off setting $\vartheta_n = 0$, and if both the effects are made off setting $\ell \rightarrow 0$ and $\vartheta_n \rightarrow 0$, it recovers the usual Kerr metric.

3.3 Geometry concerning Horizon and ergosphere

We get the expressions for event horizon and Cauchy horizon by setting $\hat{\Delta} = 0$, which are given by

$$r_{\pm} = M \pm \frac{\sqrt{-\pi\ell a^2 - \pi a^2 + \pi M^2 - 8\sqrt{\pi}M\sqrt{\vartheta_n}}}{\sqrt{\pi}}, \quad (3.12)$$

where \pm signs correspond to event horizon and Cauchy horizon respectively. The event horizon and Cauchy horizon are labelled by r_{eh} and r_{ch} respectively. What follows next is the sketch of $\hat{\Delta}$ for different values of ϑ_n and ℓ where we have taken $\hat{a} = a\sqrt{1 + \ell}$ [121].

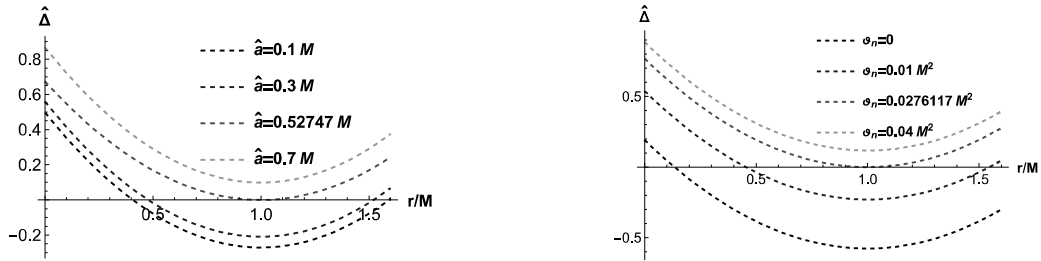


Figure 3.1: The left one gives variation of $\hat{\Delta}$ for various values of \hat{a} with $\vartheta_n = 0.02M^2$ and $\ell = 0.3$, and the right one gives variation for various values of ϑ_n with $\hat{a} = 0.5M$ and $\ell = 0.3$.

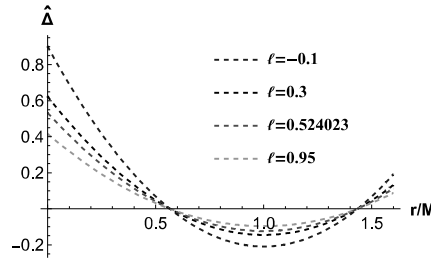


Figure 3.2: It gives variation of $\hat{\Delta}$ for various values of ℓ with $\vartheta_n = 0.01M^2$ and $\hat{a} = 0.6$.

From the above plots we see that there exists critical values of a , for fixed values of ϑ_n and ℓ , critical values of ϑ_n for fixed values of a , ℓ and critical values of ℓ for fixed values of ϑ_n , a . The critical values of a , ϑ_n and ℓ are designated by a_c , ϑ_{nc} and ℓ_c respectively. In these cases, $\hat{\Delta} = 0$ has only one root. For $a < a_c$, we have black hole and for $a > a_c$, we have naked singularity. Similarly for $\vartheta_n < \vartheta_{nc}$, we have black hole, but for $\vartheta_n > \vartheta_{nc}$ we have naked singularity and $\ell < \ell_c$ signifies the black hole, however $\ell > \ell_c$ represents the naked singularity. Numerical computation shows that we have $\hat{a}_c = 0.52747M$ for $\vartheta_n = 0.02M^2$ and $\ell = 0.3$. Similarly, for $a = 0.5M$ and $\ell = 0.3$, we have $\vartheta_{nc} = 0.0223654M^2$, and for $a = 0.6M$ and $\vartheta_n = 0.01M^2$, we find $\ell_c = 0.524023$.

There exists a black hole when the following inequality is maintained

$$-\pi\ell a^2 - \pi a^2 + \pi M^2 - 8\sqrt{\pi}M\sqrt{\vartheta_n} \geq 0. \quad (3.13)$$

3.3. GEOMETRY CONCERNING HORIZON AND ERGOSPHERE

However, when in the condition (3.13) equality is maintained it corresponds to extremal black holes, and when the condition (3.13) is strictly greater than 0, we have non-extremal black holes which have both Cauchy and Event horizons.

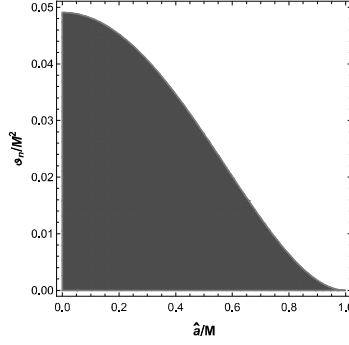


Figure 3.3: It is the parameter space $(\hat{a}/M - \vartheta_n/M^2)$. The colored region corresponds to parameter space for which we have a black hole.

Let us now focus on the static limit surface (SLS). At the SLS, the asymptotic time-translational Killing vector becomes null which is mathematically given by

$$g_{tt} = \rho^2 - 2M_{\vartheta_n}r = 0. \quad (3.14)$$

The real positive solutions of the above equation give radial coordinates of ergosphere:

$$r_{\pm}^{ergo} = \frac{2\sqrt{\pi}M \pm \sqrt{-4\pi a^2 \cos^2(\theta) - 4\pi a^2 \ell \cos^2(\theta) + 4\pi M^2 - 32\sqrt{\pi}M\sqrt{\vartheta_n}}}{2\sqrt{\pi}}. \quad (3.15)$$

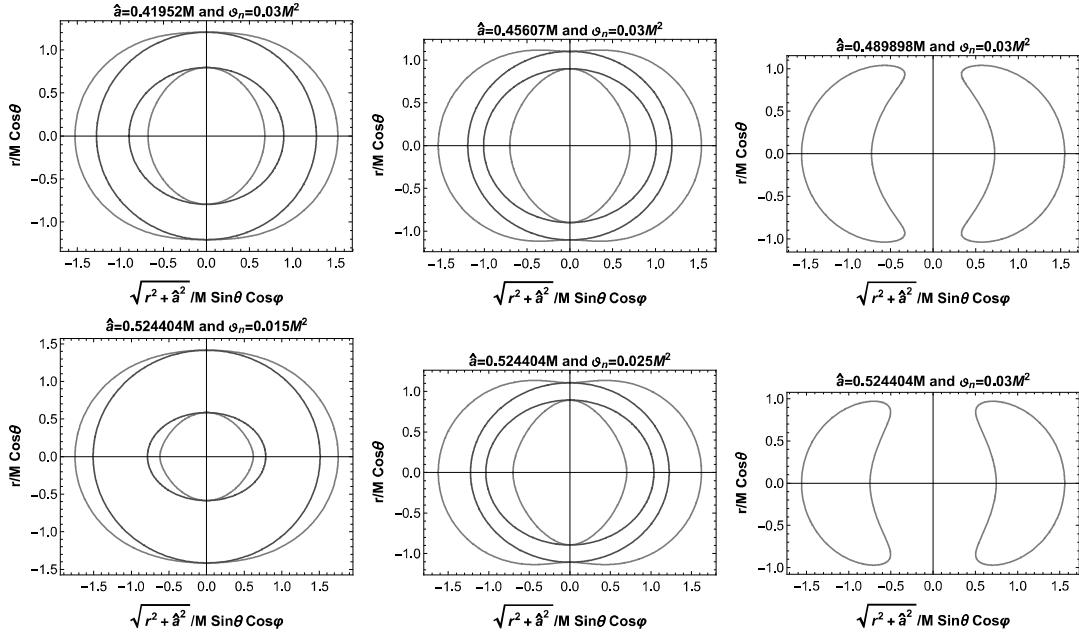


Figure 3.4: The cross-section of the event horizon (outer red line), SLS (outer blue dotted line), and ergoregion of non-commutative Kerr-like black holes.

The ergosphere, which lies between SLS and the event horizon, is depicted above. Energy can be extracted from ergosphere [27]. From the above, we can conclude that the shape and size of the ergosphere depend on rotational parameter \hat{a} and non-commutative parameter ϑ_n . The size of the ergosphere increases with the increase of ϑ_n and \hat{a} .

3.4 Photon orbit and black hole shadow

Here, we are going to describe the black hole shadow related to this modified theory which has been studied by us in [121]. There are several studies related to the black hole shadow from which we will get the necessary inputs [58–63]. In order to study the shadow, we introduce two conserved parameters ξ and η which are defined by

$$\xi = \frac{L_z}{E} \quad \text{and} \quad \eta = \frac{\mathcal{Q}}{E^2}, \quad (3.16)$$

where E , L_z , and \mathcal{Q} are the energy, the axial component of the angular momentum, and the Carter constant respectively. In the bumblebee rotating black hole spacetime, equations for null geodesics in terms of ξ are given by

$$\begin{aligned} \rho^2 \frac{dr}{d\lambda} &= \pm \sqrt{R}, \quad \rho^2 \frac{d\theta}{d\lambda} = \pm \sqrt{\Theta}, \\ (1 + \ell) \hat{\Delta} \rho^2 \frac{dt}{d\lambda} &= A - 2\sqrt{1 + \ell} M r a \xi, \\ (1 + \ell) \hat{\Delta} \rho^2 \frac{d\phi}{d\lambda} &= 2\sqrt{1 + \ell} M r a + \frac{\xi}{\sin^2 \theta} (\rho^2 - 2Mr), \end{aligned} \quad (3.17)$$

where λ is the affine parameter and

$$R(r) = \left[\frac{r^2 + (1 + \ell)a^2}{\sqrt{1 + \ell}} - a\xi \right]^2 - \hat{\Delta} \left[\eta + (\xi - a\sqrt{1 + \ell})^2 \right] \quad \text{and} \quad \Theta(\theta) = \eta + (1 + \ell)a^2 \cos^2 \theta - \xi^2 \cot^2 \theta.$$

The radial equation of motion can be written down in the familiar form

$$\left(\rho^2 \frac{dr}{d\lambda} \right)^2 + V_{eff} = 0. \quad (3.18)$$

The effective potential V_{eff} then reads

$$V_{eff} = - \left[\frac{r^2 + (1 + \ell)a^2}{\sqrt{1 + \ell}} - a\xi \right]^2 + \hat{\Delta} \left[\eta + (\xi - a\sqrt{1 + \ell})^2 \right]. \quad (3.19)$$

Conditions given in (1.70) describe the unstable spherical orbit on the equatorial plane $\theta = \frac{\pi}{2}$. We plot the potential V_{eff} versus r/M with $\xi = \xi_c + 0.2$, where ξ_c is the value of ξ for equatorial spherical unstable orbit.

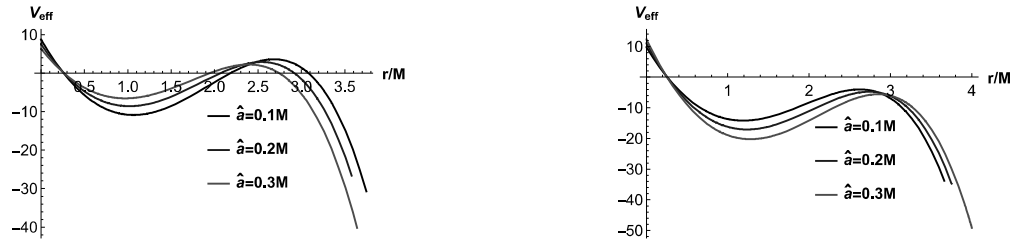


Figure 3.5: The left and the right panels describe the effective potential for prograde orbits and the retrograde orbits respectively for various values of \hat{a} with $\vartheta_n = 0.01 M^2$ and $\ell = 0.1$.

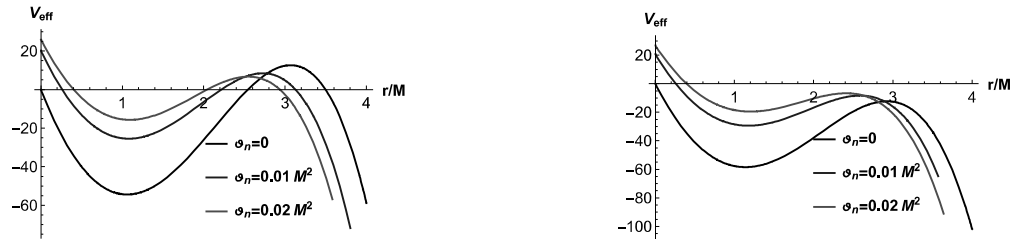


Figure 3.6: The left and the right panels describe the effective potential for prograde orbits and the retrograde orbits respectively for various values of ϑ_n with $\hat{a} = 0.1 M$ and $\ell = 0.1$.

3.4. PHOTON ORBIT AND BLACK HOLE SHADOW

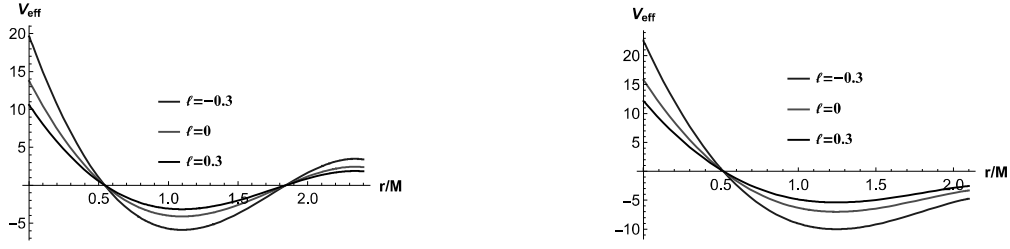


Figure 3.7: The left panel describes the effective potential for prograde orbits and right panel describes the retrograde orbits for various values of ℓ with $\hat{a} = 0.1M$ and $\vartheta_n = 0.03M^2$.

The plots depicted above show that the turning points for prograde orbits shift towards left as a or ϑ_n increases. We also plot critical radii of prograde and retrograde orbits for different scenarios in figures furnished below.

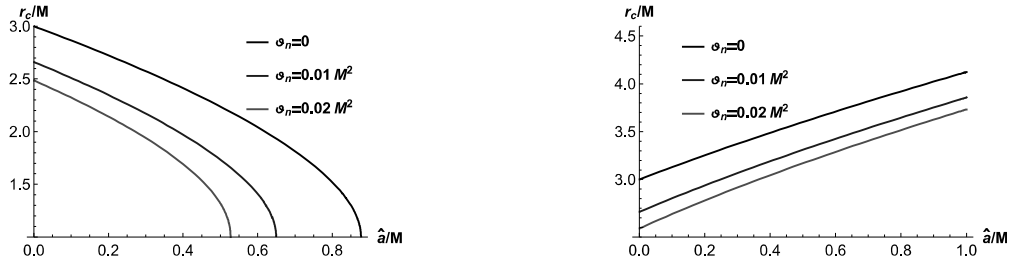


Figure 3.8: The left panel shows the variation of critical radius for prograde orbits and the right panel shows the variation of critical radius for retrograde orbits for various values of ϑ_n with $\ell = 0.3$.

It can be concluded from plots above that critical radii, both for prograde as well as retrograde orbits, decrease with an increase in the non-commutative parameter ϑ_n . For more generic orbits, we have $\theta \neq \pi/2$ and $\eta \neq 0$ and the conserved parameters for such spherical orbit of radius r_s are given by

$$\begin{aligned}\xi_s &= \frac{(a^2(1+\ell) + r^2) \hat{\Delta}'(r) - 4r\hat{\Delta}(r)}{a\sqrt{1+\ell}\hat{\Delta}'(r)}, \\ \eta_s &= \frac{r^2 \left(8\hat{\Delta}(r) \left(2a^2(1+\ell) + r\hat{\Delta}'(r) \right) - r^2\hat{\Delta}'(r)^2 - 16\hat{\Delta}'(r)^2 \right)}{a^2(1+\ell)\hat{\Delta}'(r)^2},\end{aligned}\quad (3.20)$$

where $'$ stands for differentiation with respect to radial coordinate. The above expressions, in the limit $\ell \rightarrow 0$ and $\vartheta_n \rightarrow 0$, reduce to those for Kerr black hole. It would be useful at this point to introduce two celestial coordinates for a better study of the shadow. The two celestial coordinates, which are used to describe the shape of the shadow that an observer sees in the sky, can be given by

$$\begin{aligned}\alpha(\xi, \eta; \theta) &= \lim_{r \rightarrow \infty} \frac{-rp^{(\varphi)}}{p^{(t)}} = -\xi_s \csc \theta, \\ \beta(\xi, \eta; \theta) &= \lim_{r \rightarrow \infty} \frac{rp^{(\theta)}}{p^{(t)}} = \sqrt{\eta_s + a^2 \cos^2 \theta - \xi_s^2 \cot^2 \theta},\end{aligned}\quad (3.21)$$

where $(p^{(t)}, p^{(r)}, p^{(\theta)}, p^{(\varphi)})$ are the tetrad components of the photon momentum with respect to a locally non-rotating reference frame [30].

With these inputs, we now plot black hole shadows for various cases which are depicted in the Fig. (3.9).

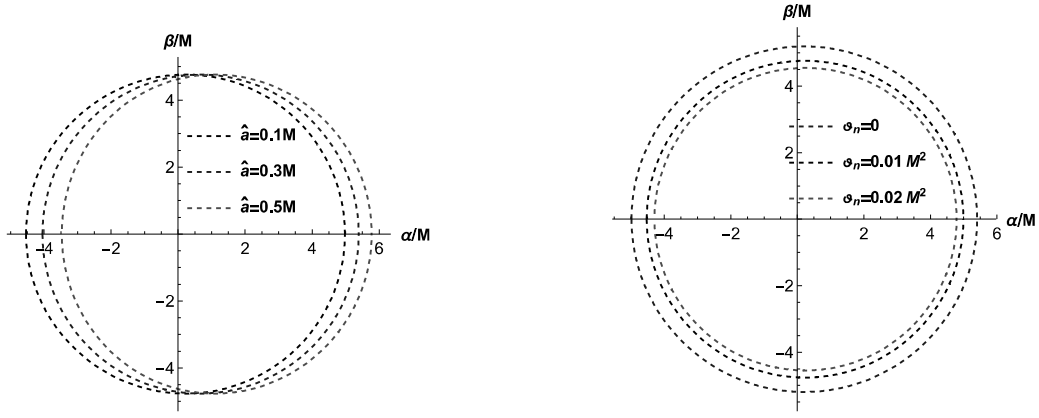


Figure 3.9: The left panel gives shapes of the shadow for various values of \hat{a} with $\vartheta_n = 0.01M^2$, $\ell = 0.1$, and $\theta = \pi/2$. The right panel gives shapes of the shadow for various values of ϑ_n with $a = 0.1M$, $\ell = 0.1$, and $\theta = \pi/2$.

From the above plots, we observe that the size of the shadow increases with an increase in \hat{a} , whereas it decreases with an increase in ϑ_n .

3.5 Deviation from the circularity δ_s and the size R_s of black hole shadow

Using the parameters which are introduced by Hioki and Maeda in [32], we analyse the deviation from the circularity form δ_s and the size R_s of the shadow cast by the black hole.

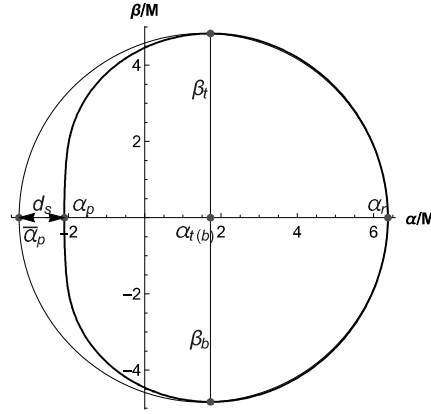


Figure 3.10: The black hole shadow and reference circle. d_s is the distance between the left points of the shadow and the reference circle.

For calculating these parameters, we consider five points, (α_t, β_t) , (α_b, β_b) , $(\alpha_r, 0)$, $(\alpha_p, 0)$, and $(\bar{\alpha}_p, 0)$, which are top, bottom, rightmost, leftmost of the shadow, and leftmost of the reference circle respectively. So, we have

$$R_s = \frac{(\alpha_t - \alpha_r)^2 + \beta_t^2}{2|\alpha_t - \alpha_r|},$$

and

$$\delta_s = \frac{|\bar{\alpha}_p - \alpha_p|}{R_s}.$$

In the following figures we plot R_s and δ_s for various scenarios to study how R_s and δ_s varies with parameters of the modified theory of gravity.

3.6. COMPUTATION OF ENERGY EMISSION RATE

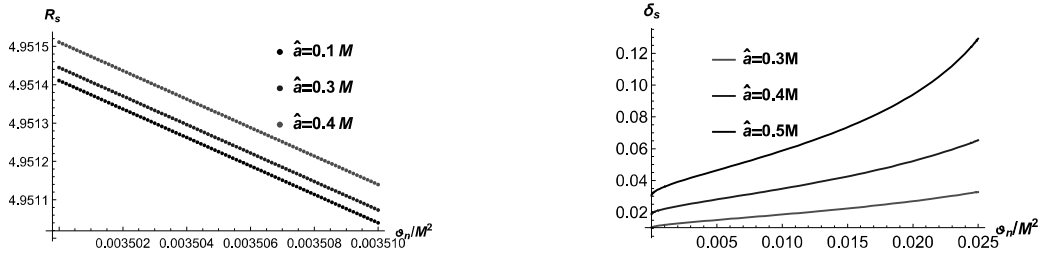


Figure 3.11: The left one shows variation of R_s for various values of \hat{a} with $\ell = -0.2$ and $\theta = \pi/2$. The right one shows variation of δ_s for various values of \hat{a} with $\ell = -0.2$ and $\theta = \pi/2$.

From the above plots we observe that R_s decreases with an increase in φ_n for fixed values of \hat{a} , whereas for fixed values of φ_n , it increases with an increase in \hat{a} . On the other hand, δ_s increases with an increase in \hat{a} for fixed value of φ_n as well as with an increase in φ_n for fixed values of \hat{a} .

3.6 Computation of energy emission rate

In this part, we describe the possible visibility of the non-commutative Kerr-like black hole through shadow [121]. In the vicinity of limiting constant value, the cross-section of the black hole's absorption moderates lightly at high energy. We know that a rotating black hole can absorb electromagnetic waves. The absorbing cross-section for a spherically symmetric black hole is [64]

$$\sigma_{lim} = \pi R_s^2. \quad (3.22)$$

Using the above equation, the energy emission rate is obtained [65] as:

$$\frac{d^2 E}{d\omega dt} = \frac{2\pi^3 R_s^2}{e\left(\frac{\omega}{T_H}\right) - 1} \omega^3, \quad (3.23)$$

where $T_H = \frac{\sqrt{1+\ell}\hat{\Delta}'(r_+)}{4\pi[r_+^2 + (1+\ell)a^2]}$ is the Hawking temperature and ω is the frequency.

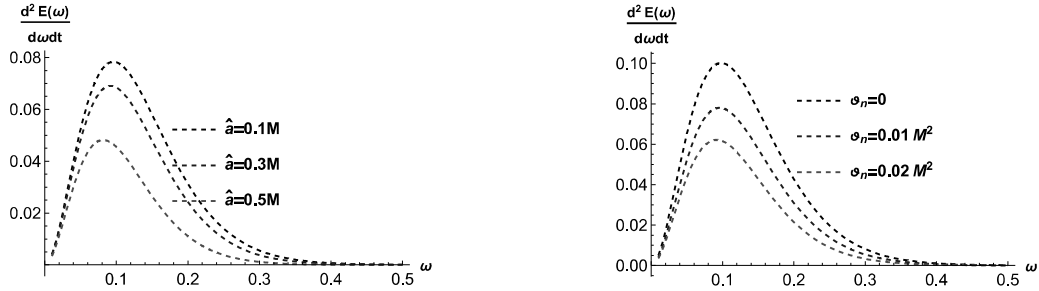


Figure 3.12: The left panel gives variation of emission rate against ω for various values of \hat{a} with $\varphi_n = 0.01M^2$ and $\ell = 0.3$. The right panel gives variation of emission rate against ω for various values of φ_n with $a = 0.1M$ and $\ell = 0.3$.

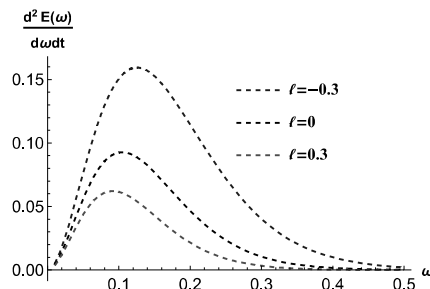


Figure 3.13: It gives variation of emission rate against ω for various values of ℓ with $\varphi_n = 0.02M^2$ and $\hat{a} = 0.1M$.

3.6. COMPUTATION OF ENERGY EMISSION RATE

In Fig. (3.12) and (3.13), we have shown the plots of energy emission rate versus ω for various cases. It is clear from the plots that the emission rate decreases with an increase in the value of ϑ_n for any set of fixed values of a and ℓ . It also decreases with an increase in ℓ , for \hat{a} and ϑ_n being fixed, and with an increase in \hat{a} , when ϑ_n and ℓ remain fixed.

Chapter 4

Kerr-Sen-like black hole

In this chapter we describe the metric for Kerr-Sen-like black hole and study various aspects of it. The Kerr-Sen-like metric is derived in [76] where we have shown that the exact Kerr-Sen-like solution can be derived from Einstein-bumblebee equations (2.13) in a similar way the Ding et al. offered the exact Kerr-like solution in [48] following the development of Koltz to reproduce the Kerr solution [49, 66]. According to the development of Koltz, the generalized form of a rotating, stationary, axially symmetric black hole metric can be written down as Eq. (3.1) [48, 49, 66]. The time t and τ have the relation

$$d\tau = dt - qd\phi. \quad (4.1)$$

In terms of t , Eq. (3.1) turns into Eq. (3.3). We now use the metric ansatz (3.3) to compute the gravitational field equations. If we consider that the bumblebee field is space-like, it can be written down as

$$b_\mu = (0, b(\zeta, \theta), 0, 0). \quad (4.2)$$

It is reasonable to consider the space-like nature of the bumblebee field since in this situation space-time curvature has greater radial variation compared to its temporal variation. Now, we have

$$\begin{aligned} b_\mu b^\mu &= b_0^2 \\ \Rightarrow g^{\mu\nu} b_\mu b_\nu &= b_0^2 \\ \Rightarrow \frac{b^2}{a(p-q)} &= b_0^2 \\ \Rightarrow b &= b_0 \sqrt{a(p-q)}. \end{aligned} \quad (4.3)$$

where b_0 is a constant. Hence, the explicit form of b_μ comes out to be

$$b_\mu = (0, b_0 \sqrt{a(p-q)}, 0, 0). \quad (4.4)$$

in a straightforward manner. Therefore, the non-vanishing components of the bumblebee field are

$$\begin{aligned} b_{\zeta\theta} &= -b_{\theta\zeta} \\ &= \partial_\zeta b_\theta - \partial_\theta b_\zeta \\ &= -\frac{\partial}{\partial\theta} b(\zeta, \theta) = -\frac{\partial}{\partial\theta} b_0 \sqrt{a(p-q)} \\ &= \frac{ab_0 q'}{2\sqrt{a(p-q)}}, \end{aligned} \quad (4.5)$$

where the prime is used to indicate a derivative with respect to its argument. In addition, the quantity $b_\mu^\alpha b_{\nu\alpha}$ has the following non-vanishing components:

$$b_\zeta^\alpha b_{\zeta\alpha} = b_\theta^\alpha b_{\theta\alpha}$$

$$\begin{aligned}
&= g^{\alpha\beta} b_{\theta\beta} b_{\theta\alpha} = g^{\zeta\zeta} b_{\theta\zeta} b_{\theta\zeta} \\
&= \frac{b_0^2 q'^2}{4(p-q)^2},
\end{aligned} \tag{4.6}$$

and the quantity $b^{\alpha\beta} b_{\alpha\beta}$ has a non-vanishing contribution

$$\begin{aligned}
b^{\alpha\beta} b_{\alpha\beta} &= g^{\mu\alpha} g^{\nu\beta} b_{\mu\nu} b_{\alpha\beta} \\
&= g^{\mu\zeta} g^{\nu\theta} b_{\mu\nu} b_{\zeta\theta} + g^{\mu\theta} g^{\nu\zeta} b_{\mu\nu} b_{\theta\zeta} \\
&= \frac{b_0^2 q'^2}{2a(p-q)^3}.
\end{aligned} \tag{4.7}$$

For the metric (3.3), we find that the nonzero components of Ricci tensor are $\mathcal{R}_{tt}, \mathcal{R}_{t\phi}, \mathcal{R}_{\zeta\zeta}, \mathcal{R}_{\zeta\theta}, \mathcal{R}_{\theta\theta}, \mathcal{R}_{\phi\phi}$. It is straightforward to see that $\bar{B}_{\zeta\theta} = 0$. The gravitational field equations, which are needed for our purpose, are

$$\begin{aligned}
\bar{R}_{\zeta\theta} &= \mathcal{R}_{\zeta\theta} - \kappa b_{\zeta\alpha} b_{\theta}^{\alpha} + \varrho b_{\zeta} b^{\alpha} \mathcal{R}_{\alpha\theta} + \varrho b_{\theta} b^{\alpha} \mathcal{R}_{\alpha\zeta} \\
&= \mathcal{R}_{\zeta\theta} - \kappa b_{\zeta\alpha} b_{\theta}^{\alpha} + \varrho b_0^2 \mathcal{R}_{\zeta\theta} \\
&= (1 + \ell) \mathcal{R}_{\zeta\theta}, \\
\bar{R}_{tt} &= \mathcal{R}_{tt} + g_{tt} \left(\frac{\kappa}{4} b^{\alpha\beta} b_{\alpha\beta} - \frac{\varrho}{2} b^{\zeta} b^{\zeta} \mathcal{R}_{\zeta\zeta} \right) + \bar{B}_{tt} \\
\bar{R}_{t\phi} &= \mathcal{R}_{t\phi} + g_{t\phi} \left(\frac{\kappa}{4} b^{\alpha\beta} b_{\alpha\beta} - \frac{\varrho}{2} b^{\zeta} b^{\zeta} \mathcal{R}_{\zeta\zeta} \right) + \bar{B}_{t\phi},
\end{aligned} \tag{4.8}$$

where $\ell = \varrho b_0^2$. The quantities $\mathcal{R}_{\zeta\theta}, \bar{B}_{tt}, \bar{B}_{t\phi}$ are given by

$$\begin{aligned}
\mathcal{R}_{\zeta\theta} &= -\frac{\bar{\Delta}_{12}}{2\bar{\Delta}} + \frac{\Delta_2 [(p-q)\bar{\Delta}_1 + 2\bar{\Delta}p_1]}{4(p-q)\bar{\Delta}^2}, \\
\bar{B}_{tt} &= \ell \left[\frac{\gamma_{11}}{2a(p-q)} + \frac{\gamma}{4a(p-q)\bar{\Delta}} p_1 \gamma_1 - \frac{1}{4a\bar{\Delta}} \gamma_1^2 \right], \\
\bar{B}_{t\phi} &= \ell \left[-\frac{q\gamma_{11}}{2a(p-q)} + \frac{q(2-\gamma)}{4a(p-q)\bar{\Delta}} p_1 \gamma_1 + \frac{q}{4a\bar{\Delta}} \gamma_1^2 \right].
\end{aligned} \tag{4.9}$$

where $\bar{\Delta} = q + \gamma(p-q)$. The differentiation with respect to variables ζ and θ are denoted by suffixes 1 and 2 respectively in the Eq. (4.9). Note that $\bar{R}_{\zeta\theta} = 0$ implies that $\mathcal{R}_{\zeta\theta}$ vanishes. This helps us to set $\bar{\Delta}_2 = 0$ which, in turn, yields

$$\begin{aligned}
\gamma_2 p + (1-\gamma) q_2 - \gamma_2 q &= 0 \\
\Rightarrow \gamma_2 &= -\frac{(1-\gamma)q_2}{p-q}.
\end{aligned} \tag{4.10}$$

A few steps of algebra gives the expression of γ as:

$$\gamma = 1 - \frac{2h(\zeta)}{p(\zeta) - q(\theta)} \tag{4.11}$$

We introduce below new independent variable σ exploiting the condition $\bar{\Delta}_2 = 0$ explicitly which is

$$\sigma = \int \sqrt{\bar{\Delta}} d\zeta, \tag{4.12}$$

where $\bar{\Delta} = p - 2h$. Now, taking the derivatives of p with respect to ζ we have

$$\begin{aligned}
p_1 &= \frac{dp}{d\zeta} = \frac{d\sigma}{d\zeta} \frac{dp}{d\sigma} = \sqrt{\bar{\Delta}} \frac{dp}{d\sigma}, \\
p_{11} &= \frac{d^2 p}{d\zeta^2} = \frac{d}{d\zeta} \left(\sqrt{\bar{\Delta}} \frac{dp}{d\sigma} \right)
\end{aligned} \tag{4.13}$$

$$\begin{aligned}
&= \sqrt{\bar{\Delta}} \frac{d^2 p}{d\sigma^2} \frac{d\sigma}{d\zeta} + \frac{dp}{d\sigma} \frac{d}{d\zeta} \left(\sqrt{\bar{\Delta}} \right) \\
&= \bar{\Delta} \frac{d^2 p}{d\sigma^2} + \frac{1}{2} \left(\frac{dp}{d\sigma} \right)^2 - \frac{dh}{d\sigma} \frac{dp}{d\sigma}.
\end{aligned}$$

A careful look at Eqs. (2.13) and (4.8) reveals that the following equation holds

$$g_{t\phi} \bar{R}_{tt} - g_{tt} \bar{R}_{t\phi} = 0. \quad (4.14)$$

After inserting the expressions of $g_{t\phi}$, \bar{R}_{tt} , g_{tt} , and $\bar{R}_{t\phi}$ in (4.14), we find

$$\begin{aligned}
&p \left[4(1+\ell) \frac{\dot{h}\dot{p}}{h} q^2 - 2qq_{22} + q_2^2 + 2(1+\ell) \ddot{p} q^2 \right] \\
&- 4(1+\ell) \dot{p}^2 q^2 - 2(p-q)^2 q^2 \ddot{h} \left(1 + \frac{\ell}{h} \right) \\
&- q \left[4(1+\ell) \frac{\dot{h}\dot{p}}{h} q^2 - 2qq_{22} + 5q_2^2 + 2(1+\ell) \ddot{p} q^2 \right] = 0,
\end{aligned} \quad (4.15)$$

where dot denotes derivative with respect to σ . Here p and h are functions of σ and q is a function of θ . We, therefore, can write the following

$$\frac{\dot{h}\dot{p}}{h} = k, \quad \dot{p}^2 = cp + n, \quad \text{and} \quad \ddot{h} = 0, \quad (4.16)$$

without any loss of generality. Note that k , c , and n are some constants. We find that $\ddot{p} = k = c/2$, and Eq. (4.15) can be reduced to

$$\begin{aligned}
&4(1+\ell)(k-c)q^2 - 2qq_{22} + q_2^2 + (1+\ell)cq^2 = 0, \\
&4k(1+\ell)q^2 - 2qq_{22} + 5q_2^2 + (1+\ell)cq^2 + 4(1+\ell)nq = 0.
\end{aligned} \quad (4.17)$$

They both give

$$q_2^2 = -(1+\ell)(cq^2 + nq), \quad (4.18)$$

which gives the following

$$q = -\frac{n}{c} \sin^2[\sqrt{(1+\ell)c}\theta/2]. \quad (4.19)$$

By setting the constants $c = 4/(1+\ell)$ and $n = -4a$, we obtain

$$q = (1+\ell)a \sin^2 \theta. \quad (4.20)$$

From conditions (4.16), we find that

$$p = \frac{\sigma^2}{1+\ell} + a(1+\ell), \quad h = c'\sigma, \quad \text{and} \quad \gamma = 1 - \frac{2(1+\ell)c'\sigma}{\sigma^2 + a(1+\ell)^2 \cos^2 \theta}, \quad (4.21)$$

where c' is a constant. After choosing $\sigma = \sqrt{\frac{\ell+1}{a} \frac{r+b}{r}} r$, $c' = M/\sqrt{(\ell+1)a \frac{r+b}{r}}$, and $\phi = \varphi/\sqrt{1+\ell}$ for Boyer-Lindquist coordinates, we arrive at

$$p = \frac{r(r+b)}{a} + a(\ell+1), \quad h = \frac{Mr}{a}, \quad \text{and} \quad \gamma = 1 - \frac{2Mr}{\rho^2}, \quad (4.22)$$

where $\rho^2 = r(r+b) + (1+\ell)a^2 \cos^2 \theta$. Finally, substituting these quantities into Eqs. (3.3) and (4.4), we obtain the bumblebee field as $b_\mu = (0, b_0\rho, 0, 0)$ and the rotating metric in the bumblebee gravity as

$$ds^2 = - \left(1 - \frac{2Mr}{\rho^2} \right) dt^2 - \frac{4Mra\sqrt{1+\ell} \sin^2 \theta}{\rho^2} dt d\varphi + \frac{\rho^2}{\Delta} dr^2 + \rho^2 d\theta^2 + \frac{A \sin^2 \theta}{\rho^2} d\varphi^2, \quad (4.23)$$

where

$$\Delta = \frac{r(r+b) - 2Mr}{1+\ell} + a^2 \quad \text{and} \quad A = [r(r+b) + (1+\ell)a^2]^2 - \Delta(1+\ell)^2 a^2 \sin^2 \theta. \quad (4.24)$$

If $\ell \rightarrow 0$, it recovers the usual Kerr-Sen metric and for $a \rightarrow 0$ and $b \rightarrow 0$, it becomes

$$ds^2 = - \left(1 - \frac{2M}{r}\right) dt^2 + \frac{1+\ell}{1-2M/r} dr^2 + r^2 d\theta^2 + r^2 \sin^2 \theta d\varphi^2, \quad (4.25)$$

which is the same as that of the article [67]. The metric (4.23) represents a purely radial Lorentz-violating black hole solution with angular momentum per unit mass a and charge \sqrt{bM} . It is singular at $\rho^2 = 0$ and at $\Delta = 0$. The horizons are given by

$$r_{\pm} = M - \frac{b}{2} \pm \frac{\sqrt{(b-2M)^2 - 4a^2(1+\ell)}}{2}, \quad (4.26)$$

where \pm signs correspond to the event horizon labelled by r_{ch} and Cauchy horizon labelled by r_{ch} respectively. We will have a black hole when the condition given below is satisfied

$$|b - 2M| \geq 2a\sqrt{1+\ell} \quad (4.27)$$

We present below parameter space (a, b) for various values of ℓ .

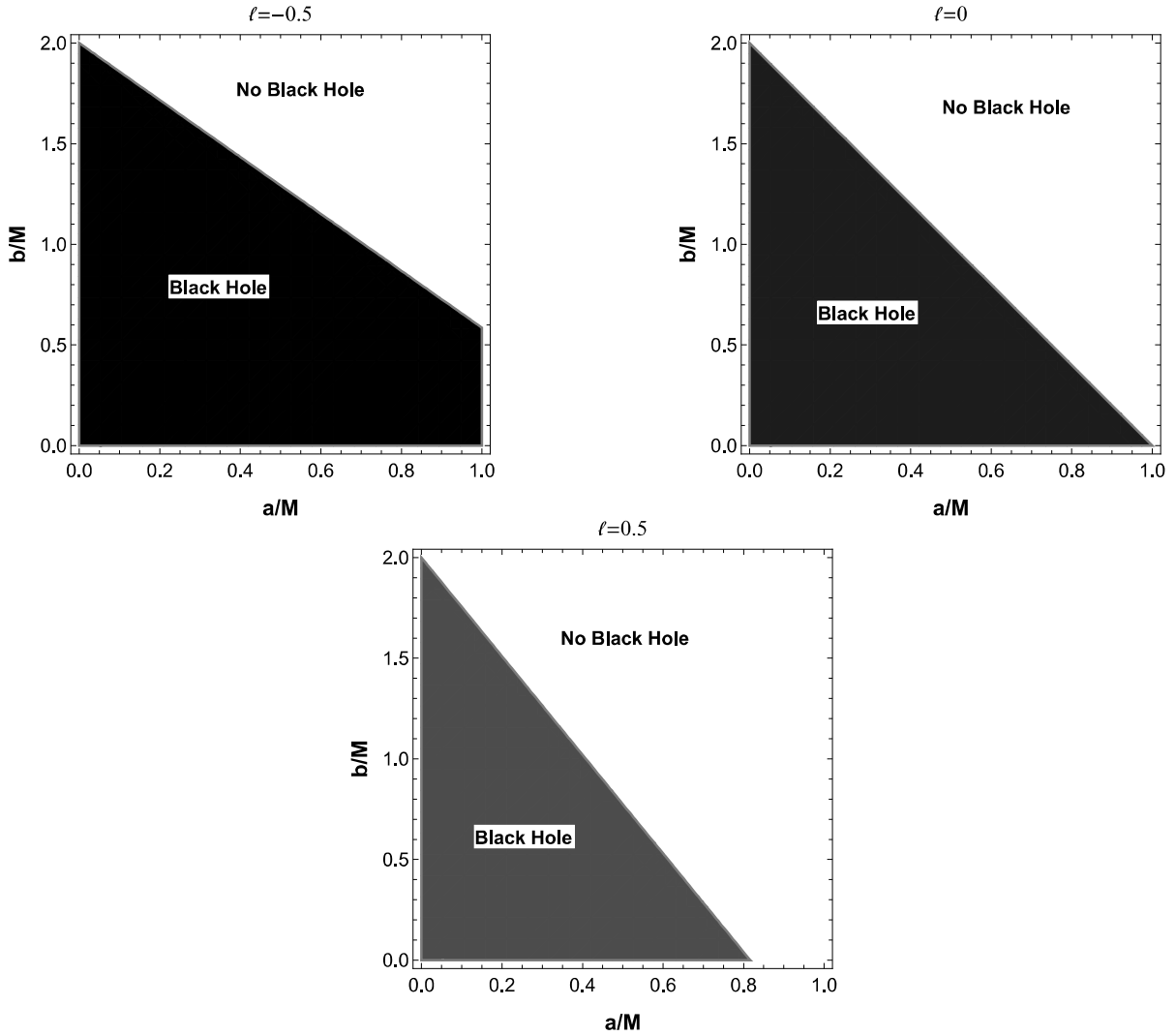


Figure 4.1: Parameter space (a, b) for various values of ℓ .

From above we see that the parameter space for which we have black hole is shrinking with increase in ℓ . Plots of Δ against r/M for various cases are furnished below.

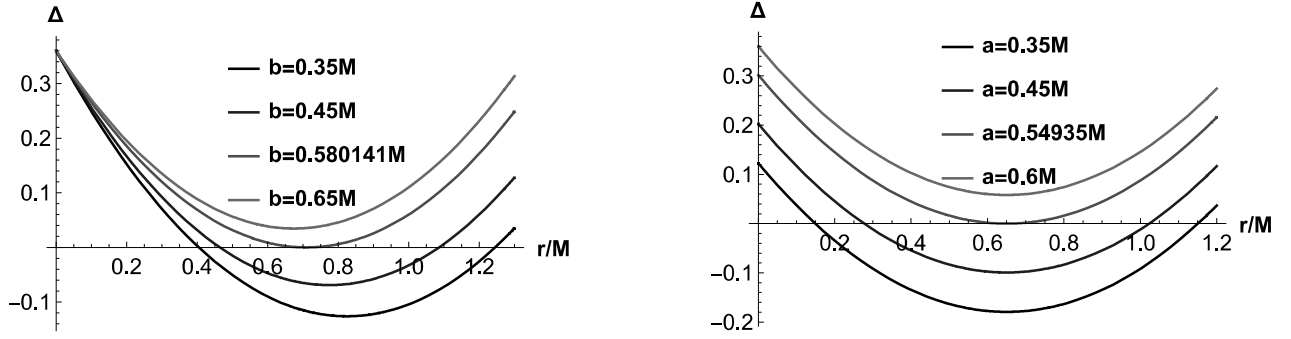


Figure 4.2: The left one gives the variation of Δ for various values of b with $a = 0.6M$ and $\ell = 0.4$ and the right one gives the variation for various values of a with $b = 0.7M$ and $\ell = 0.4$.

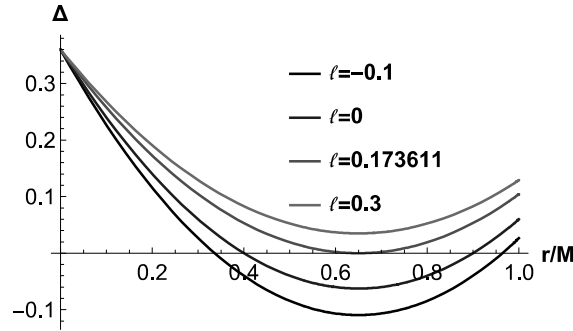


Figure 4.3: It gives the variation of Δ for various values of ℓ with $b = 0.7M$ and $a = 0.6M$.

From the above plots, we see that there exist critical values of a , i.e. a_c , for fixed values of b, ℓ , critical values of b , i.e. b_c , for fixed values of a, ℓ and critical values of ℓ , i.e. ℓ_c , for fixed values of b, a for which $\Delta = 0$ has only one root, i.e. we have extremal black hole. For $a < a_c$, we have black hole and for $a > a_c$, we have naked singularity. Similarly, for $b < b_c$, we have black hole, for $b > b_c$ we have naked singularity, and for $\ell < \ell_c$, we have black hole, for $\ell > \ell_c$ we have naked singularity. For example, with $b = 0.7M, \ell = 0.4$, we have $a_c = 0.54935$, with $a = 0.6M, \ell = 0.4$, we have $b_c = 0.580141M$, and with $a = 0.6M, b = 0.7M$, we have $\ell_c = 0.173611$.

Now, at the static limit surface (SLS) the asymptotic time-translational Killing vector becomes null which gives

$$g_{tt} = \rho^2 - 2Mr = 0 \quad (4.28)$$

The real positive solutions of above equation give radial coordinates of ergosphere given by

$$r_{\pm}^{ergo} = M - \frac{b}{2} \pm \frac{\sqrt{(b - 2M)^2 - 4a^2(1 + \ell) \cos^2 \theta}}{2}. \quad (4.29)$$

Inside the SLS, no observer can stay static and they are bound to co-rotate around the black hole. Ergosphere is the region that lies between the SLS and the event horizon. It is depicted below. According to Penrose [27], energy can be extracted from black hole's ergosphere. From the plots below we observe that the shape of the ergosphere strongly depends on parameters a, b , and ℓ .

4.1. HAWKING TEMPERATURE

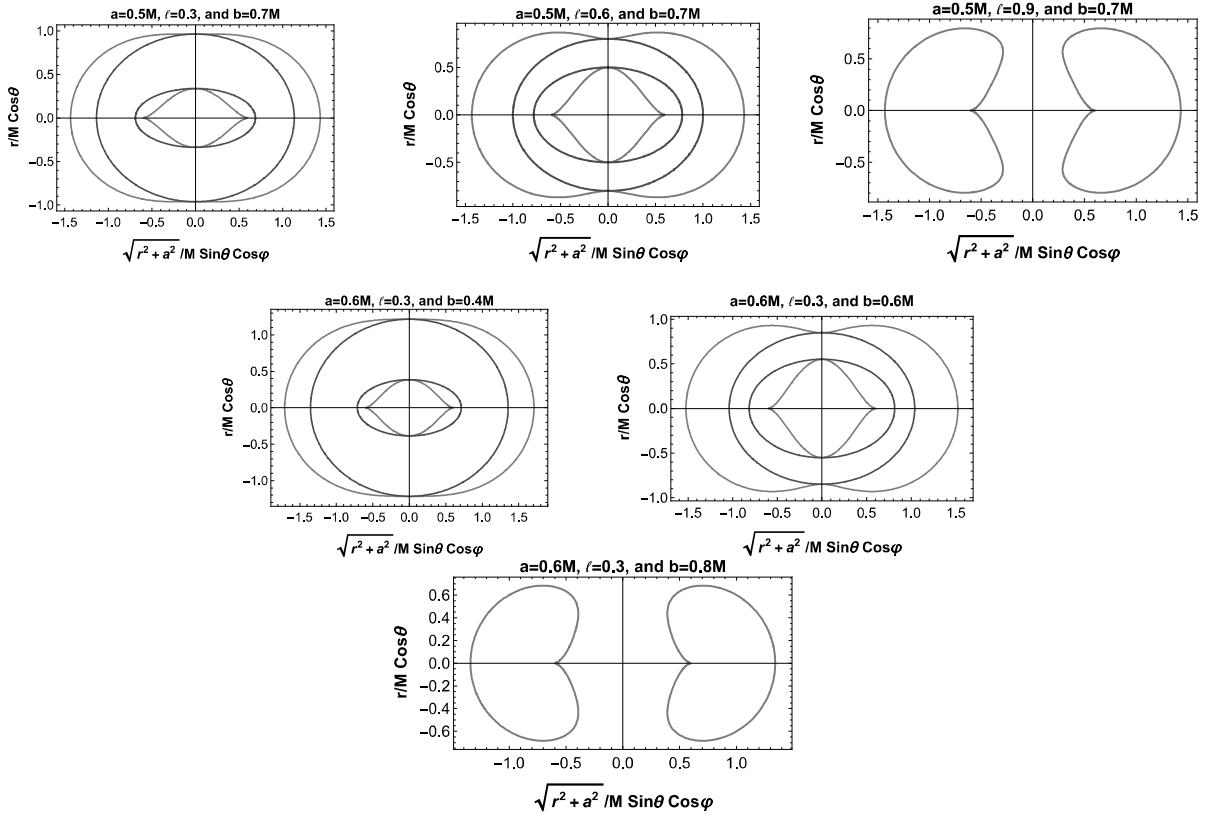


Figure 4.4: The cross-section of event horizon (outer red line), SLS (outer blue dotted line) and ergoregion of Kerr-Sen-like black holes

Angular velocity at horizon is found out to be

$$\hat{\Omega}_h = \frac{a\sqrt{1+\ell}}{r_{eh}(r_{eh}+b) + a^2(1+\ell)}. \quad (4.30)$$

4.1 Hawking temperature

The Hawking temperature in terms of surface gravity κ is given by [28]

$$T_H = \frac{\kappa}{2\pi}, \kappa = -\frac{1}{2} \lim_{r \rightarrow r_+} \sqrt{\frac{-1}{X}} \frac{dX}{dr}, X \equiv g_{tt} - \frac{g_{t\varphi}^2}{g_{\varphi\varphi}}. \quad (4.31)$$

Inserting corresponding metric components from Eq. (4.23) in above equation, we get

$$T_H = \frac{\sqrt{(2M-b)^2 - 4a^2(1+\ell)}}{4\pi M\sqrt{1+\ell} \left(2M-b + \sqrt{(2M-b)^2 - 4a^2(1+\ell)} \right)}. \quad (4.32)$$

4.2 Photon orbit and black-hole shadow

In order to study black hole shadow we introduce in [76] two conserved parameters ξ and η which are defined by

$$\xi = \frac{L_z}{E} \quad \text{and} \quad \eta = \frac{Q}{E^2}, \quad (4.33)$$

4.2. PHOTON ORBIT AND BLACK-HOLE SHADOW

where E , L_z , and Q are the energy, the axial component of the angular momentum and the Carter constant, respectively. Then, equations for the null geodesics in the bumblebee rotating black hole spacetime turned into

$$\begin{aligned}\rho^2 \frac{dr}{d\lambda} &= \pm \sqrt{R}, \quad \rho^2 \frac{d\theta}{d\lambda} = \pm \sqrt{\Theta} \\ (1 + \ell) \Delta \rho^2 \frac{dt}{d\lambda} &= A - 2\sqrt{1 + \ell} M r a \xi \\ (1 + \ell) \Delta \rho^2 \frac{d\phi}{d\lambda} &= 2\sqrt{1 + \ell} M r a + \frac{\xi}{\sin^2 \theta} (\rho^2 - 2Mr),\end{aligned}\quad (4.34)$$

where λ is the affine parameter and

$$R(r) = \left[\frac{r(r+b) + (1+\ell)a^2}{\sqrt{1+\ell}} - a\xi \right]^2 - \Delta \left[\eta + (\xi - \sqrt{1+\ell}a)^2 \right], \quad \Theta(\theta) = \eta + (1+\ell)a^2 \cos^2 \theta - \xi^2 \cot^2 \theta.$$

The plots of V_{eff} vs r/M and r_c/M vs a/M are given in figures (4.5)-(4.10) for various values of b and ℓ .

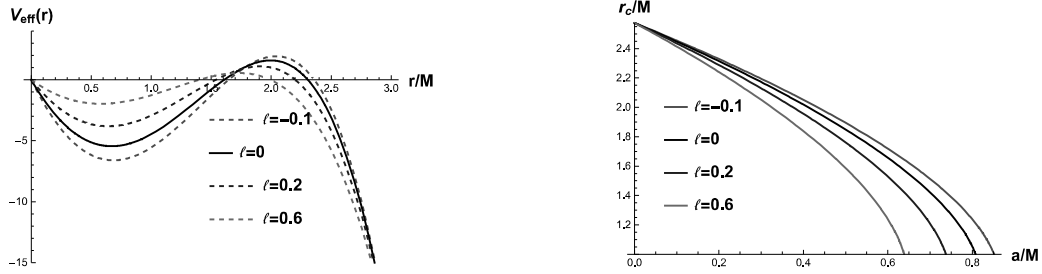


Figure 4.5: The left panel describes the effective potential for various values of ℓ with $b = 0.36M$, $a = 0.5M$, and the right panel describes critical radius for various values of ℓ with $b = 0.36M$ in case of prograde orbits.

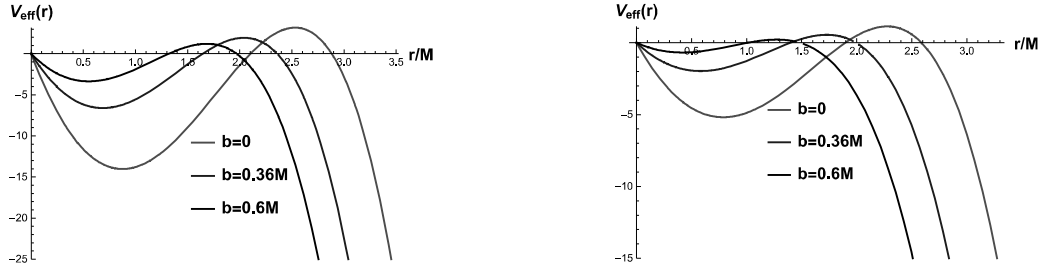


Figure 4.6: The left panel describes effective potential for various values of b with $a = 0.5M$, $\ell = -0.1$, and the right panel describes effective potential for various values of b with $a = 0.5M$ and $\ell = 0.6$ in case of prograde orbits.

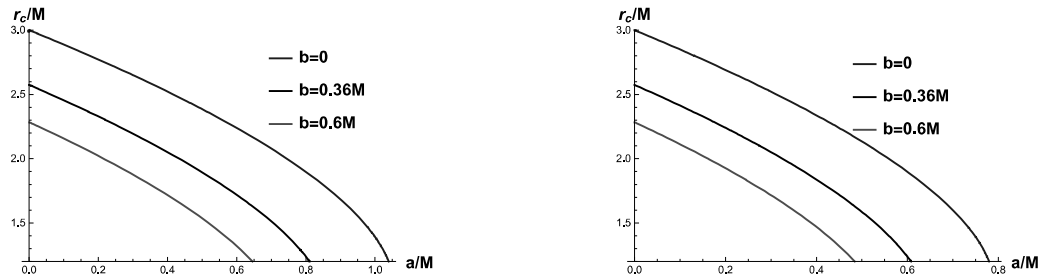


Figure 4.7: The left panel describes critical radius for various values of b with $\ell = -0.1$ and right panel describes critical radius for various values of b with $\ell = 0.6$ in case of prograde orbits.

4.2. PHOTON ORBIT AND BLACK-HOLE SHADOW

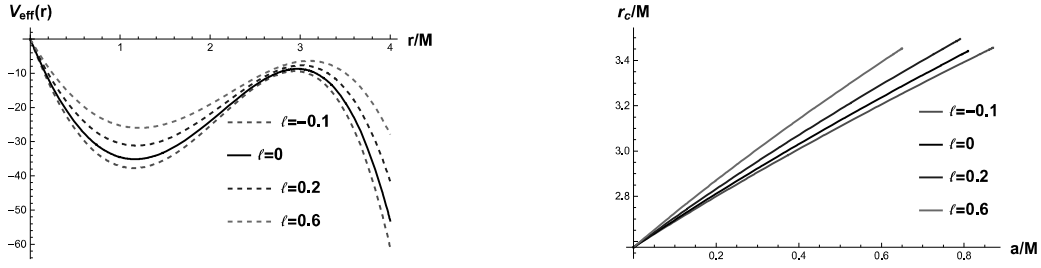


Figure 4.8: The left panel describes the effective potential for various values of ℓ with $b = 0.36M$, $a = 0.5M$, and the right panel describes critical radius for various values of ℓ with $b = 0.36M$ for retrograde orbits.

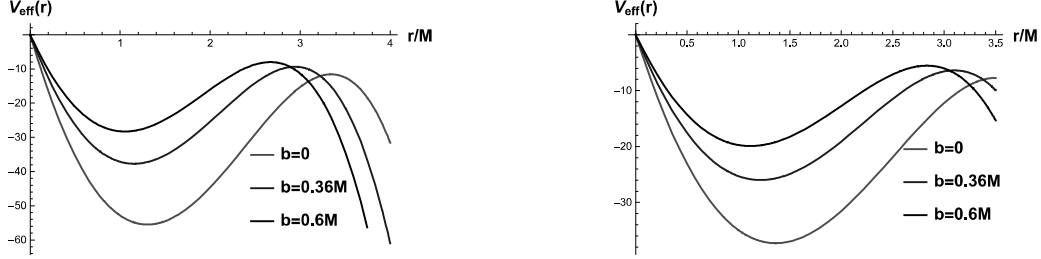


Figure 4.9: The left panel describes effective potential for various values of b with $a = 0.5M$, $\ell = -0.1$, and the right panel describes effective potential for various values of b with $a = 0.5M$, $\ell = 0.6$ in case of retrograde orbits.

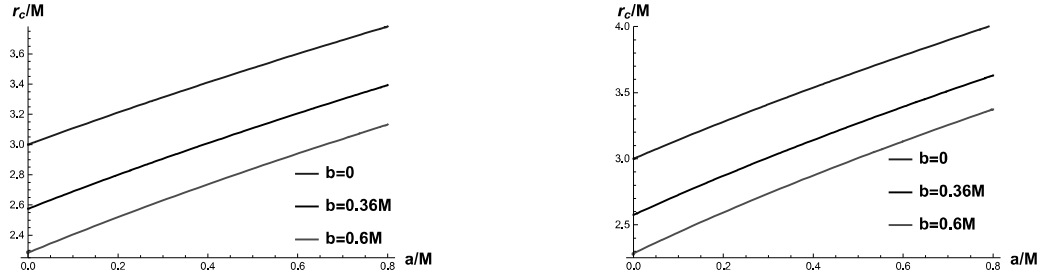


Figure 4.10: The left panel describes critical radius for various values of b with $\ell = -0.1$ and the right panel describes critical radius for various values of b with $\ell = 0.6$ in case of retrograde orbits.

The radial equation of motion can be written down in the form

$$\left(\rho^2 \frac{dr}{d\lambda}\right)^2 + V_{eff} = 0. \quad (4.35)$$

The effective potential V_{eff} reads

$$V_{eff} = -\left[\frac{r(r+b) + (1+\ell)a^2}{\sqrt{1+\ell}} - a\xi\right]^2 + \Delta \left[\eta + (\xi - \sqrt{1+\ell}a)^2\right]. \quad (4.36)$$

Note that $V_{eff}(0) = 0$ and $V_{eff}(r \rightarrow \infty) \rightarrow \infty$.

The unstable spherical orbit on the equatorial plane is given by the equation (1.70). We plot V_{eff} against r/M with $\xi = \xi_c + 0.2$ where ξ_c is the value of ξ for equatorial spherical unstable orbit. Plots of V_{eff} for prograde orbits show that the photon starting from infinity will meet a turning point, and then turns back to infinity. When $\xi = \xi_c$, this turning point is an unstable spherical orbit which gives the boundary of the shadow [68]. It also shows that the deviation from GR (Kerr-Sen): when LV constant $\ell > 0$, the turning point shifts to the left, however, when $\ell < 0$ it shifts to the right. These shifts are similar to those of the Einstein-aether black hole [69], which is also a LV black hole. The same type of shifting was reported in [48] for Kerr-like black-hole. Let us look towards critical radii of prograde and retrograde orbits. We have plotted radius r_c of unstable equatorial spherical direct (prograde) orbit as well as retrograde orbit against a/M for various scenarios. It shows that r_c

decreases with $\ell > 0$, for direct orbit, however, it increases when $\ell < 0$, which are similar to those of the non-commutative black hole [68]. This is also similar to the observation made in the article [48]. The r_c decreases with b for a particular ℓ irrespective of its sign. For retrograde orbit, r_c increases with the increase in ℓ or b .

For more generic orbits, $\theta \neq \pi/2$ and $\eta \neq 0$, and the conserved parameters for such spherical orbits of radius r_s are given by

$$\begin{aligned}\xi_s &= \frac{a^2 (1 + \ell) (2M + 2r_s + b) + r_s (2r_s^2 + 3br_s + b^2 - 2M (3r_s + b))}{a\sqrt{1 + \ell} (2M - 2r_s - b)}, \\ \eta_s &= -\frac{r_s^2 \left(-8a^2 (1 + \ell) M (2r_s + b) + (2r_s^2 + 3br_s + b^2 - 2M (3r_s + b))^2 \right)}{a^2 (1 + \ell) (2M - 2r_s - b)^2}.\end{aligned}\quad (4.37)$$

The two celestial coordinates, which are used to describe the shape of the shadow that an observer see in the sky, can be given by

$$\begin{aligned}\alpha(\xi, \eta; \theta) &= \lim_{r \rightarrow \infty} \frac{-rp^{(\varphi)}}{p^{(t)}} = -\xi_s \csc \theta, \\ \beta(\xi, \eta; \theta) &= \lim_{r \rightarrow \infty} \frac{rp^{(\theta)}}{p^{(t)}} = \sqrt{\eta_s + a^2 \cos^2 \theta - \xi_s^2 \cot^2 \theta},\end{aligned}\quad (4.38)$$

where $(p^{(t)}, p^{(r)}, p^{(\theta)}, p^{(\varphi)})$ are tetrad components of the photon momentum with respect to a locally non-rotating reference frame [30].

The shadow of the collapsed object is defined as follows. Suppose some light rays are emitted at infinity ($r = +\infty$) and propagate near the collapsed object. If they can reach the observer at infinity after scattering, then its direction is not dark. On the other hand, when they fall into the event horizon of a black hole, the observer will never see such light rays. Such a direction becomes dark. It makes a shadow. We define the apparent shape of a black hole by the boundary of the shadow [29]. We have seen the shapes of the shadows as given below [76].

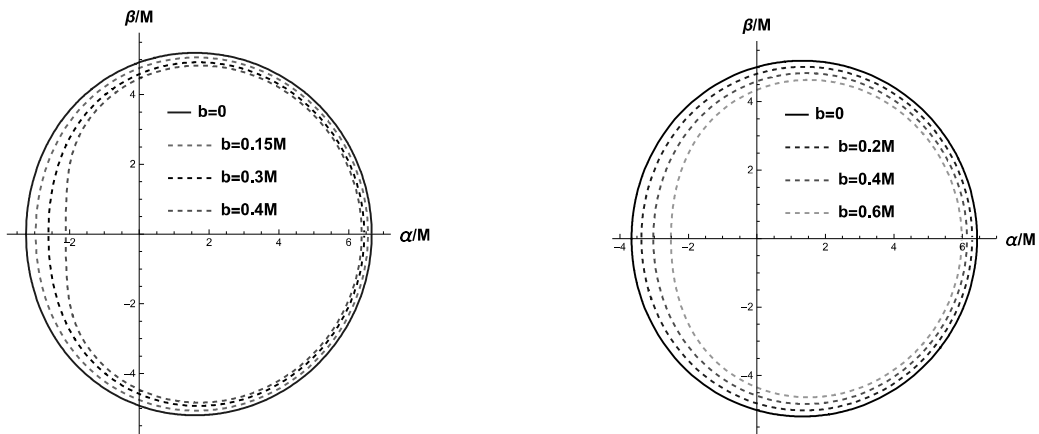


Figure 4.11: The left one gives shapes of the shadow for various values of b with $a = 0.7M$, $\ell = 0.3$, and $\theta = \pi/2$. The right one gives shapes of the shadow for various values of b with $a = 0.7M$, $\ell = -0.1$, and $\theta = \pi/2$.

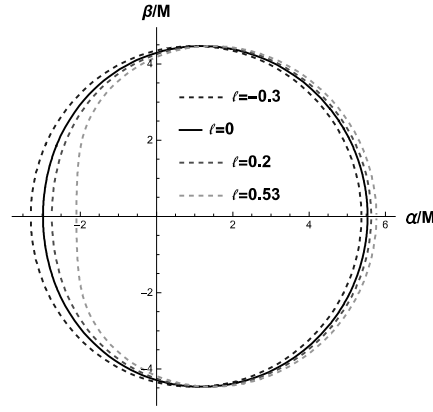


Figure 4.12: The shapes of the shadow for various values of ℓ with $a = 0.5M$, $b = 0.76M$, and $\theta = \pi/2$.

The Fig. (4.12) shows that the left end of the shadow shifts towards right for positive values of ℓ for a particular b and reverse is the case when ℓ is negative. However, irrespective of the sign of ℓ the shifting of the left end of the shadow is towards right for increasing b . Using the parameters which are introduced by Hioki and Maeda [32], we analyse deviation from circular form (δ_s) and the size (R_s) of the shadow image of the black hole.

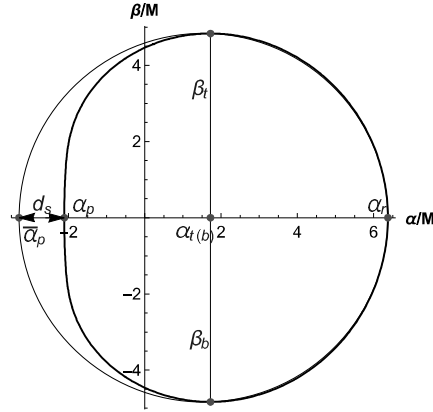


Figure 4.13: A sketch of the black hole shadow and the reference circle. Here d_s represents the distance between the extreme left point of the shadow and the reference circle.

For calculating these parameters, we have considered five points (α_t, β_t) , (α_b, β_b) , $(\alpha_r, 0)$, $(\alpha_p, 0)$ and $(\bar{\alpha}_p, 0)$ which are top, bottom, rightmost, leftmost of the shadow, and leftmost of the reference circle respectively. So, we have

$$R_s = \frac{(\alpha_t - \alpha_r)^2 + \beta_t^2}{2(\alpha_t - \alpha_r)},$$

and

$$\delta_s = \frac{(\bar{\alpha}_p - \alpha_p)}{R_s}.$$

4.3. ENERGY EMISSION RATE

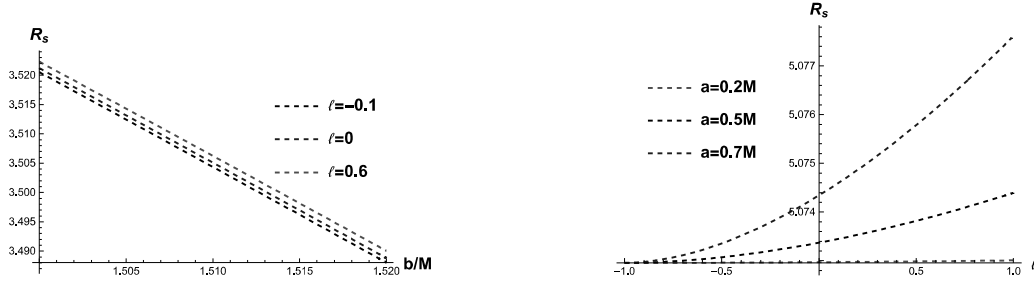


Figure 4.14: The left one gives variation of R_s for various values of ℓ with $a = 0.2M$ and $\theta = \pi/2$, and the right one gives variation of R_s against ℓ for various values of a with $b = 0.14M$ and $\theta = \pi/2$.

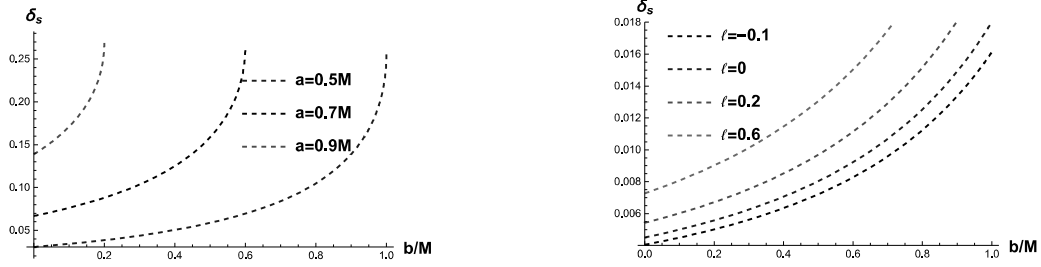


Figure 4.15: The left one gives the variation of δ_s for various values of a with $\ell = 0$ and $\theta = \pi/2$, and the right one gives variation of δ_s for various values of ℓ with $a = 0.2M$ and $\theta = \pi/2$.

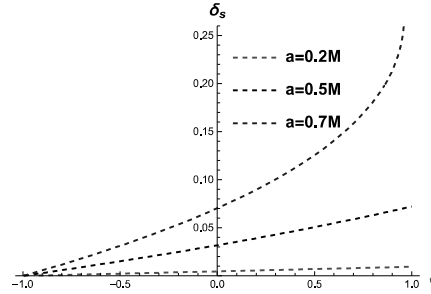


Figure 4.16: The variation of δ_s against ℓ for various values of a with $b = 0.04M$ and $\theta = \pi/2$.

From the plots above we observe that as we increase b for a fixed value ℓ and a , R_s decreases and δ_s increases. For fixed values of b and a , both R_s and δ_s increases but the nature of variation differ for different values of a . Thus, the Lorentz violating term has a significant impact on the size of the shadow and its deviation from the circular form. For all plots, we have taken $M = 1$.

4.3 Energy emission rate

Scattering of electromagnetic and gravitational waves from rotating black hole whose gravitational field is described by the Kerr metric is calculated in [70] and insight for absorption phenomena is well understood from there. Here, we study the possible visibility of the Kerr-Sen-like black hole through the shadow. In the vicinity of limiting constant value, the cross-section of the black hole's absorption moderates lightly at high energy. We know that a rotating black hole can absorb electromagnetic waves, so the absorbing cross-section for a spherically symmetric black hole is [64]

$$\sigma_{lim} = \pi R_s^2. \quad (4.39)$$

Using above equation the energy emission rate is [65]

$$\frac{d^2 E}{d\omega dt} = \frac{2\pi^3 R_s^2}{e^{\left(\frac{\omega}{T_H}\right)} - 1} \omega^3, \quad (4.40)$$

4.3. ENERGY EMISSION RATE

where T_H is the Hawking temperature and ω is the frequency of the electromagnetic radiation.

Taking into account the angular velocity of black hole, and then from the information available in the article [71], the above equation gets modified into

$$\frac{d^2 E}{d\omega dt} = \frac{2\pi^3 R_s^2}{e^{\left(\frac{\omega - \Omega_h}{T_H}\right)} - 1} \omega^3, \quad (4.41)$$

where $\Omega_h = \frac{a\sqrt{1+\ell}}{r_+(r_++b)+(1+\ell)a^2}$ is the angular velocity of the black hole. Let us first give different plots without considering the black hole frequency in Fig. (4.17), Fig. (4.18), and Fig. (4.20). After that, in Fig. (4.21), we have given the sketch considering the black hole frequency. Here, both cases $\omega > \Omega_h$ as well as $\omega < \Omega_h$ are considered. The figure indicates that depending on the value of electromagnetic frequency, both absorption and emission may happen.

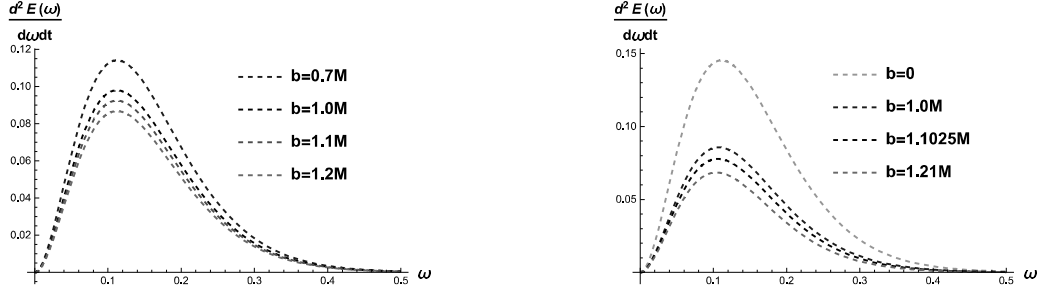


Figure 4.17: The left one gives variation of emission rate against ω for various values of b with $a = 0$ and $\ell = 0$, and the right one gives variation of emission rate against ω for various values of b with $a = 0.2M$ and $\ell = 0$.

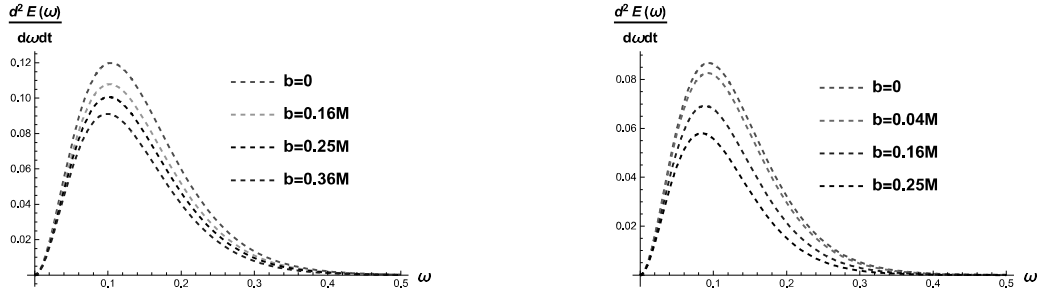


Figure 4.18: The left one gives variation of emission rate against ω for various values of b with $a = 0.5M$ and $\ell = 0$, and the right one gives variation of emission rate against ω for various values of b with $a = 0.7M$ and $\ell = 0$.

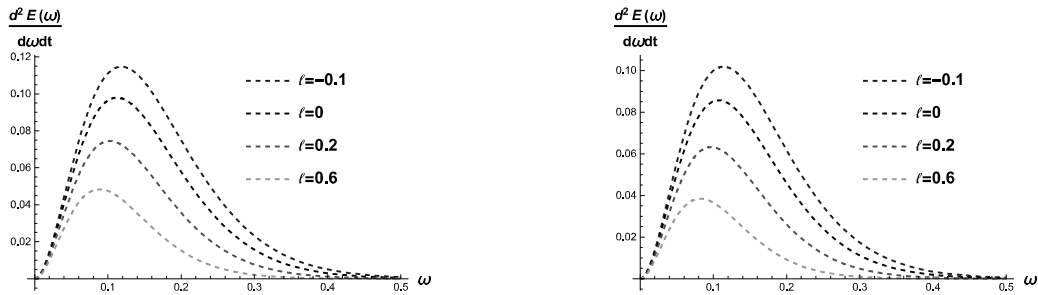


Figure 4.19: The left one gives variation of emission rate against ω for various values of ℓ with $a = 0$ and $b = M$, and the right one gives variation of emission rate against ω for various values of ℓ with $a = 0.2M$ and $b = M$.

We have plotted the energy emission rate versus ω for various cases in [76] which are shown in figures (4.17)-(4.21). It is clear from the graphs that the emission rate decreases with the increase in b for any set of fixed values of a and ℓ . It also decreases when ℓ increases for any set of fixed values of a and b . However, there is a crucial difference in the situation when ℓ increases. It is true that the emission rate decreases with the increase in ℓ like the case when b increases, but unlike the situation when b increases, the pick of the curve gets shifted when ℓ increases. From the plot (4.21), we see there is a discontinuity at $\omega = \Omega_h$ and the graphs shift to the right as we increase the value of ℓ .

4.4. COMPARISON BETWEEN SCHWARZSCHILD-LIKE, KERR-LIKE AND KERR-SEN-LIKE BLACK HOLES

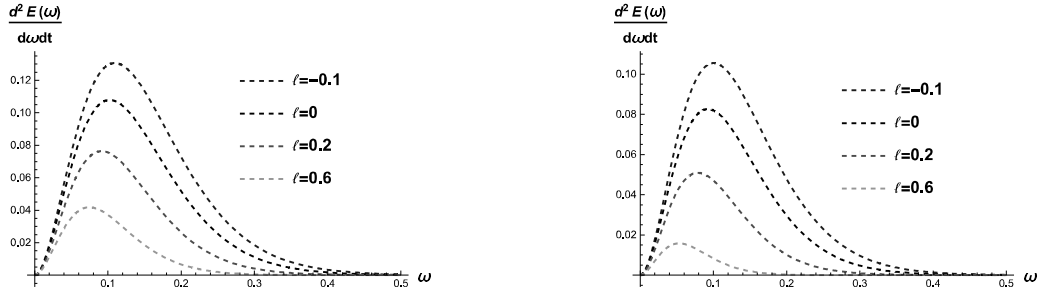


Figure 4.20: The left one gives variation of emission rate against ω for various values of ℓ with $a = 0.5M$ and $b = 0.16M$, and the right gives variation of emission rate against ω for various values of ℓ with $a = 0.7M$ and $b = 0.04M$.

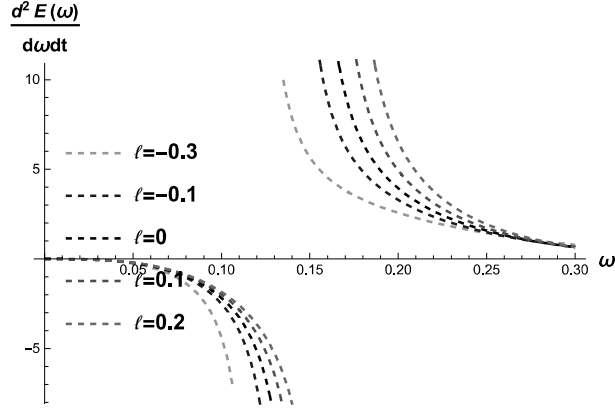


Figure 4.21: It gives emission rate for various values of ℓ with $b = 0.16M$ and $a = 0.5M$ taking angular velocity of black hole into consideration.

4.4 Comparison between Schwarzschild-like, Kerr-like and Kerr-Sen-like Black holes

It is beneficial if a comparison for the shift of the shadows corresponding to the Schwarzschild-like, Kerr-like and Kerr-Sen-like Black holes is made. In this context, we have included the sketch of the shadows for these three black holes for different values of $\ell = 0, 0.2, -0.2$ keeping $a = 0.5M$ and $b = 0.4M$ fixed in all the cases.

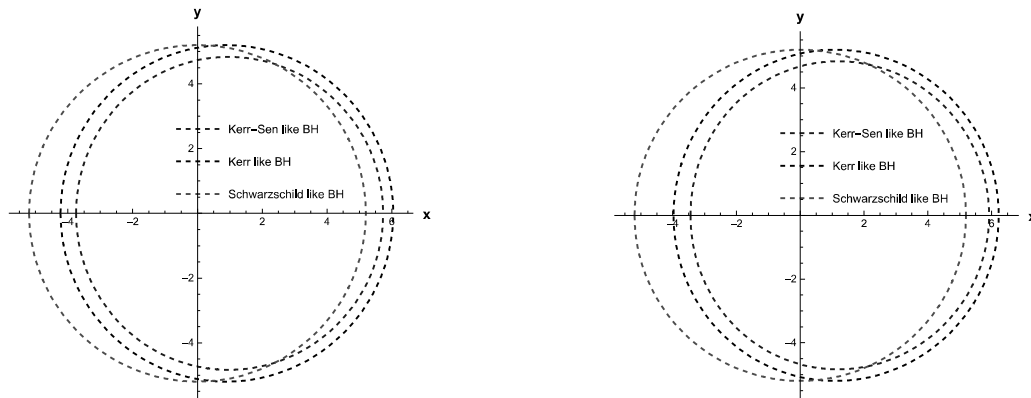
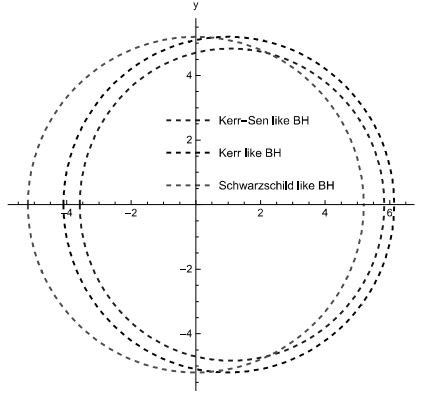


Figure 4.22: The left one gives shapes of the shadow for various black holes with $\ell = -0.2$ and $\theta = \pi/2$, and the right one gives shapes of the shadow for various black holes with $\ell = 0.2$ and $\theta = \pi/2$.


 Figure 4.23: This one gives shapes of the shadow for various black holes with $\ell = 0$ and $\theta = \pi/2$.

The Plots in the figure (4.22) and 4.23 clearly show that the size of the shadow of Schwarzschild-like black hole does not depend on the Lorentz-violation parameter ℓ . However, the shadows of Kerr-like black hole and Kerr-Sen-like black hole shift to the right of the shadow of Schwarzschild-like black hole. It is also clear from the plots that the size of the shadow of Kerr-like black hole is bigger than that of Kerr-Sen-like black hole. Deviations of Kerr-like black hole and Kerr-Sen-like black hole from Schwarzschild-like black hole are given in the table below.

Table 4.1: .Deviations of Kerr-like BH and Kerr-Sen-like BH from Schwarzschild-like BH

	$\ell = -0.2$	$\ell = 0$	$\ell = 0.2$
Deviation of Kerr-like BH from Schwarzschild-like BH	0.97095	1.09989	1.22045
Deviation of Kerr-Sen-like BH from Schwarzschild-like BH	1.45049	1.60503	1.75373

It is evident from the table that as value of ℓ is increased, deviation is increasing for both Kerr-like and Kerr-Sen-like black holes.

4.5 Bending of light

Let us describe the bending of light which may be considered as an observable on the angular plane [76]. With the change of variable $r + b = 1/v$, and following the same procedure as adopted in [72], the equation of the orbit at an angular plane (i.e. $\theta = \pi/2$) for massless test particles can be written down as

$$\left(\frac{dv}{d\phi}\right)^2 = \frac{\left[j^2 \left((1-bv)^2 + (1-bv)a^2(1+\ell)v^2 + 2Ma^2(1+\ell)v^3\right) - 4jMa\sqrt{(1+\ell)}v^3 - B(v)v^2\right]}{\mathcal{B}^2(v)} \times (\mathcal{B}(v) + 2Mbv^2 + a^2(1+\ell)v^2) (\mathcal{B}(v) + a^2(1+\ell)v^2), \quad (4.42)$$

where $j = a\sqrt{(1+\ell)}/M$, $b = Q^2/M$, and $\mathcal{B}(u) = 1 - (b + 2M)v$. Expanding the right hand side of the above equation and retaining the terms up to cubic power in v we obtain

$$\frac{d\phi}{dv} = \frac{1}{\sqrt{j^2 + \mathcal{G}v + \mathcal{H}v^2 + \mathcal{I}v^3}} \Rightarrow \phi - \phi_0 = \int_{v_0}^v \frac{dv}{\sqrt{j^2 + \mathcal{G}v + \mathcal{H}v^2 + \mathcal{I}v^3}}. \quad (4.43)$$

Here, $\mathcal{G} = -2j^2b$, $\mathcal{H} = j^2(b^2 + 2Mb + 3a^2(1+\ell)) - 1$, and $\mathcal{I} = j^2[a^2(1+\ell)(2M-5) - 4Mb^2] - 4a^2(1+\ell) + y[1 - 2(a^2(1+\ell) + Mb)]$. Hence, we have

$$\Delta\phi = \frac{C}{\mathcal{N}} \arctan \left[\frac{\mathcal{N}v + j^2b}{\mathcal{N}\sqrt{j^2 - 2j^2bv - \mathcal{N}v^2}} \right], \quad (4.44)$$

4.5. BENDING OF LIGHT

with $\mathcal{N} = [1 - j^2 (2bM + 3a^2 (1 + \ell)) - j^2 b^2]^{1/2}$. The corresponding equation for Kerr-like black holes is obtained if we set $b = 0$ and the expression for $\Delta\phi$ turns into

$$\Delta\phi = \frac{C}{\mathcal{P}} \arctan \left[\frac{\mathcal{P}v}{\mathcal{P}\sqrt{j^2 - \mathcal{P}v^2}} \right], \quad (4.45)$$

with $r = 1/v$, $j = \frac{a\sqrt{1+\ell}}{M}$, and $\mathcal{P} = [1 - 3j^2 a^2 (1 + \ell)]^{1/2}$.

Chapter 5

Kerr-Sen-like black hole in the presence of a dispersive medium

In general relativity, light is attributed to the null geodesic of the spacetime metric and the in-medium effect is negligible for most of the frequency ranges. It is, however, significant for the radio frequency range. In this context, it is worth mentioning the impact of Solar corona on the time of travel and on the deflection angle of radio signals that come close to the Sun. Since 1960s, this influence has been routinely observed. In this case, one may assume that the medium is a non-magnetized pressure less plasma and for the gravitational field, the linearized theory is considered to be sufficient. The relevant theoretical development has been made by Muhleman et al. in articles [73, 74]. With the available information, the shadow of black holes in presence of plasma has become an interesting field of research for physicists since there is a good reason for considering that black holes and other compact objects are surrounded by plasma. So, naturally, interest grows to investigate whether the presence of plasma leads to any observational effect on the radio signals and several investigations have been carried out in that direction [75, 78, 80, 193, 213–220].

In this context, we study the LV effect on the shadow of a black hole in the presence of a dispersive media like plasma in [119]. There are several recent investigations to study the deformation of black hole shadow due to the LV effect [48, 76]. In these studies, the in-medium (plasma) effect has not been considered so far. Therefore, we have studied the deformation of the shadow of the black hole connected with Kerr-Sen-like spacetime, the emission of energy from this black hole due to radiation, and the weak lensing in the presence of plasma in [119] which we are describing in this chapter. The black hole metric (4.23) associated with Kerr-Sen-like spacetime contains an LV parameter as both the Schwarzschild-like and Kerr-like spacetime contain [44, 48]. This Kerr-Sen-like spacetime will enable us to study the LV effect in presence of plasma.

We consider a static inhomogeneous plasma in the gravitational field with a refractive index n . The expression of refractive index n , as formulated by Synge [77], in terms of dynamical variables reads

$$n^2 = 1 + \frac{p_\mu p^\mu}{(p_\nu u^\nu)^2}, \quad (5.1)$$

where p_μ and u^ν are four-momentum and four-velocity of the massless particle respectively. The Hamiltonian for massless particles like photon is

$$H(x^\mu, p_\mu) = \frac{1}{2} \left[g^{\mu\nu} p_\mu p_\nu - (n^2 - 1) \left(p_0 \sqrt{-g^{00}} \right)^2 \right]. \quad (5.2)$$

The standard definitions, $x^\mu = \partial H / \partial p_\mu$ and $\dot{p}_\mu = \partial H / \partial x^\mu$, lead us to write down the equations of motion for photon in the plasma medium as

$$\rho^2 \frac{dr}{d\lambda} = \pm \sqrt{R}, \quad \rho^2 \frac{d\theta}{d\lambda} = \pm \sqrt{\Theta}, \quad (5.3)$$

$$(1 + \ell) \Delta \rho^2 \frac{dt}{d\lambda} = An^2 - 2\sqrt{1 + \ell} Mra\xi, \quad (5.4)$$

$$(1 + \ell)\Delta\rho^2\frac{d\varphi}{d\lambda} = 2Mra\sqrt{1 + \ell} + \frac{\xi}{\sin^2\theta}(\rho^2 - 2Mr), \quad (5.5)$$

where λ is the affine parameter and

$$\begin{aligned} R(r) &= \left[\frac{r(r+b) + (1+\ell)a^2}{\sqrt{1+\ell}} - a\xi \right]^2 - \Delta \left[\eta + (\xi - \sqrt{1+\ell}a)^2 \right] + (n^2 - 1) \frac{[r(r+b) + a^2(1+\ell)]^2}{1+\ell}, \\ \Theta(\theta) &= \eta + (1+\ell)a^2 \cos^2\theta - \xi^2 \cot^2\theta - (n^2 - 1)a^2(1+\ell) \sin^2\theta. \end{aligned} \quad (5.6)$$

In equation (5.6), we introduce two conserved parameters ξ and η as usual, which are defined by

$$\xi = \frac{L_z}{E} \quad \text{and} \quad \eta = \frac{\mathcal{Q}}{E^2}, \quad (5.7)$$

where E , L_z and \mathcal{Q} are the energy, the axial component of the angular momentum, and the Carter constant respectively.

In terms of ω , the square of the refractive index n is defined by [78]

$$n^2 = 1 - \frac{\omega_e^2}{\omega^2}, \quad (5.8)$$

where ω and ω_e are, respectively, the frequency of photon and the electron-plasma frequency. In the general theory of relativity, the redshift scenario entails that frequency of photons depends on the spatial coordinates due to the presence of the gravitational field. Besides, the electron-plasma frequency has the expression [65]

$$\omega_e^2 = \frac{4\pi e^2 N(r)}{m}, \quad (5.9)$$

where $N(r)$ is the concentration of electron in the inhomogeneous plasma. The mass and the charge of the electron are respectively denoted by m and e . We now consider a radial power-law density as

$$N(r) = \frac{N_0 r_0}{r^h}, \quad (5.10)$$

where N_0 is the density number at the radial position of the inner edge of plasma environment r_0 . Therefore, we have

$$\omega_e^2 = \frac{4\pi e^2 N_0 r_0}{m r^h}, \quad (5.11)$$

where $h \geq 0$. Here we consider $h = 1$, as it has been considered in the article [79], so that we have

$$n = \sqrt{1 - \frac{k}{r}}. \quad (5.12)$$

5.1 Effective potential and Critical radius

With the specific form of refractive index (5.12), we have studied various aspects of photon geodesics in [119] with the spacetime metric given in Eq. (4.23). The radial equation of motion has the known form

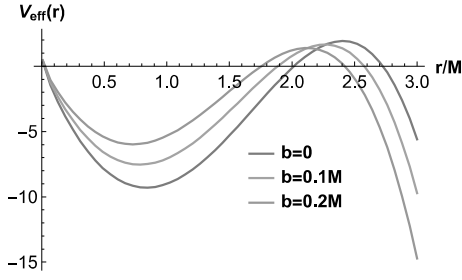
$$\left(\rho^2 \frac{dr}{d\lambda} \right)^2 + V_{eff} = 0. \quad (5.13)$$

The effective potential V_{eff} in this situation reads

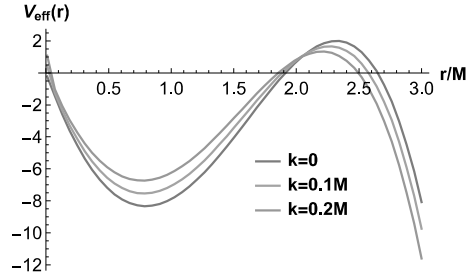
$$V_{eff} = - \left[\frac{r(r+b) + (1+\ell)a^2}{\sqrt{1+\ell}} - a\xi \right]^2 + \Delta \left[\eta + (\xi - \sqrt{1+\ell}a)^2 \right] - (n^2 - 1) \frac{[r(r+b) + a^2(1+\ell)]^2}{1+\ell}.$$

Note that it contains both factors ℓ and k .

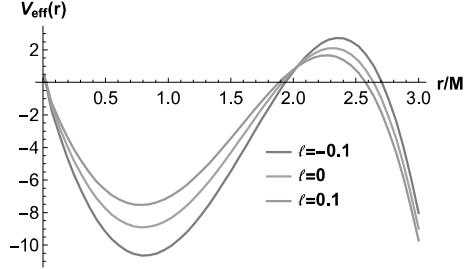
5.1. EFFECTIVE POTENTIAL AND CRITICAL RADIUS



(a) Variation of the effective potential V_{eff} with respect to r/M for various values of b with $a = 0.5M$, $\ell = 0.1$, $k = 0.1M$, and $\theta = \pi/2$.



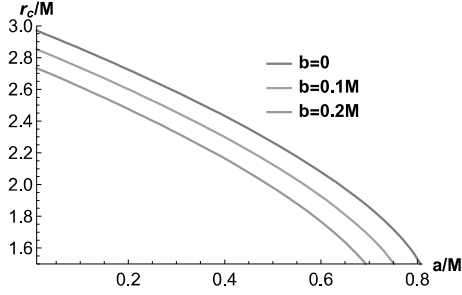
(b) Variation of the effective potential V_{eff} with respect to r/M for various values of k with $a = 0.5M$, $\ell = 0.1$, $b = 0.1M$, and $\theta = \pi/2$.



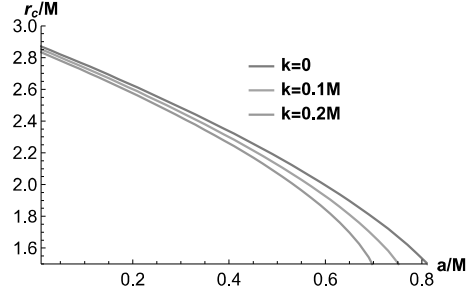
(c) Variation of effective potential V_{eff} with respect to r/M for various values of ℓ with $a = 0.5M$, $k = 0.1M$, $b = 0.1M$, and $\theta = \pi/2$.

Figure 5.1: Plots of the effective potential for various scenarios.

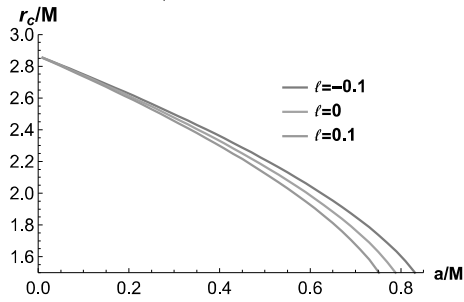
We also plot critical radius versus a/M keeping $\theta = \frac{\pi}{2}$. To plot it, we consider variation of parameters b , k and ℓ involved in our proposed model.



(a) Variation of the critical radius r_c with respect to a/M for various values of b with $\ell = 0.1$, $k = 0.1M$, and $\theta = \pi/2$.



(b) Variation of the critical radius r_c with respect to a/M for various values of k with $\ell = 0.1$, $b = 0.1M$, and $\theta = \pi/2$.



(c) Variation of the critical radius r_c with respect to a/M for various values of ℓ with $k = 0.1M$, $b = 0.1M$, and $\theta = \pi/2$.

Figure 5.2: Plots of critical radius for various scenarios.

The shape of the orbit crucially depends on the nature of the effective potential. Therefore, it is natural that the orbit will have crucial dependence on both factors ℓ and k . The unstable spherical orbit on the equatorial plane will be obtained if the conditions given in Eq. (1.70) are met. We plot V_{eff} versus r/M with $\xi = \xi_c + 0.2$, where ξ_c is the value of ξ for equatorial spherical unstable direct

orbit. In Fig. (5.1), we find that the turning point moves to the left with the increase of the value of b for fixed values of k and ℓ . It also shifts to the left with the increasing value of k when b and ℓ remain fixed. For the positive value of the Lorentz violating parameter ℓ , it also shifts to the left and for the negative value of the ℓ , it gets shifted towards the right like the case when plasma was absent [76]. In Fig. (5.2), if we observe the plot of the critical radius we find that r_c decreases with the increase of the value of b for fixed k and ℓ , and it increases with the increase of the value of k when b and ℓ remain fixed.

5.2 Photon orbit and black hole shadow

For generic spherical orbits where $\theta \neq \pi/2$ and $\eta \neq 0$, the conserved quantities ξ_s and η_s for the spherical orbit of radius $r = r_s$, are given by the simultaneous solutions of the equations

$$R = 0 \quad \text{and} \quad \frac{dR}{dr} = 0, \quad (5.14)$$

where

$$R(r) = \left[\frac{r(r+b) + (1+\ell)a^2}{\sqrt{1+\ell}} - a\xi \right]^2 - \Delta \left[\eta + (\xi - \sqrt{1+\ell}a)^2 \right] + (n^2 - 1) \frac{[r(r+b) + a^2(1+\ell)]^2}{1+\ell},$$

and

$$\frac{dR}{dr} = 2 \frac{2r+b}{\sqrt{1+\ell}} \left[\frac{r(r+b) + (1+\ell)a^2}{\sqrt{1+\ell}} - a\xi \right] - \frac{2r+b-2M}{1+\ell} \left[\eta + (\xi - \sqrt{1+\ell}a)^2 \right] + \frac{k}{r^2} \frac{[r(r+b) + a^2(1+\ell)]^2}{1+\ell} - 2 \frac{k}{r(1+\ell)} (2r+b) [r(r+b) + a^2(1+\ell)]. \quad (5.15)$$

The conserved quantities ξ_s and η_s are obtained by solving the equations

$$R|_{r=r_s} = 0 \quad \text{and} \quad \frac{dR}{dr}|_{r=r_s} = 0, \quad (5.16)$$

which give

$$\xi_s = - \frac{1}{a^2 \sqrt{1+\ell} (b-2M+2r)} \left(2a^3 M + 2a^3 \ell M - 2a M r^2 + \sqrt{1+\ell} \left(\frac{a^2}{(1+\ell)r^2} \left(4M^2 r^2 (-a^2(1+\ell) + r^2)^2 + (b-2M+2r) (a^2(1+\ell) + r(b+r)) (a^4 k(1+\ell)^2 + r^3 (b^2 + 4kM - b(k+2M-3r) - (k+6M)r + 2r^2) + a^2(1+\ell)r(-4kM + b(k+r) + 2r(M+r))) \right)^{1/2} \right) \right),$$

$$\eta_s = \frac{1}{a^3(1+\ell)^{3/2} r (b-2M+2r)^2} \left(-a^5 k(1+\ell)^{5/2} (b-2M+2r)(2b-4M+3r) - 2a^3(1+\ell)^{3/2} r (bk(b-2M)^2 + 4bk(b-2M)r + (5bk - 2(b+k)M)r^2 + 2(k-2M)r^3) - ar^3 \sqrt{1+\ell} (b(b-2M)(b^2 + 4kM - b(k+2M)) + 2(3b^3 - 4kM^2 + 8bM(k+M) - 2b^2(k+5M))r + (13b^2 + 10M(k+2M) - b(5k+32M))r^2 + 2(6b-k-8M)r^3 + 4r^4) + 4(1+\ell)Mr^3 \left(\frac{a^8 k(1+\ell)^2 (b-2M+2r)}{r^2} + \frac{a^6(1+\ell)(2k(b-2M)^2 + (b^2 + 5bk - 10kM)r + 2(2b+k)r^2 + 4r^3)}{r} + \frac{a^2 r^2}{1+\ell} (b(b-2M)(b^2 + 4kM - b(k+2M)) + 2(3b^3 - 4kM^2 + 8bM(k+M) - 2b^2(k+5M))r + (13b^2 + 2M(5k+8M) - b(5k+32M))r^2 + 2(6b-k-8M)r^3 + 4r^4) + a^4(bk(b-4M)(b-2M) + 2b(b(k+k) - 2(b+2k)M)r + (10b^2 + 2kM - b(k+16M))r^2 + 2(8b-k-8M)r^3 + 8r^4) \right)^{1/2} \right).$$

5.2. PHOTON ORBIT AND BLACK HOLE SHADOW

To describe the nature of the shadow, that an observer see in the sky, the following two celestial coordinates are found helpful: $\alpha(\xi, \eta; \theta) = -\frac{\xi_s \csc \theta}{n}$ and $\beta(\xi, \eta; \theta) = \frac{\sqrt{\eta_s + (1+\ell)a^2 \cos^2 \theta - \xi_s^2 \cot^2 \theta - (n^2-1)a^2(1+\ell)\sin^2 \theta}}{n}$. Let us now proceed to see the shape and size of the shadows. The nature of the shadow will depend on various parameters. So, we sketch the black hole shadow for various possible cases.

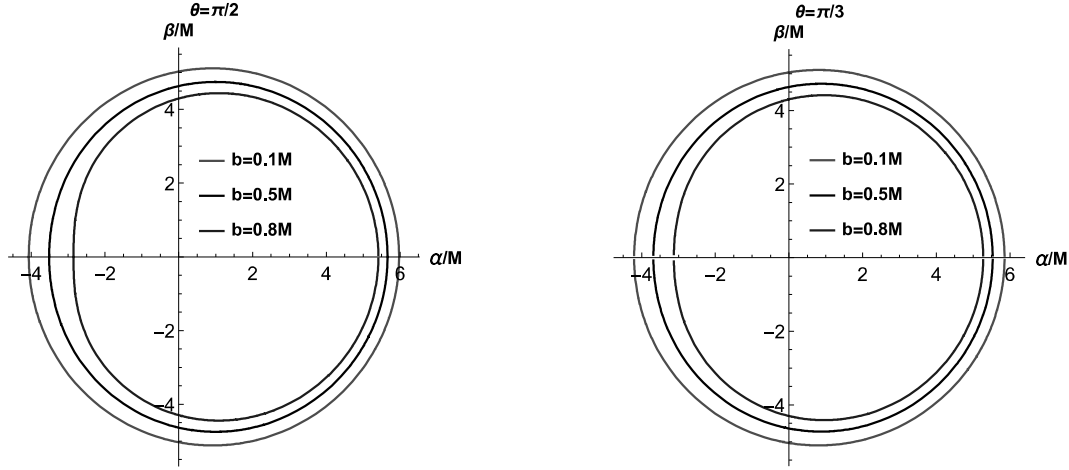


Figure 5.3: Shadows for different values of b when $\theta = \frac{\pi}{2}$ and $\theta = \frac{\pi}{3}$ with $a = 0.4M$, $k = 0.2M$, and $\ell = 0.2$.

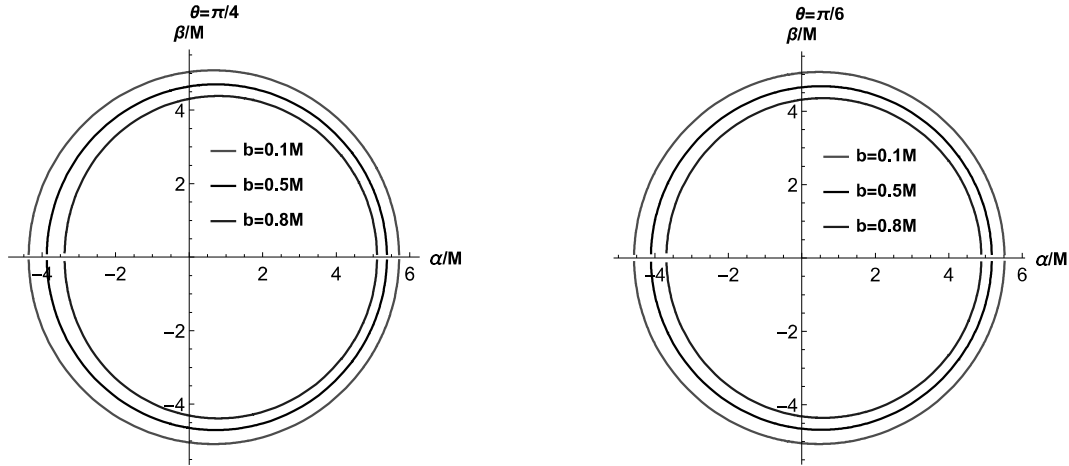


Figure 5.4: Shadows for different values of b when $\theta = \frac{\pi}{4}$ and $\theta = \frac{\pi}{6}$ with $a = 0.4M$, $k = 0.2M$, and $\ell = 0.2$.

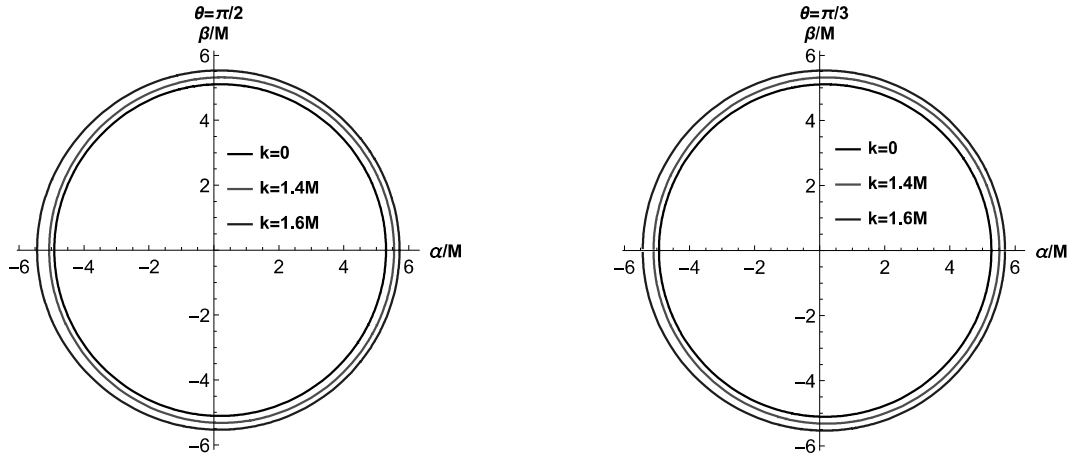


Figure 5.5: Shadows for different values of k when $\theta = \frac{\pi}{2}$ and $\theta = \frac{\pi}{3}$ with $a = 0.1M$, $b = 0.1M$, and $\ell = -0.1$.

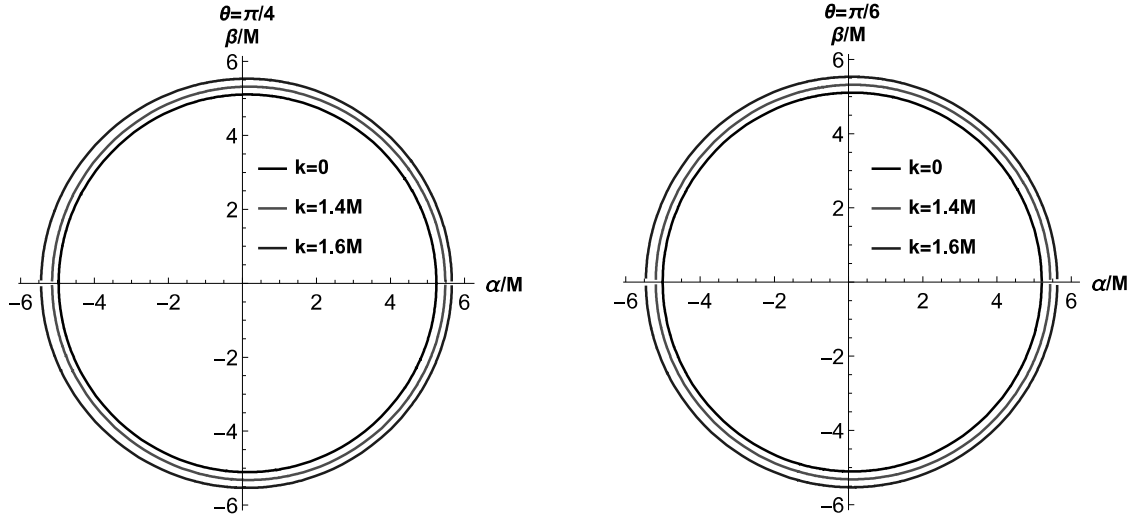


Figure 5.6: Shadows for different values of k when $\theta = \frac{\pi}{4}$ and $\theta = \frac{\pi}{6}$ with $a = 0.1M$, $b = 0.1M$, and $\ell = -0.1$.

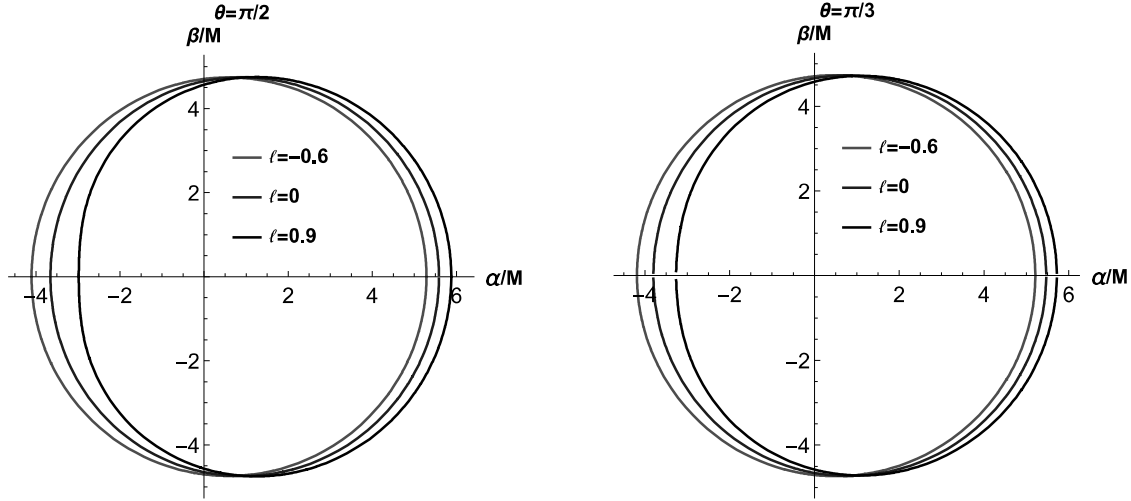


Figure 5.7: Shadows for different values of ℓ when $\theta = \frac{\pi}{2}$ and $\theta = \frac{\pi}{3}$ with $a = 0.4M$, $b = 0.5M$, and $k = 0.2M$.

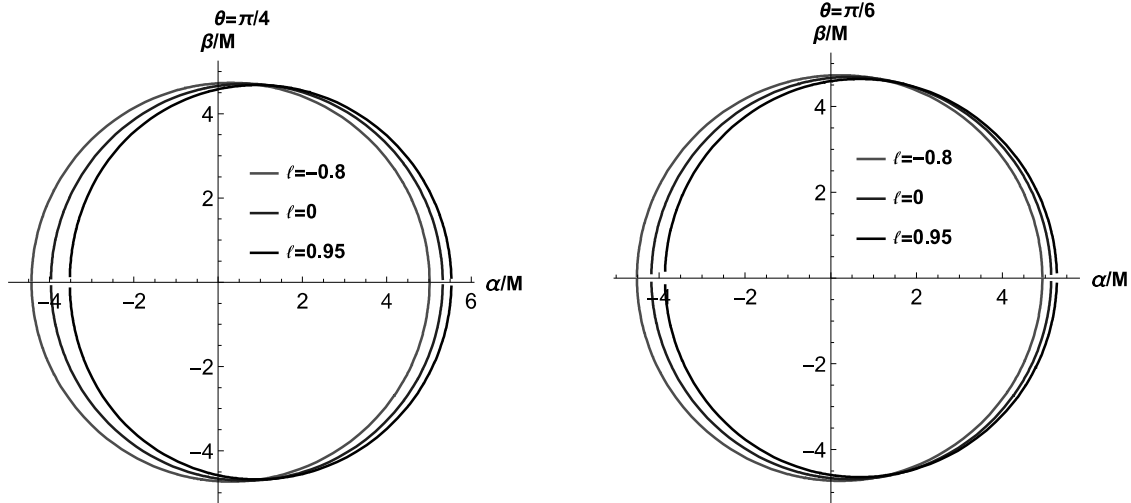


Figure 5.8: Shadows for different values of ℓ when $\theta = \frac{\pi}{4}$ and $\theta = \frac{\pi}{6}$ with $a = 0.4M$, $b = 0.5M$, and $k = 0.2M$.

In Fig. (5.3) and Fig. (5.4) we see that with the increase in the value of b , keeping k and ℓ fixed, the size of the shadow decreases and the left end of the shadow moves a little to the right. Fig. (5.5) and Fig. (5.6) show the change of shape of the shadow with a variation of the plasma parameter k keeping

5.3. THE DEVIATION FROM THE CIRCULAR FORM OF THE SHADOW (δ_s) AND THE SIZE (R_s) OF THE SHADOW

b and ℓ fixed. Figures show that the size of the shadow increases with the increase in the value of k . Here, deformation of the shape of the shadow cannot be found pictorially, however, mathematically very little deviation is observed, which can be concluded from table (5.1). Fig. (5.7) and Fig. (5.8) show that for a negative value of ℓ the left end of the shadow shifts towards the left and for a positive value of ℓ it shifts towards the right. Deformation of the shape of the shadows have been found prominent in all cases.

5.3 The deviation from the circular form of the shadow (δ_s) and the size (R_s) of the shadow

Using the parameters, which are introduced by Hioki and Maeda in [32], we analyse the deviation from the circular form of the shadow (δ_s) and the size (R_s) of the shadow image of the black hole.

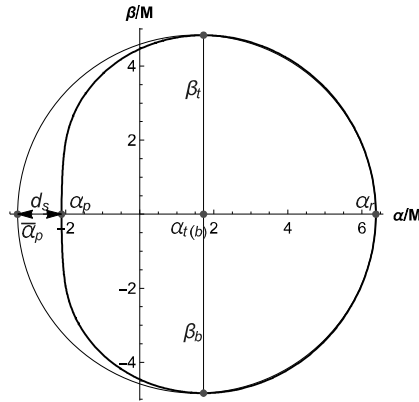


Figure 5.9: A sketch of the black hole shadow and the reference circle. The distance between the extreme left point of the shadow, and the reference circle is represented by d_s .

For calculating these parameters, we consider five points. The four points (α_t, β_t) , (α_b, β_b) , $(\alpha_r, 0)$ and $(\alpha_p, 0)$ are, respectively, the top, bottom, rightmost, and the leftmost point of the shadow; and $(\bar{\alpha}_p, 0)$ is the leftmost point of the reference circle. From simple geometry, we have the expressions for the radius R_s given in Eq. (1.89) and the deviation from circularity δ_s given in Eq. (1.90). In figures below we plot R_s and δ_s for various scenarios. For all subsequent plots, we have taken $\theta = \pi/2$.

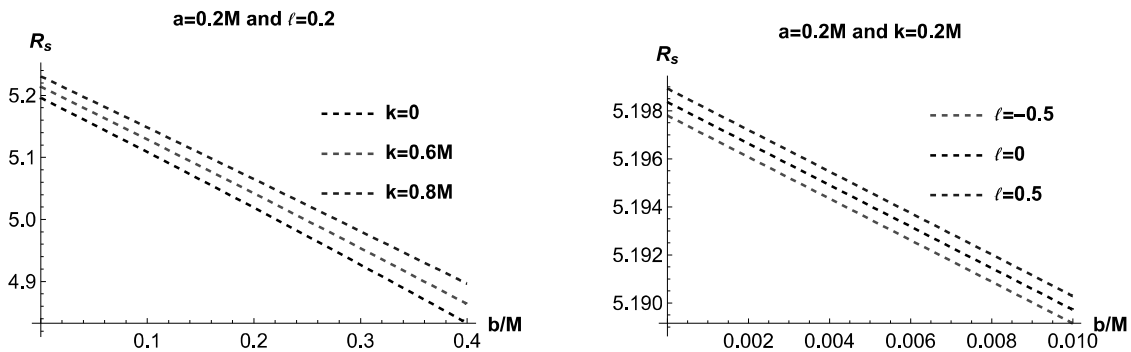


Figure 5.10: The figure at the left side represents the variation of shadow radius R_s with b for different values of k with $a = 0.2M$ and $\ell = 0.2$. The figure at the right side represents the variation of R_s with b for different values of ℓ with $a = 0.2M$ and $k = 0.2M$.

5.3. THE DEVIATION FROM THE CIRCULAR FORM OF THE SHADOW (δ_s) AND THE SIZE (R_s) OF THE SHADOW

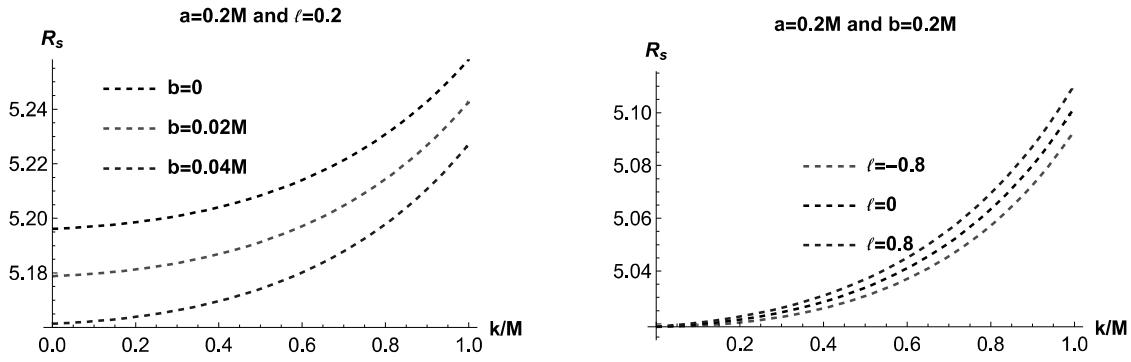


Figure 5.11: The left one represents the variation of shadow radius R_s with k for different values of b with $a = 0.2M$ and $\ell = 0.2M$. The right one represents the variation of R_s with k for different values of ℓ with $a = 0.2M$ and $b = 0.2M$.

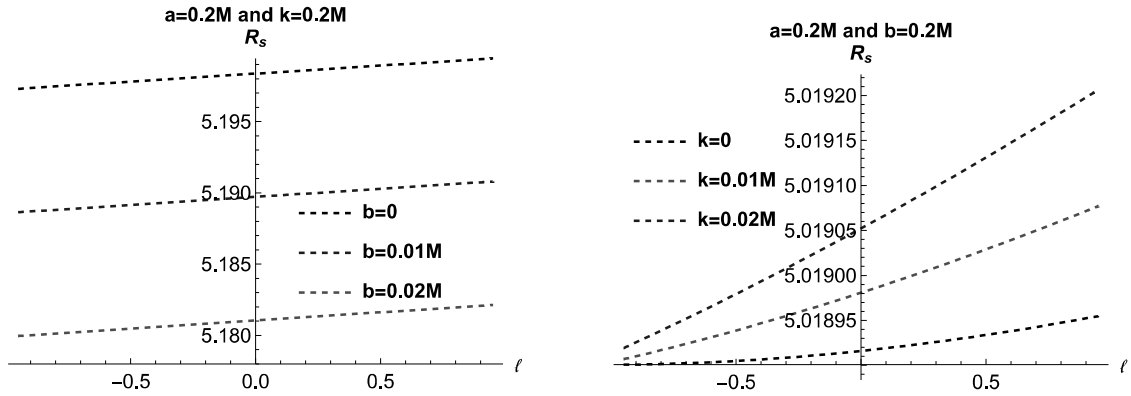


Figure 5.12: The figure at the left side represent the variation of R_s with ℓ for different values of b with $a = 0.2M$ and $k = 0.2M$. The figure at the right side represents the variation of R_s with ℓ for different values of k with $a = 0.2M$ and $b = 0.2M$.

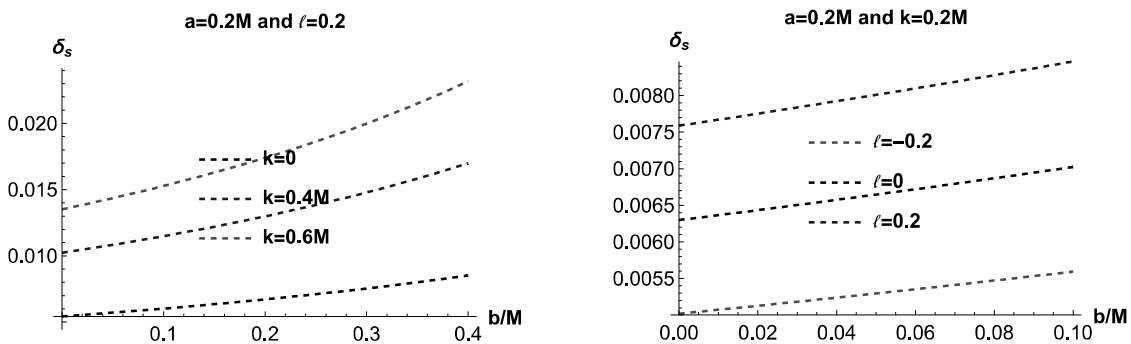


Figure 5.13: The figure at the left side represent the variation of deviation from circularity δ_s with b for different values of k with $a = 0.2M$ and $\ell = 0.2$. The figure at the right side represents the variation of δ_s with b for different values of ℓ with $a = 0.2M$ and $k = 0.2M$.

5.4. THE RATE OF ENERGY EMISSION

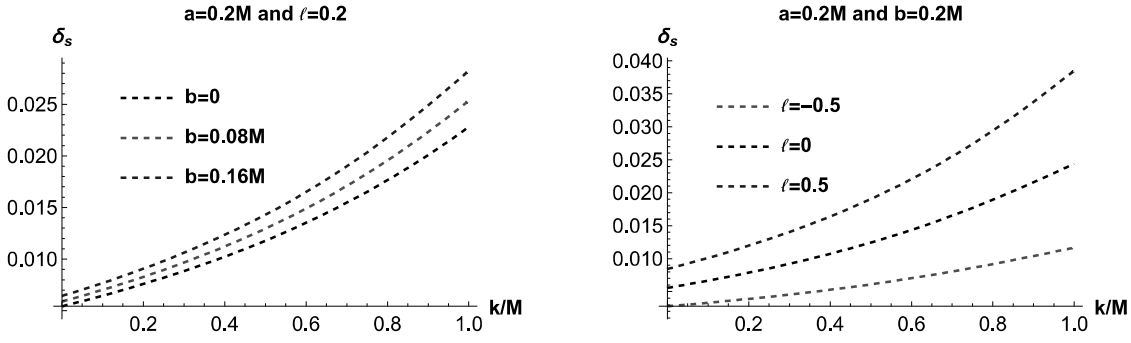


Figure 5.14: The figure at the left side represents the variation of deviation from circularity δ_s with k for different values of b with $a = 0.2M$ and $\ell = 0.2$. The figure at the right side represents the variation of δ_s with k for different values of ℓ with $a = 0.2M$ and $b = 0.2M$.

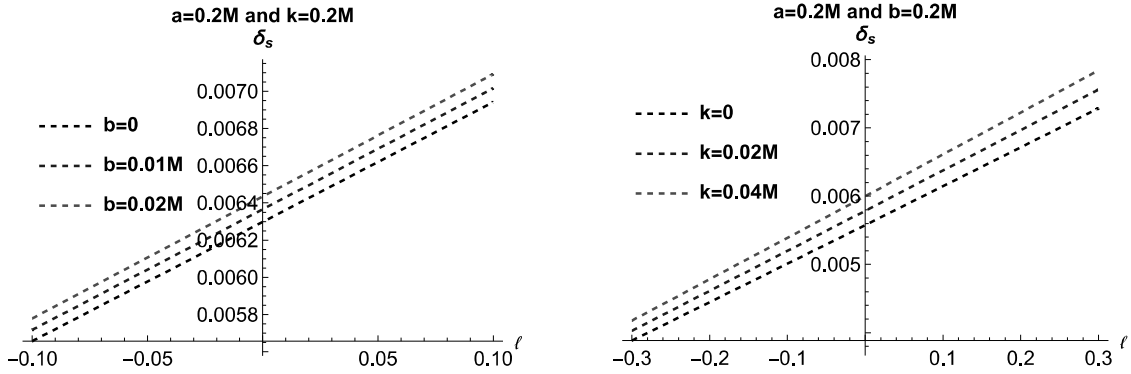


Figure 5.15: The figure at the left side represents the variation of deviation from circularity δ_s with ℓ for different values of b with $a = 0.2M$ and $k = 0.2M$. The figure at the right side represents the variation of δ_s with ℓ for different values of k with $a = 0.2M$ and $b = 0.2M$.

Here, we have given, in a tabular form, the deviation of the image δ_s of the Kerr-Sen-like black hole for set of values $k \equiv \{0, .01M, .02M\}$ and $\ell \equiv \{-0.2, 0, .2\}$ with $a = b = 0.2M$ and $\theta = \frac{\pi}{2}$. From the

Table 5.1: Deviation δ_s for Kerr-Sen-like black hole with $a = 0.2$ and $b = 0.2$.

	$\ell = -0.2$	$\ell = 0$	$\ell = 0.2$
$k = 0$	0.00444613	0.00557717	0.00671623
$k = 0.01M$	0.00452873	0.00568118	0.00684196
$k = 0.02M$	0.00461217	0.00578625	0.00696899

table (5.1) we can conclude that the deviation δ_s increases with an increase in ℓ as well as an increase in k . This was also observed in plots of δ_s given above.

5.4 The rate of energy emission

It is well known that all black holes emit radiation. As a result, mass of the black holes decrease and the process continues until the black holes collapse down completely. In the introductory part in Sec. (1.4.6) a brief discussion of emission of energy has already been given. Here we discuss the energy emission in presence of plasma following the motivation from the article [36] which we have studied in [119]. The energy emission rate of radiation with the frequency ω is given by Eq. (1.92).

The Hawking temperature is given by [76]

$$T_H = \frac{\sqrt{(2M-b)^2 - 4a^2(1+\ell)}}{4\pi M\sqrt{1+\ell} \left(2M-b + \sqrt{(2M-b)^2 - 4a^2(1+\ell)} \right)}. \quad (5.17)$$

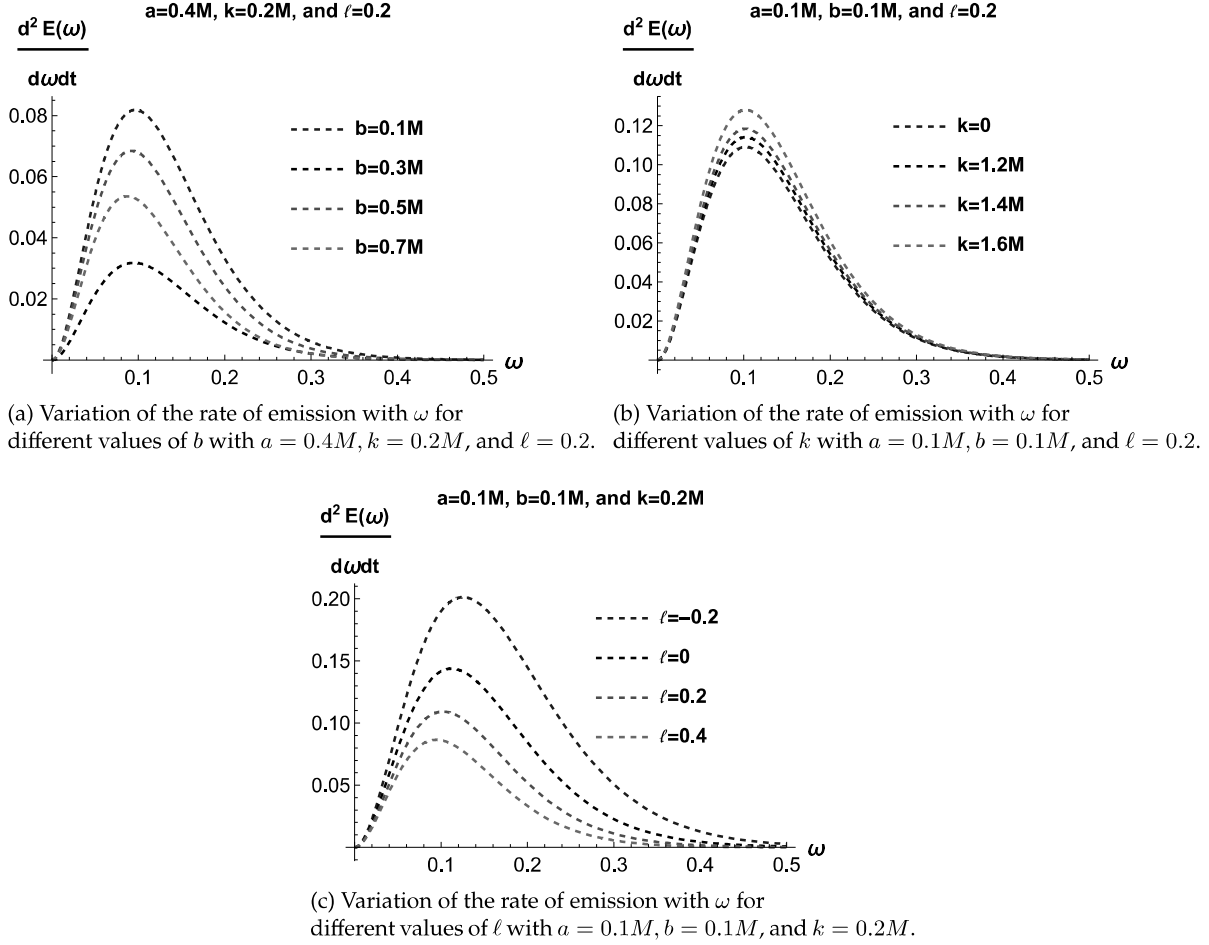


Figure 5.16: Variation of the rate of emission with ω for different situations.

In Fig. (5.16), we have studied how the energy emission rate will behave with the variation of the parameters b , ℓ , and k . It is observed that the rate of emission is higher for smaller values of b . However, the reverse is the case when k increases. It is evident from the spectrum that in the absence of plasma, the minimum energy will be released from the black hole, which indeed agrees with the Kerr-Newman black hole [80]. From the plots, we see that for negative ℓ , there is an enhancement of emission whereas, for increasing positive value of ℓ , there is a reduction in the emission of radiation.

Chapter 6

Superradiance

Superradiance is a radiation enhancement process. The concept of superradiance was introduced by Dicke in 1954 in his work [86]. In a gravitational system, the scattering of radiation off absorbing rotating objects produce waves with amplitude larger than incident one under certain conditions which is known as rotational superradiance [87, 88]. It was showed by Zel'dovich in 1971 that, under certain conditions, scattering of radiation off rotating absorbing surfaces results in waves with a larger amplitude [88, 89]. The black hole superradiance can be explained using the thermodynamic laws of black hole [89]. According to first law of black hole thermodynamics, the changes in mass M , angular momentum J , horizon area A_h and charge Q of a stationary black hole in the vacuum, are related to each other by

$$\delta M = \frac{\kappa}{8\pi} \delta A_h + \Omega_h \delta J + \phi_h \delta Q, \quad (6.1)$$

where κ is the surface gravity, Ω_h is the angular velocity of the black hole and Φ_h is the electrostatic potential at the horizon. Now, we consider a neutral black hole for which we have $\Phi_h = 0$. The ratio of angular momentum flux L to energy E of a wave is given by $L/E = m/\omega$, where m is the azimuthal number and ω is the frequency of the wave. Putting this in Eq. (6.1) yields

$$\delta M = \frac{\omega \kappa}{8\pi} \frac{\delta A_h}{\omega - m\Omega_h}. \quad (6.2)$$

The second law of black hole thermodynamics states that $\delta A_h \geq 0$. It implies that for $\omega < m\Omega_h$, waves can extract energy from black holes. This result applies to all stationary black holes in vacuum. One consequence of superradiance is black hole bomb. It corresponds to a situation when the amplified wave is reflected back towards black hole. This leads to repeated amplification of the wave causing a run-away growth i.e. an explosion. Superradiant instability is the mechanism by which the black hole bomb works. The important contemporary contributions in articles [70, 71, 90–92] related to superradiance made this astounding astronomical phenomena a tempting field of research. For review, we would like to mention the lecture notes [93], and the references therein.

Rotational superradiance belongs to a wider class of classical problems displaying stimulated or spontaneous energy emission, such as the Vavilov-Cherenkov effect, the anomalous Doppler effect. When quantum effects were incorporated, it was argued that rotational superradiance would become a spontaneous process and that rotating bodies including black holes would slow down by the spontaneous emission of photons. From the historic perspective, the discovery of black-hole evaporation was well understood from the studies of black-hole superradiance [33]. Interest in the study of black-hole superradiance has recently been revived in different areas, including astrophysics, high-energy physics via the gauge/gravity duality along with fundamental issues in general theory of relativity. Superradiant instabilities can be used to constrain the mass of ultra-light degrees of freedom [94–97], with important applications to dark-matter searches. The black hole superradiance is also associated with the existence of new asymptotically flat hairy black-hole solutions [98]. Finally, the knowledge of superradiance is instrumental in describing the stability of black holes and in determining the fate of the gravitational collapse in confining geometries [99]. In this chapter we will study the superradiance effect in the background of Kerr-Sen-like black hole given by the metric (4.23) and non-commutative Kerr-like black hole given by the metric (3.11).

6.1 Superradiance scattering of the scalar field off non-commutative Kerr-like black hole

We consider the Klein-Gordon equation in curved spacetime to study the superradiance scattering of a scalar field Φ .

$$(\nabla_\alpha \nabla^\alpha + \mu^2) \Phi(t, r, \theta, \phi) = \left[\frac{-1}{\sqrt{-g}} \partial_\sigma (g^{\sigma\tau} \sqrt{-g} \partial_\tau) + \mu^2 \right] \Phi(t, r, \theta, \phi) = 0. \quad (6.3)$$

Here, μ represents the mass of the scalar field Φ . We now adopt the standard separation of variables method to the equation Eq. (6.3) in order to separate it into radial and angular part using the following ansatz. With the standard Boyer-Lindquist coordinates (t, r, θ, ϕ) we can write

$$\Phi(t, r, \theta, \phi) = R_{\omega jm}(r) \Theta(\theta) e^{-i\omega t} e^{im\phi}, \quad j \geq 0, \quad -j \leq m \leq j, \quad \omega > 0, \quad (6.4)$$

where $R_{\omega jm}(r)$ represents the radial function and $\Theta(\theta)$ refers to the oblate spheroidal wave function. The symbols j , m , and ω respectively stand for the angular eigenfunction, angular quantum number, and the positive frequency of the field under investigation as viewed by a far away observer. Using the ansatz (6.4), the differential equation (6.3) for the metric (3.11), is found to get separated into the following two ordinary differential equations. For the radial part, the equation reads [121]

$$\begin{aligned} \frac{d}{dr} \left(\hat{\Delta} \frac{dR_{\omega jm}(r)}{dr} \right) + \left(\frac{((r^2 + a^2(1 + \ell))\omega - am\sqrt{1 + \ell})^2}{\hat{\Delta}(1 + \ell)} \right) R_{\omega jm}(r) \\ - (\mu^2 r^2 + j(j + 1) + a^2(1 + \ell)\omega^2 - 2m\omega a\sqrt{1 + \ell}) R_{\omega jm}(r) = 0, \end{aligned} \quad (6.5)$$

and the angular part of it is

$$\begin{aligned} \sin \theta \frac{d}{d\theta} \left(\sin \theta \frac{d\Theta_{\omega jm}(\theta)}{d\theta} \right) + \left(j(j + 1) \sin^2 \theta - \left((a\sqrt{1 + \ell}\omega \sin^2 \theta - m)^2 \right) \right) \Theta_{\omega jm}(\theta) \\ + a^2(1 + \ell)\mu^2 \sin^2 \theta \cos^2 \theta \Theta_{\omega jm}(\theta) = 0, \end{aligned} \quad (6.6)$$

where $\hat{\Delta} = \frac{r^2 - 2M_{\vartheta n}r}{1 + \ell} + a^2$, $M_{\vartheta n} = -\frac{4\sqrt{\vartheta_n}M}{\sqrt{\pi}r} + M$. Following the earlier investigation [100, 101] we may have a general solution of the radial equation (6.5). However, we are intended to study the scattering of the field Φ . So, in this situation, we have used the asymptotic matching procedure used in [70, 71, 92, 102, 103]. The road map of the important contributions [70, 71, 92, 102–104] and the recent studies [104–106] led us to reach to the required result without using the general solution. First of all, we consider the radial part of the equation (6.5) to find an asymptotic solution. Use of Regge-Wheeler-like coordinate r_* is helpful in this situation in order to deal with the radial equation as per our requirement, which is given by

$$r_* \equiv \int dr \frac{r^2 + a^2(1 + \ell)}{\hat{\Delta}}, \quad (r_* \rightarrow -\infty \text{ at event horizon, } r_* \rightarrow \infty \text{ at infinity}). \quad (6.7)$$

To have the equation into the desired shape, we take on a new radial function $\mathcal{R}_{\omega jm}(r_*) = \sqrt{r^2 + a^2(1 + \ell)} R_{\omega jm}(r)$. A few steps of algebra leads us to obtain the radial equation in our desired form

$$\frac{d^2 \mathcal{R}_{\omega lm}(r_*)}{dr_*^2} + V_{\omega jm}(r) \mathcal{R}_{\omega jm}(r_*) = 0. \quad (6.8)$$

An effective potential takes entry into the picture that reads

$$\begin{aligned} V_{\omega jm}(r) = & \frac{1}{1 + \ell} \left(\omega - \frac{m\hat{a}}{r^2 + \hat{a}^2} \right)^2 - \frac{\hat{\Delta}}{(r^2 + \hat{a}^2)^2} [j(j + 1) + \hat{a}^2\omega^2 - 2m\hat{a}\omega + \mu^2 r^2] \\ & + \sqrt{r^2 + \hat{a}^2} \frac{d}{dr} \left(\frac{r\hat{\Delta}}{(r^2 + \hat{a}^2)^{\frac{3}{2}}} \right), \end{aligned} \quad (6.9)$$

6.1. SUPERRADIANCE SCATTERING OF THE SCALAR FIELD OFF NON-COMMUTATIVE KERR-LIKE BLACK HOLE

where $\hat{a} = a(1 + \ell)^{\frac{1}{2}}$. So, it appears that it is equivalent to the study of the scattering of the scalar field Φ under this effective potential (6.9). It is beneficial to study the asymptotic behaviour of the scattering potential at the event horizon and at spatial infinity in this regard. The potential at the event horizon in the asymptotic limit simplifies into

$$\lim_{r \rightarrow r_{eh}} V_{\omega jm}(r) = \frac{1}{1 + \ell} \left(\omega - m\hat{\Omega}_h \right)^2 \equiv k_{eh}^2, \quad (6.10)$$

where $\hat{\Omega}_h = \frac{\hat{a}}{r_{eh}^2 + \hat{a}^2}$ and the same at spatial infinity turns into the following

$$\lim_{r \rightarrow \infty} V_{\omega jm}(r) = \frac{\omega^2}{1 + \ell} - \lim_{r \rightarrow \infty} \frac{\mu^2 r^2 \hat{\Delta}}{(r^2 + \hat{a}^2)^2} = \frac{\omega^2}{1 + \ell} - \hat{\mu}^2 \equiv k_{\infty}^2, \quad \hat{\mu} = \frac{\mu}{\sqrt{\ell + 1}}. \quad (6.11)$$

Note that the potential turns into a constant at the two extremal points namely at event horizon and at spatial infinity. However, the numerical values of the constants are different indeed at the two extremal points.

Since the behaviour of the potential at the two extremal points are known, we now move to observe the asymptotic behavior of the radial solution. A little algebra shows that the radial equation (6.8) has the following solutions

$$R_{\omega jm}(r) \rightarrow \left\{ \begin{array}{ll} \frac{\mathcal{D}_{in}^{eh} e^{-ik_{eh} r_*}}{\sqrt{r_{eh}^2 + \hat{a}^2}} & \text{for } r \rightarrow r_{eh} \\ \mathcal{D}_{in}^{\infty} \frac{e^{-ik_{\infty} r_*}}{r} + \mathcal{D}_{ref}^{\infty} \frac{e^{ik_{\infty} r_*}}{r} & \text{for } r \rightarrow \infty \end{array} \right\}, \quad (6.12)$$

in the asymptotic limit. Here \mathcal{D}_{in}^{eh} is the amplitude of the incoming scalar wave at event horizon (r_{eh}), and $\mathcal{D}_{in}^{\infty}$ is the corresponding quantity of the incoming scalar wave at infinity (∞). The amplitude of the reflected part of scalar wave at infinity (∞) is designated by $\mathcal{D}_{ref}^{\infty}$. So the stage is set to compute the Wronskian for the region adjacent to the event horizon and at infinity. The Wronskian at the event horizon is found out to be

$$W_{eh} = \left(R_{\omega jm}^{eh} \frac{dR_{\omega jm}^{*eh}}{dr_*} - R_{\omega jm}^{*eh} \frac{dR_{\omega jm}^{eh}}{dr_*} \right), \quad (6.13)$$

and the Wronskian at infinity results out to be

$$W_{\infty} = \left(R_{\omega jm}^{\infty} \frac{dR_{\omega jm}^{*\infty}}{dr_*} - R_{\omega jm}^{*\infty} \frac{dR_{\omega jm}^{\infty}}{dr_*} \right). \quad (6.14)$$

The knowledge of standard theory of ordinary differential equation provides the information that the Wronskian corresponding to the solutions will be independent of r_* since the solutions are linearly independent. Thus, the Wronskian evaluated at horizon is compatible to equate with the Wronskian evaluated at infinity. In fact, in the physical sense, it is associated with the flux conservation of the process [93]. From the matching condition, an important relation between the amplitudes of incoming and reflected waves at different regions of interest results

$$|\mathcal{D}_{ref}^{\infty}|^2 = |\mathcal{D}_{in}^{\infty}|^2 - \frac{k_{eh}}{k_{\infty}} |\mathcal{D}_{in}^{eh}|^2. \quad (6.15)$$

A careful look reveals that if $\frac{k_{eh}}{k_{\infty}} < 0$ i.e., $\omega < m\hat{\Omega}_h$, the scalar wave will be superradiantly amplified, since the relation $|\mathcal{D}_{ref}^{\infty}|^2 > |\mathcal{D}_{in}^{\infty}|^2$ holds explicitly in this situation.

6.2 Amplification factor Z_{jm} for superradiance

It is straightforward to express the radial equation (6.5) in the following form

$$\hat{\Delta}^2 \frac{d^2 R_{\omega jm}(r)}{dr^2} + \hat{\Delta} \frac{d\hat{\Delta}}{dr} \cdot \frac{dR_{\omega jm}(r)}{dr} + \left(\frac{((r^2 + \hat{a}^2)\omega - \hat{a}m)^2}{1 + \ell} - \hat{\Delta} (\mu^2 r^2 + j(j+1) + \hat{a}^2 \omega^2 - 2m\hat{a}\omega) \right) R_{\omega jm}(r) = 0. \quad (6.16)$$

We now proceed to derive the solution for the near and the far region and try to find out a single solution by matching the solution for near-region at infinity with solution for the far-region at its initial point such that this specific single solution be useful in the vicinity of the cardinal region. It is beneficial at this stage to introduce a new variable y which is defined by $y = \frac{r-r_{eh}}{r_{eh}-r_{ch}}$. In terms of y , the equation (6.16) turns into

$$\frac{y^2(y+1)^2}{(\ell+1)^2} \frac{d^2 R_{\omega jm}(y)}{dy^2} + \frac{y(y+1)(2y+1)}{(\ell+1)^2} \frac{dR_{\omega jm}(y)}{dy} + \left(\frac{Q^2 y^4}{1+\ell} + \frac{B^2}{1+\ell} - \frac{j(j+1)}{\ell+1} y(y+1) - \frac{\hat{\mu}^2 Q^2}{\omega^2} y^3(y+1) - \hat{\mu}^2 r_{eh}^2 y(y+1) - \frac{2\hat{\mu}^2 r_{eh} Q}{\omega} y^2(y+1) \right) R_{\omega jm}(y) = 0, \quad (6.17)$$

under the approximation $\hat{a}\omega \ll 1$, where $Q = (r_{eh} - r_{ch})\omega$ and $B = \frac{(\omega - m\hat{\Omega}_h)}{r_{eh}-r_{ch}} r_{eh}^2$. For the near-region, we have $Py \ll 1$ and $\hat{\mu}^2 r_{eh}^2 \ll 1$. The above equation is simplified into

$$y^2(y+1)^2 \frac{d^2 R_{\omega jm}(y)}{dy^2} + y(y+1)(2y+1) \frac{dR_{\omega jm}(y)}{dy} + ((\ell+1)B^2 - j(j+1)(\ell+1)y(y+1)) R_{\omega jm}(r) = 0.$$

Since the Compton wavelength of the boson participating in the scattering process is much smaller than the size of the black hole, the approximation ($\hat{\mu}^2 r_{eh}^2 \ll 1$) holds good. The general solution of the above equation in terms of associated Legendre function of the first kind $P_\lambda^\nu(y)$ can be written down as

$$R_{\omega jm}(y) = d P_{\frac{\sqrt{1+4j(j+1)(\ell+1)}-1}{2}}^{2i\sqrt{1+B}}(1+2y). \quad (6.18)$$

If we now use the relation

$$P_\lambda^\nu(z) = \frac{1}{\Gamma(1-\nu)} \left(\frac{1+z}{1-z} \right)^{\nu/2} {}_2F_1 \left(-\lambda, \lambda+1; 1-\nu; \frac{1-z}{2} \right), \quad (6.19)$$

it enables us to express $R_{\omega jm}(y)$ in terms of the ordinary hypergeometric functions ${}_2F_1(a, b; c; z)$:

$$R_{\omega jm}(y) = d \left(\frac{y}{y+1} \right)^{-i\sqrt{\ell+1}B} {}_2F_1 \left(\frac{1-\sqrt{1+4(\ell+1)j(j+1)}}{2}, \frac{1+\sqrt{1+4(\ell+1)j(j+1)}}{2}; 1-2i\sqrt{\ell+1}B; -y \right). \quad (6.20)$$

We are intended to find out a single solution using the matching condition at the desired position where the two solutions mingle with each other. In this respect, we need to observe the large y behavior of the above expression. The Eq. (6.20) for large y , i.e. ($y \rightarrow \infty$), reduces to

$$R_{\text{near-large } y} \sim d \left(\frac{\Gamma(\sqrt{1+4(\ell+1)j(j+1)})\Gamma(1-2i\sqrt{\ell+1}B)}{\Gamma\left(\frac{1+\sqrt{1+4(\ell+1)j(j+1)}}{2} - 2i\sqrt{\ell+1}B\right)\Gamma\left(\frac{1+\sqrt{1+4(\ell+1)j(j+1)}}{2}\right)} y^{\frac{\sqrt{1+4(\ell+1)j(j+1)}-1}{2}} + \frac{\Gamma(-\sqrt{1+4(\ell+1)j(j+1)})\Gamma(1-2i\sqrt{\ell+1}B)}{\Gamma\left(\frac{1-\sqrt{1+4(\ell+1)j(j+1)}}{2}\right)\Gamma\left(\frac{1-\sqrt{1+4(\ell+1)j(j+1)}}{2} - 2i\sqrt{\ell+1}B\right)} y^{-\frac{\sqrt{1+4(\ell+1)j(j+1)}+1}{2}} \right). \quad (6.21)$$

6.2. AMPLIFICATION FACTOR Z_{jm} FOR SUPERRADIANCE

For the far-region, we can use the approximations $y+1 \approx y$ and $\hat{\mu}^2 r_{eh}^2 \ll 1$. We may drop all the terms except those which describe the free motion with momentum j and that reduces equation (6.16) to

$$\frac{d^2 R_{\omega jm}(y)}{dy^2} + \frac{2}{y} \frac{dR_{\omega jm}(y)}{dy} + \left(k_\ell^2 - \frac{j(j+1)(\ell+1)}{y^2} \right) R_{\omega jm}(y) = 0, \quad (6.22)$$

where $k_\ell \equiv \frac{\mathcal{Q}\sqrt{1+\ell}}{\omega} \sqrt{\omega^2 - \mu^2}$. Equation (6.22) has the general solution

$$R_{\omega jm, \text{far}} = e^{-iky} \left(c_1 y^{\frac{\sqrt{1+4(\ell+1)j(j+1)}-1}{2}} M\left(\frac{1+\sqrt{1+4(\ell+1)j(j+1)}}{2}, 1+\sqrt{1+4(\ell+1)j(j+1)}, 2ik_\ell y\right) + c_2 y^{-\frac{\sqrt{1+4(\ell+1)j(j+1)}+1}{2}} M\left(\frac{1-\sqrt{1+4(\ell+1)j(j+1)}}{2}, 1-\sqrt{1+4(\ell+1)j(j+1)}, 2ik_\ell y\right) \right). \quad (6.23)$$

Here $M(a; b; y)$ stands for the confluent hypergeometric Kummer function of the first kind. In order to match the solution with (6.21), we look for the small y behaviour of the solution (6.23). For small y ($y \rightarrow 0$), the equation (6.23) turns into

$$R_{\omega jm, \text{far-small } y} \sim c_1 y^{\frac{\sqrt{1+4(\ell+1)j(j+1)}-1}{2}} + c_2 y^{-\frac{1+\sqrt{1+4(\ell+1)j(j+1)}}{2}}. \quad (6.24)$$

The solution (6.21) and (6.24) are susceptible for matching, since these two have common region of interest. The matching of the asymptotic solutions (6.21) and (6.24) enable us to compute the scalar wave flux at infinity that results in

$$\begin{aligned} c_1 &= d \frac{\Gamma(\sqrt{1+4(\ell+1)j(j+1)})\Gamma(1-2i\sqrt{\ell+1}B)}{\Gamma\left(\frac{1+\sqrt{1+4(\ell+1)j(j+1)}}{2}-2i\sqrt{\ell+1}B\right)\Gamma\left(\frac{1+\sqrt{1+4(\ell+1)j(j+1)}}{2}\right)}, \\ c_2 &= d \frac{\Gamma(-\sqrt{1+4(\ell+1)j(j+1)})\Gamma(1-2i\sqrt{\ell+1}B)}{\Gamma\left(\frac{1-\sqrt{1+4(\ell+1)j(j+1)}}{2}-2i\sqrt{\ell+1}B\right)\Gamma\left(\frac{1-\sqrt{1+4(\ell+1)j(j+1)}}{2}\right)}. \end{aligned} \quad (6.25)$$

We expand equation (6.23) around infinity which, after expansion, results

$$\begin{aligned} c_1 &\frac{\Gamma(1+\sqrt{1+4(\ell+1)j(j+1)})}{\Gamma\left(\frac{1+\sqrt{1+4(\ell+1)j(j+1)}}{2}\right)} k_\ell^{-\frac{1+\sqrt{1+4(\ell+1)j(j+1)}}{2}} \left((-2i)^{-\frac{1+\sqrt{1+4(\ell+1)j(j+1)}}{2}} \frac{e^{-ik_\ell y}}{y} + (2i)^{-\frac{1+\sqrt{1+4(\ell+1)j(j+1)}}{2}} \frac{e^{ik_\ell y}}{y} \right) + \\ c_2 &\frac{\Gamma(1-\sqrt{1+4(\ell+1)j(j+1)})}{\Gamma\left(\frac{1-\sqrt{1+4(\ell+1)j(j+1)}}{2}\right)} k_\ell^{\frac{\sqrt{1+4(\ell+1)j(j+1)}-1}{2}} \left((-2i)^{\frac{\sqrt{1+4(\ell+1)j(j+1)}-1}{2}} \frac{e^{-ik_\ell y}}{y} + (2i)^{\frac{\sqrt{1+4(\ell+1)j(j+1)}-1}{2}} \frac{e^{ik_\ell y}}{y} \right). \end{aligned}$$

With the approximations $\frac{1}{y} \sim \frac{\mathcal{Q}}{\omega} \cdot \frac{1}{r}$, $e^{\pm ik_\ell y} \sim e^{\pm i\sqrt{(1+\ell)(\omega^2 - \mu^2)}r}$, if we match the above solution with the radial solution (6.12)

$$R_\infty(r) \sim \mathcal{D}_{in}^\infty \frac{e^{-i\sqrt{\frac{\omega^2}{1+\ell} - \hat{\mu}^2} r^*}}{r} + \mathcal{D}_{ref}^\infty \frac{e^{i\sqrt{\frac{\omega^2}{1+\ell} - \hat{\mu}^2} r^*}}{r}, \quad \text{for } r \rightarrow \infty,$$

we get

$$\begin{aligned} \mathcal{D}_{in}^\infty &= \frac{\mathcal{Q}}{\omega} \left(c_1 (-2i)^{-\frac{1+\sqrt{1+4(\ell+1)j(j+1)}}{2}} \frac{\Gamma(1+\sqrt{1+4(\ell+1)j(j+1)})}{\Gamma\left(\frac{1+\sqrt{1+4(\ell+1)j(j+1)}}{2}\right)} k_\ell^{-\frac{1+\sqrt{1+4(\ell+1)j(j+1)}}{2}} + \right. \\ &\quad \left. c_2 (-2i)^{\frac{\sqrt{1+4(\ell+1)j(j+1)}-1}{2}} \frac{\Gamma(1-\sqrt{1+4(\ell+1)j(j+1)})}{\Gamma\left(\frac{1-\sqrt{1+4(\ell+1)j(j+1)}}{2}\right)} k_\ell^{\frac{\sqrt{1+4(\ell+1)j(j+1)}-1}{2}} \right), \end{aligned}$$

and

$$\begin{aligned} \mathcal{D}_{ref}^\infty &= \frac{\mathcal{Q}}{\omega} \left(c_1 (2i)^{-\frac{1+\sqrt{1+4(\ell+1)j(j+1)}}{2}} \frac{\Gamma(1+\sqrt{1+4(\ell+1)j(j+1)})}{\Gamma\left(\frac{1+\sqrt{1+4(\ell+1)j(j+1)}}{2}\right)} k_\ell^{-\frac{1+\sqrt{1+4(\ell+1)j(j+1)}}{2}} + \right. \\ &\quad \left. c_2 (2i)^{\frac{\sqrt{1+4(\ell+1)j(j+1)}-1}{2}} \frac{\Gamma(1-\sqrt{1+4(\ell+1)j(j+1)})}{\Gamma\left(\frac{1-\sqrt{1+4(\ell+1)j(j+1)}}{2}\right)} k_\ell^{\frac{\sqrt{1+4(\ell+1)j(j+1)}-1}{2}} \right). \end{aligned}$$

Substituting the expressions of c_1 and c_2 from Eq. (6.25) into the above expressions we have [121]

$$\begin{aligned} \mathcal{D}_{in}^{\infty} = & \frac{d(-2i)^{-\frac{1+\sqrt{1+4(\ell+1)j(j+1)}}{2}}}{\sqrt{(1+\ell)(\omega^2-\mu^2)}} \cdot \frac{\Gamma(\sqrt{1+4(\ell+1)j(j+1)})\Gamma(1+\sqrt{1+4(\ell+1)j(j+1)})}{\Gamma\left(\frac{1+\sqrt{1+4(\ell+1)j(j+1)}}{2}-2i\sqrt{\ell+1}B\right)\left(\Gamma\left(\frac{1+\sqrt{1+4(\ell+1)j(j+1)}}{2}\right)\right)^2} \times \quad (6.26) \\ & \Gamma(1-2i\sqrt{\ell+1}B)k_{\ell}^{\frac{1-\sqrt{1+4(\ell+1)j(j+1)}}{2}} + \frac{d(-2i)^{\frac{\sqrt{1+4(\ell+1)j(j+1)}-1}{2}}}{\sqrt{(1+\ell)(\omega^2-\hat{\mu}^2)}} \times \\ & \frac{\Gamma(1-\sqrt{1+4(\ell+1)j(j+1)})\Gamma(-\sqrt{1+4(\ell+1)j(j+1)})}{\left(\Gamma\left(\frac{1-\sqrt{1+4(\ell+1)j(j+1)}}{2}\right)\right)^2\Gamma\left(\frac{1-\sqrt{1+4(\ell+1)j(j+1)}}{2}-2i\sqrt{\ell+1}B\right)} \Gamma(1-2i\sqrt{\ell+1}B)k_{\ell}^{\frac{1+\sqrt{1+4(\ell+1)j(j+1)}}{2}}, \end{aligned}$$

and

$$\begin{aligned} \mathcal{D}_{ref}^{\infty} = & \frac{d(2i)^{-\frac{1+\sqrt{1+4(\ell+1)j(j+1)}}{2}}}{\sqrt{(1+\ell)(\omega^2-\mu^2)}} \cdot \frac{\Gamma(\sqrt{1+4(\ell+1)j(j+1)})\Gamma(1+\sqrt{1+4(\ell+1)j(j+1)})}{\Gamma\left(\frac{1+\sqrt{1+4(\ell+1)j(j+1)}}{2}-2i\sqrt{\ell+1}B\right)\left(\Gamma\left(\frac{1+\sqrt{1+4(\ell+1)j(j+1)}}{2}\right)\right)^2} \times \quad (6.27) \\ & \Gamma(1-2i\sqrt{\ell+1}B)k_{\ell}^{\frac{1-\sqrt{1+4(\ell+1)j(j+1)}}{2}} + \frac{d(2i)^{\frac{\sqrt{1+4(\ell+1)j(j+1)}-1}{2}}}{\sqrt{(1+\ell)(\omega^2-\hat{\mu}^2)}} \times \\ & \frac{\Gamma(1-\sqrt{1+4(\ell+1)j(j+1)})\Gamma(-\sqrt{1+4(\ell+1)j(j+1)})}{\left(\Gamma\left(\frac{1-\sqrt{1+4(\ell+1)j(j+1)}}{2}\right)\right)^2\Gamma\left(\frac{1-\sqrt{1+4(\ell+1)j(j+1)}}{2}-2i\sqrt{\ell+1}B\right)} \Gamma(1-2i\sqrt{\ell+1}B)k_{\ell}^{\frac{1+\sqrt{1+4(\ell+1)j(j+1)}}{2}}. \end{aligned}$$

The amplification factor ultimately results out to be

$$Z_{jm} \equiv \frac{|\mathcal{D}_{ref}^{\infty}|^2}{|\mathcal{D}_{in}^{\infty}|^2} - 1. \quad (6.28)$$

Equation (6.28) is a general expression of the amplification factor obtained by making use of the asymptotic matching method. When $\frac{|\mathcal{D}_{ref}^{\infty}|^2}{|\mathcal{D}_{in}^{\infty}|^2}$ acquires a value greater than unity there will be a gain in amplification factor that corresponds to superradiance phenomena. However, a negative value of the amplification factor indicates a loss that corresponds to the non-appearance of superradiance. To study the effect of Lorentz violation on the superradiance phenomena, it will be useful to plot Z_{jm} versus $M\omega$ for different values of Lorentz violation parameters. In Fig. (6.2), we present the variation Z_{jm} versus $M\omega$ for the leading multipoles $j = 1$ and 2 taking different values (both negative and positive) of the Lorentz violation parameter. From the Fig. (6.1) along with Fig. (6.2), it is evident that superradiance for a particular j occurs when the allowed values of m are restricted to $m > 0$.

For negative m , amplification factor takes negative value which refers to the non-occurrence of superradiance. The plots also show transparently that with the decrease in the value of the Lorentz violation parameters the superradiance process enhances and the reverse is the case when the value of the Lorentz violation parameter decreases. In Fig. (6.4) we have also studied the effect of the parameter ϑ_n on the superradiance scenario. It shows that the superradiance scenario gets diminished with the increase in the value of the parameter ϑ_n . However, with the increase in \hat{a} , the superradiance effect increases as is found from Fig. (6.3).

6.2. AMPLIFICATION FACTOR Z_{jm} FOR SUPERRADIANCE

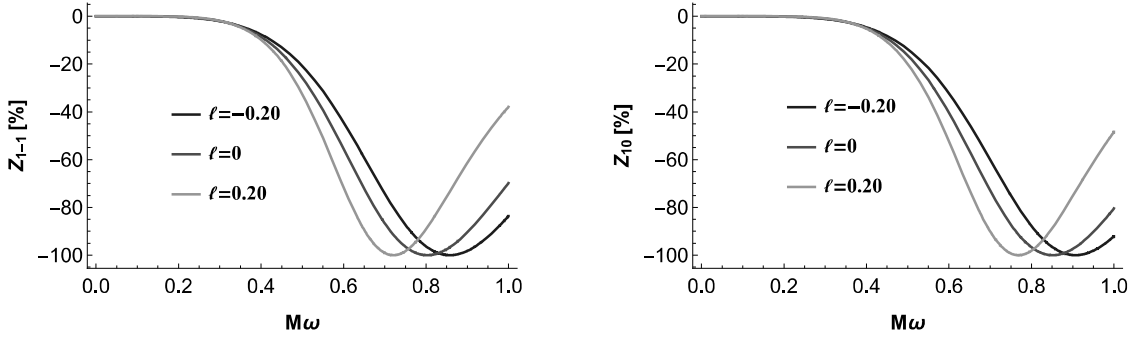


Figure 6.1: Variation of amplification factors with ℓ for non-superradiant multipoles with $\hat{\mu} = 0.1$, $\vartheta_n = 0.01M^2$, and $\hat{a} = 0.3M$.

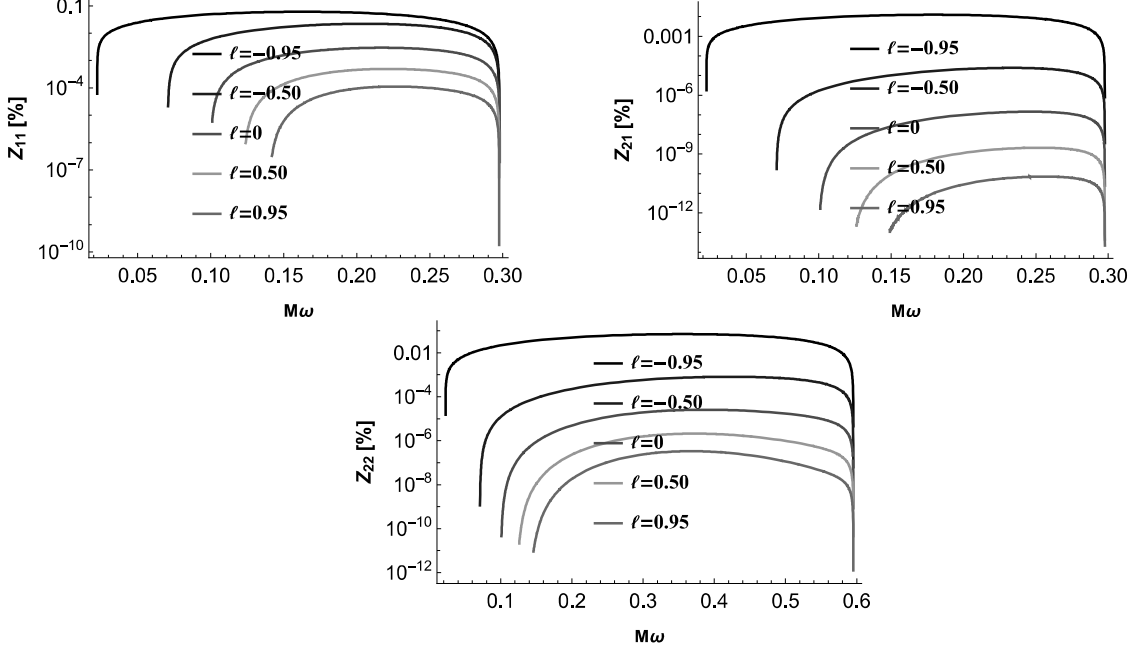


Figure 6.2: Variation of amplification factors with ℓ for various multipoles with $\hat{\mu} = 0.1$, $\vartheta_n = 0.02M^2$, and $\hat{a} = 0.55M$.

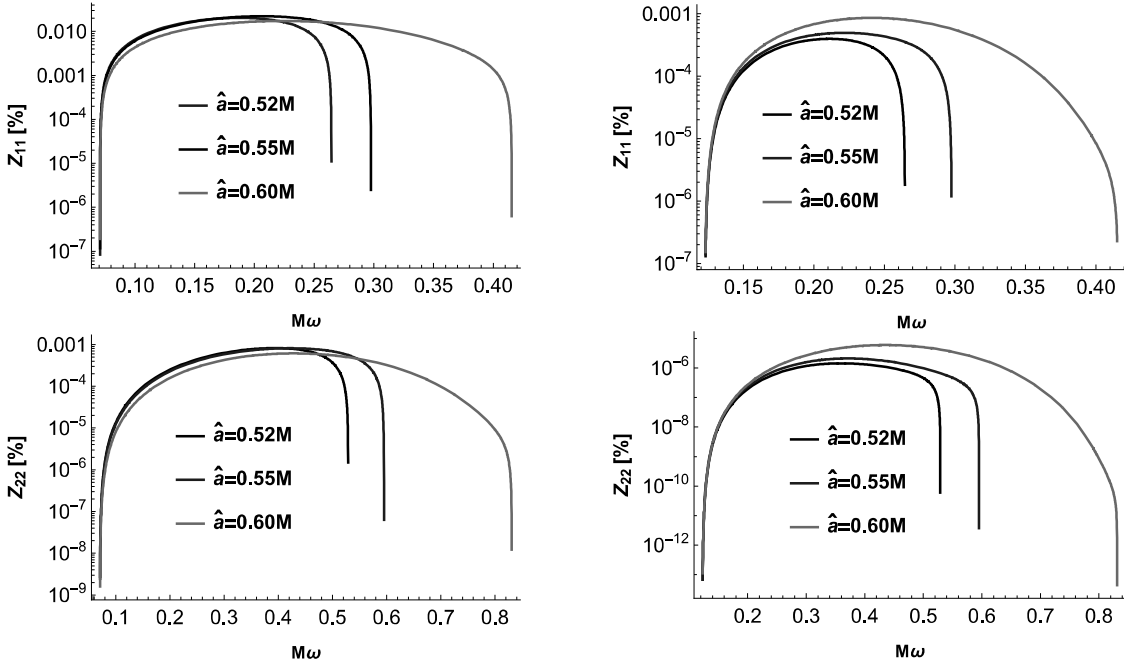


Figure 6.3: Variation of amplification factors with \hat{a} for various multipoles with $\hat{\mu} = 0.1$ and $\vartheta_n = 0.02M^2$. For left ones $\ell = -0.5$ and for right ones $\ell = 0.5$.

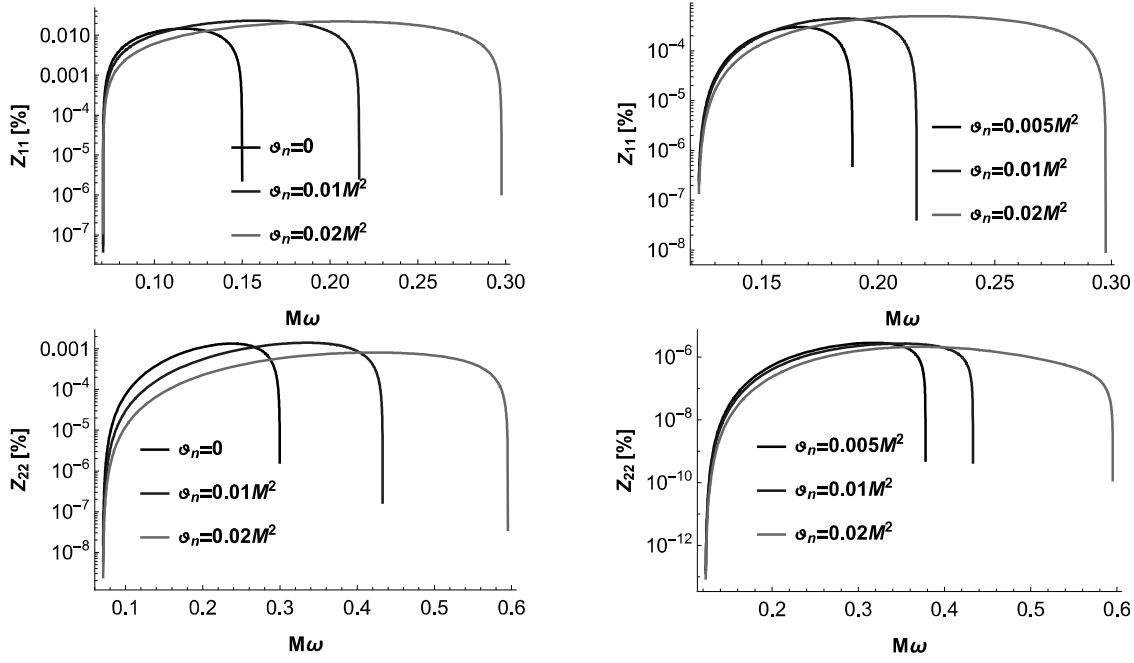


Figure 6.4: Variation of amplification factors with ϑ_n for various multipoles with $\hat{\mu} = 0.1$ and $\hat{a} = 0.55M$. For left ones $\ell = -0.5$ and for right ones $\ell = 0.5$.

6.3 Superradiant instability for Lorentz violating and non-commutative Kerr-like black hole

From equation (6.5) we have

$$\hat{\Delta} \frac{d}{dr} \left(\hat{\Delta} \frac{dR_{\omega jm}}{dr} \right) + \mathcal{F} R_{\omega jm} = 0, \quad (6.29)$$

where for a slowly rotating black hole ($\hat{a}\omega \ll 1$)

$$\mathcal{F} \equiv \frac{((r^2 + \hat{a}^2)\omega - m\hat{a})^2}{1 + \ell} + \hat{\Delta} (2m\hat{a}\omega - j(j+1) - \mu^2 r^2). \quad (6.30)$$

If we now look for the black hole bomb mechanism, we would have the following solutions for the radial equation (6.29)

$$R_{\omega jm} \sim \begin{cases} e^{-i(\omega - m\hat{\Omega}_h)r_*} & \text{as } r \rightarrow r_{ch} (r_* \rightarrow -\infty) \\ \frac{e^{-\sqrt{\mu^2 - \omega^2}r_*}}{r} & \text{as } r \rightarrow \infty (r_* \rightarrow \infty) \end{cases} \quad (6.31)$$

The above solution represents the physical boundary condition that the scalar wave at the black hole horizon is purely ingoing while at spatial infinity it is decaying exponentially (bounded), provided that $\omega^2 < \mu^2$. With the new radial function

$$\psi_{\omega jm} \equiv \sqrt{\hat{\Delta}} R_{\omega jm}, \quad (6.32)$$

the radial equation (6.29) turns into

$$\left(\frac{d^2}{dr^2} + \omega^2 - V \right) \psi_{\omega jm} = 0, \quad (6.33)$$

with

6.3. SUPERRADIANT INSTABILITY FOR LORENTZ VIOLATING AND NON-COMMUTATIVE KERR-LIKE BLACK HOLE

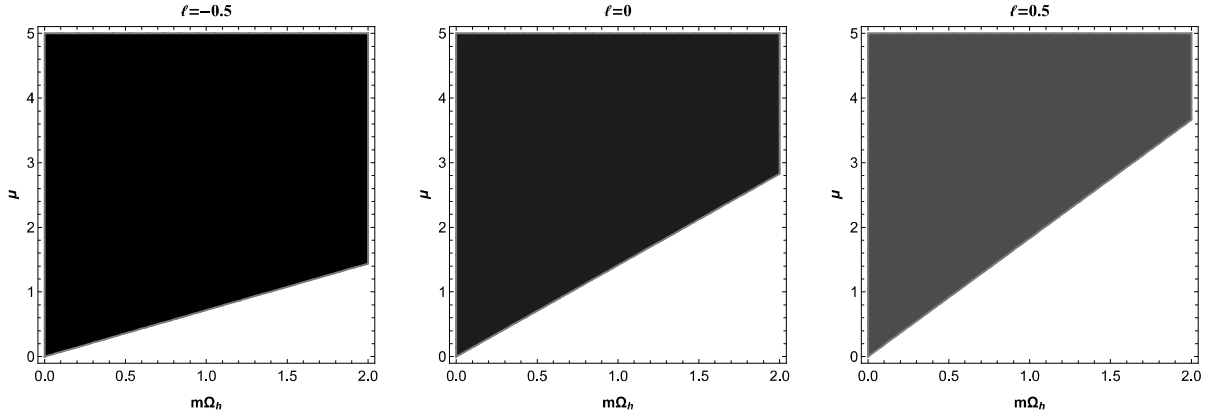


Figure 6.5: Parameter space($m\Omega_h$ - μ) for massive scalar field where coloured area represents region with stable dynamics and non-coloured area represents region with unstable dynamics. Here $\hat{a} = 0.51M$ and $\vartheta_n = 0.01M^2$.

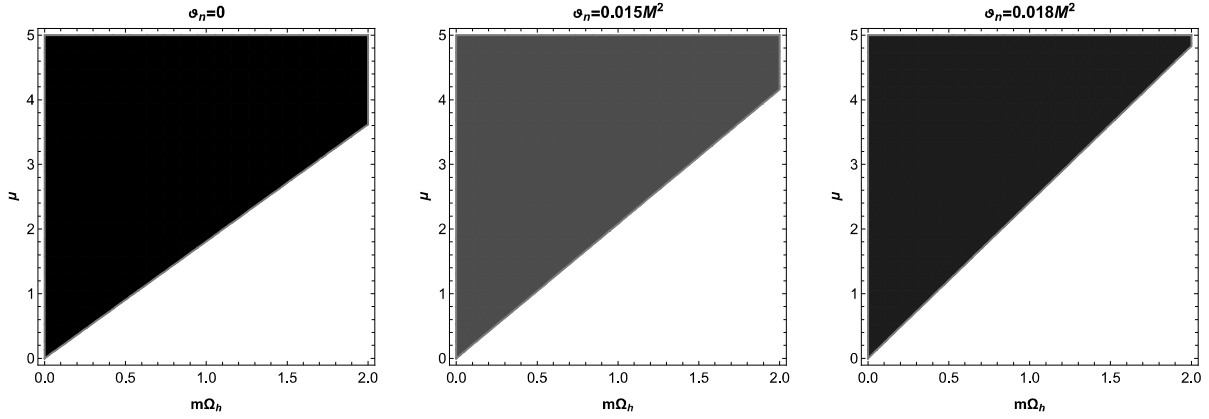


Figure 6.6: Parameter space($m\Omega_h$ - μ) for massive scalar field where coloured area represents region with stable dynamics and non-coloured area represents region with unstable dynamics. Here $\hat{a} = 0.51M$ and $\ell = 0.5$.

$$\omega^2 - V = \frac{\mathcal{F} + \frac{M\left(M - \frac{8\sqrt{\vartheta_n}}{\sqrt{\pi}}\right) - a^2(\ell+1)}{(\ell+1)^2}}{\hat{\Delta}^2}, \quad (6.34)$$

which is the Regge-Wheel equation. By discarding the terms $\mathcal{O}(1/r^2)$, the asymptotic form of the effective potential $V(r)$ looks

$$V(r) = \mu^2(1 + \ell) - (1 + \ell) \frac{4M\omega^2}{r} + (\ell + 1) \frac{2M\mu^2}{r}. \quad (6.35)$$

To realize the trapping meaningfully by the above effective potential it is necessary that its asymptotic derivative be positive i.e. $V' \rightarrow 0^+$ as $r \rightarrow \infty$ [107]. This along with the fact that superradiance amplification of scattered waves occurs when $\omega < m\hat{\Omega}_h$ we get the regime [121]

$$\frac{\mu}{\sqrt{2}} < \omega^2 < m\hat{\Omega}_h, \quad (6.36)$$

in which the integrated system of non-commutative Kerr bumblebee black hole and massive scalar field may experience a superradiant instability, known as the black hole bomb. The dynamics of the massive scalar field in non-commutative Kerr-like black hole will remain stable when $\mu \geq \sqrt{2}m\hat{\Omega}_h$.

6.4 Superradiance scattering of the scalar field off Kerr-Sen-like black hole

To study the superradiance scattering of a scalar field Φ with mass μ , we consider the Klein-Gordon equation (6.3) and the ansatz (6.4). For the Kerr-Sen-like black hole given by metric (4.23), radial part of the equation reads [120]

$$\frac{d}{dr} \left(\Delta \frac{dR_{\omega jm}(r)}{dr} \right) + \left(\frac{((r(r+b) + a^2(1+\ell))\omega - am\sqrt{1+\ell})^2}{\Delta(1+\ell)} \right) R_{\omega jm}(r) - (\mu^2 r(r+b) + j(j+1) + a^2(1+\ell)\omega^2 - 2m\omega a\sqrt{1+\ell}) R_{\omega jm}(r) = 0, \quad (6.37)$$

and for the angular part, it is

$$\sin \theta \frac{d}{d\theta} \left(\sin \theta \frac{d\Theta_{\omega jm}(\theta)}{d\theta} \right) + \left(j(j+1) \sin^2 \theta - \left((a\sqrt{1+\ell}\omega \sin^2 \theta - m)^2 \right) \right) \Theta_{\omega jm}(\theta) + a^2(1+\ell)\mu^2 \sin^2 \theta \cos^2 \theta \Theta_{\omega jm}(\theta) = 0, \quad (6.38)$$

where $\Delta = \frac{r(r+b)-2Mr}{1+\ell} + a^2$. The Regge-Wheeler-like coordinate r_* for Kerr-Sen-like black hole is given by

$$r_* \equiv \int dr \frac{r(r+b) + a^2(1+\ell)}{\Delta}, \quad (r_* \rightarrow -\infty \text{ at event horizon, } r_* \rightarrow \infty \text{ at infinity}). \quad (6.39)$$

To transform the equation into a desired shape, a new radial function $\mathcal{R}_{\omega jm}(r_*) = \sqrt{r(r+b) + a^2(1+\ell)} R_{\omega jm}(r)$ is introduced. After a few steps of algebra, we obtain below the radial equation with our desired form where an effective potential is visible clearly,

$$\frac{d^2 \mathcal{R}_{\omega jm}(r_*)}{dr_*^2} + V_{\omega jm}(r) \mathcal{R}_{\omega jm}(r_*) = 0. \quad (6.40)$$

The effective potential that leads to scattering reads

$$V_{\omega jm}(r) = \frac{1}{1+\ell} \left(\omega - \frac{m\hat{a}}{r(r+b) + \hat{a}^2} \right)^2 - \frac{\Delta}{(r(r+b) + \hat{a}^2)^2} [j(j+1) + \hat{a}^2\omega^2 - 2m\hat{a}\omega + \mu^2 r(r+b) + \sqrt{r(r+b) + \hat{a}^2} \frac{d}{dr} \left(\frac{\Delta(2r+b)}{2(r(r+b) + \hat{a}^2)^{\frac{3}{2}}} \right)], \quad (6.41)$$

where $\hat{a} = a(1+\ell)^{\frac{1}{2}}$. We are intended to study the scattering of the scalar field Φ under this effective potential. In this context, it is beneficial to study the asymptotic behaviour of the scattering potential at the event horizon and at spatial infinity. In the asymptotic limit, the potential at the event horizon looks

$$\lim_{r \rightarrow r_{eh}} V_{\omega jm}(r) = \frac{1}{1+\ell} \left(\omega - m\hat{\Omega}_{eh} \right)^2 \equiv k_{eh}^2, \quad (6.42)$$

where $\hat{\Omega}_{eh} = \frac{\hat{a}}{r_{eh}(r_{eh}+b) + \hat{a}^2}$ and the same at spatial infinity reads

$$\lim_{r \rightarrow \infty} V_{\omega jm}(r) = \omega^2 - \lim_{r \rightarrow \infty} \frac{\mu^2 r(r+b)\Delta}{(r(r+b) + \hat{a}^2)^2} = \frac{\omega^2}{1+\ell} - \hat{\mu}^2 \equiv k_{\infty}^2, \quad \hat{\mu} = \frac{\mu}{\sqrt{\ell+1}}. \quad (6.43)$$

Note that at the two extremal points, event horizon and spatial infinity, the potential asymptotically shows constant behaviour. However, the values of the constants are different indeed.

We are now in a position to see asymptotic behaviour of the radial equation. It is found that the radial equation (6.40) has the following asymptotic solutions

$$R_{\omega jm}(r) \rightarrow \begin{cases} \frac{A_{in}^{eh} e^{-ik_{eh}r_*}}{\sqrt{r_{eh}(r_{eh}+b) + \hat{a}^2}} & \text{for } r \rightarrow r_{eh} \\ \mathcal{A}_{in}^{\infty} \frac{e^{-ik_{\infty}r_*}}{r} + \mathcal{A}_{ref}^{\infty} \frac{e^{ik_{\infty}r_*}}{r} & \text{for } r \rightarrow \infty \end{cases} \quad (6.44)$$

Here \mathcal{A}_{in}^{eh} represents the amplitude of the incoming scalar wave at event horizon and \mathcal{A}_{in}^∞ is the corresponding quantity of the incoming scalar wave at infinity (∞). Along with these, the amplitude of the reflected part of scalar wave at infinity (∞) is \mathcal{A}_{ref}^∞ .

Let us now compute the Wronskian for the region near the event horizon and at infinity. It is found that Wronskian for this region is

$$W_{eh} = \left(R_{\omega jm}^{eh} \frac{dR_{\omega jm}^{*eh}}{dr_*} - R_{\omega jm}^{*eh} \frac{dR_{\omega jm}^{eh}}{dr_*} \right), \quad (6.45)$$

and the Wronskian at infinity reads

$$W_\infty = \left(R_{\omega jm}^\infty \frac{dR_{\omega jm}^{*\infty}}{dr_*} - R_{\omega jm}^{*\infty} \frac{dR_{\omega jm}^\infty}{dr_*} \right). \quad (6.46)$$

The solutions are linearly independent. From knowledge of standard theory of ordinary differential equation it can be inferred that their Wronskian will be independent of r_* . Thus, the Wronskian evaluated near the horizon must be equal to Wronskian evaluated at infinity. As a result, these two together give an important relation between the amplitudes of incoming and reflected waves at different regions of interest.

$$|\mathcal{A}_{ref}^\infty|^2 = |\mathcal{A}_{in}^\infty|^2 - \frac{k_{eh}}{k_\infty} |\mathcal{A}_{in}^{eh}|^2. \quad (6.47)$$

The above equation transpires that if $\frac{k_{eh}}{k_\infty} < 0$ i.e., $\omega < m\hat{\Omega}_{eh}$, the scalar wave will be superradiantly amplified, because in this situation, the relation $|\mathcal{A}_{ref}^\infty|^2 > |\mathcal{A}_{in}^\infty|^2$ holds transparently.

6.5 Calculation of the amplification factor Z_{jm} for superradiance

We rewrite the radial equation (6.37) as

$$\begin{aligned} & \Delta^2 \frac{d^2 R_{\omega jm}(r)}{dr^2} + \Delta \frac{d\Delta}{dr} \cdot \frac{dR_{\omega jm}(r)}{dr} \\ & + \left(\frac{((r(r+b) + \hat{a}^2)\omega - \hat{a}m)^2}{1+\ell} - \Delta (\mu^2 r(r+b) + j(j+1) + \hat{a}^2 \omega^2 - 2m\hat{a}\omega) \right) R_{\omega jm}(r) = 0. \end{aligned} \quad (6.48)$$

We will derive the near-region and the far-region solution and try to find out a single solution matching the near region at infinity with far-region solution at its initial point. We apply the change of variable $x = \frac{r-r_{eh}}{r_{eh}-r_{ch}}$. Using this change of variable, equation(6.49), under the approximation $\hat{a}\omega \ll 1$, turns into

$$\begin{aligned} & \frac{x^2(x+1)^2}{(\ell+1)^2} \frac{d^2 R_{\omega jm}(x)}{dx^2} + \frac{x(x+1)(2x+1)}{(\ell+1)^2} \frac{dR_{\omega jm}(x)}{dx} \\ & + \left(\frac{P^2 x^4}{1+\ell} + \frac{B^2}{1+\ell} - \frac{j(j+1)}{\ell+1} x(x+1) - \frac{\hat{\mu}^2 P^2}{\omega^2} x^3(x+1) - \hat{\mu}^2 r_{eh}^2 x(x+1) - \frac{2\hat{\mu}^2 r_{eh} P}{\omega} x^2(x+1) \right. \\ & \left. - \frac{\hat{\mu}^2 P b}{\omega} x^2(1+x) - \hat{\mu}^2 b r_{eh} x(1+x) \right) R_{\omega jm}(x) = 0, \end{aligned} \quad (6.49)$$

where $P = (r_{eh} - r_{ch})\omega$ and $B = \frac{(\omega - m\hat{\Omega}_{eh})}{r_{eh}-r_{ch}} r_{eh}^2$. For near region we have $Px \ll 1$ and $\hat{\mu}^2 r_{eh}^2 \ll 1$ and hence the above equation reduces to

$$x^2(x+1)^2 \frac{d^2 R_{\omega jm}(r)}{dx^2} + x(x+1)(2x+1) \frac{dR_{\omega jm}(r)}{dx} + ((\ell+1)B^2 - j(j+1)(\ell+1)x(x+1)) R_{\omega jm}(r) = 0 \quad (6.50)$$

The approximation ($\hat{\mu}^2 r_{eh}^2 \ll 1$) originated from the consideration that the Compton wavelength of the boson participating in the scattering phenomena is much smaller than the size of the black hole.

6.5. CALCULATION OF THE AMPLIFICATION FACTOR Z_{jm} FOR SUPERRADIANCE

The general solution of above equation in terms of Legendre function of the first kind $P_\lambda^\nu(y)$ can be written down as

$$R_{\omega jm}(x) = c P_{\frac{\sqrt{1+4(\ell+1)j(j+1)}-1}{2}}^{2i\sqrt{1+\ell}B}(1+2x). \quad (6.51)$$

If we now use relation

$$P_\lambda^\nu(z) = \frac{1}{\Gamma(1-\nu)} \left(\frac{1+z}{1-z} \right)^{\nu/2} {}_2F_1 \left(-\lambda, \lambda+1; 1-\nu; \frac{1-z}{2} \right), \quad (6.52)$$

it enables us to express $R_{\omega jm}(x)$ in terms of ordinary hypergeometric functions ${}_2F_1(a, b; c; z)$:

$$R_{\omega jm}(x) = c \left(\frac{x}{x+1} \right)^{-i\sqrt{\ell+1}B} {}_2F_1 \left(\frac{1-\sqrt{1+4(\ell+1)j(j+1)}}{2}, \frac{1+\sqrt{1+4(\ell+1)j(j+1)}}{2}; 1-2i\sqrt{\ell+1}B; -x \right). \quad (6.53)$$

We require a single solution using the matching condition at the desired position where two solutions exist. In this respect, we need to observe the large x behaviour of the above expression. The Eq. (6.53) for large x ($x \rightarrow \infty$) reads

$$R_{\text{near-large } x} \sim c \left(\frac{\Gamma(\sqrt{1+4(\ell+1)j(j+1)})\Gamma(1-2i\sqrt{\ell+1}B)}{\Gamma\left(\frac{1+\sqrt{1+4(\ell+1)j(j+1)}}{2}-2i\sqrt{\ell+1}B\right)\Gamma\left(\frac{1+\sqrt{1+4(\ell+1)j(j+1)}}{2}\right)} x^{\frac{\sqrt{1+4(\ell+1)j(j+1)}-1}{2}} + \frac{\Gamma(-\sqrt{1+4(\ell+1)j(j+1)})\Gamma(1-2i\sqrt{\ell+1}B)}{\Gamma\left(\frac{1-\sqrt{1+4(\ell+1)j(j+1)}}{2}\right)\Gamma\left(\frac{1-\sqrt{1+4(\ell+1)j(j+1)}}{2}-2i\sqrt{\ell+1}B\right)} x^{-\frac{\sqrt{1+4(\ell+1)j(j+1)}+1}{2}} \right) \quad (6.54)$$

For far-region we can use the approximations $x+1 \approx x$ and $\hat{\mu}^2 r_{eh}^2 \ll 1$. We may drop all the terms except those which describe the free motion with momentum j and that reduces equation (6.49) into

$$\frac{d^2 R_{\omega jm}(x)}{dx^2} + \frac{2}{x} \frac{dR_{\omega jm}(x)}{dx} + \left(k_l^2 - \frac{j(j+1)(\ell+1)}{x^2} \right) R_{\omega jm}(x) = 0, \quad (6.55)$$

where $k_l \equiv \frac{P\sqrt{1+\ell}}{\omega} \sqrt{\omega^2 - \mu^2}$. Equation (6.55) has the general solution

$$R_{\omega jm, \text{far}} = e^{-ikx} \left(d_1 x^{\frac{\sqrt{1+4(\ell+1)j(j+1)}-1}{2}} U \left(\frac{1+\sqrt{1+4(\ell+1)j(j+1)}}{2}, 1+\sqrt{1+4(\ell+1)j(j+1)}, 2ik_l x \right) + d_2 x^{-\frac{\sqrt{1+4(\ell+1)j(j+1)}+1}{2}} U \left(\frac{1-\sqrt{1+4(\ell+1)j(j+1)}}{2}, 1-\sqrt{1+4(\ell+1)j(j+1)}, 2ik_l x \right) \right), \quad (6.56)$$

where $U(a, b, y)$ refers to the first Kummer function. In order to match the solution with (6.54) we require the small x behaviour of the solution (6.56). For small x ($x \rightarrow 0$), the equation (6.56) takes the form

$$R_{\omega jm, \text{far-small } x} \sim d_1 x^{\frac{\sqrt{1+4(\ell+1)j(j+1)}-1}{2}} + d_2 x^{-\frac{1+\sqrt{1+4(\ell+1)j(j+1)}}{2}}. \quad (6.57)$$

The solution (6.54) and (6.57) has common region of interest and are amenable for matching. The matching of the asymptotic solutions (6.54) and (6.57) enable us to compute the scalar wave flux at infinity.

$$d_1 = c \frac{\Gamma(\sqrt{1+4(\ell+1)j(j+1)})\Gamma(1-2i\sqrt{\ell+1}B)}{\Gamma\left(\frac{1+\sqrt{1+4(\ell+1)j(j+1)}}{2}-2i\sqrt{\ell+1}B\right)\Gamma\left(\frac{1+\sqrt{1+4(\ell+1)j(j+1)}}{2}\right)},$$

$$d_2 = c \frac{\Gamma(-\sqrt{1+4(\ell+1)j(j+1)})\Gamma(1-2i\sqrt{\ell+1}B)}{\Gamma\left(\frac{1-\sqrt{1+4(\ell+1)j(j+1)}}{2}-2i\sqrt{\ell+1}B\right)\Gamma\left(\frac{1-\sqrt{1+4(\ell+1)j(j+1)}}{2}\right)}. \quad (6.58)$$

We expand equation (6.56) around infinity which gives

$$\begin{aligned} d_1 \frac{\Gamma(1+\sqrt{1+4(\ell+1)j(j+1)})}{\Gamma\left(\frac{1+\sqrt{1+4(\ell+1)j(j+1)}}{2}\right)} k_l^{-\frac{1+\sqrt{1+4(\ell+1)j(j+1)}}{2}} & \left((-2i)^{-\frac{1+\sqrt{1+4(\ell+1)j(j+1)}}{2}} \frac{e^{-ik_l x}}{x} + (2i)^{-\frac{1+\sqrt{1+4(\ell+1)j(j+1)}}{2}} \frac{e^{ik_l x}}{x} \right) + \\ d_2 \frac{\Gamma(1-\sqrt{1+4(\ell+1)j(j+1)})}{\frac{1-\sqrt{1+4(\ell+1)j(j+1)}}{2}} k_l^{\frac{\sqrt{1+4(\ell+1)j(j+1)}-1}{2}} & \left((-2i)^{\frac{\sqrt{1+4(\ell+1)j(j+1)}-1}{2}} \frac{e^{-ik_l x}}{x} + (2i)^{\frac{\sqrt{1+4(\ell+1)j(j+1)}-1}{2}} \frac{e^{ik_l x}}{x} \right). \end{aligned}$$

With the approximations $\frac{1}{x} \sim \frac{P}{\omega} \cdot \frac{1}{r}$, $e^{\pm ik_l x} \sim e^{\pm i\sqrt{(1+\ell)(\omega^2-\hat{\mu}^2)}r}$ if we match the above solution with the radial solution (6.44)

$$R_\infty(r) \sim \mathcal{A}_{in}^\infty \frac{e^{-i\sqrt{\frac{\omega^2}{1+\ell}-\hat{\mu}^2}r^*}}{r} + \mathcal{A}_{ref}^\infty \frac{e^{i\sqrt{\frac{\omega^2}{1+\ell}-\hat{\mu}^2}r^*}}{r}, \quad \text{for } r \rightarrow \infty,$$

we get

$$\begin{aligned} \mathcal{A}_{in}^\infty = \frac{P}{\omega} & \left(d_1 (-2i)^{-\frac{1+\sqrt{1+4(\ell+1)j(j+1)}}{2}} \frac{\Gamma(1+\sqrt{1+4(\ell+1)j(j+1)})}{\Gamma\left(\frac{1+\sqrt{1+4(\ell+1)j(j+1)}}{2}\right)} k_l^{-\frac{1+\sqrt{1+4(\ell+1)j(j+1)}}{2}} + \right. \\ & \left. d_2 (-2i)^{\frac{\sqrt{1+4(\ell+1)j(j+1)}-1}{2}} \frac{\Gamma(1-\sqrt{1+4(\ell+1)j(j+1)})}{\Gamma\left(\frac{1-\sqrt{1+4(\ell+1)j(j+1)}}{2}\right)} k_l^{\frac{\sqrt{1+4(\ell+1)j(j+1)}-1}{2}} \right), \quad (6.59) \end{aligned}$$

and

$$\begin{aligned} \mathcal{A}_{ref}^\infty = \frac{P}{\omega} & \left(d_1 (2i)^{-\frac{1+\sqrt{1+4(\ell+1)j(j+1)}}{2}} \frac{\Gamma(1+\sqrt{1+4(\ell+1)j(j+1)})}{\Gamma\left(\frac{1+\sqrt{1+4(\ell+1)j(j+1)}}{2}\right)} k_l^{-\frac{1+\sqrt{1+4(\ell+1)j(j+1)}}{2}} + \right. \\ & \left. d_2 (2i)^{\frac{\sqrt{1+4(\ell+1)j(j+1)}-1}{2}} \frac{\Gamma(1-\sqrt{1+4(\ell+1)j(j+1)})}{\Gamma\left(\frac{1-\sqrt{1+4(\ell+1)j(j+1)}}{2}\right)} k_l^{\frac{\sqrt{1+4(\ell+1)j(j+1)}-1}{2}} \right) \quad (6.60) \end{aligned}$$

Putting the values of d_1 and d_2 from (6.58) into the above expressions we get [120]

$$\begin{aligned} \mathcal{A}_{in}^\infty = \frac{c(-2i)^{-\frac{1+\sqrt{1+4(\ell+1)j(j+1)}}{2}}}{\sqrt{(1+\ell)(\omega^2-\hat{\mu}^2)}} & \cdot \frac{\Gamma(\sqrt{1+4(\ell+1)j(j+1)})\Gamma(1+\sqrt{1+4(\ell+1)j(j+1)})}{\Gamma\left(\frac{1+\sqrt{1+4(\ell+1)j(j+1)}}{2}-2i\sqrt{\ell+1}B\right)\left(\Gamma\left(\frac{1+\sqrt{1+4(\ell+1)j(j+1)}}{2}\right)\right)^2} \times \\ & \Gamma(1-2i\sqrt{\ell+1}B)k_l^{\frac{1-\sqrt{1+4(\ell+1)j(j+1)}}{2}} + \frac{c(-2i)^{\frac{\sqrt{1+4(\ell+1)j(j+1)}-1}{2}}}{\sqrt{(1+\ell)(\omega^2-\hat{\mu}^2)}} \times \\ & \frac{\Gamma(1-\sqrt{1+4(\ell+1)j(j+1)})\Gamma(-\sqrt{1+4(\ell+1)j(j+1)})}{\left(\Gamma\left(\frac{1-\sqrt{1+4(\ell+1)j(j+1)}}{2}\right)\right)^2} \Gamma(1-2i\sqrt{\ell+1}B)k_l^{\frac{1+\sqrt{1+4(\ell+1)j(j+1)}}{2}}, \quad (6.61) \end{aligned}$$

and

$$\begin{aligned}
 \mathcal{A}_{ref}^{\infty} = & \frac{c(2i)^{-\frac{1+\sqrt{1+4(\ell+1)j(j+1)}}{2}}}{\sqrt{(1+\ell)(\omega^2 - \hat{\mu}^2)}} \cdot \frac{\Gamma(\sqrt{1+4(\ell+1)j(j+1)})\Gamma(1+\sqrt{1+4(\ell+1)j(j+1)})}{\Gamma\left(\frac{1+\sqrt{1+4(\ell+1)j(j+1)}}{2} - 2i\sqrt{\ell+1}B\right)\left(\Gamma\left(\frac{1+\sqrt{1+4(\ell+1)j(j+1)}}{2}\right)\right)^2} \times \\
 & \Gamma(1-2i\sqrt{\ell+1}B)k_l^{\frac{1-\sqrt{1+4(\ell+1)j(j+1)}}{2}} + \frac{c(2i)^{\frac{\sqrt{1+4(\ell+1)j(j+1)}-1}{2}}}{\sqrt{(1+\ell)(\omega^2 - \hat{\mu}^2)}} \times \\
 & \frac{\Gamma(1-\sqrt{1+4(\ell+1)j(j+1)})\Gamma(-\sqrt{1+4(\ell+1)j(j+1)})}{\left(\Gamma\left(\frac{1-\sqrt{1+4(\ell+1)j(j+1)}}{2}\right)\right)^2\Gamma\left(\frac{1-\sqrt{1+4(\ell+1)j(j+1)}}{2} - 2i\sqrt{\ell+1}B\right)} \Gamma(1-2i\sqrt{\ell+1}B)k_l^{\frac{1+\sqrt{1+4(\ell+1)j(j+1)}}{2}}.
 \end{aligned} \tag{6.62}$$

The amplification factor is given by

$$Z_{jm} \equiv \frac{|\mathcal{A}_{ref}^{\infty}|^2}{|\mathcal{A}_{in}^{\infty}|^2} - 1. \tag{6.63}$$

Equation (6.63) is a general expression of amplification factor obtained making use of the asymptotic matching method. When $\frac{|\mathcal{A}_{ref}^{\infty}|^2}{|\mathcal{A}_{in}^{\infty}|^2}$ acquires a value greater than unity there will be gain in amplification factor that corresponds to superradiance. However, when the amplification factor is negative it indicates a loss which corresponds to the non-occurrence of superradiance.

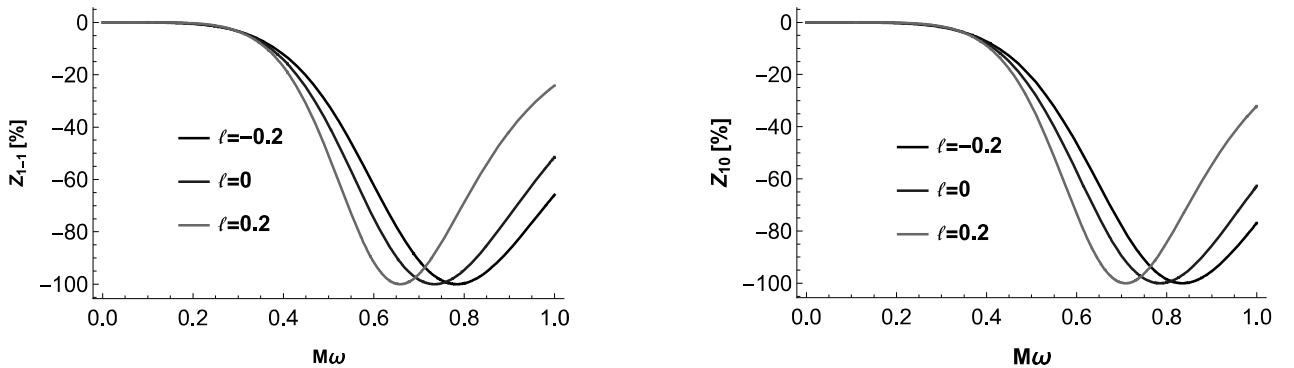


Figure 6.7: Variation of amplification factors with ℓ for non-superradiant multipoles with $\hat{\mu} = 0.1, b = 0.1M$, and $\hat{a} = 0.4M$

6.5. CALCULATION OF THE AMPLIFICATION FACTOR Z_{jm} FOR SUPERRADIANCE

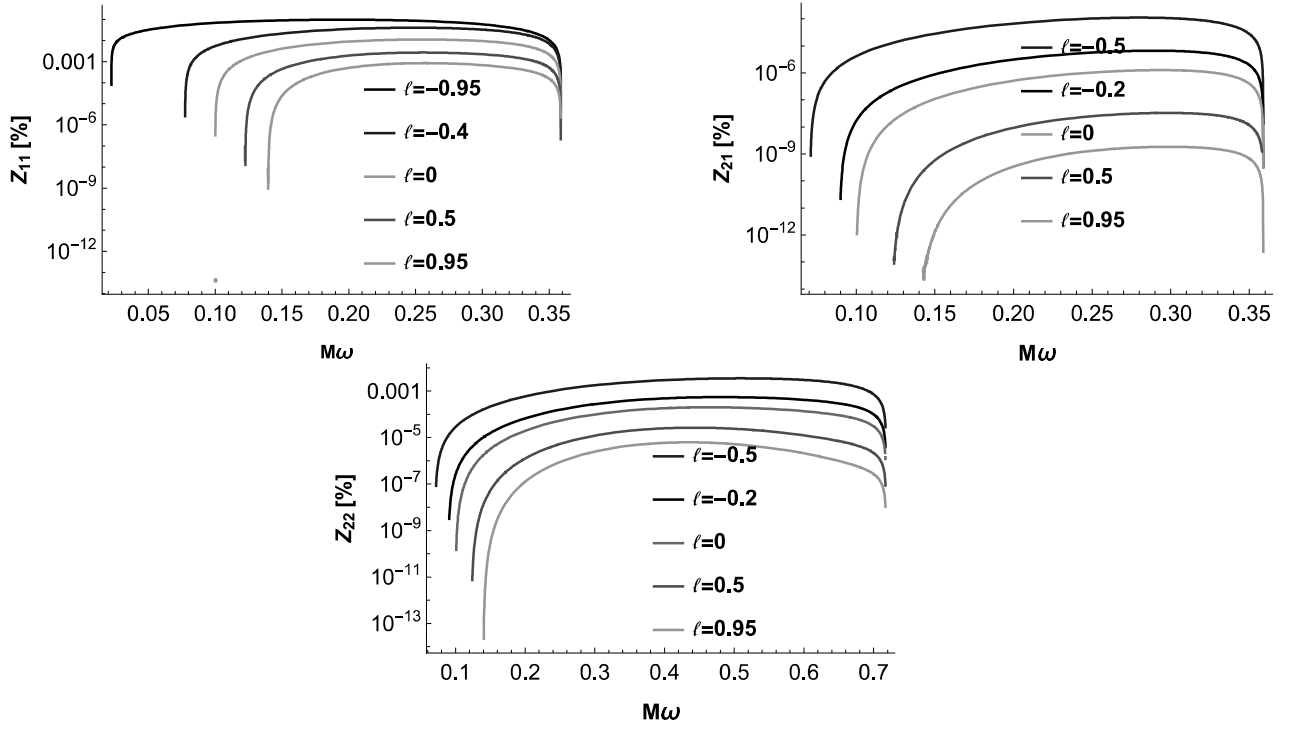


Figure 6.8: Variation of amplification factors with ℓ for various multipoles with $\hat{\mu} = 0.1$, $b = 0.1M$, and $\hat{a} = 0.9M$

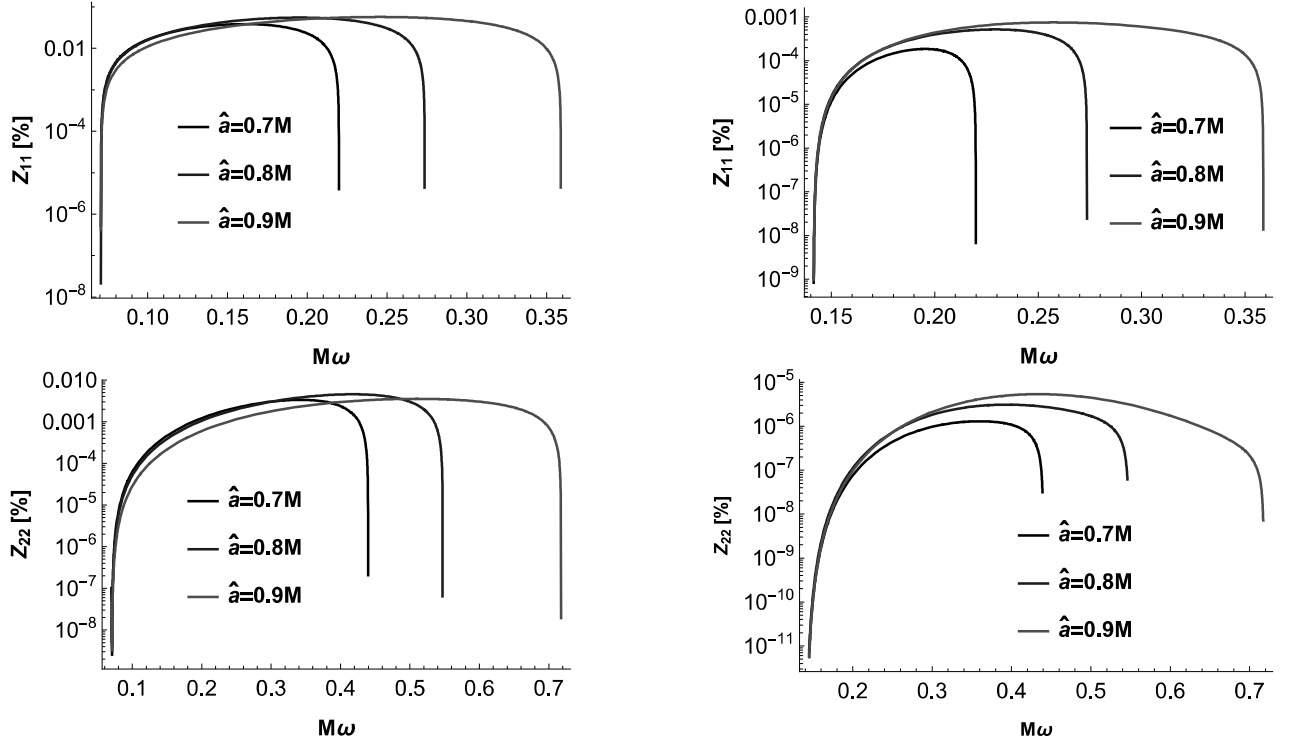


Figure 6.9: Variation of amplification factors with \hat{a} for various multipoles with $\hat{\mu} = 0.1$ and $b = 0.1M$. For left ones $\ell = -0.5$ and for right ones $\ell = 1$

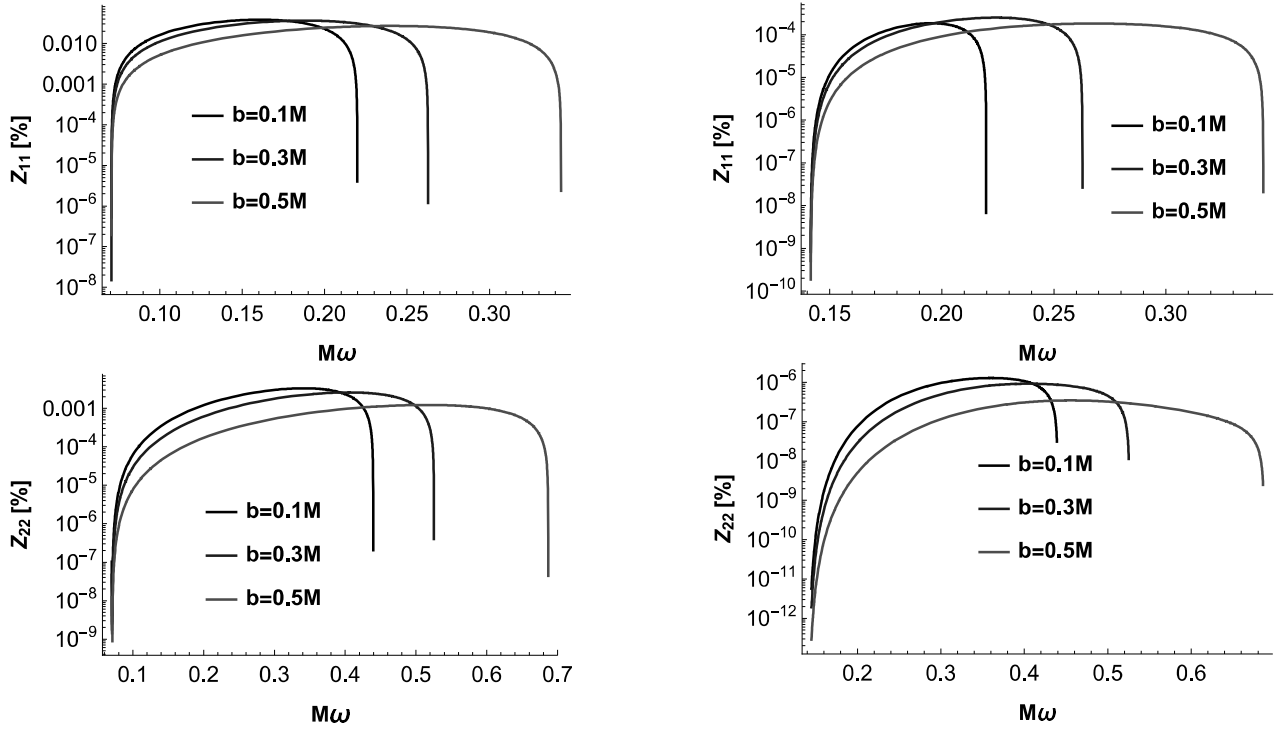


Figure 6.10: Variation of amplification factors with b for various multipoles with $\hat{\mu} = 0.1$ and $\hat{a} = 0.7M$. For left ones $\ell = -0.5$ and for right ones $\ell = 1$

To study the effect of Lorentz violation on the superradiance phenomena, it will be useful to plot Z_{jm} versus $M\omega$ for different LV parameter. In Fig. (6.8) we present the variation Z_{jm} versus $M\omega$ for leading multipoles $j = 1$ and 2 taking different values (both negative and positive) of LV parameter. From the Fig. (6.7) it is evident that superradiance for a particular j occurs when the allowed values of m are restricted to $m > 0$. For negative m , amplification factor takes negative value indicating the non-occurrence of superradiance. The plots also show transparently that with the decrease in LV parameter, the superradiance process gets enhanced and the reverse is the case when the LV parameter decreases. In Fig. (6.10) we have also studied the effect of the parameter $b = \frac{Q^2}{M}$ on the superradiance scenario. It shows that the superradiance scenario gets diminished with the increase in the value of the parameter b . In [76], we have noticed that the size of the shadow decreases with the increase of the value of both the parameters ℓ and b . The only difference is that ℓ can take both positive values, however, b , as per definition, cannot be negative. Therefore, an indirect relation of superradiance with the size of the shadow is being revealed through this analysis. A decrease in the value of b and ℓ indicates the increase in the size of the shadow. From Fig. (6.9) we can also conclude that superradiance process enhances with the increase in \hat{a} . Here, we have considered modes with $m > 0$ as modes $m \geq 0$ are not superradiant.

6.6 Superradiant instability for Kerr-Sen-like black hole

From equation (6.37) we have

$$\Delta \frac{d}{dr} \left(\Delta \frac{dR_{\omega jm}}{dr} \right) + \xi_\ell R_{\omega jm} = 0, \quad (6.64)$$

where for a slowly rotating black hole ($\hat{a}\omega \ll 1$)

$$\xi_\ell \equiv \frac{((r(r+b) + \hat{a}^2)\omega - m\hat{a})^2}{1 + \ell} + \Delta (2m\hat{a}\omega - j(j+1) - \mu^2 r(r+b)). \quad (6.65)$$

Demanding the black hole bomb mechanism, we should have the following solutions for the radial equation (6.64)

$$R_{\omega jm} \sim \begin{cases} e^{-i(\omega - m\hat{\Omega}_{eh})r_*} & \text{as } r \rightarrow r_{eh} \ (r_* \rightarrow -\infty) \\ \frac{e^{-\sqrt{\mu^2 - \omega^2}r_*}}{r} & \text{as } r \rightarrow \infty \ (r_* \rightarrow \infty). \end{cases} \quad (6.66)$$

The above solutions represent the physical boundary conditions that the scalar wave at the black hole horizon is purely ingoing while at spatial infinity it is decaying exponentially (bounded), provided that $\omega^2 < \mu^2$. With the new radial function

$$\psi_{\omega jm} \equiv \sqrt{\Delta} R_{\omega jm}, \quad (6.67)$$

the radial equation (6.64) becomes

$$\left(\frac{d^2}{dr^2} + \omega^2(1 + \ell) - V \right) \psi_{\omega jm} = 0, \quad (6.68)$$

with

$$\omega^2 - V = \frac{\xi_\ell + \frac{M^2 - \hat{a}^2 + \frac{b^2}{4} - bM}{(1+\ell)^2}}{\Delta^2}, \quad (6.69)$$

which is the Regge-Wheel equation. Asymptotic form of the effective potential V , by discarding terms $\mathcal{O}(1/r^2)$, is

$$V(r) = \mu^2(1 + \ell) - (1 + \ell) \frac{4M\omega^2}{r} + (\ell + 1) \frac{2M\mu^2}{r}. \quad (6.70)$$

To realize a trapping well by the above effective potential, it is necessary that its asymptotic derivative be positive i.e. $V' \rightarrow 0^+$ as $r \rightarrow \infty$ [107]. This along with the fact that superradiance amplification of scattered waves occur when $\omega < m\hat{\Omega}_{eh}$ we get the regime [120]

$$\frac{\mu}{\sqrt{2}} < \omega^2 < m\hat{\Omega}_{eh}, \quad (6.71)$$

in which the integrated system of Kerr-Sen-like bumblebee black hole and massive scalar field may experience a superradiant instability. It is known as the black hole bomb. The dynamics of the massive scalar field in Kerr-Sen-like black hole will remain stable when $\mu \geq \sqrt{2}m\hat{\Omega}_{eh}$

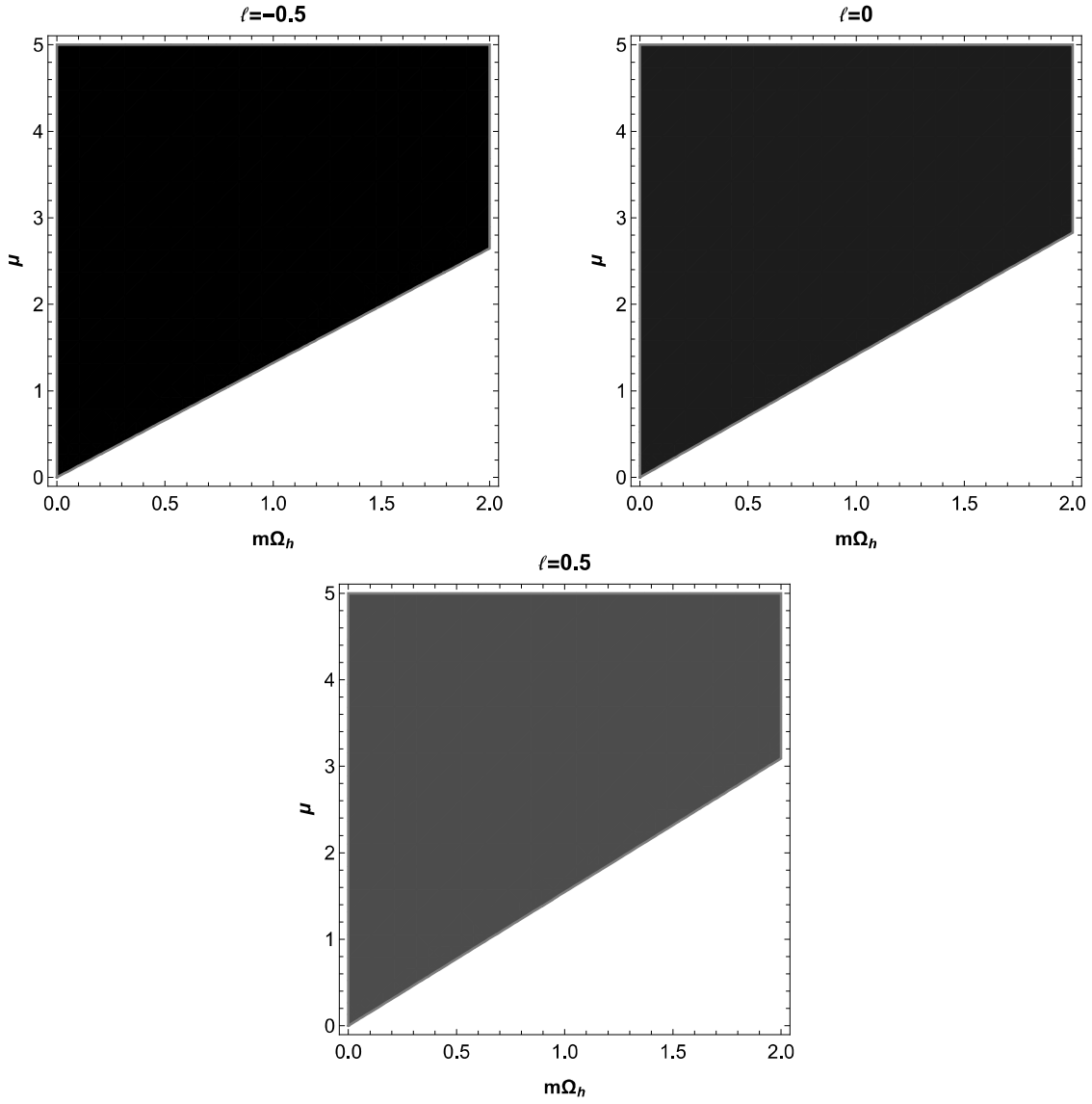


Figure 6.11: Parameter space($m\Omega_h, \mu$) for massive scalar field where coloured area represent region with stable dynamics and non-coloured area represent region with unstable dynamics.

Chapter 7

Constraining parameters involved in modified gravity using observational data for $M87^*$ black hole

The modified theories of gravity contain various free parameters. The recent data concerning $M87^*$ and SgrA* super-massive black holes in the core of $M87^*$ galaxy and our Milky way galaxy respectively provide us with an opening which enables us to constrain the free parameters involved in the modified theories. With this in view we compare the shadows produced, from numerical calculations, by the non-commutative Kerr-like black hole in vacuum, the Kerr-Sen-like black hole in vacuum and when surrounded by plasma with the observed one for the $M87^*$ black hole. For comparison, we consider the following experimentally obtained astronomical data [108]:

$$\Delta C \leq 0.10 \quad \text{and} \quad \theta_d = 42 \pm 3 \mu\text{as}, \quad (7.1)$$

where ΔC is the circularity deviation and θ_d is the angular diameter. The boundary of the shadow is described by the polar coordinates $(R(\phi), \phi)$ with the origin at the center of the shadow (α_C, β_C) where $\alpha_C = \frac{|\alpha_{max} + \alpha_{min}|}{2}$ and $\beta_C = 0$.

If a point (α, β) over the boundary of the image subtends an angle ϕ on the α axis at the geometric center, $(\alpha_C, 0)$ and $R(\phi)$ be the distance between the point (α, β) and $(\alpha_C, 0)$, then the average radius R_{avg} of the image is given by [114]

$$R_{\text{avg}}^2 \equiv \frac{1}{2\pi} \int_0^{2\pi} d\phi R^2(\phi), \quad (7.2)$$

where $R(\phi) \equiv \sqrt{(\alpha(\phi) - \alpha_C)^2 + \beta(\phi)^2}$, and $\phi = \tan^{-1} \frac{\beta(\phi)}{\alpha(\phi) - \alpha_C}$.

With the above inputs, the deviation from circularity ΔC is defined by [115],

$$\Delta C \equiv 2 \sqrt{\frac{1}{2\pi} \int_0^{2\pi} d\phi (R(\phi) - R_{\text{avg}})^2}. \quad (7.3)$$

We also consider the angular diameter of shadow, which is define by

$$\theta_d = \frac{2}{d} \sqrt{\frac{A}{\pi}}, \quad (7.4)$$

where $A = 2 \int_{r_-}^{r_+} \beta d\alpha$ is the shadow area and $d = 16.8 \text{ Mpc}$ is the distance of $M87^*$ from the earth. In case of $M87^*$, the mass has been estimated to be $M = (6.6 \pm 0.4) \times 10^9 M_\odot$, M_\odot being the mass of Sun [116]. We consider $M = 6.5 \times 10^9 M_\odot$ for the $M87^*$ black hole. These relations will enable us to accomplish a comparison between the theoretical predictions and the experimental findings of the Event Horizon Telescope collaboration.

7.1 Constraining LV parameter ℓ for the Kerr-Sen-like black hole surrounded by plasma

Here, we will be constraining the parameter ℓ using the findings (7.1). Figures below represent the deviation from circularity ΔC as it is obtained for Kerr-Sen-like black hole surrounded by plasma for the angles of inclinations $\theta = 90^\circ$ and 17° respectively.

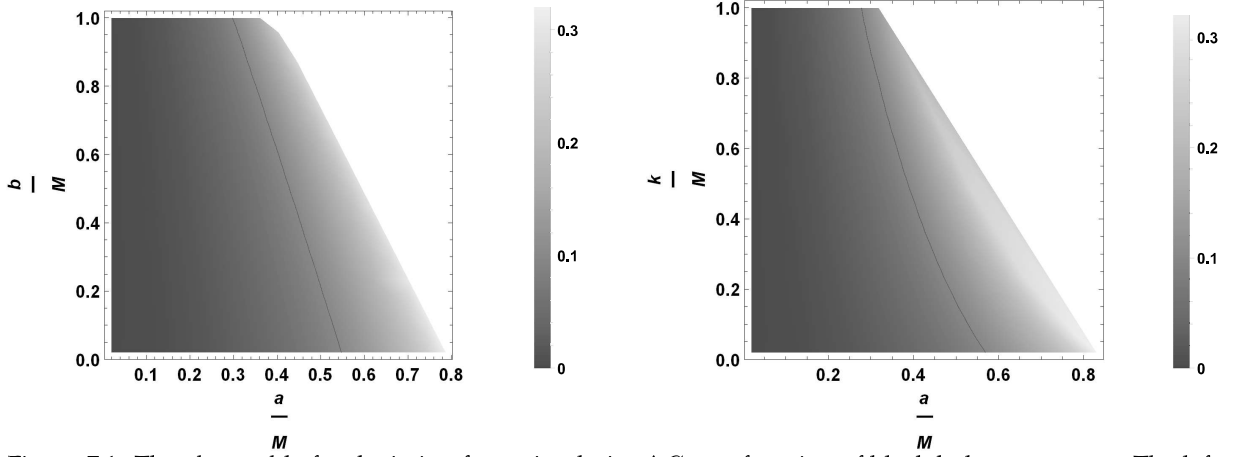


Figure 7.1: The observable for deviation from circularity ΔC as a function of black hole parameters. The left one is for $\ell = 0.1$ and $k = 0.1M$. The right one is for $\ell = 0.1$ and $b = 0.1M$. The angle of inclination is $\theta = 90^\circ$. The black lines in the figures correspond to $\Delta C = 0.1$.

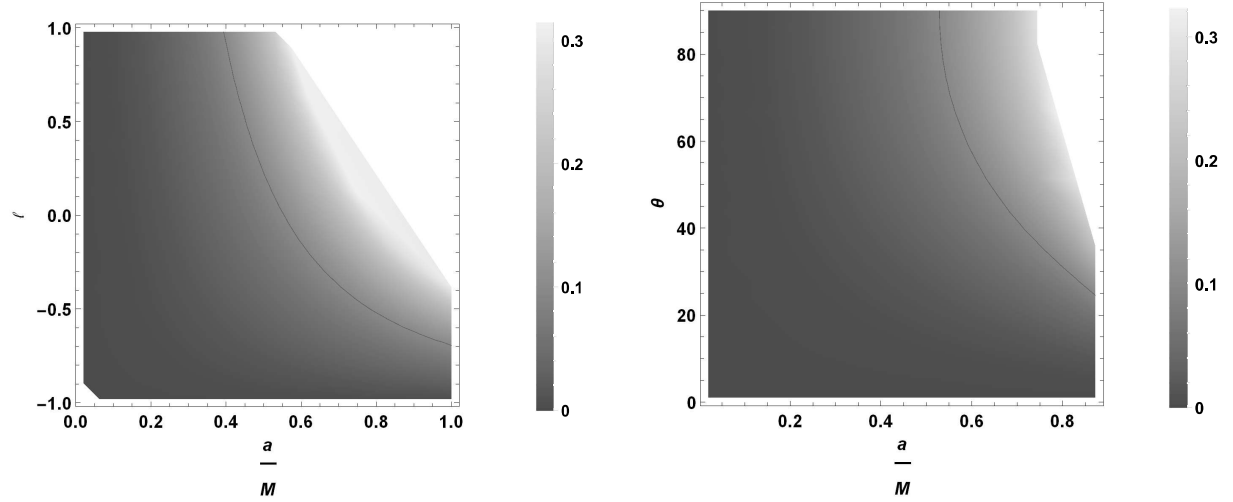


Figure 7.2: The observable for deviation from circularity ΔC as a function of black hole parameters. The left one is for $b = 0.1M$ and $k = 0.1M$. Here, the angle of inclination is $\theta = 90^\circ$. The right one is for $\ell = 0.1$, $b = 0.1M$, and $k = 0.1M$. The black lines in the figures correspond to $\Delta C = 0.1$.

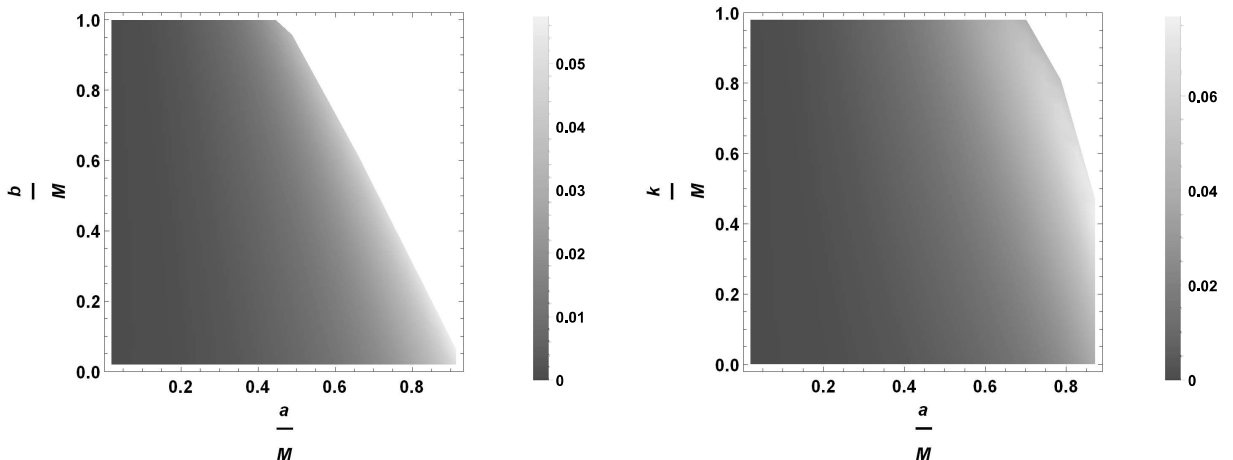


Figure 7.3: The observable for deviation from circularity ΔC as a function of black hole parameters. The left one is for $\ell = 0.1$ and $k = 0.1M$. The right one is for $\ell = 0.1$ and $b = 0.1M$. Here, the angle of inclination is $\theta = 17^\circ$.

7.1. CONSTRAINING LV PARAMETER ℓ FOR THE KERR-SEN-LIKE BLACK HOLE SURROUNDED BY PLASMA

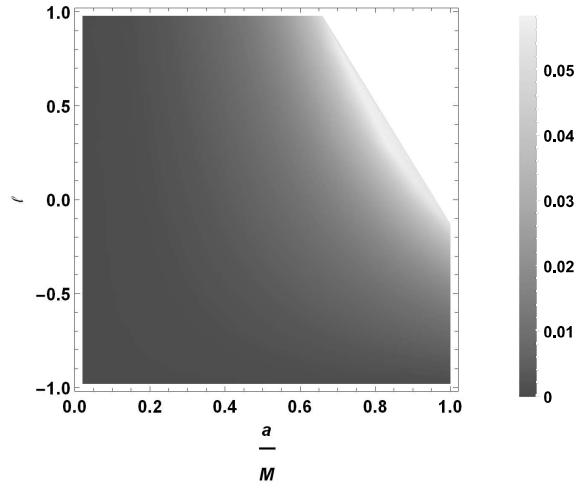


Figure 7.4: The observable for deviation from circularity ΔC as a function of black hole parameters. This is for $b = 0.1M$ and $k = 0.1M$ with the angle of inclination $\theta = 17^\circ$.

Figures below represent the angular diameter θ_d as it is obtained for Kerr-Sen-like black holes for the angles of inclinations $\theta = 90^\circ$ and 17° respectively.

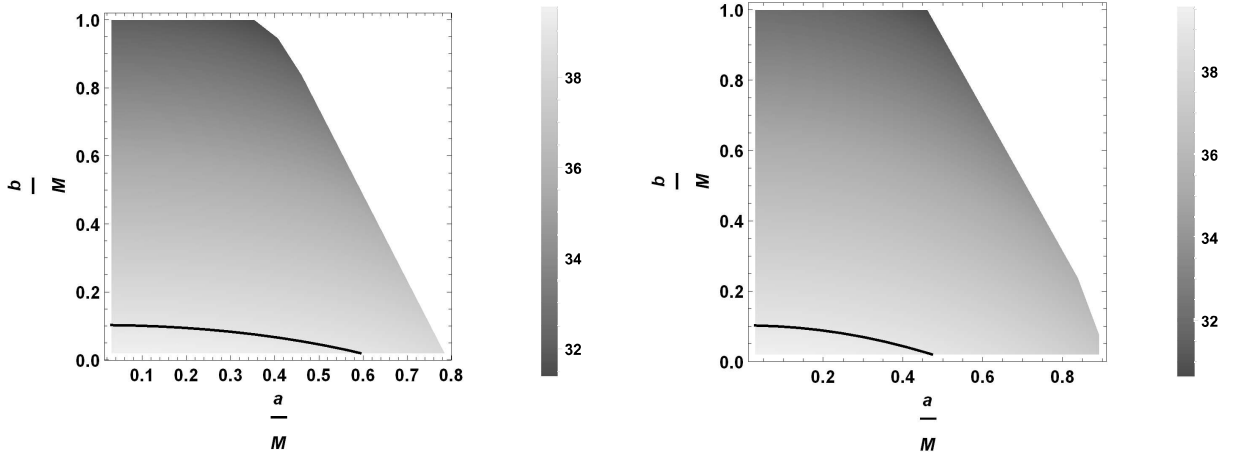


Figure 7.5: The observable for angular diameter θ_d as a function of black hole parameters. The left one is for $\ell = 0.1$, $k = 0.1M$, and the angle of inclination $\theta = 90^\circ$. The right one is for $\ell = 0.1$, $k = 0.1M$, and $\theta = 17^\circ$. Black solid lines correspond to $\theta_d = 39\mu as$.

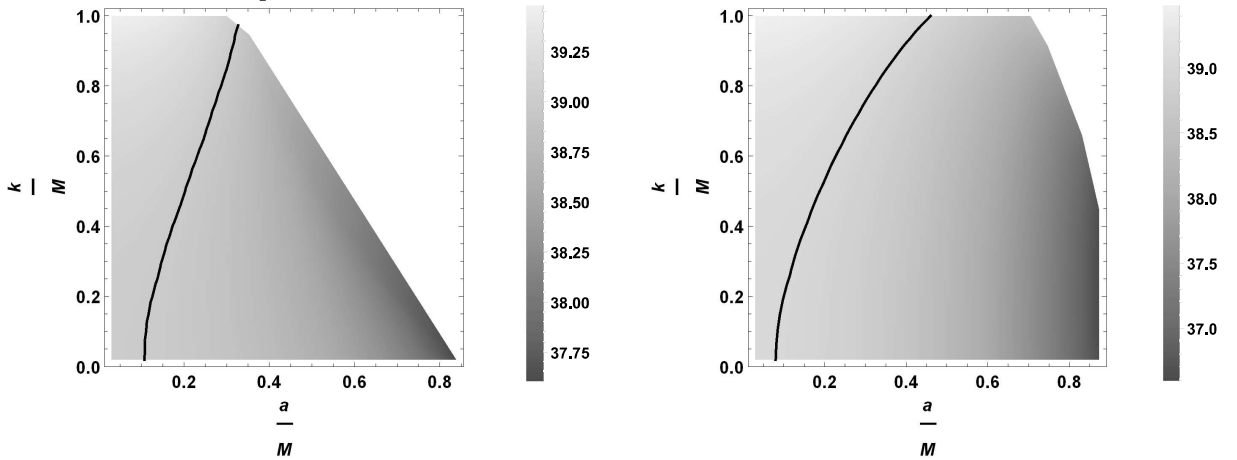


Figure 7.6: The observable for angular diameter θ_d as a function of black hole parameters. The left one is for $\ell = 0.1$, $b = 0.1M$, and angle of inclination $\theta = 90^\circ$. The right one is for $\ell = 0.1$, $b = 0.1M$, and $\theta = 17^\circ$. Black solid lines correspond to $\theta_d = 39\mu as$.

7.1. CONSTRAINING LV PARAMETER ℓ FOR THE KERR-SEN-LIKE BLACK HOLE SURROUNDED BY PLASMA

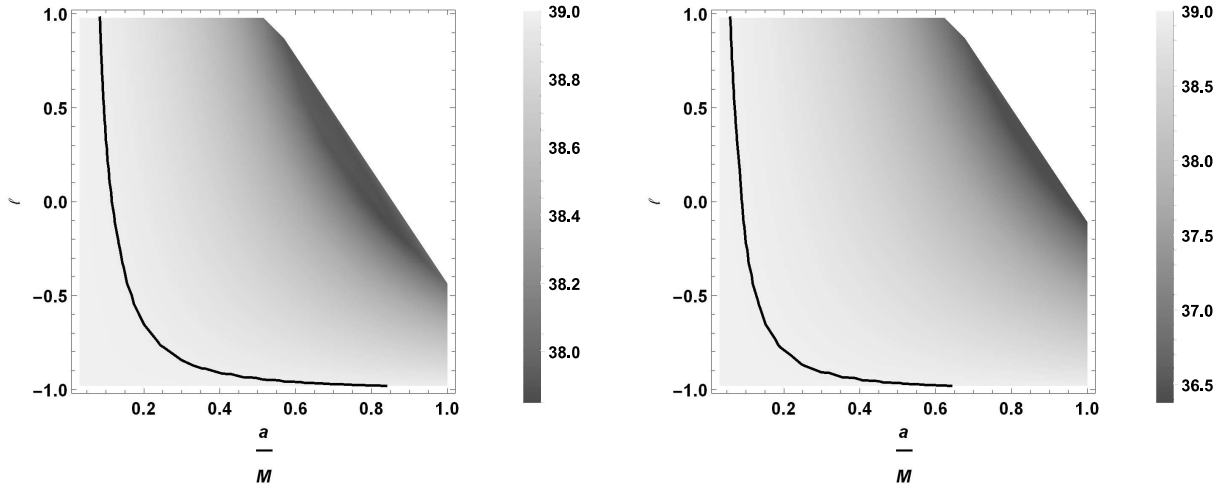


Figure 7.7: The observable for angular diameter θ_d as a function of black hole parameters. The left one is for $k = 0.1M$, $b = 0.1M$, and angle of inclination $\theta = 90^\circ$. The right one is for $k = 0.1M$, $b = 0.1M$, and $\theta = 17^\circ$. Black solid lines correspond to $\theta_d = 39\mu as$.

Table 7.1: Deviation ΔC of Kerr-Sen-like black hole with $k = 0.1M$ and $\ell = 0.1$. The left one is for the inclination angle $\theta = 90^\circ$ and the right one is for the inclination angle $\theta = 17^\circ$.

a/M	b/M	ΔC	a/M	b/M	ΔC
0.020	0.020	0.000108539	0.020	0.020	0.0000106680
0.020	0.265	0.000135858	0.020	0.265	0.0000132214
0.020	0.510	0.000175677	0.020	0.510	0.0000154633
0.020	0.755	0.000237773	0.020	0.755	0.0000203415
0.020	1.000	0.000343416	0.020	1.000	0.0000294412
0.265	0.020	0.019818100	0.265	0.020	0.0017091800
0.265	0.265	0.025141500	0.265	0.265	0.0021694100
0.265	0.510	0.033223300	0.265	0.510	0.0028655300
0.265	0.755	0.046671500	0.265	0.755	0.0040104600
0.265	1.000	0.072912500	0.265	1.000	0.0061582600
0.510	0.020	0.085970200	0.510	0.020	0.0073562800
0.510	0.265	0.112077000	0.510	0.265	0.0097972700
0.510	0.510	0.165146000	0.510	0.510	0.0140271000

From Fig. (7.1) and Fig. (7.2), it is clear that the bound $\Delta C \leq 0.10$ is satisfied by black hole shadows over a finite parameter space. Fig. (7.3) and Fig. (7.4) reveal that the condition $\Delta C \leq 0.10$ is satisfied by the Kerr-Sen-like black hole in presence of plasma for the entire parameter space when the angle of inclination is 17° . From Fig. (7.5), Fig. (7.6), and Fig. (7.7) it is clear that, for finite parameter space, angular diameters are within 1σ region. From figures above we can also conclude that for fixed values of black hole parameters, the apparent shadow circularity deviation and angular diameter decrease as the observer moves away from the equatorial plane toward the polar axis.

By modelling M87* black hole as Kerr black hole, the author in the article [117] has found a lower limit of a for the M87* black hole. If we bring this result under consideration in the present situation,

*7.1. CONSTRAINING LV PARAMETER ℓ FOR THE KERR-SEN-LIKE BLACK HOLE
SURROUNDED BY PLASMA*

the interval of interest for a becomes $[0.50M, 0.99M]$ with $b = k = 0$. Now, if we combine the constraints (7.1) and the knowledge that $a \in [0.50M, 0.99M]$, we observe that $\ell \in (-1, 0.621031]$. Here, we find an upper bound of ℓ , which comes out to be 0.621031.

7.2 Constraining the charge parameter b in Kerr-Sen-like black hole in vacuum from the observed data for M87*

Here, we consider the Kerr-Sen-like black in vacuum given by the metric (4.23). In this section we intend to constrain the charge parameter b using the conditions (7.1) and the definitions given in Eq. (7.3) and Eq. (7.4). In the figures below, the deviation from circularity ΔC is shown for Kerr-Sen-like black holes for inclination angles $\theta = 90^\circ$ and 17° respectively.

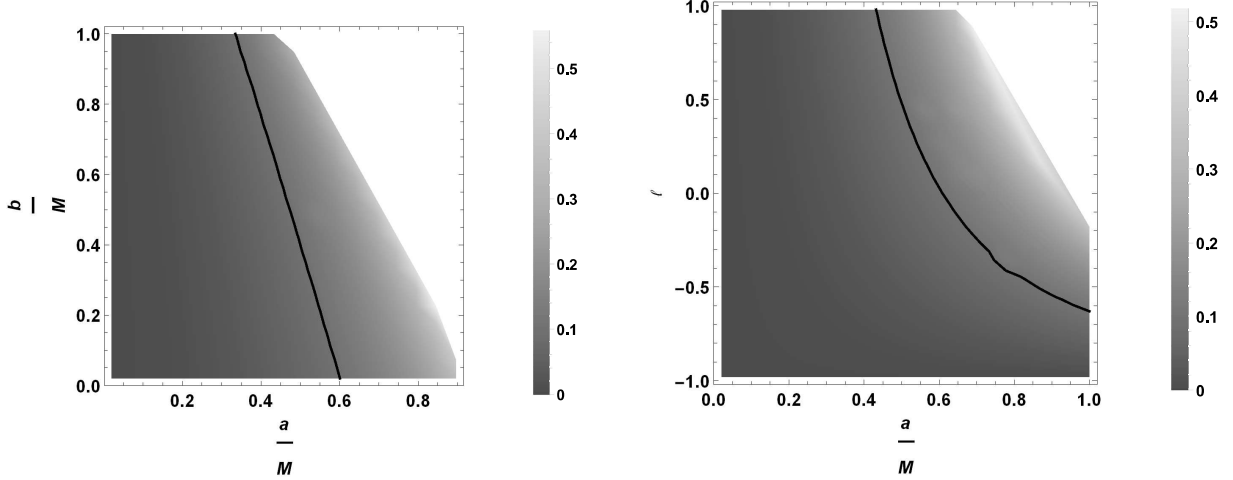


Figure 7.8: The left one is for $\ell = 0.1$ and the right one is for $b = 0.1M$ where the inclination angle is 90° . The black solid lines correspond to $\Delta C = 0.1$.

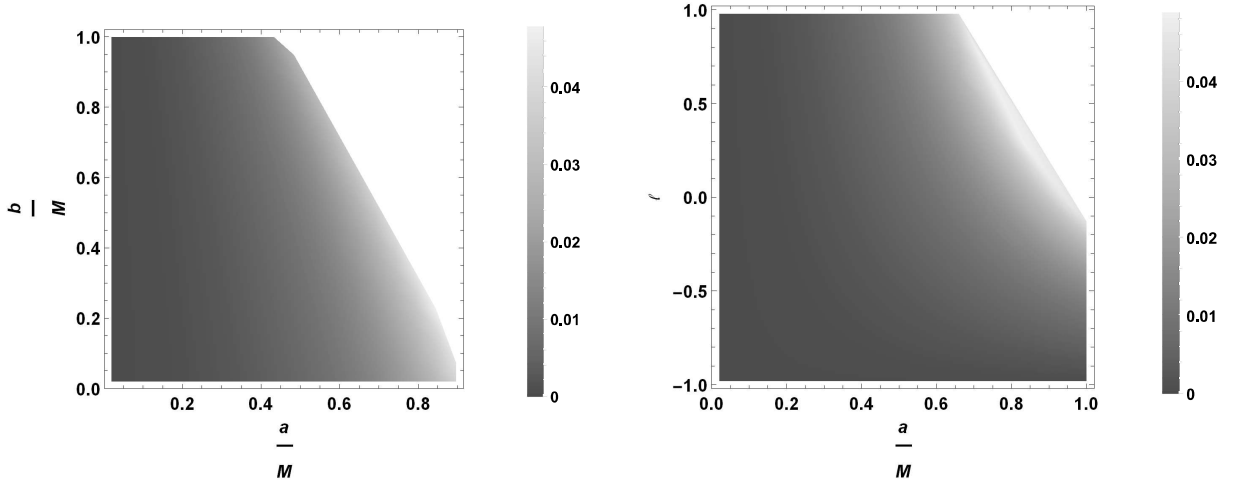


Figure 7.9: The left one is for $\ell = 0.1$ and the right one is for $b = 0.1M$ where the inclination angle is 17° .

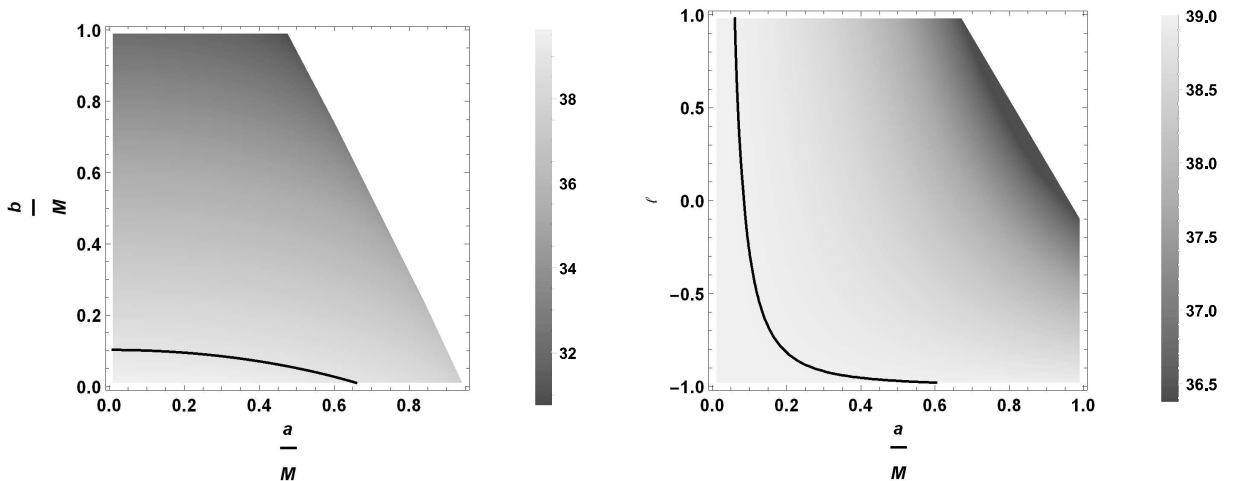


Figure 7.10: The left one is for $\ell = 0.1$ and the right one is for $b = 0.1M$ where the inclination angle is 90° . The black solid lines correspond to $\theta_d = 39 \mu as$.

7.3. CONSTRAINING THE NON-COMMUTATIVE PARAMETER ϑ_n FROM THE OBSERVED DATA FOR M87*

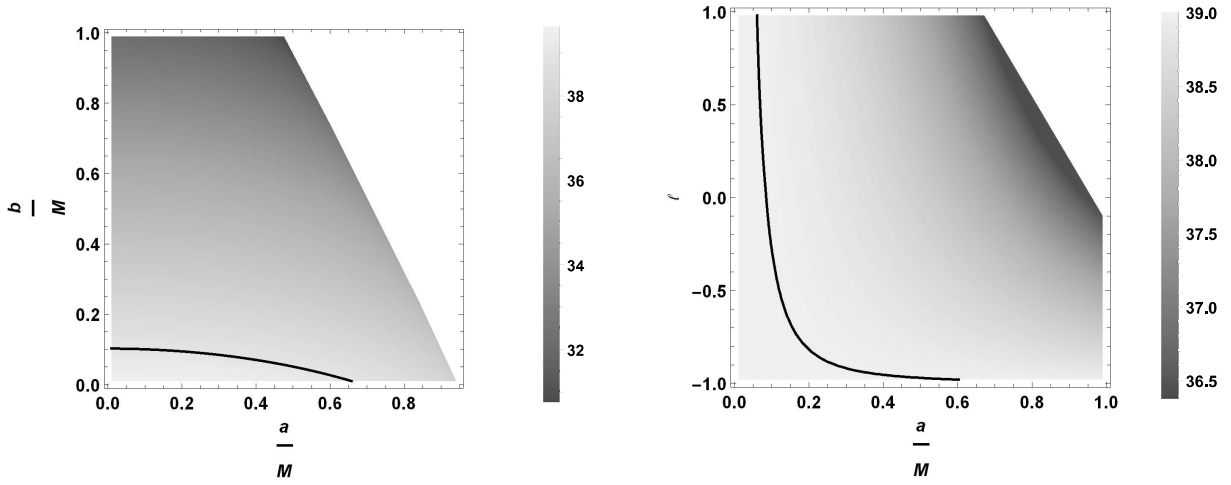


Figure 7.11: The left one is for $\ell = 0.1$ and the right one is for $b = 0.1M$ where the inclination angle is 90° . The black solid lines correspond to $\theta_d = 39\mu as$.

From figures (7.8) and (7.9) we can clearly conclude that the condition $\Delta C \leq 0.10$ is satisfied for finite parameter space when the inclination angle is 90° but for the inclination angle 17° , the condition is satisfied for the entire parameter space. It is also clear from figures (7.10) and (7.11) that the constrain $\theta_d = 42 \pm 3\mu$ within 1σ region is satisfied for finite parameter space for both inclination angles. To constrain the charge parameter b , we consider $a \in [0.50M, 0.99M]$ [117] and $\ell \in (-1, 0.621031]$ [119]. With these findings along with the constrains (7.1), we find that $b \in [0, 0.10242M]$. Here, the upper bound of b is found out to be $0.10242M$.

7.3 Constraining the non-commutative parameter ϑ_n from the observed data for M87*

This section is devoted to constraining the parameter ϑ_n . We here also use the constraints given by (7.1) and definitions given in Eq. (7.3) and in Eq. (7.4). In the figures below, the deviation from circularity, ΔC and the angular diameter θ_d are shown for non-commutative Kerr-like black holes for inclination angles $\theta = 90^\circ$ and $\theta = 17^\circ$.

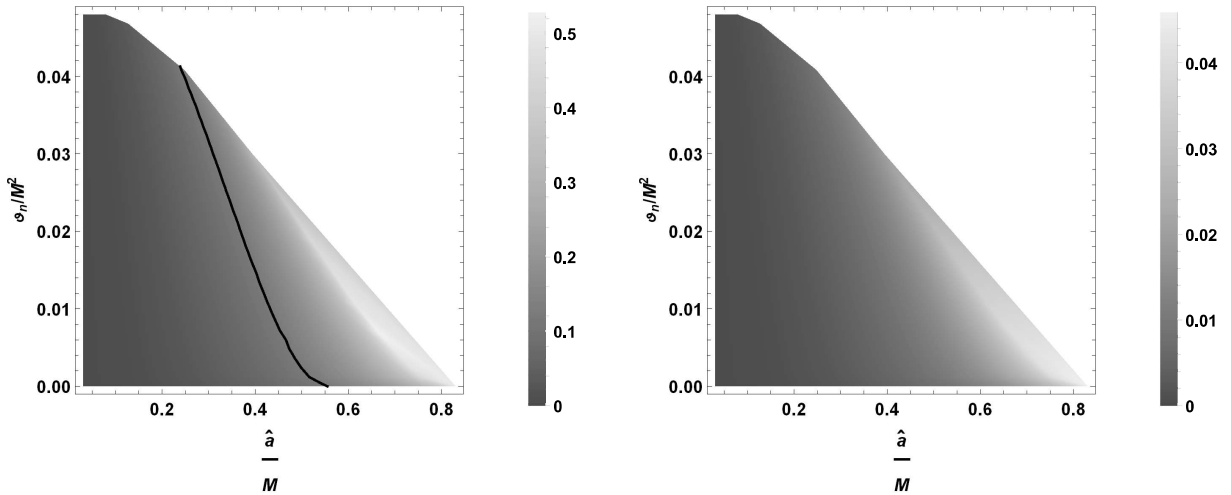


Figure 7.12: For the left panel the inclination angle is 90° and for the right panel the inclination angle is 17° . The black solid lines correspond to $\Delta C = 0.1$.

From the plot (7.12), we can conclude that the constrain $\Delta C \leq 0.1$ is satisfied for finite parameter space when the inclination angle is 90° , whereas, when the inclination angle is 17° , the constrain is satisfied for the entire parameter space.

7.3. CONSTRAINING THE NON-COMMUTATIVE PARAMETER ϑ_n FROM THE OBSERVED DATA FOR M87*

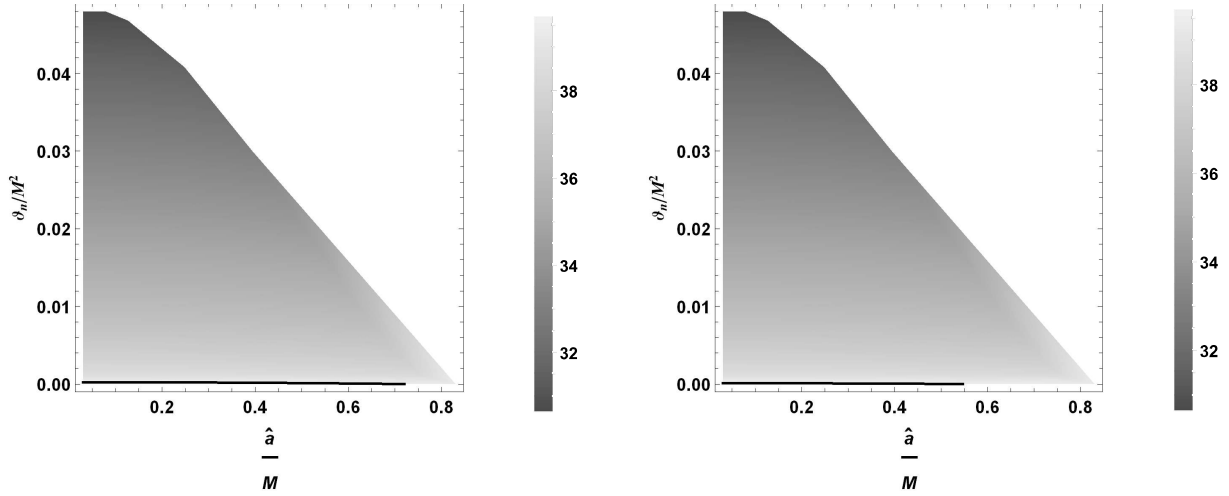


Figure 7.13: For the left panel the inclination angle is 90° and for the right panel the inclination angle is 17° . The black solid lines correspond to $\theta_d = 39\mu as$.

From the plot (7.13), we can conclude that for inclination angles $\theta = 90^\circ$ and $\theta = 17^\circ$, the constrain $\theta_d = 42 \pm 3\mu$ within 1σ region is satisfied for finite parameter space. The circular asymmetry in the M87* shadow can also be defined in terms of the axial ratio D_X which is the ratio of the major to the minor diameter of the shadow [108]. It is defined by [122]

$$D_X = \frac{\Delta Y}{\Delta X} = \frac{\beta_t - \beta_b}{\alpha_r - \alpha_p}. \quad (7.5)$$

We should have $1 < D_X \lesssim 4/3$ in accordance with the EHT observations of M87* [108]. Note that D_X is another way of defining ΔC . Axial ratio of 4 : 3 indeed corresponds to a $\Delta C \leq 0.1$ [108]. In the figures below axial ratio, D_X , is shown for non-commutative Kerr-like black holes for inclination angles $\theta = 90^\circ$ and $\theta = 17^\circ$ respectively.

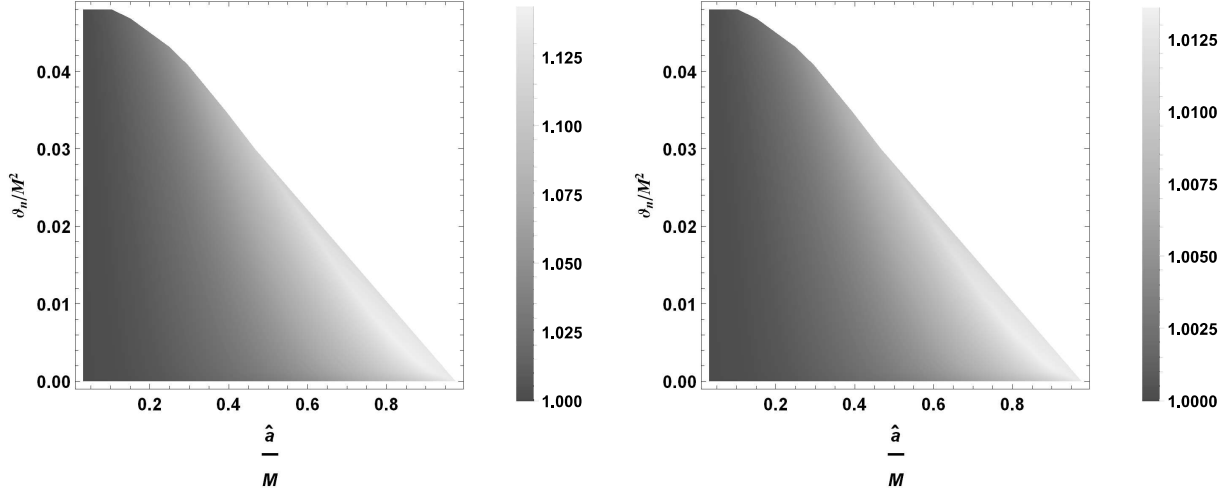


Figure 7.14: For the left panel the inclination angle is 90° and for the right panel the inclination angle is 17° .

From the plots above we see that the condition $1 < D_X \lesssim 4/3$ is satisfied for the entire parameter space of non-commutative Kerr-like black holes. Thus, non-commutative Kerr-like black holes are remarkably consistent with EHT images of M87*. Therefore, we cannot rule out non-commutative Kerr-like black holes from the observational data of M87* black hole shadow.

We can have the bound of the parameter ϑ_n associated with the non-commutativity of the space-time in a similar way we determined the bound of the parameter ℓ in [119]. By modelling M87* black hole as Kerr black hole, the author of the paper [117] obtained a lower limit of a for the M87*

7.3. CONSTRAINING THE NON-COMMUTATIVE PARAMETER ϑ_n FROM THE OBSERVED DATA FOR M87*

black hole. Bringing this result under consideration in [119] we put the interval of interest for a as $[0.50M, 0.99M]$, and using the experimental constraints $\Delta C \leq 0.10$ and $\theta_d = 42 \pm 3\mu as$ with the information $a \in [0.50M, 0.99M]$, we observed that $\ell \in (-1, 0.621031]$. In a similar way, taking into account the bounds $a \in [0.50M, 0.99M]$ and $\ell \in (-1, 0.621031]$ and the experimental constraints $\Delta C \leq 0.1$ and $\theta_d = 39 \pm 3\mu as$, we get a bound on the parameter ϑ_n which is linked with the non-commutativity of spacetime. We find that the parameter $\vartheta_n \in [0, 0.000505973M^2]$. It is intriguing to have an upper bound of ϑ_n which is found out to be $0.000505973M^2$. To the best of our knowledge, the bound of the parameter ϑ_n from the shadow of the astronomical black hole has not yet been reported so far.

Chapter 8

Strong gravitational lensing in hairy Schwarzschild background

According to Einstein's theory of general relativity, spacetime is a concept where time and space get merged and are to be treated on the same footing. Gravity is just the curvature of spacetime, which is caused by large objects according to this theory. Since light travels through spacetime, the general theory of relativity predicts that the path covered by light in spacetime will also be curved as a result of a massive object. A fascinating and observable example of Einstein's theory is gravitational lensing. Spacetime is significantly curved by extremely enormous astronomical objects, such as supermassive black holes. They, in other words, serve as gravitational lenses. The path of the light is curved when it travels through a gravitational lens, creating a distorted image of the distant object that can be seen as a ring or halo of light surrounding the gravitational lens. Magnification, which enables humans to view objects that would otherwise be too weak and far away to be seen, is a significant effect of this lensing distortion. The study of gravitational lensing is interesting in this regard. This chapter is devoted to describe the Strong and weak gravitational lensing in hairy Schwarzschild background which we have studied in [241].

In the article [242–244], Ovalle et al. introduced gravitational decoupling to describe deformations of known spherically symmetric solutions induced by an additional source. The Einstein field equations, in this situation, became

$$\tilde{G}_{\mu\nu} = \kappa (T_{\mu\nu} + S_{\mu\nu}) \quad (8.1)$$

where $T_{\mu\nu}$ and $S_{\mu\nu}$ were the energy-momentum tensors of known solution in general relativity and the corresponding quantity of the additional source respectively. In the article [242], Ovalle et al. considered Schwarzschild black hole surrounded by spherically symmetric matter. The ansatz for the hairy Schwarzschild black used there was

$$\begin{aligned} ds^2 &= - \left(1 - \frac{2M}{r} + \alpha_h e^{-r/(M-\frac{\ell_0}{2})} \right) dt^2 + \left(1 - \frac{2M}{r} + \alpha_h e^{-r/(M-\frac{\ell_0}{2})} \right)^{-1} dr^2 + r^2 (d\theta^2 + \sin^2 \theta d\phi^2) \\ &= -f(r)dt^2 + f(r)^{-1}dr^2 + r^2 (d\theta^2 + \sin^2 \theta d\phi^2). \end{aligned} \quad (8.2)$$

where $f(r) = \left(1 - \frac{2M}{r} + \alpha_h e^{-r/(M-\frac{\ell_0}{2})} \right)$, M represents the mass of the black hole and α_h refers to a parameter that induces deformation due to additional sources. Here $\ell_0 = \alpha_h \hat{\ell}$ represents the increase in entropy caused by the hair and to ensure asymptotic flatness, it must satisfy the condition $\ell_0 \leq 2M = \ell_K$. It is evident from Fig.(1) that the event horizon $r_{eh} = 2M x_{eh}$ increases with ℓ_0 . As r_{eh} increases with ℓ_0 , the horizon area A_h increases and hence the entropy of black hole increases with an increase in ℓ_0 . In the limit $\alpha_h \rightarrow 0$, the (8.2) reduces to the standard metric corresponding to the Schwarzschild black hole. To study gravitational lensing in the this background of hairy Schwarzschild black hole we introduce the following two dimensionless variables

$$x = \frac{r}{2M} \quad \text{and} \quad \tilde{\ell}_0 = \frac{\ell_0}{2M}. \quad (8.3)$$

We define $t \rightarrow \frac{t}{2M}$ and rewrite the metric (8.2) in the following form [261–263]

$$d\tilde{s}^2 = (2M)^{-2}ds^2 = -F(x)dt^2 + F(x)^{-1}dx^2 + H(x)(d\theta^2 + \sin^2\theta d\phi^2), \quad (8.4)$$

where the lapse function $F(x)$ is given by

$$F(x) = 1 - \frac{1}{x} + \alpha_h e^{-2x/(1-\tilde{\ell}_0)} \quad \text{and} \quad H(x) = x^2 \quad (8.5)$$

The radius of the horizon x_{eh} is obtained by solving the equation

$$F(x) = 0. \quad (8.6)$$

Let us now plot $F(x)$ versus x for different values of ℓ_0 , taking a fixed value $\alpha_h = 2$, and x_{eh} versus α_h for different values ℓ_0 to examine the geometry associated with black hole described by the metric (8.4)

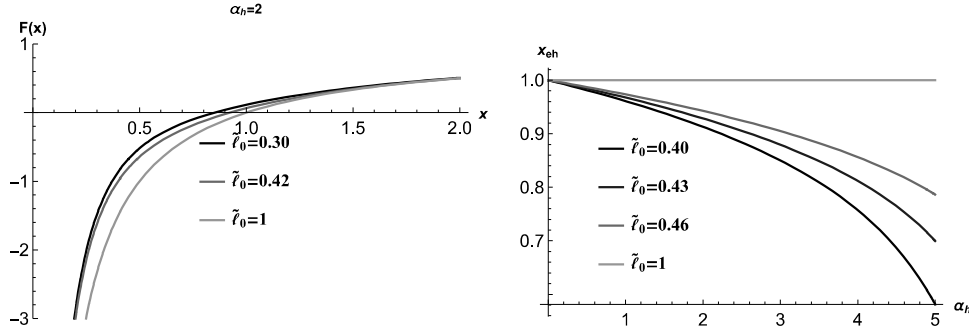


Figure 8.1: The left one shows the variation of $F(x)$ with x for various values of ℓ_0 with $\alpha_h = 2$. The right one shows the variation of x_{eh} with respect to α_h for various values of ℓ_0 .

Fig. 8.1 shows that the horizon radius decreases with α_h , but it increases with ℓ_0 . Note that for $\alpha_h = 0$, that corresponds to $\tilde{\ell}_0 = 1$, we have $x_{eh} = 1$ which resembles the Schwarzschild metric. However, when $\tilde{\ell}_0$ is kept constant the horizon radius decreases with an increase in α_h , but the radius increases with an increase in $\tilde{\ell}_0$ when α_h remains constant. It reflects that the horizon radius for the hairy Schwarzschild black hole is smaller than that for the Schwarzschild black hole. Therefore, the presence of hair has a reducing effect on the Schwarzschild radius. Therefore, it is expected to show its effect on entropy, energy emission, and shadow. Here we present the strong gravitational lensing and the impact of deformation parameters on strong gravitational lensing.

8.1 Strong and weak gravitational lensing

This section is devoted to study the gravitational deflection of light in the static, spherically symmetric, hairy Schwarzschild black hole (8.4). Since we can apply the same results to all θ due to spherical symmetry, we can consider the propagation of light on the equatorial plane without any loss of generality. Then, the ansatz (8.4) becomes

$$d\tilde{s}^2 = -F(x)dt^2 + F(x)^{-1}dx^2 + H(x)d\phi^2. \quad (8.7)$$

It is the static and spherically symmetric nature of spacetime that ensures the conservation of the projection of photon four-momentum along the Killing vectors of isometries. Therefore, the energy $\mathcal{E} = -p_\mu \xi_{(t)}^\mu$ and the angular momentum $\mathcal{L} = p_\mu \xi_{(\phi)}^\mu$ remain constant along the geodesics, where $\xi_{(t)}^\mu$ and $\xi_{(\phi)}^\mu$ are representing the Killing vectors due to time-translational and rotational invariance [137] respectively. So we have

$$\frac{dt}{d\lambda} = \frac{\mathcal{E}}{F(x)}, \quad \frac{d\phi}{d\lambda} = \frac{\mathcal{L}}{H(x)}, \quad (8.8)$$

where λ is the affine parameter along the geodesics. From Eq. (8.8) and Eq. (8.7) we obtain the following equation for the null geodesics

$$\left(\frac{dx}{d\lambda}\right)^2 \equiv \dot{x}^2 = \mathcal{E}^2 - \frac{\mathcal{L}^2 F(x)}{H(x)}. \quad (8.9)$$

Thus, the effective potential $V_{\text{eff}}(x)$ comes out to be

$$V_{\text{eff}}(x) = \frac{\mathcal{L}^2 F(x)}{H(x)} = \frac{\mathcal{L}^2}{x^2} \left(1 - \frac{1}{x} + \alpha_h e^{-2x/(1-\tilde{\ell}_0)}\right). \quad (8.10)$$

For circular photon orbits of radius x_m the effective potential has to satisfy the condition

$$\frac{dV_{\text{eff}}}{dx}\bigg|_{x=x_m} = 0, \quad (8.11)$$

which yields

$$\frac{F'(x)}{F(x)} = \frac{H'(x)}{H(x)}. \quad (8.12)$$

With the use of the above equation we have

$$(2x - 3)(1 - \tilde{\ell}_0) + 2\alpha_h e^{(-2x/(1-\tilde{\ell}_0))} (x(1 - \tilde{\ell}_0) + x^2) = 0. \quad (8.13)$$

Note that at $x = x_m$ the condition $\frac{d^2 V_{\text{eff}}}{dx^2} < 0$ is maintained which indicates that the orbits of the photon experience instability against any arbitrary small radial perturbations. The photons from the infinitely large distance source that approaches the black hole with some impact parameter b_h maintaining a minimum distance x_0 will be deflected back symmetrically to infinity. The impact parameter b_h and the minimum distance x_0 are related to each other through the equation

$$b_h = \sqrt{\frac{H(x_0)}{F(x_0)}} \quad (8.14)$$

which follows from

$$V_{\text{eff}}(x_0) = \mathcal{E}^2 \Rightarrow b_h \equiv \frac{\mathcal{L}}{\mathcal{E}} \quad (8.15)$$

The impact parameter b_m corresponds to $x_0 = x_m$.

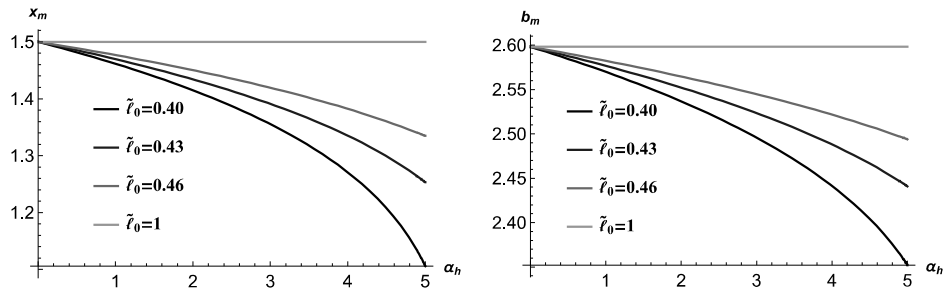


Figure 8.2: Plot showing variation of x_m and b_m with respect to α_h for various values of ℓ_0 .

We can infer from Fig. 8.2 that the radius x_m and the impact parameter b_h at x_m i.e b_m decrease with the increase in α_h but these two appear to increase with the increase in ℓ_0 . Let us look into the gravitational deflection angle of light. It has been formulated in the article [265,266] as follows

$$\alpha_D(x_0) = I(x_0) - \pi, \quad (8.16)$$

where

$$I(x_0) = \int_{x_0}^{\infty} \frac{2}{\sqrt{F(x)H(x)} \sqrt{\frac{F(x_0)H(x)}{H(x_0)F(x)} - 1}} dx. \quad (8.17)$$

In the absence of a black hole total change in ϕ is π as photons follow a straight line trajectory and hence, from Eq. (8.16) we find that the deflection angle will render a vanishing contribution. From Fig.(4) we can conclude that the deflection angle $\alpha_D(x_0)$ enhances with a decrease in the impact parameter b_h and additionally, at some point, it exceeds 2π which implies the completion of loops within the path of the photon encompassing the black hole. Note that a special situation is expected to occur when $x_0 = x_m$, i.e., where the minimum distance approaches the radius of the photon sphere. In such a situation the deflection angle diverges. However, for $b_h < b_m$, photons will get captured by the black hole. In the strong field limit, light rays will be able to pass close to the black hole.

Keeping in view the approximation method used in [261], we expand the deflection angle about the photon sphere where it shows a diverging nature which necessitates bringing in a new variable $z = 1 - x_0/x$. With this new variable, the integral (8.17) can be written down as [35]

$$I(x_0) = \int_0^1 \mathcal{R}(z, x_0) f(z, x_0) dz, \quad (8.18)$$

where $\mathcal{R}(z, x_0)$ and $f(z, x_0)$ are given by

$$\mathcal{R}(z, x_0) = \frac{2x^2 \sqrt{H(x_0)}}{x_0 H(x)}, \quad (8.19)$$

$$f(z, x_0) = \frac{1}{\sqrt{F(x_0) - \frac{F(x)}{H(x)} H(x_0)}}. \quad (8.20)$$

The function $\mathcal{R}(z, x_0)$ is regular for all possible values of z and x_0 , however, the function $f(z, x_0)$ is not, it diverges when $z \rightarrow 0$. In order to avoid the divergence of $f(z, x_0)$ at $z \rightarrow 0$ we expand the function contained within the square root of the Eq. (8.20) in Taylor's series and retain the required term with appropriate approximation to get rid of the divergences. It leads to the following equation

$$f_0(z, x_0) = \frac{1}{\sqrt{a_1(x_0)z + a_2(x_0)z^2}}, \quad (8.21)$$

where $a_1(x_0)$ and $a_2(x_0)$ are having the following algebraic expression:

$$a_1(x_0) = \frac{x_0}{H(x_0)} [(H'(x_0)F(x_0) - F'(x_0)H(x_0))], \quad (8.22)$$

$$a_2(x_0) = \frac{1}{2} \left[\frac{(2x_0 H(x_0) - 2x_0^2 H'(x_0))(H'(x_0)F(x_0) - F'(x_0)H(x_0))}{H^2(x_0)} + \frac{x_0}{H(x_0)} (H''(x_0)F(x_0) - F''(x_0)F(x_0)) \right].$$

This enables us to split the integral (8.18) into the following two integrals [261]

$$I(x_0) = I_D(x_0) + I_R(x_0). \quad (8.23)$$

Explicitly, the integrals are

$$I_D(x_0) = \int_0^1 \mathcal{R}(0, x_m) f_0(z, x_0) dz, \quad (8.24)$$

$$I_R(x_0) = \int_0^1 (\mathcal{R}(z, x_0) f(z, x_0) - \mathcal{R}(0, x_m) f_0(z, x_0)) dz. \quad (8.25)$$

Note that at $x_0 = x_m$, $a_1(x_0)$ reduces to zero. Therefore, $f_0(z, x_0) = 1/\sqrt{a_2(x_m)z}$ which makes the integral (8.24) divergent at $x_0 = x_m$. However, $I_D(x_0)$ has an exact solution which is given by

$$I_D(x_0) = \mathcal{R}(0, x_m) \frac{2}{\sqrt{a_2(x_0)}} \log \frac{\sqrt{a_2(x_0)} + \sqrt{a_1(x_0) + a_2(x_0)}}{\sqrt{a_1(x_0)}}. \quad (8.26)$$

Now, we expand $a_1(x_0)$ in the following fashion

$$a_1(x_0) = \frac{2x_m a_2(x_m)}{H(x_m)} (x_0 - x_m) + O(x_0 - x_m)^2, \quad (8.27)$$

and retain the terms up to $O(x_0 - x_m)$. With this, we can re-write the integral (8.26) as

$$I_D(x_0) = -a \log \left(\frac{x_0}{x_m} - 1 \right) + \bar{b}_D + O(x_0 - x_m), \quad (8.28)$$

where a and \bar{b}_D are given by

$$a = \frac{R(0, x_m)}{\sqrt{a_2(x_m)}} \quad (8.29)$$

$$\bar{b}_D = \frac{R(0, x_m)}{\sqrt{a_2(x_m)}} \log \frac{2H(x_m)}{x_m^2}. \quad (8.30)$$

Let us now expand Eq. (8.25) in powers of $x_0 - x_m$ and retain terms up to $O(x_0 - x_m)$. With this, we will have

$$I_{\mathcal{R}}(x_0) = \int_0^1 g(z, x_m) dz + O(x_0 - x_m) \quad (8.31)$$

$$= \bar{b}_{\mathcal{R}} + O(x_0 - x_m), \quad (8.32)$$

where

$$\bar{b}_{\mathcal{R}} = I_{\mathcal{R}}(x_m). \quad (8.33)$$

Thereafter, we need to expand the Eq. (8.14) about b_m , which yields

$$b_h - b_m = P (x_0 - x_m)^2, \quad (8.34)$$

where

$$P = \frac{a_2(x_m)}{2x_m^2} \sqrt{\frac{H(x_m)}{F(x_m)^3}}. \quad (8.35)$$

With the help of equations (8.28), (8.32), and (8.34), we ultimately have the expression of the angle of deflection in terms of the impact parameter b :

$$\alpha_D(b_h) = -\bar{a} \log \left(\frac{b_h}{b_m} - 1 \right) + \bar{b} + O(b_h - b_m), \quad (8.36)$$

$$\text{where} \quad (8.37)$$

$$\begin{aligned} \bar{a} &= \frac{a}{2} = \frac{\mathcal{R}(0, x_m)}{2\sqrt{a_2(x_m)}}, \\ \bar{b} &= -\pi + \bar{b}_{\mathcal{R}} + \bar{a} \log \frac{2H^2(x_m)a_2(x_m)}{F(x_m)x_m^4}. \end{aligned} \quad (8.38)$$

What follows next is to examine the variation of strong lensing coefficients \bar{a} and \bar{b} with respect to α_h . Therefore, a graphical presentations of \bar{a} and \bar{b} with respect to α_h are given for various values of ℓ_0 .

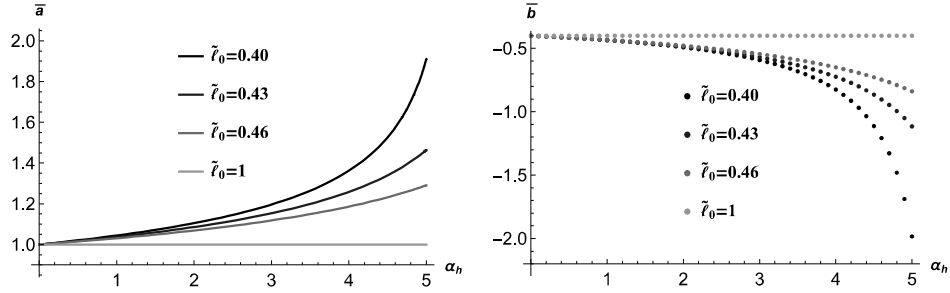


Figure 8.3: Plot showing the variation of strong lensing coefficients \bar{a} and \bar{b} with respect to α_h for various values of ℓ_0 .

A careful look at Fig. 8.3 and the table (8.1) reveals that the coefficient \bar{a} increases with the increase in α_h but it drops down with the increase in ℓ_0 . The coefficient \bar{b} , on the other hand, follows the reverse pattern to what is followed by \bar{a} . It reduces with α_h and enhances with ℓ_0 . The green line signifies its status for $\ell_0 \rightarrow 1$. The ansatz (8.2) in that case, reduces to that of the Schwarzschild black hole. In the following Fig. (8.4), the variation of deflection angle in strong gravitation lensing with respect to α_h and b is presented graphically.

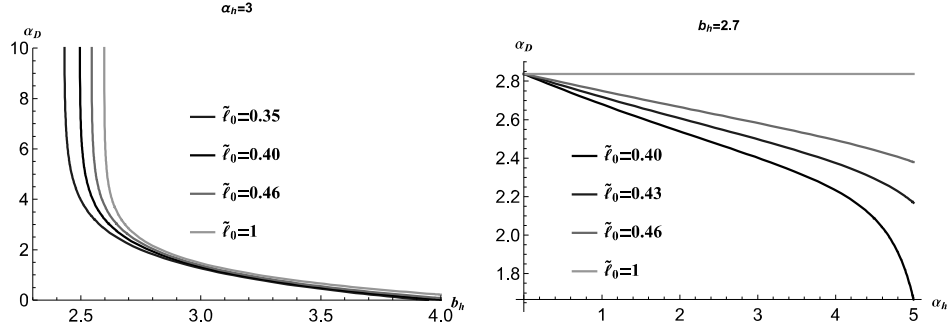


Figure 8.4: The left panel shows the variation of the deflection angle α_D with respect to the impact parameter b_h for different values of ℓ_0 with $\alpha_h = 3$. The right panel shows the variation of the deflection angle with respect to α_h with $b_h = 2.7$.

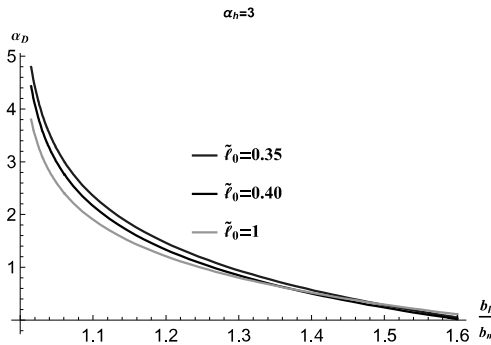


Figure 8.5: It shows the variation of the deflection angle α_D with respect to $\frac{b_h}{b_m}$ for different values of ℓ_0 with $\alpha_h = 3$.

From above plots we see that the deflection angle α_D decreases with $\tilde{\ell}_0$. It is because as we decrease $\tilde{\ell}_0$, b_m and \bar{b} decrease as it is evident from Fig. (1) and Fig. (3) and at the same time \bar{a} increases. Thus, with the help of Eq. (8.36) we can see that as we decrease $\tilde{\ell}_0$, the deflection angle α_D should decrease.

It would be beneficial to compare the lensing coefficients in the presence of hair and the absence of it in connection to the Schwarzschild black hole. It is furnished below in a tabular form in 8.1. Here $u_m = \sqrt{\frac{x_m^2}{F(x_m)}}$ and $R_s = 1$ is x_{eh} for Schwarzschild black hole. The deflection angle as a function of

α_h	ℓ_0	\bar{a}	\bar{b}	b_m/R_s	$\delta\bar{a}$	$\delta\bar{b}$	$\delta u_m/R_s$
1	0.40	1.04441	-0.435351	2.56985	0.0444121	-0.035121	-0.0282291
	0.50	1.02268	-0.429227,	2.58807	0.0226802	-0.028997	-0.0100077
	0.60	1.0077	-0.414335	2.5959	0.00769851	-0.0141049	-0.00218009
2	0.40	1.10507	-0.491267	2.53661	0.105066	-0.0910372	-0.0614685
	0.50	1.04924	-0.465694	2.57728	0.0492353	-0.0654637	-0.0207955
	0.60	1.01582	-0.429526	2.59366	0.0158171	-0.0292962	-0.00441136
3	0.40	1.19637	-0.592265	2.49574	0.196367	-0.192035	-0.102341
	0.50	1.08101	-0.512881	2.56555	0.0810136	-0.112651	-0.0325222
	0.60	1.0244	-0.445935	2.59138	0.0243984	-0.0457052	-0.00669681

Table 8.1: The lensing coefficients for the hairy Schwarzschild black holes and deviation of these coefficients from Schwarzschild black holes ($\alpha_h = 0$). Here, δ indicates the difference between the presence of hair and in its absence.

the angular separation of the image from lens θ can be written down as

$$\alpha_D(\theta) = -\bar{a} \log \left(\frac{\theta D_{OL}}{b_m} - 1 \right) + \bar{b} + O(b_h - b_m). \quad (8.39)$$

Here D_{OL} refers to the distance between the observer and the black hole. If we draw a line between the center of the black hole and the observer and draw another line between the observer and the point of minimum distance then the angle of intersection between these two lines is θ .

8.2 Observables in the strong field limit

In this section, we present derivation of the expressions for the position and magnification of relativistic images with the help of Eq. (8.39) and the lens equation derived in the article [262]. The substantial information in the article [262] enables us to write down the lens equation for the present situation. The angular separation between the source and the lens $\tilde{\eta}$ is given by

$$\tilde{\eta} = \theta - \frac{D_{LS}}{D_{OS}} \Delta\alpha_n. \quad (8.40)$$

where D_{LS} is the lens to source distance, $D_{OS} = D_{OL} + D_{LS}$ is the distance between the observer to source, and $\Delta\alpha_n = \alpha_s(\theta) - 2n\pi$ is the offset of the deflection angle. By the positive integer number n the winding number of loops around the black hole is designated here.

We are now in a position to calculate the offset angle. We, therefore, need to find the angle θ_n^0 which is the solution of the equation

$$\alpha_s(\theta) = 2n\pi. \quad (8.41)$$

The solution is given by

$$\theta_n^0 = \frac{b_m}{D_{OL}} (1 + e_n), \quad (8.42)$$

8.2. OBSERVABLES IN THE STRONG FIELD LIMIT

$$e_n = e^{\frac{\bar{b}-2n\pi}{\bar{a}}}. \quad (8.43)$$

Thereafter, we consider $\Delta\theta_n = \theta - \theta_n^0$ and expand $\alpha_s(\theta)$ around $\theta = \theta_n^0$ in order to compute offset angle. Ultimately, we land onto the following desired expression of the offset angle.

$$\Delta\alpha_n = -\frac{\bar{a}D_{OL}}{b_me_n}\Delta\theta_n. \quad (8.44)$$

If we use the expression $\theta = \theta_n^0 + \Delta\theta_n$ in Eq. (8.40) we obtain the final algebraic expression for $\tilde{\eta}$:

$$\tilde{\eta} = \theta_n^0 + \Delta\theta_n + \left(\frac{\bar{a}D_{OL}}{b_me_n} \frac{D_{LS}}{D_{OS}} \right) \Delta\theta_n. \quad (8.45)$$

Since the condition $b_m \ll D_{OL}$ holds for physically acceptable cases, we can neglect the second term in the above equation in comparison to the last term. Hence, the position of the n^{th} image is expressed by [261]

$$\theta_n = \theta_n^0 + \frac{b_me_n(\eta - \theta_n^0)D_{OS}}{\bar{a}D_{LS}D_{OL}}. \quad (8.46)$$

When $\tilde{\eta} = \theta_n^0$ the position of the image and the source coincide. It implies that the n^{th} image has not acquired any correction. Therefore, Eq. (8.46) will describe an image on the same side where the source is standing. To get the position of the image on the other side of the source, we need to replace $\tilde{\eta}$ with $-\tilde{\eta}$.

The study of the magnification of the images is also instructive. Magnification of the images is another good source of information [261], in addition to the position of the source. The magnification of the image is given by

$$\mu_n = \left(\frac{\tilde{\eta}}{\theta} \frac{d\tilde{\eta}}{d\theta} \bigg|_{\theta_n^0} \right)^{-1} \quad (8.47)$$

$$= e_n \frac{b_m^2(1+e_n)D_{OS}}{\bar{a}\tilde{\eta}D_{OL}^2D_{LS}} \quad (8.48)$$

It is transparent from the Eq. (8.48) that the magnification decreases with an increase in n . It is beneficial to consider a special situation where the outermost single-loop image θ_1 is assumed to appear (resolved) as a single image, while all the other inner-packed images are considered to be clubbed together at θ_∞ . Three observables which are necessary to consider here are given by

$$\theta_\infty = \frac{b_m}{D_{OL}}, \quad (8.49)$$

$$s = \theta_1 - \theta_\infty = \theta_\infty e^{\frac{\bar{b}-2\pi}{\bar{a}}}, \quad (8.50)$$

$$r = \frac{\mu_1}{\sum_{n=2}^{\infty} \mu_n} = e^{\frac{2\pi}{\bar{a}}}, \quad r_{\text{mag}} = 2.5 \log(r) = \frac{5\pi}{\bar{a} \ln 10}. \quad (8.51)$$

Here, θ_∞ gives the position of the innermost packed images, s gives the angular separation between the first image and the others and r gives the ratio of the flux from the first image to those from the remaining images. It must be noted that, although θ_∞ and s depend on the distance between black hole and the observer, r_{mag} does not depend on that.

Now, we consider the supermassive black holes *SgrA** and *M87** in order to calculate lensing observables for these black holes using the ansatz (8.2). The mass of the *SgrA** and *M87** black holes are $3.98 \times 10^6 M_\odot$ and $(6.5 \pm 0.7) \times 10^9 M_\odot$ respectively and the distance of these two from the Earth, D_{OL} , are 7.97 Mpc and $(16.8 \pm 0.8) \text{ Mpc}$ respectively [108, 109].

Fig.8.6 demonstrate the variation of lensing observables with respect to α_h for different values of ℓ_0 for the *SgrA** and *M87** black holes. We can infer from the plots that θ_∞ and $r(\text{mag})$ decrease with the increase in α_h , whereas these two increase with an increase in ℓ_0 . The lensing observable s

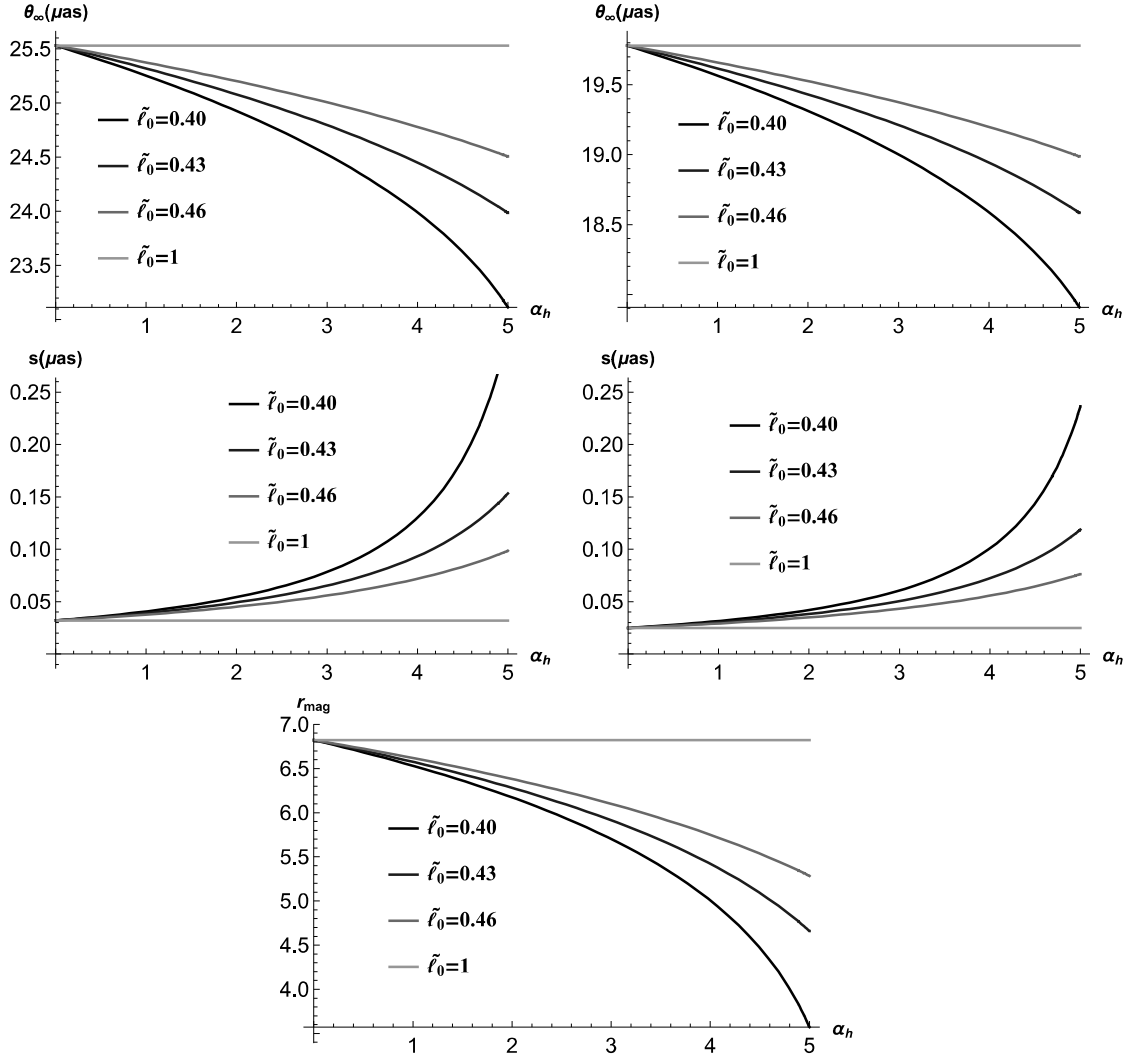


Figure 8.6: Lensing observables, θ_∞ , r_{mag} , and s as a function of α_h for $Sgr A^*$ (left panel) and $M87^*$ (right panel) black holes.

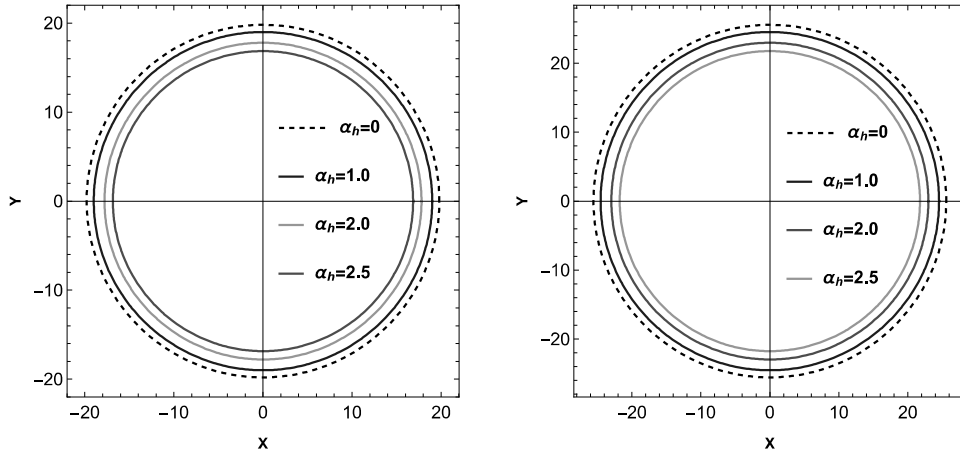


Figure 8.7: Plots showing the outermost Einstein Rings. The left one is for $M87^*$ and the right one is for $Sgr A^*$. Here we have taken $\ell_0 = 0.2$

α_h	ℓ_0	Sgr A*		M87*		r_{mag}
		$\theta_\infty (\mu as)$	$s (\mu as)$	$\theta_\infty (\mu as)$	$s (\mu as)$	
1	0.40	25.2524	0.0406027	19.5651	0.0314583	6.53179
	0.50	25.4314	0.0358804	19.7038	0.0277995	6.67059
	0.60	25.5084	0.033129	19.7634	0.0256677	6.76976
2	0.40	24.9258	0.0542333	19.312	0.042019	6.17328
	0.50	25.3254	0.0407468	19.6217	0.0315698	6.50177
	0.60	25.4864	0.0343882	19.7464	0.0266433	6.71566
3	0.40	24.5241	0.078294	19.0008	0.0606608	5.70217
	0.50	25.2102	0.0469109	19.5324	0.0363457	6.31063
	0.60	25.464	0.0357364	19.729	0.0276879	6.6594

Table 8.2: Strong-lensing observables for the black hole *Sgr A** and *M87**.

increases with respect to α_h and decreases with respect to ℓ_0 . The table (8.2) shows some values of lensing observables for the *Sgr A** and *M87** black holes.

Let us consider a special case called Einstein Ring which is associated with gravitational lensing. It is created when light from a galaxy or star after passing through the close vicinity of a massive object finds its way toward the Earth. The light gets diverted due to gravitational lensing and it appears that it is coming from different places. In this case, if the source, lens, and observer are all in perfect alignment, the light appears as a ring. We obtain the Einstein Ring when we have perfect alignment, i.e. when $\tilde{\eta} = 0$ [260]. Solving the Eq. (8.46) for $\tilde{\eta} = 0$ we get

$$\theta_n^E = \left(1 - \frac{b_m e_n D_{OS}}{\bar{a} D_{LS} D_{OL}}\right) \theta_n^0, \quad (8.52)$$

where θ_n^E is the position of the n th Einstein ring. Considering the case where the lens is midway between source and observer, i.e., $D_{OS} = 2D_{OL}$ and considering $D_{OL} \gg b_m$, from Eq. (8.52) we find that

$$\theta_n^E = \frac{b_m}{D_{OL}} (1 + e_n). \quad (8.53)$$

It is the angular radius of the n_{th} relativistic Einstein Ring. For $n = 1$ we display Einstein rings for *Sgr A** and *M87** in Fig. (8.7).

Fig. (8.7) shows that the radius decreases with an increase in α_h for both black holes. So, the angular radius of Einstein Rings shows a crucial dependence on the hair parameter.

8.3 Time delay

In this section, we study the time delay between relativistic images for various black holes. The time delay causes due to the different paths that photons take while winding the black hole. Here, we follow the method developed by Bozza and Manchini [263] to study time delay. The time taken by a photon to reach an observer at infinity from the source is given by [263]

$$\tilde{T}(u) = -\tilde{a} \log \left(\frac{b_h}{b_m} - 1 \right) + \tilde{b} + \mathcal{O}(b_h - b_m), \quad (8.54)$$

where

$$\tilde{a} = \frac{\tilde{R}(0, x_m)}{2\sqrt{a_2(x_m)}} \quad (8.55)$$

$$\tilde{b} = -\pi + \tilde{b}_D + \tilde{b}_R + \tilde{a} \log \frac{Px_m^2}{b_m} \quad (8.56)$$

with

$$\begin{aligned} \tilde{R}(z, x_0) &= 2 \frac{1 - F(x_0)}{F'(x)} \sqrt{F(x_0)} \left(1 - \frac{1}{\sqrt{F(x_0)} f(z, x_0)} \right) \\ \tilde{b}_D &= 2\tilde{a} \log \frac{2(1 - F(x_m))}{F'(x_m)x_m} \\ \tilde{b}_R &= \int_0^1 \left[\tilde{R}(z, x_m) f(z, x_m) - \tilde{R}(0, x_m) f_0(z, x_m) \right] dz. \end{aligned} \quad (8.57)$$

Using the Eq. (8.54) we can calculate the time difference between two relativistic images. The images are highly demagnified and they are separated by a distance of the order of μas . Here we consider the time delay between the first and second relativistic image assuming that the two images are on the same side of the source. The time delay is given by [263]

$$\Delta T_{2,1} = 2\pi b_m = 2\pi D_{OL} \theta_\infty. \quad (8.58)$$

It is useful at this stage to study the time delay corresponding to different black holes sitting at the center of the neighbouring galaxies. In this context, we furnish the time delay of a few black holes in tabular form in 8.3 where we have taken $\ell_0 = 0.2$. This is all about strong gravitational lensing in connection to the hairy Schwarzschild black hole. From our study, it has transpired that the strong lensing effect gets considerably influenced by the hair parameter α_h . Let us now turn to its effect on the weak gravitational lensing.

8.4 Weak gravitational lensing

For the sake of a complete study on gravitational lensing, we should also bring the weak lensing scenarios into our consideration. This section is therefore devoted to studying weak lensing associated with this black hole. We, therefore, proceed to deduce the deflection angle in the weak field limit using the Gauss-Bonnet theorem. This method was first proposed by Gibbons and Werner in their seminal work [264]. Let us assume that the black hole (L) is sitting at the center of the coordinate system. The receiver (R) and the source (S) are at finite distances from the black hole (L). Following the earlier works [268, 269] and the assumption employed there, the deflection angle can be written down as

$$\gamma_D = \psi_R - \psi_S + \phi_{OS}, \quad (8.59)$$

where $\phi_{OS} = \phi_O - \phi_S$ is the angular separation between observer and source, ψ_R is the angle subtended by the light rays at the receiver (R) and ψ_S is the angle that is made by light rays at the source (S). Now, we consider the quadrilateral $\infty \square_S^\infty$. It consists of spatial light ray curves from the source (S) to the observer (O), a circular arc segment C_r , and two outgoing radial lines from the observer O and the source S . Please vide the Fig. (8.8). Consequently, the angle of deflection is given by

$$\gamma_D = - \int \int_{\infty \square_S^\infty} K dS, \quad (8.60)$$

where K is the Gaussian curvature. For null geodesics we have $ds^2 = 0$ and thus, from Eq. (8.2) we have

$$dt = \pm \sqrt{\zeta_{ij} dx^i dx^j}, \quad (8.61)$$

Galaxy	$M(M_\odot)$	D_{OL} (Mpc)	M/D_{OL}	$\Delta T_{2,1}$	$\Delta T_{2,1}$	$\Delta T_{2,1}$
				$\alpha_h = 0$	$\alpha_h = 1.0$	$\alpha_h = 1.5$
Milky Way	4.3×10^6	0.0083	2.471×10^{-11}	11.4967	11.0193	10.702
M87	6.5×10^9	16.8	1.846×10^{-11}	17378.7	16657.1	16177.5
NGC 4472	2.54×10^9	16.72	7.246×10^{-12}	6791.06	6509.07	6321.66
NGC 1332	1.47×10^9	22.66	3.094×10^{-12}	3930.26	3767.06	3658.6
NGC 4374	9.25×10^8	18.51	2.383×10^{-12}	2473.12	2370.43	2302.18
NGC 1399	8.81×10^8	20.85	2.015×10^{-12}	2355.48	2257.67	2192.67
NGC 3379	4.16×10^8	10.70	1.854×10^{-12}	1112.24	1066.05	1035.36
NGC 4486B	6×10^8	16.26	1.760×10^{-12}	1604.19	1537.58	1493.3
NGC 1374	5.90×10^8	19.57	1.438×10^{-12}	1577.45	1511.95	1468.42
NGC 4649	4.72×10^9	16.46	1.367×10^{-12}	12619	12095.6	11747.3
NGC 3608	4.65×10^8	22.75	9.750×10^{-13}	1243.25	1191.62	1157.31
NGC 3377	1.78×10^8	10.99	7.726×10^{-13}	475.909	456.148	443.014
NGC 4697	2.02×10^8	12.54	7.684×10^{-13}	540.077	517.651	502.746
NGC 5128	5.69×10^7	3.62	7.498×10^{-13}	152.131	145.813	141.615
NGC 1316	1.69×10^8	20.95	3.848×10^{-13}	451.816	433.084	420.614
NGC 3607	1.37×10^8	22.65	2.885×10^{-13}	366.265	351.08	340.971
NGC 4473	0.90×10^8	15.25	2.815×10^{-13}	240.628	230.636	223.996
NGC 4459	6.96×10^7	16.01	2.073×10^{-13}	186.086	178.359	173.223
M32	2.45×10^6	0.8057	1.450×10^{-13}	6.5504	6.27844	6.09766
NGC 4486A	1.44×10^7	18.36	3.741×10^{-14}	38.5005	36.9018	35.8393
NGC 4382	1.30×10^7	17.88	3.468×10^{-14}	34.7574	33.3141	32.3549

Table 8.3: Estimation of time delay for various black holes at the center of nearby galaxies. Mass (M) and distance (D_{OL}) are given in the units of solar mass and Mpc, respectively. Time Delays are expressed in minutes.

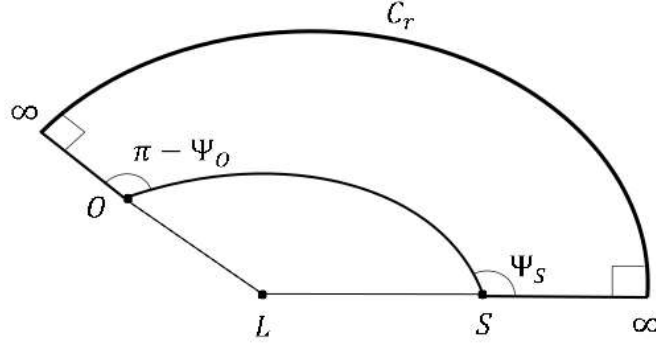
with the following expression of $\zeta_{ij}dx^i dx^j$

$$\zeta_{ij}dx^i dx^j = \frac{1}{f(r)^2} dr^2 + \frac{r^2}{f(r)} (d\theta^2 + \sin^2 \theta d\phi^2). \quad (8.62)$$

We now need the expression of Gaussian curvature of the surface where light propagation is taking place. It is defined by [270]

$$\begin{aligned} K &= \frac{{}^3R_{r\phi r\phi}}{\zeta}, \\ &= \frac{1}{\sqrt{\zeta}} \left(\frac{\partial}{\partial \phi} \left(\frac{\sqrt{\zeta}}{\zeta_{rr}} {}^{(3)}\Gamma_{rr}^\phi \right) - \frac{\partial}{\partial r} \left(\frac{\sqrt{\zeta}}{\zeta_{rr}} {}^{(3)}\Gamma_{r\phi}^\phi \right) \right), \end{aligned} \quad (8.63)$$

where $\zeta = \det(\zeta_{ij})$. For the hairy Schwarzschild black hole metric (8.2), in the weak-field limits, Eq.

Figure 8.8: Schematic diagram of the quadrilateral $\infty_O \square_S^\infty$.

(8.63) with the leading order terms reads

$$K = \frac{3M^2}{r^4} - \frac{2M}{r^3} + \alpha_h \left(-\frac{2Me^{-\frac{r}{M-\frac{\ell_0}{2}}}}{r^3} + \frac{Me^{-\frac{r}{M-\frac{\ell_0}{2}}}}{r^2 \left(M - \frac{\ell_0}{2}\right)} - \frac{Me^{-\frac{r}{M-\frac{\ell_0}{2}}}}{r \left(M - \frac{\ell_0}{2}\right)^2} + \frac{e^{-\frac{r}{M-\frac{\ell_0}{2}}}}{2 \left(M - \frac{\ell_0}{2}\right)^2} \right) + \mathcal{O} \left(\frac{\alpha_h^2}{\left(M - \frac{\ell_0}{2}\right)^2} \right) \quad (8.64)$$

The surface integral of Gaussian curvature over the closed quadrilateral $\infty_O \square_S^\infty$ has the expression [272]

$$\int \int_{\infty_O \square_S^\infty} K dS = \int_{\phi_S}^{\phi_O} \int_{\infty}^{r_0} K \sqrt{\zeta} dr d\phi, \quad (8.65)$$

where r_0 refers to the distance of the closest approach to the black hole. Because of the exponential term we cannot get a closed form of the angle of deflection. Thus, we evaluate them numerically. First assuming that the light rays follow a straight-line trajectory, i.e., $r = \frac{b_h}{\sin \phi}$, we calculate the angle of deflection γ_D^0 . An improved article [273] surfaced later. In order to include the higher-order corrections, we take the trajectory

$$u = \frac{\sin \phi}{b_h} + \frac{M(1 - \cos \phi)^2}{b_h^2} - \frac{M^2(60\phi \cos \phi + 3 \sin 3\phi - 5 \sin \phi)}{16b_h^3} + \mathcal{O} \left(\frac{M^2 \alpha_h}{b_h^5} \right), \quad (8.66)$$

where $u = \frac{1}{r}$, and b_h is the impact parameter as usual. We can now recast the integral Eq. (8.65) in the following form

$$\int \int_{\infty_O \square_S^\infty} K dS = \int_0^{\pi + \gamma_D^0} \int_0^u -\frac{K \sqrt{\zeta}}{u^2} du d\phi. \quad (8.67)$$

Next, we evaluate above expression numerically. Before closing our discussion we furnish a graphical presentation of variation of deflection with the impact parameter in the weak gravitational field limit.

8.4. WEAK GRAVITATIONAL LENSING

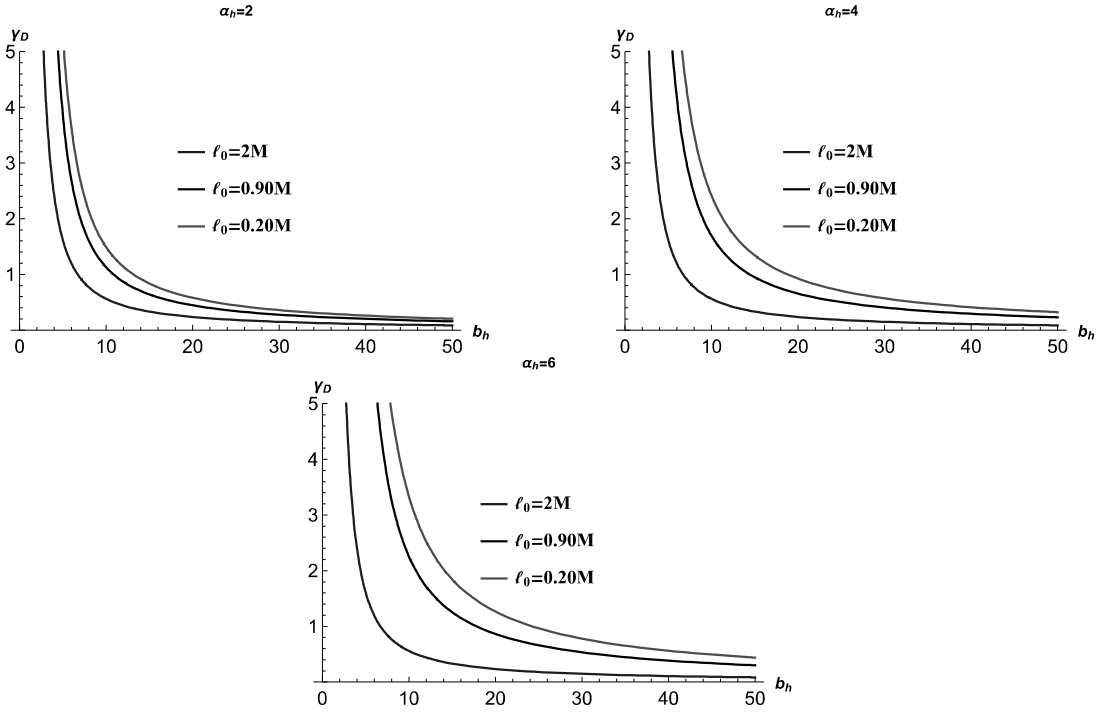


Figure 8.9: Deflection angle for weak gravitational lensing. The upper left panel is for $\alpha_h = 2$, the upper right panel is for $\alpha_h = 4$, and the lower panel is for $\alpha_h = 6$. $M = 1$ is set for computation.

The plots transpire that the deflection angle in weak gravitational lensing decreases with the impact parameter b_h but increases with α_h and decreases with ℓ_0 . It is important to note that hair has a significant influence on lensing scenarios both for the strong gravity field and its weak limit. We also give a table which clearly shows that γ_D increases with α_h but decreases with ℓ_0 . As we put $\ell_0 = 2M$ we recover the value for Schwarzschild black hole.

α_h	ℓ_0/M	γ_D
2	0.20	1.48676
	0.90	1.12654
	2.00	0.56048
4	0.20	2.41303
	0.90	1.69259
	2.00	0.56048
6	0.20	3.33931
	0.90	2.25865
	2.00	0.56048

Table 8.4: Angle of deflection for various values of α_h and ℓ_0 . Here we have taken the impact parameter $b_h = 10$.

References

- [1] C. M. Will, Living Rev. Rel. 17, 4 (2006).
- [2] I. H. Stairs, Living Rev. Rel. 6, 5 (2003).
- [3] B. P. Abbott et al. (Virgo, LIGO Scientific), Phys. Rev. Lett. 116, 061102 (2016).
- [4] B. P. Abbott et al. (Virgo, LIGO Scientific), Annalen der Physik 529, 1600209 (2017).
- [5] B. S. Sathyaprakash and B. F. Schutz, Living Rev. Rel. 12, 2 (2009).
- [6] J. R. Gair, M. Vallisneri, S. L. Larson, and J. G. Baker, Living Rev. Rel. 16, 7 (2013).
- [7] H. Nakano, T. Tanaka, and T. Nakamura, Phys. Rev. D 92, 064003 (2015).
- [8] A. D. Sakharov, Dokl. Ak
- [9] V. Sahni and A. A. Starobinsky, Int. J. Mod. Phys. D 9, 373 (2000).
- [10] T. Padmanabhan, Phys. Rept. 380, 235 (2003).
- [11] P. J. E. Peebles and B. Ratra, Rev. Mod. Phys. 75, 559 (2003),
- [12] G. Amelino-Camelia, J.R. Ellis, N.E. Mavromatos, D.V. Nanopoulos, Int. J. Mod. Phys. A 12 (1997) 607.
- [13] J.R. Ellis, N.E. Mavromatos, D.V. Nanopoulos, Phys. Lett. B 293 (1992) 37. Available from: ; For reviews see: J.R. Ellis, N.E. Mavromatos, D.V. Nanopoulos, Erice Subnucl. Phys. Series 31 (1) (1994). Available from: (World Sci.); J.R. Ellis, N.E. Mavromatos, D.V. Nanopoulos, J. Chaos Soliton. Fract. 10 (1999) 345.
- [14] R. Gambini, J. Pullin, Phys. Rev. D 59 (1999) 124021. Available from: ; J. Alfaro, H.A. Morales-Tecotl, L.F. Urrutia, Phys. Rev. D 65 (2002) 103509. Available from:
- [15] V. A. Kostelecky and S. Samuel, Phys. Rev. D 39 683 (1989).
- [16] G. Amelino-Camelia, Int. J. Mod. Phys. D 11 (2002) 35. Available from: .
- [17] R.C. Myers, M. Pospelov, Phys. Rev. Lett. 90 (2003) 211601. Available from: .
- [18] G. Amelino-Camelia, J. Ellis, N. Mavromatos, D. Nanopoulos S. Sarkar, Nature 393 (1998) 763.
- [19] S.D. Biller et al., Phys. Rev. Lett. 83 (1999) 2108.
- [20] B.E. Schafer, Phys. Rev. Lett. 82 (1999) 4964.
- [21] S.E. Boggs, C.B. Wunderer, K. Hurley, W. Coburn, Astrophys. J. 611 (2004) L77. Available from:
- [22] P. Kaaret. Available from: .
- [23] T. Jacobson, S. Liberati, D. Mattingly, Phys. Rev. D 66 (2002) 081302. Available from: .

- [24] J. Alfaro, G. Palma, Phys. Rev. D 67 (2003) 083003. Available from: ; F.W. Stecker, S.L. Glashow, Astropart. Phys. 16 (2001) 97. Available from: ; S.R. Coleman, S.L. Glashow, Phys. Rev. D 59 (1999) 116008. Available from:
- [25] V.A. Kostelecky, M. Mewes, Phys. Rev. D 66 (2002) 056005.
- [26] R. P. Kerr, Phys. Rev. Lett. 11, 237 (1963).
- [27] R. Penrose: Riv. Nuovo Cim. 1, 252 (1969).
- [28] R. M. Wald, Phys. Rev. D 48, R3427 (1993).
- [29] P. J. Young, Phys. Rev. D 14, 3281 (1976).
- [30] J. M. Bardeen, W. H. Press and S. A. Teukolsky, Astro-phys. J. 178, 347 (1972).
- [31] A. Sen. Phys.Rev.Lett.69 1006 (1992)
- [32] K. Hioki and K. I. Maeda, Phys. Rev. D 80, 024042 (2009)
- [33] S. Hawking, Commun.Math.Phys. 43 (1975) 199
- [34] S.-W. Wei and Y.-X. Liu, J. Cosmol. Astropart. Phys. 11 063 (2013).
- [35] U. Papnoi, F. Atamurotov, S. G. Ghosh, B. Ahmedov: Phys. Rev. D 90, 024073 (2014).
- [36] A. Abdujabbarov, M. Amir, B. Ahmedov, S. G. Ghosh: Phys. Rev. D 93, 104004 (2016)
- [37] V. A. Kostelecky, S. Samuel: Phys. Rev. Lett. 63, 224 (1989).
- [38] V. A. Kostelecky and S. Samuel: Phys. Rev. D 40, 1886 (1989)
- [39] D. Colladay and V. A. Kostelecky, Phys. Rev. D 55, 6760 (1997).
- [40] V. A. Kostelecky and R. Potting, Phys. Lett. B 381 (1996) 89
- [41] D. Colladay and V. A. Kostelecky, Phys. Rev. D 55 (1997) 6760
- [42] D. Colladay and V. A. Kostelecky, Phys. Rev. D 58 (1998) 116002
- [43] S. R. Coleman and S. L. Glashow, Phys. Rev. D 59 (1999) 116008
- [44] R. Casana, A. Cavalcante, F. P. Poulis, E. B. Santos: Phys. Rev. D 97, 104001 (2018)
- [45] S. Mignemi, R. Strajn: Phys.Rev. D90 044019 (2014)
- [46] H.S. Snyder: Phys. Rev. 71 38 (1947)
- [47] B. Ivetic, S Meljanac, S Mignemi: Class. Quantum Grav. 31 105010 (2014)
- [48] C. Ding, C. Liu, R. Casana, A. Cavalcante C80 178 (2020)
- [49] A. H. Klotz, Gen. Rel. Grav. 14, 727 (1982);
- [50] S. Kanzi, I. Sakalli: EPJC Doi:10.1140/epjc/s10052-022-10044-2
- [51] P. Nicolini, Int. J. Mod. Phys. A 24 (2009) 1229
- [52] R.J. Szabo, Class. Quantum Gravity 23 (2006) R199
- [53] A. Smailagic, E. Spallucci, J. Phys. A 36 (2003) L467
- [54] P. Nicolini, A. Smailagic, E. Spallucci: Phys. Lett. B 632, 547-551 (2006).
- [55] K. Nozari, S.H. Mehdipour, Class. Quantum Gravity 25 (2008) 175015

- [56] K. Nozari and S. H. Mehdipour: *Class. Quant. Grav.* 25, 175015 (2008)
- [57] M. A. Anacleto, F. A. Brito, J. A. V. Campos, E. Passos: *Phys. Lett. B* 803, 135334 (2020)
- [58] F. Atamurotov, B. Ahmedov, A. Abdujabbarov: *Phys. Rev. D* 92, 084005 (2015).
- [59] X. G. Lan. and J. Pu: *Mod. Phys. Lett A* 33, 1850099 (2018)
- [60] Shao-Wen Wei, Yu-Xiao Liu: *JCAP* 11, 063 (2013)
- [61] V. Perlick, O. Y. Tsupko: *Phys. Rev. D* 95, 104003 (2017).
- [62] A. Abdujabbarov, B. Toshmatov, Z. Stuchlik, B. Ahmedov: *Int. Jour. Mod. Phys. D* 26, 1750051 (2017)
- [63] G. Z. Babar, A. Z. Babar, F. Atamurotov: *Euro. Phys. Jour. C* 80, 761 (2020).
- [64] B. Mashhoon, *Phys. Rev. D* 7, 2807 (1973)
- [65] A. Abdujabbarov, M. Amir, B. Ahmedov, S. G. Ghosh: *Phys. Rev. D* 93, 104004 (2016)
- [66] Y. X. Gui, J. G. Zhang, Y. Zhang and F. P. Chen, *Acta Phys. Sin.* 33, 1129 (1984).
- [67] R. Casana and A. Cavalcante: *Phys. Rev. D* 97, 104001 (2018).
- [68] S. W. Wei, P. Cheng, Y. Zhong and X. N. Zhou, *J. Cos. Astro. Phys.* 08, 004 (2015).
- [69] T. Tao, Q. Wu, M. Jamil and K. Jusufi, *Phys. Rev. D* 100, 044055 (2019).
- [70] A. A. Starobinsky, S. M. Churilov: *Zh. Eksp. Teor. Fiz.* 65, 3 (1973)
- [71] A. A. Starobinsky: *Zh. Eksp. Teor. Fiz.* 64, 48 (1973)
- [72] R. Uniyala, H. Nandanb K. D. Purohit: *Class.Quant.Grav.* 35 025003 (2018)
- [73] D. O. Muhleman, I. D. Johnston, *Phys. Rev. Lett.* 17, 455 (1966)
- [74] D. O. Muhleman, R. D. Ekers, E. D. Fomalont, *Phys. Rev. Lett.* 24, 1377 (1970)
- [75] G. S. Bisnovatyi-Kogan and O. Y. Tsupko: *Mon. Not. R. Astron. Soc.* 404 1790 (2010)
- [76] S. K. Jha, A. Rahaman: *Eur. Phys. J. C* (2021) 81:345
- [77] J. L. Synge: *MNRAS* 131 463 1966.
- [78] F. Atamurotov, B. Ahmedov and A. Abdujabbarov *Phys. Rev. D* 92 084005 (2015)
- [79] A. Rogers, *Mon. Not. Roy. Astron. Soc.* 451 17 (2015).
- [80] G. Z. Babarr, A. Z. Babar, F. Atamurotov: *Eur.Phys.J. C* 80 761 (2020)
- [81] O. Y. Tsupko and G. S. Bisnovatyi-Kogan, *Gravitation and Cosmology* 20, 220 (2014).
- [82] A. Abdujabbarov, B. Toshmatov, J. Schee, Z. Stuchlik, B. Ahmedov, *Int. J. Mod. Phys. D* 26 1741011 (2017).
- [83] O. Y. Tsupko and G. S. Bisnovatyi-Kogan, *Gravitation and Cosmology* 18, 117 (2012).
- [84] O. Y. Tsupko and G. S. Bisnovatyi-Kogan, *Gravitation and Cosmology* 15, 184 (2009).
- [85] V. S. Morozova, B. J. Ahmedov and A. A. Tursunov, *Astrophys. Space Sci.* 346, 513 (2013).
- [86] R. Dicke, *Coherence in Spontaneous Radiation Processes*, *Phys.Rev.* 93 (1954) 99-110.
- [87] Y. B. Zel'dovich *Pis'ma Zh. Eksp. Teor. Fiz.* 14 (1971) 270 [*JETP Lett.* 14, 180 (1971)].

- [88] Y. B. Zel'dovich Zh. Eksp. Teor. Fiz 62 (1972) 2076 [Sov.Phys. JETP 35, 1085 (1972)].
- [89] J. Bekenstein, Extraction of energy and charge from a black hole, Phys.Rev. D7 (1973) 949-953.
- [90] W. H. Press, Saul A. Teukolsky: Astrophysical. Journal 185649(1973)
- [91] S. A. Teukolsky: Phys. Rev. Lett. 29 1114, (1972)
- [92] S. A. Teukolsky, W. H. Press: Astrophys. J. 193 443 (1974)
- [93] R. Brito, V. Cardoso, P. Pani: Lecture Notes in Physics (2nd edition) 971 (2020)
- [94] A. Arvanitaki, S. Dimopoulos, S. Dubovsky, N. Kaloper, and J. March-Russell, Phys.Rev. D81(2010) 123530,
- [95] A. Arvanitaki, S. Dubovsky, Phys.Rev. D83 (2011) 044026,
- [96] P. Pani, V. Cardoso, L. Gualtieri, E. Berti, A. Ishibashi, Phys.Rev.Lett. 109 (2012) 131102,
- [97] R. Brito, V. Cardoso, P. Pani, Phys. Rev. D88 (2013) 023514
- [98] C. A. R. Herdeiro and E. Radu, Phys.Rev.Lett. 112 (2014) 221101,
- [99] V. Cardoso and O. J. Dias, Phys.Rev. D70 (2004) 084011,
- [100] V. B. Bezerra , H. S. Vieira, A. A. Costa: Class.Quantum Grav. 31 045003 (2014)
- [101] G. V. Kraniotis: Class.Quant.Grav. 33 225011 (2016)
- [102] D. N. Page: Phys. Rev. D13 198 (1976)
- [103] Ran Li: Phys. Lett. B714 337 (2012)
- [104] M. Khodadi: Phys.Rev. D103, 064051 (2021)
- [105] M. Khodadi, R. Pourkhodabakhshi: Phys. Lett. B823 136775(2021)
- [106] M. Khodadi, A. Talebian, H. Firouzjahi arXiv:2002.10496
- [107] S. Hod, Phys. Lett. B 708 (2012) 320 [arXiv:1205.1872 [gr-qc]].
- [108] K. Akiyama et al.: Astrophys. J. 875, L1 (2019).
- [109] K. Akiyama et al.: Astrophys. J. 875, L2 (2019).
- [110] K. Akiyama et al.: Astrophys. J. 875, L3 (2019).
- [111] K. Akiyama et al.: Astrophys. J. 875, L4 (2019).
- [112] K. Akiyama et al.: Astrophys. J. 875, L5 (2019).
- [113] K. Akiyama et al.: Astrophys. J. 875, L6 (2019).
- [114] C. Bambi, K. Freese, S. Vagnozzi, L. Visinelli: Phys.Rev.D100 044057 (2019).
- [115] T. Johannsen and D. Psaltis, Astrophys. J. 718, 446 (2010).
- [116] K. Gebhardt, J. Adams, D. Richstone, T. R. Lauer, S. M. Faber, K. Gultekin, J. Murphy, S. Tremaine: Astrophys.J. 729, 119 (2011)
- [117] R. Nemmen: Astrophys J. Letts L26 880 (2019)
- [118] S. K. Jha, H. barman, A. Rahaman:: JCAP04 (2021) 036
- [119] S. K. Jha, S. Aziz, A. Rahaman: Eur. Phys. J. C (2022) 82:106

- [120] S. K. Jha, A. Rahaman: Eur. Phys. J. C (2022) 82:411
- [121] S. K. Jha, A. Rahaman: Eur. Phys. J. C (2022) 82:728
- [122] I. Banerjee, S. Chakraborty, S. Sengupta: Phys. Rev. D101, 041301 (2020).
- [123] A. Abdujabbarov, F. Atamurotov, Y. Kucukakca, B. Ahmedov, U. Camci, Astrophys. Space Sci. 344 429. (2013)
- [124] O. J. Dias, P. Figueras, S. Minwalla, P. Mitra, R. Monteiro, et al. JHEP 1208(2012) 117
- [125] O. J. Dias, G. T. Horowitz, and J. E. Santos, JHEP 1107 (2011) 115,
- [126] L. Amarilla, E. F. Eiroa and G. Giribet: Phys. Rev. D. 81 124045 (2010).
- [127] S. Bhattacharyya, S. Gangopadhyay, A. Saha: Class.Quant.Grav. 36 055006 (2019)
- [128] F. Atamurotov, B. Ahmedov and A. Abdujabbarov: Phys. Rev. D. 88 064004 (2013)
- [129] Zonghai Li, G. Zhang, A. Ovgun Phys. Rev. D101, 124058 (2020)
- [130] Zonghai Li, Ali Ovgun Phys. Rev. D101, 024040 (2020)
- [131] S. Kanzi, I. Sakalli Nucl.Phys. B946, 114703 2019
- [132] A. Ovgun, K. Jusufi, I. Sakalli Phys. Rev. D99, 024042 (2019)
- [133] V. A. Kostelecky and S. Samuel: Phys. Rev. Lett. 63, 224 (1989);
- [134] V. A. Kostelecky and S. Samuel, Phys. Rev. D 39, 683 (1989); Phys. Rev. D 40, 1886 (1989).
- [135] Carlos A. Benavides-Gallego, A. A. Abdujabbarov, Cosimo Bambi: Eur. Phys. J. C78 694 (2018)
- [136] S. Carroll: Spacetime and Geometry an Introduction to Special Relativity: Cambdridge University Press 2019
- [137] S. Chandrasekhar, The Mathematical Theory of Black Holes, Oxford University Press, New York, (1992)
- [138] C. B Luo, F. Y. Hou, Z. F Cui, X. J. Liu, H. S. Zong: Phys.Rev. D91 036009 (2015)
- [139] C. W. Misner, K. S. Thorne, and I. A. Wheeler, Gravitation, Freeman, San Francisco (1973).
- [140] S. Dastan, R. Saffari, S. Soroushfar: arXiv:1610.09477
- [141] D. Mattingly, Living Rev. Rel. 8, 5 (2005).
- [142] D. Colladay and P. McDonald, Phys. Rev. D 79, 125019 (2009)
- [143] V. E. Mouchrek-Santos and M. M. Ferreira, Jr., Phys. Rev. D 95, 071701(R) (2017)
- [144] D. Psaltis, et al, Event Horizon Telescope, Phys. Rev. Lett. 125, 14 141104, 2020,
- [145] K. Bakke and H. Belich, Eur. Phys. J. Plus 129: 147 (2014)
- [146] S. Carroll, G.B. Field, and R. Jackiw: Phys. Rev. D 41, 1231 (1990).
- [147] C. Adam and F. R. Klinkhamer, Nucl. Phys. B 607, 247 (2001)
- [148] W. F. Chen and G. Kunstatter, Phys. Rev. D 62, 105029 (2000)
- [149] C. D. Carone, M. Sher, M. Vanderhaeghen: Phys. Rev. D74, 077901 (2006).
- [150] F.R. Klinkhamer and M. Schreck, Nucl. Phys. B848, 90 (2011)

- [151] M. Schreck: Phys. Rev. D86, 065038 (2012).
- [152] M. A. Hohensee, R. Lehnert, D. F. Phillips, and R. L. Walsworth, Phys. Rev. D 80, 036010 (2009).
- [153] B. Altschul and V. A. Kostelecky: Phys. Lett. B628, 106.
- [154] V. A. Kostelecky and C. D. Lane, Journal of Mathematical Physics 40, 6245 (1999).
- [155] T. J. Yoder and G. S. Adkins, Phys. Rev. D 86, 116005 (2012)
- [156] R. Lehnert, Phys. Rev. D 68, 085003 (2003).
- [157] O. G. Kharlanov, V. Ch. Zhukovsky: J. Math. Phys. 48, 092302 (2007).
- [158] V. A. Kostelecky and M. Mewes, Phys. Rev. Lett. 87, 251304 (2001)
- [159] V. A. Kostelecky and M. Mewes, Phys. Rev. Lett. 97, 140401 (2006)
- [160] V. A. Kostelecky, Phys. Rev. D 69, 105009 (2004).
- [161] D. Colladay, V.A. Kostelecky, Phys. Rev. D 55, 6760 (1997)
- [162] D. Colladay, V.A. Kostelecky: Phys. Rev. D 58, 116002 (1998)
- [163] F. Atamurotov, A. Abdujabbarov and B. Ahmedov, Astrophys. Space Sci. 348 179 (2013)
- [164] Y. Decanini, G. Esposito-Farese and, A. Folacci, Phys. Rev. D 83 (2011) 044032
- [165] A. H. Buchdahl: Monthly Notices of the Royal Astronomical Socie: 150 1
- [166] A. A. Starobinsky: B91, 99 (1980)
- [167] G. Amelino-Camelia, Liv. Rev. Rel. 16, 5 (2013).
- [168] A. Abdujabbarov, M. Amir, B. Ahmedov and S. G. Ghosh, Phys. Rev. D. 93 104004 (2016)
- [169] R. Fresneda, D.M. Gitman, A. E. Shabad: Phys.Rev. D91 085005 (2015)
- [170] G. Rubtsov, P. Satunin and, S. Sibiryakov, J. Cosmo. Astro. Phys. (JCAP) 05(2017)049.
- [171] A. Grenzebach, V. Perlick and C. I. Nammerzahl, Phys. Rev. D. 89 124004 (2014)
- [172] G. S. Bisnovatyi-Kogan and O. Y. Tsupko: Phys. Rev. D. 98 084020 (2018)
- [173] K. S. Gupta, T. Juric, A. Samsarov: JHEP 1706, 107 (2017)
- [174] G. V. Kraniotis: Gen.Rel.Grav. 46 1818 (2014)
- [175] R. Bluhm, V. Alan Kostelecky, Phys. Rev. D 71, 065008 (2005).
- [176] R. V. Maluf, V. Santos, W. T. Cruz, C. A. S. Almeida: Phys. Rev. D88, 025005 (2013).
- [177] Q. G. Bailey and V. A. Kostelecky: Phys. Rev. D74, 045001 (2006).
- [178] Q. G. Bailey and V. A. Kostelecky, Phys. Rev. D 74, 045001 (2006).
- [179] V. A. Kostelecky, A. C. Melissinos and M. Mewes, Phys. Lett. B 761, 1 (2016)
- [180] V. A. Kostelecky and M. Mewes, Phys. Lett. B 757, 510 (2016).
- [181] E. Harikumar, T. Juric and S. Meljanac: Phys. Rev. D 86, 045002 (2012)
- [182] K. Nozari and S. Islamzadeh: Astrophys. Space Sci. 347, 299
- [183] Jian Jing, Ling-Bao Kong, Qing Wang, Shi-Hai Dong: Phys.Lett. B808 135660 (2020)

- [184] Jun-Jin Peng, *Gen. Rel. Grav.* 41, 147 (2009).
- [185] J. P. Luminet: *Astronomy and Astrophysics*, 75, 228 (1979).
- [186] W. Kim, E. J. Son, M. Yoon: *JHEP* 0804, 042 (2008)
- [187] K. Nozari, S. H. Mehdipour: *JHEP* 0903, 061 (2009)
- [188] K. Schwarzschild, *Sitzungsber. Preuss. Akad. Wiss. (Math. Phys.)* 7, 189 (1916).
- [189] R. Kumar, S. G. Ghosh, A. Wang, *Phys. Rev. D.* 100 124024 (2019)
- [190] Z. Li, A. Ovgun: *Phys. Rev. D* 101, 024040 (2020)
- [191] J. Liang and B. Liu: *Eur. Phys. Lett.* 100, 30001 (2012)
- [192] John Ellis, N. E. Mavromatos, D. V. Nanopoulos, *Gen. Rel. Grav.* 32, 127 (2000).
- [193] V. Perlick, O. Yu. Tsupko: *Phys. Rev. D* 95, 104003 (2017)
- [194] S. W. Wei, Y. X. Liu, R. B. Mann: *Phys. Rev. D.* 99 041303 (2019)
- [195] B. Mashhoon, *Phys. Rev. D* 7 (1973) 2807
- [196] S. H. Mehdipour: *Commun. Theor. Phys.* 52, 865 (2009)
- [197] S. H. Mehdipour: *Phys. Rev. D* 81, 124049 (2010)
- [198] M. Fathi, M. Olivares, J. R. Villanueva, *Eur. Phys. J. C* 81 987 (2021)
- [199] M. Ghasemi-Nodehi, Z. Li and C. Bambi, *Eur. Phys. J. C.* 75 (2015)
- [200] M. H. Dickinson, F. O. Lehmann and S. P. Sane, *Science* 284, 1954 (1999).
- [201] Y. G. Miao, Z. Xue and S. J. Zhang: *Gen. Rel. Grav.* 44, 555 (2012)
- [202] M. Afrin, R. Kumar, S. G. Ghosh: *MNRAS* 504 5927 (2021)
- [203] C. W. Misner, K. S. Thorne and J. A. Wheeler, *Gravitation*, Freeman, San Francisco (1973).
- [204] M. Khodadi, A. Allahyari, S. Vagnozzi, D. F. Mota: *JCAP* 2009 026 (2020)
- [205] M. Khodadi, A. Allahyari, S. Vagnozzi, D. F. Mota: *JCAP* 2002 003 (2020)
- [206] N. Ashish, S. Mohanty, and A. Kumar, *arXiv:2002.12786*, 2020
- [207] M. Shibata and H. Yoshino, *Phys. Rev. D* 81 (2010) 104035,
- [208] W.-M. Dai, Z.-K. Guo, R.-G. Cai and Y.-Z. Zhang, *Eur. Phys. J. C* 77 386 (2017)
- [209] S. M. Carroll, J. A. Harvey, V. A. Kostelecky, C. D. Lane, T. Okamoto: *Phys. Rev. Lett.* 87, 141601 (2001)
- [210] K. Glampedakis, G. Pappas *arXiv:2102.13573*, 2021
- [211] P. Aschieri, C. Blohmann, M. Dimitrijevic, F. Meyer, P. Schupp, J. Wess: *Class. Quant. Grav.* 22, 3511 (2005)
- [212] P. Aschieri, M. Dimitrijevic, F. Meyer, J. Wess: *Class. Quant. Grav.* 23, 1883 (2006)
- [213] O. Y. Tsupko and G. S. Bisnovatyi-Kogan: *Gravit. Cosmol.* 18 117 (2012)
- [214] O. Y. Tsupko and G. S. Bisnovatyi-Kogan, *Gravit. Cosmol.* 20 220 (2014)
- [215] V. Morozova, B. Ahmedov, A. Tursunov, *Astrophys. Space. Sci.* 346 513 (2013)

- [216] G. S. Bisnovatyi-Kogan and O. Y. Tsupko: Universe. 3 1 (2017).
- [217] A. Abdujabbarov, B. Toshmatov, J. Schee, Z. Stuchlyk B. Ahmedov: Int. J. Mod. Phys. D26 1741011 (2017).
- [218] A. Abdujabbarov, B. Ahmedov, N. Dadhich, F. Atamurotov: Phys. Rev. D96 (2017) 084017.
- [219] C. A. Benavides-Gallego, A. A. Abdujabbarov, C. Bambi: Eur. Phys. J. C78 (2018) 694.
- [220] V. Perlick, O. Y. Tsupko, G. S. Bisnovatyi-Kogan: Phys. Rev. D92 104031 (2015)
- [221] P. V. P. Cunha, C. A. R. Herdeiro, E. Radu Phys. Rev. Lett. 123, 1 011101, 2019,
- [222] R. Banerjee, B. R. Majhi and S. Samanta: Phys. Rev. D77, 124035 (2008)
- [223] R. Bluhm, N. L. Gagne, R. Potting and A. Vrublevskis, Phys. Rev. D 77, 125007 (2008).
- [224] Rong-Jia Yang, He Gao, Yao-Guang Zheng and Qin Wu, Commun. Theor. Phys. 71, 568 (2019).
- [225] A. Rogers: MNRAS, 451 17 2015
- [226] R. P. Kerr, Phys. Rev. Lett. 11, 237 (1963).
- [227] S. U. Islam, S. G. Ghosh arXiv:2102.08289
- [228] F. Atamurotov, S. G. Ghosh, B. Ahmedov: Eur. Phys. J. C. 76 (2016)
- [229] G. Rubtsov, P. Satunin, S. Sibiryakov, J. Cosmo. Astro. Phys. (JCAP) 05, 049 (2017)
- [230] S. Meljanac, A. Samsarov, M. Stojic, K. S. Gupta: Eur. Phys. J. C 53, 295 (2008)
- [231] S. R. Coleman and S. L. Glashow, Phys. Lett. B 405, 249 (1997); Phys. Rev. D 59, 116008 (1999); R.C. R. C. Myers, M. Pospelov, Phys. Rev. Lett. 90, 211601 (2003).
- [232] Z. Stuchlik, D. Charbulak, J. Schee Eur.Phys. J. C78 180 (2018)
- [233] A. Ovgun and K. Jusufi: Eur. Phys. J. Plus 131 177 (2016)
- [234] R. Uniyal, H. Nandan, P. Jetzer: Phys.Lett. B782 (2018) 185 D.
- [235] V. A. Kostelecky and S. Samuel, Phys. Rev. D 40, 1886 (1989).
- [236] S. H. Volkel, E. Barausse, N. Franchini, A. E. Broderick arXiv:2011.06812, 2020
- [237] W.-M. Dai, Z.-K. Guo, R.-G. Cai and Y.-Z. Zhang, Eur. Phys. J. C 77 386 (2017).
- [238] Y. X. Gui, J. G. Zhang, Y. Zhang and F. P. Chen, Acta Phys. Sin. 33, 1129 (1984).
- [239] R. J. Szabo: Phys. Rept. 378 207 (2003)
- [240] Z. Li and C. Bambi, Journal of Cosmology and Astroparticle Physics, 2014 041 (2014).
- [241] S. K. Jha, A. Rahaman: arXiv:2205.06052, to appear in EPJP, DOI: 10.1140/epjp/s13360-023-03650-w
- [242] J. Ovalle, R. Casadio, E. Contreras, and A. Sotomayor: Phys. Dark Univ. 31, 100744 (2021).
- [243] J. Ovalle, Phys. Rev. D 95, 104019 (2017).
- [244] J. Ovalle, Phys. Lett. B 788, 213 (2019); J. Ovalle,
- [245] E. Contreras, J. Ovalle, R. Casadio, Phys. Rev. D 103, 044020 (2021).
- [246] Mod. Phys. Lett. A 23, 3247 (2008).

- [247] J. Ovalle and R. Casadio, *Beyond Einstein Gravity*, Springer Briefs in Physics (Springer Nature, Cham, 2020).
- [248] T. P. Sotiriou and V. Faraoni, *Phys. Rev. Lett.* 108, 081103 (2012)
- [249] E. Babichev and C. Charmousis, *JHEP* 08, 106 (2014),
- [250] A. Cisterna and C. Erices, *Phys. Rev. D* 89, 084038 (2014),
- [251] T.P. Sotiriou and S.-Y. Zhou, *Phys. Rev. Lett.* 112, 251102 (2014),
- [252] G. Antoniou, A. Bakopoulos, P. Kanti, *Phys. Rev. Lett.* 120, 131102 (2018)
- [253] G. Antoniou, A. Bakopoulos, P. Kanti, *Phys. Rev. D* 97, 084037 (2018),
- [254] M. Volkov and D. Galtsov, *JETP Lett.* 50, 346 (1989).
- [255] P. Kanti, N. Mavromatos, J. Rizos, K. Tamvakis, E. Winstanley, *Phys. Rev. D* 54, 5049 (1996),
- [256] P. Kanti, N. Mavromatos, J. Rizos, K. Tamvakis, E. Winstanley, *Phys. Rev. D* 57, 6255 (1998)
- [257] C. Martinez, R. Troncoso, and J. Zanelli, *Phys. Rev. D* 70, 084035 (2004),
- [258] T. P. Sotiriou, *Class. Quant. Grav.* 32, 214002 (2015)
- [259] J. Ovalle, R. Casadio, R. d. Rocha, A. Sotomayor, Z. Stuchlik, *Eur. Phys. J. C* 78, 960 (2018),
- [260] A. Einstein, *Science*, 84 (1936) 506.
- [261] V. Bozza, *Phys. Rev. D* 66, 103001 (2002).
- [262] V. Bozza, S. Capozziello, G. Iovane G. Scarpetta, *Gen. Rel. Grav.* 33, 1535 (2001).
- [263] V. Bozza and L. Mancini, *Gen. Rel. Grav.* 36, 435 (2004).
- [264] G. W. Gibbons and M. C. Werner, *Class. Quant. Grav.* 25, 235009 (2008).
- [265] K. S. Virbhadra and G. F. R. Ellis, *Phys. Rev. D* 62, 084003 (2000).
- [266] S. Weinberg, *Gravitation, and Cosmology: Principles and Applications of the General Theory of Relativity* (New York:Wiley, 1972).
- [267] S. G. Ghosh, R. Kumar, and S. U. Islam, *J. Cosmol. Astropart. Phys.* 03, 030 (2021).
- [268] A. Ishihara, Y. Suzuki, T. Ono, T. Kitamura, H. Asada. *Phys. Rev.*, D94(8):084015, (2016).
- [269] M. P. Do Carmo, *Differential Geometry of Curves and Surfaces*, (Prentice-Hall, New Jersey, 1976).
- [270] M. C. Werner, *Gen. Rel. Grav.* 44, 3047 (2012).
- [271] T. Do et al., *Science* 365, 664 (2019).
- [272] T. Ono, A. Ishihara and H. Asada, *Phys. Rev. D* 96, 104037 (2017).
- [273] G. Crisnejo, E. Gallo and K. Jusufi, *Phys. Rev. D* 100, 104045 (2019)
- [274] M. Afrin, R. Kumar, S. G. Ghosh: *MNRAS* 504 5927 (2021)
- [275] R. Kumar, S. G. Ghosh: *Class.Quant.Grav.* 38 085010 (2021)
- [276] K. Jusufi, M. Azreg-Ainou, M. Jamil, E. N. Saridakis: *Universe* 8 102 (2022).
- [277] A. Allahyari, M. Khodadi, S. Vagnozzi and D. F. Mota, *Magnetically charged black holes from non-linear electrodynamics and the Event Horizon Telescope*, *JCAP* 02: 003 (2020).

Published Papers

Journal of Cosmology and
Astroparticle Physics



PAPER

Bumblebee gravity and particle motion in Snyder noncommutative spacetime structures

To cite this article: Sohan Kumar Jha *et al* JCAP04(2021)036

View the [article online](#) for updates and enhancements.

The advertisement for IOP ebooks features a grayscale image of a book cover on the left. The cover has a grid-like pattern with various scientific diagrams and text, including the words 'Infrared Imaging' and 'Particle and Nuclear Physics'.

IOP ebooks™

Bringing together innovative digital publishing with leading authors from the global scientific community.

Start exploring the collection—download the first chapter of every title for free.

This content was downloaded from IP address 103.238.192.149 on 30/04/2021 at 09:48



Bumblebee gravity with a Kerr–Sen like solution and its Shadow

Sohan Kumar Jha¹, Anisur Rahaman^{2,a}

¹ Chandernagore College, Hooghly, Chandernagore, West Bengal, India

² Hooghly Mohsin College, Hooghly, Chinsurah, West Bengal 712101, India

Received: 30 November 2020 / Accepted: 9 April 2021 / Published online: 21 April 2021
© The Author(s) 2021

Abstract We have considered the bumblebee gravity model where lorentz-violating (LV) scenario gets involved through a bumblebee field vector field B_μ . A spontaneous symmetry breaking allows the field to acquire a vacuum expectation value that generates LV into the system. A Kerr–Sen-like solution has been found out starting from the generalized form of a radiating stationary axially symmetric black hole metric. We compute the effective potential offered by the null geodesics in the bumblebee rotating black hole spacetime. The shadow has been sketched for different variations of the parameters involved in the system. A careful investigation has been carried out to study how the shadow gets affected when Lorentz violation enters into the picture. The emission rate of radiation has also been studied and how it varies with the LV parameter ℓ is studied scrupulously.

1 Introduction

Various kinds of astronomical observations strongly confirm the existence of the black-hole in the Universe. The recent message of the detection of gravitational waves (GWs) [1] by the *LIGO* and *VIRGO* observatories, and the captured image of the black hole shadow of a super-massive $M87^*$ black hole by the Event Horizon Telescope based on the very long baseline interferometry [2,3] provides substantial evidence in support of the existence of black-hole. The perception of the fundamental nature of spacetime would also likely be enriched with the information accessible from these recent astronomical observations. So physics of black-hole acquire renewed interest.

General relativity and the standard model of particle physics are two very successful field theoretical models that assist us to describe our Universe. The formulation of both these theories is based on the well celebrated Lorentz symmetry. However, the regime of applicability and the nature of

service towards describing the Universe by these two theories are profoundly different. The general relativity describes the gravitational interaction and it is a classical field theory in the curved spacetime and there is no direct way to include the quantum effect. On the contrary, the standard model describes the other fundamental interactions and it is the quantum field theory in the flat spacetime that neglects all gravitational effects, but to study the physical system in the vicinity of the Planck scale (10^{-19} GeV), the effect due to gravity cannot be ignored, since the gravitational interaction is strong enough in that energy scale. Therefore, the study of physics in the vicinity of the Planck scale necessarily entails the unification of general relativity and standard model particle physics. Unfortunately, it is not yet developed with its full wings because there is no straightforward way to quantize the gravity. Moreover, Lorentz invariance is not tenable in the regime where spacetime is discrete in nature. So in the vicinity of the Planck scale, it would not be unreasonable to discard Lorentz invariance. On the other hand, Lorentz symmetry breaking in nature is considered as an interesting and useful idea because it arises as a possibility in the context of string theory [4–7], noncommutative field theories [8] or loop quantum gravity theory [9,10]. As a consequence, nowadays Lorentz violation is considered as relevant as well as a beneficial tool to probe the foundations of modern physics. This fact suggests that signals associated with LV are a promising way to investigate quantum gravity at the Planck scale. The LV in the neutrino sector [11], the extended standard model (ESM) [12], and the LV effect on the formation of atmospheric shower [13] are some important studies involving LV in this regard.

The theory that would be compatible should contain the LV sector. The Standard model Extension (SME) is an effective field theory which is worth mentioning that describes the general relativity and the standard model at low energies, that includes additional terms containing information about the LV occurring at the Planck scale [12]. The electromagnetic sector of the SME has been extensively studied in the litera-

^a e-mails: anisur.rahaman@saha.ac.in; manisurn@gmail.com (corresponding author)



Study of Einstein-bumblebee gravity with Kerr-Sen-like solution in the presence of a dispersive medium

Sohan Kumar Jha¹, Sahazada Aziz², Anisur Rahaman^{3,a}

¹ Chandernagore College, Chandernagore, Hooghly, West Bengal 712136, India

² Ramananda Centenary College, Laulaha, Purulia, West Bengal 723151, India

³ Durgapur Govt. College, Durgapur, Burdwan, West Bengal 713214, India

Received: 12 October 2021 / Accepted: 19 January 2022 / Published online: 3 February 2022
© The Author(s) 2022

Abstract A Kerr-Sen-like black hole solution appears in the Einstein-bumblebee theory of gravity. The solution contains a Lorentz violating parameter in an explicit manner. We study the null geodesics in the background of this Kerr-Sen-like black hole surrounded by a dispersive medium like plasma. We investigate the effect of the charge of the black hole, the Lorentz violation parameter, and the plasma parameter on the photon orbits with the evaluation of the effective potential in the presence of both the Lorentz violation parameter and the plasma parameter. We also study the influence of the Lorentz violation parameter and plasma parameter on the emission of energy from the black hole due to thermal radiation. Besides, we compute the angle of deflection of massless particles with weak-field approximation in this generalized situation and examine how it varies with the Lorentz violation parameter in presence of plasma. Constraining the parameters of this Lorentz violating Kerr-Sen-like black hole is also attempted here with the result obtained from the observations of the Event Horizon Telescope (EHT) collaboration.

1 Introduction

The physics of black holes has got renewed interest after the announcement of the detection of gravitational waves (GWs) [1] by the LIGO and VIRGO observatories and the captured image of the black hole shadow of a super-massive M87* black hole by the EHT based on the very long baseline interferometry (VLBI) [2–7]. The shadow of black-hole is well studied from the theory of General relativity. A black hole shadow is a two-dimensional dark zone in the celestial sphere caused by the strong gravity of the black hole. In the

article [8], Synge studied the shadow of the Schwarzschild black hole, which was then termed as the escape cone of light. The radius of the shadow of the black hole was calculated in terms of the mass of the black hole and the radial coordinate where the observer is located. In general, the shadow of a non-rotating black hole is a standard circle, whereas it is known that the shadow of a rotating black hole is not a circular disk. The different features of the black hole have been widely investigated for various gravity backgrounds, adopting an almost similar approach based on classical dynamics [9–26].

In General Relativity, light is attributed to the null geodesic of the spacetime metric and the in-medium effect, which is negligible for most of the frequency ranges, is significant for the radio frequency range. In this context, it is worth mentioning the impact of Solar corona on the time of travel and on the deflection angle of radio signals that come close to the Sun. Since the 1960s, this influence has been routinely observed. In this case, one may assume that the medium is a non-magnetized pressureless plasma and for the gravitational field, the linearized theory is sufficient. The relevant theoretical development has been made by Muhleman et al. in the articles [27,28]. With the available information, the shadow of black holes in presence of plasma has become an interesting field of research for physicists since there is a good reason for considering that black holes and other compact objects are surrounded by plasma. So, naturally, interest grows to investigate whether the presence of plasma leads to any observational effect on the radio signals and several investigations have been carried out in that direction [29–40]. The physics of black holes is crucially linked with the Planck energy scale where gravity is sufficiently strong and a classical field theory of curved spacetime is not adequate to capture the finer details of the Planck scale. It needs quantization of gravity, which is not well-developed. However, it is reasonable to accept that the nature of the spacetime is discrete in that scale. Lorentz symmetry being a continuous symme-

^a e-mails: anisur.associates@iucaa.ac.in; manisurn@gmail.com (corresponding author)



Kerr–Sen-like Lorentz violating black holes and superradiance phenomena

Sohan Kumar Jha¹, Anisur Rahaman^{2,a}

¹ Chandernagore College, Chandernagore, Hooghly, West Bengal, India

² Durgapur Government College, Durgapur, Burdwan, West Bengal 713214, India

Received: 5 October 2021 / Accepted: 9 April 2022 / Published online: 6 May 2022
© The Author(s) 2022

Abstract A Kerr–Sen-like black hole solution results from Einstein–bumblebee gravity. It contains a Lorentz violating (LV) parameter that enters when the bumblebee field receives vacuum expectation value through a spontaneously breaking of the symmetry of the classical action. The geometrical structure concerning the singularity of this spacetime is studied with reference to the parameters involved in the Kerr–Sen-like metric. We introduce this Einstein–bumblebee modified gravity to probe the role of spontaneous Lorentz violation on the superradiance scattering phenomena and the instability associated with it. We observe that for the low-frequency range of the scalar wave the superradiance scattering gets enhanced when the Lorentz-violating parameter ℓ takes the negative values and it reduces when values of ℓ are positive. The study of the black hole bomb issue reveals that for the negative values of ℓ , the parameter space of the scalar field instability increase prominently, however, for its positive values, it shows a considerable reduction. We also tried to put constraints on the parameters contained in the Kerr–Sen-like black hole by comparing the deformation of the shadow produced by the black hole parameters with the observed deviation from circularity and the angular deviation from the $M87^*$ data.

1 Introduction

In a gravitational system, the scattering of radiation off absorbing rotating objects produce waves with amplitude larger than incident one under certain conditions which is known as rotational superradiance [1–4]. In 1971, Zel’dovich showed that scattering of radiation off rotating absorbing surfaces result in waves with a larger amplitude as $\omega < m\Omega$ where ω is the frequency of the incident monochromatic

radiation with m , the azimuthal number with respect to the rotation axis and Ω is the angular velocity of the rotating gravitational system. For review we would like to mention the lecture notes [5], and the references therein. Rotational superradiance belongs to a wider class of classical problems displaying stimulated or spontaneous energy emission, such as the Vavilov–Cherenkov effect, the anomalous Doppler effect. When quantum effects were incorporated, it was argued that rotational superradiance would become a spontaneous process and that rotating bodies including black holes would slow down by spontaneous emission of photons. From the historic perspective, the discovery of black-hole evaporation [6] was well understood from the studies of black-hole superradiance.

Interest in the study of black-hole superradiance has recently been revived in different areas, including astrophysics, high-energy physics via the gauge/gravity duality along with fundamental issues in General Relativity. Superradiant instabilities can be used to constrain the mass of ultra-light degrees of freedom [7–10], with important applications to dark-matter searches. The black hole superradiance is also associated with the existence of new asymptotically flat hairy black-hole solutions [11] and with phase transitions between spinning or charged black objects and asymptotically anti-de Sitter (AdS) spacetime [12–14] or in higher dimensions [15]. Finally, the knowledge of superradiance is instrumental in describing the stability of black holes and in determining the fate of the gravitational collapse in confining geometries [13].

During the last few decades, the standard theories of general relativity have been continuing to explain many important experimental results. However, there is still some room to the use of alternative theories of the general theory of relativity. From a theoretical viewpoint, having an ultraviolet complete theory of general relativity is complementary as well as supportive. Moreover from the observational point of view, general relativity has shortcomings to describe some

^a e-mails: anisur.associates@aucaa.ac.in; manisurn@gmail.com (corresponding author)



Superradiance scattering off Kerr-like black hole and its shadow in the bumblebee gravity with noncommutative spacetime

Sohan Kumar Jha¹, Anisur Rahaman^{2,a}

¹ Chandernagore College, Chandernagore, Hooghly, West Bengal, India

² Durgapur Government College, Durgapur, Burdwan 713214, West Bengal, India

Received: 6 May 2022 / Accepted: 17 July 2022 / Published online: 21 August 2022
© The Author(s) 2022

Abstract We consider a bumblebee gravity-based Kerr-like black hole in a noncommutative (NC) background and study the superradiance effect and the shadow cast. We extensively study the different aspects of the black hole associated with a generalized Kerr-like spacetime metric endowed with the corrections jointly linked with Lorentz violation and NC spacetime effect. We examine the deviation of shape, and size of the ergosphere, energy emission rate, in this generalized situation. We also examine the influence of admissible values of Lorentz violating parameter ℓ and NC parameter b on the superradiance effect and shadow of the black hole. The admissible range has been determined from the observation of the Event Horizon Telescope (EHT) collaboration concerning $M87^*$ astronomical black hole. We observe that the superradiance phenomena has a crucial dependence on the parameter ℓ and b apart from its dependence on a or $\hat{a} = \sqrt{\ell + 1}a$ which is linked with the spin of the black hole. We also observe that with the increase in Lorentz violating parameter ℓ , the size of the black hole shadow increases, and with the increase in the NC parameter b the size of the black hole decreases. We have made an attempt to constrain the NC parameters b of this modified Kerr-like black hole by using the data available from the Event Horizon Telescope (EHT) collaboration. This study shows that black holes associated with NC Kerr-like spacetime may be a suitable candidate for the astrophysical black holes.

1 Introduction

Different exciting optical phenomena have been encountered when light approaches the vicinity of a black hole. Lensing (strong and weak), superradiance, and formation of the shadow of the black holes are essential in this context. From

the time of Einstein, the study of the optical effect in the vicinity of a black hole was started and this field has been getting enriched through the investigation by different scientists. In the lensing effect, the black hole behaves as a natural celestial lens that makes a deviation in the path of the light. Here bending takes place due to the strong gravitational field of the black hole. Here, we concentrate on investigating the impact of quantum gravity effect on the superradiance phenomenon and the shadow of black holes.

In a gravitational system, the scattering of radiation off absorbing rotating objects produce waves with amplitude larger than incident one under certain conditions which is known as rotational superradiance [1,2]. In 1971, Zel'dovich showed that scattering of radiation off rotating absorbing surfaces result in waves with a larger amplitude as $\omega < m\Omega$ where ω is the frequency of the incident monochromatic radiation with m , the azimuthal number with respect to the rotation axis and Ω is the angular velocity of the rotating gravitational system [1,2]. The important contemporary contributions in the articles [3–7] related to superradiance made these astounding astronomical phenomena a tempting field of research. For review, we would like to mention the lecture notes [8], and the references therein. Rotational superradiance belongs to a wider class of classical problems displaying stimulated or spontaneous energy emission, such as the Vavilov-Cherenkov effect and the anomalous Doppler effect. When quantum effects were incorporated it was argued that rotational superradiance would become a spontaneous process and that rotating bodies including black holes would slow down by the spontaneous emission of photons. From the historical perspective, the discovery of black hole evaporation was well understood from the studies of black hole superradiance [9]. Interest in the study of black hole superradiance has recently been revived in different areas, including astrophysics and high-energy physics via the gauge/gravity duality along with fundamental issues in General Theory of Relativity (GTR). Superradiant instabilities can be used to

^a e-mails: anisur@associales.iucaa.in; manisurn@gmail.com (corresponding author)



Strong gravitational lensing in hairy Schwarzschild background

Sohan Kumar Jha^{1,a}, Anisur Rahaman^{2,b}

¹ Chandernagore College, Chandernagore, Hooghly, West Bengal, India

² Durgapur Government College, Durgapur, Burdwan, West Bengal 713214, India

Received: 11 September 2022 / Accepted: 31 December 2022

© The Author(s), under exclusive licence to Società Italiana di Fisica and Springer-Verlag GmbH Germany, part of Springer Nature 2023

Abstract We consider the hairy Schwarzschild black hole that evades the no-hair theorem. The hair is induced by additional sources from the surroundings, namely dark matter, that has a constant energy-momentum tensor (EMT). Hair parameter was designated by ℓ_0 . We study the strong gravitational lensing of light in the background of the hairy Schwarzschild black hole. We observe that the lensing coefficient \bar{a} increases with deviation parameter α , but decreases with primary hair ℓ_0 . The opposite effect is observed for the lensing coefficient \bar{b} and the impact parameter b_m . We also notice that the angular position θ_∞ decreases with α but increases with ℓ_0 , whereas the angular separation s increases with α and decreases with ℓ_0 . For all parameters mentioned, we regain their values for the Schwarzschild black hole whenever we put either $\alpha = 0$ or take the limit $\ell_0 \rightarrow 2M$. With the help of the Gauss-Bonnet theorem, we briefly describe the weak gravitational lensing in the background of the hairy Schwarzschild black hole.

1 Introduction

Deflection of a light ray in the gravitational field due to astronomical objects is in general referred to as gravitational lensing and the celestial object that gives rise to a deflection of light is termed a gravitational lens. Gravitational lensing by a black hole is one of the most significant and powerful astrophysical tools for probing the strong field characteristics of gravity. It is anticipated to render a veritable assessment of the implementation of modified theories of gravity in the strong field regimes. The general theory of relativity got its important operation through gravitational lensing quite a long ago [1]. Recently the Event Horizon Telescope (EHT) collaboration has announced that it has successfully photographed the supermassive black hole $M87^*$ at the heart of the nearby elliptical galaxy $M87$ [2–7]. It indeed represents a significant achievement in the study of general relativity and opens up a new window for studying strong gravity. In general, the image of the black hole that is expected to be surrounded by the accretion disk appears distorted due to the strong gravitational lensing effect. In this way, black holes are anticipated to cast marks on the bright background which is related to the existences of an event horizon and thus an unstable photon region [8]. The shadow and the lensing effect associated with that are of great significance and scientific importance. It enables us to probe the geometrical structure of the event horizon and maybe the externally observable classical parameters, like mass, electric charge, and angular momentum through which a black hole is characterized. The gravitational lensing proposition was primarily established using a weak field approximation approach, and it was effectively planted to explain the physical compliances. In contrast, researchers started looking at the unexpected from the perspective of a strong gravitational field around two and half decades years ago, mentioning [8–15].

A semi-analytical treatment was adopted for the disquisition of geodesics in Kerr spacetime geometry in the article [9]. In the article [10], the appearance of a black hole in front of a uniform background was studied and in [11], the authors considered the emission of the accretion inflow as the source. In an important composition, Virbhadra and Ellis [12] showed that one set of infinite relativistic images would be produced on each side of the black hole by a source behind a Schwarzschild black hole. These images are produced when light rays with small impact parameter wind one or several times around the black hole before it becomes free from the gravitational field. Later on, in the article [13] the authors derived an exact lens equation through an indispensable exposition of the problem and compared their results with the earlier work presented in [12]. The same problem was delved into by Bozza et al. in the article [8] where a strong field limit was first defined for the Schwarzschild black hole lensing effect. It was used analytically to determine the position and characteristics of all the relativistic images. The article [14] was devoted to the Reissner-Nordstrom black hole in the same fashion. Lately, in another work [15], Virbhadra and Ellis made an attempt to distinguish the main features of gravitational lensing by normal black holes and by naked singularities utilizing the Janis-Newman-Winicour metric. They asserted that this study may facilitate the probable test for the cosmic censorship hypothesis.

^a e-mail: sohan00slg@gmail.com

^b emails: anisur@associates.iucaa.in; manisurn@gmail.com (corresponding author)



Impact of the generalized uncertainty principle on the thermodynamic characteristics of Schwarzschild black hole veiled with quintessence matter

Himangshu Barman¹, Sohan Kumar Jha², Anisur Rahaman^{3,a}

¹ Hooghly Mohsin College, Chinsurah, Hooghly, West Bengal 712101, India

² Chandernagore College, Chandernagore, Hooghly, West Bengal, India

³ Durgapur Government College, Durgapur, Burdwan, West Bengal 713214, India

Received: 6 September 2022 / Accepted: 30 October 2022

© This is a U.S. Government work and not under copyright protection in the US; foreign copyright protection may apply 2022

Abstract We conduct an analysis to examine the thermodynamic character of a Schwarzschild black hole surrounded by quintessence matter under a generalized Heisenberg algebra with a quadratic and linear terms in momentum. We compute the temperature, heat capacity, and entropy associated with this black hole using this modified algebra in the presence of quintessence matter surrounding the black hole. When computing the thermodynamical variables for this black hole using this deformed algebra, we also examine the behavior of the isotherms for this black hole. We compare each computed result with the standard result of the Schwarzschild black hole. As we can see, a remnant of the black hole is indicated by this modified algebra, which is seen to be a plausible solution to the information loss problem.


1 Introduction

A fascinating prediction of the general theory of relativity is the possibility of the existence of black holes. Astronomical observation has now made it clear that black holes might exist in nature. Strong evidence for the existence of black holes includes the observation of gravitational waves, the success in capturing the shadow of the $M87^*$ supermassive black hole, and the subsequent success in capturing the shadow of the $SgrA^*$. Naturally, the study of different aspects of black holes has gained renewed interest. It is generally agreed that black holes are thermal bodies, and the laws of thermodynamics can be used to describe their characteristics. This proposal was put forward a little more than half a century ago by Hawking and Bekenstein [1–3]. According to the information obtained from these papers [1–3], a black hole is a thermodynamic system that emits radiation with a characteristic temperature closely related to its surface gravity. Moreover, the entropy of these objects is linearly proportional to the area covered by the event horizon in Planck units. With these innovative proposals, they tested several models of black holes by computing Hawking temperature and mass in the framework of statistical mechanics and reached the conclusion that the basic laws of thermodynamics are no longer violated [4].

According to the most recent observational astronomical data, our Universe is expanding at an accelerating rate [5–7]. To explain this acceleration, the existence of a distinctly different form of matter having negative pressure has been postulated. This dark energy content is expected to be around seventy percent of the total energy density of the Universe. Although the use of the concept of the cosmological constant could have been an effective technique to characterize this acceleration, its experimental value is found to be significantly smaller than what is theoretically anticipated [8]. Different alternative models were consequently suggested. These compelling models [9–14] differ from one another in terms of the parameters relating to the ratio of pressure to the density of dark energy. These models are essentially based on the dynamics of specific scalar fields. Black hole thermodynamics is thought to be significantly influenced by the dark energy surrounding them. The literature of recent times contains a wealth of studies on this subject. We suggest readers to the review [15] and the references therein for an in-depth discussion and evaluation of those models. The quintessence matter, which is notable among the dark energy contenders, was taken into consideration by Kiselev in the foundational work, and a useful study has been conducted. The literature of recent times contains a wealth of studies on this subject [16]. A few years later, Chen et al. investigated the Hawking radiation of any D -dimensional, spherically symmetric, static black hole, where the very nature of matter is thought to be a potential candidate for dark matter [17]. The study of the thermodynamic characteristics of black holes, inspired by the quintessence, attracted more and more attention throughout time. Therefore, exploration of thermodynamics in the presence of quintessence matter for the Reissner–Nordstrom (NR) black hollow [18], the NR black hollow in de-Sitter spacetime [19], Narai-kind black holes [20, 21] was carried out. Bardeen-type regular black holes were presented later in due course [22]. Shahjalal recently compared the thermodynamics of this black hollow in the presence of the quintessence matter

^a emails: anisur@associates.iucaa.in; manisurn@gmail.com (corresponding author)

The inflationary scenario in the $f(R)$ gravity model with a R^4 term

Sahazada Aziz¹ , Sohan Kumar Jha² and Anisur Rahaman^{3,*} 

¹ Ramananda Centenary College, Laulara-723151, Purulia, West Bengal, India

² Chandernagore College, Chandernagore-712136, Hooghly, West Bengal, India

³ Durgapur Government College, Durgapur-713214, Burdwan, West Bengal, India

E-mail: sahzada@outlook.com and anisur.associates@aucaa.ac.in

Received 17 June 2021, revised 12 September 2021

Accepted for publication 7 October 2021

Published 26 October 2021



Abstract

We investigate the cosmic inflation scenario of a specific $f(R)$ model that contains more than one higher-order term in R . The $f(R)$ considered here has the terms R^2 , R^3 , and R^4 along with the linear term. A rigorous investigation has been carried out in the presence of these higher-order terms to figure out whether it leads to a physically sensible cosmic inflationary model. We examine in detail, subject to which conditions this $f(R)$ model renders a viable inflationary scenario, and it has been found that the outcomes of our study agree well with the recent Planck results.

Keywords: inflation, $f(r)$ gravity, Planck scale physics

(Some figures may appear in colour only in the online journal)

1. Introduction

There has been a huge interest in the study of cosmic inflation over the decades since it is considered as an effective scenario for explaining the origin of structure formation of the Universe. Starobinsky, in his seminal work [1], showed that Einstein's equations with quantum one-loop contributions of conformally covariant matter fields admit a class of nonsingular isotropic homogeneous solutions and it attracted immense attentions since it was found that successful slow-roll inflation could be achieved with a single parameter which is the very coefficient of the R^2 curvature term. The predictions related to inflation of this model were well consistent with the Planck data. The idea, therefore, was extended to a class of Starobinsky-like models having common properties during inflation [2–7]. The Higgs inflation as a particular case was studied in [8]. In the article [4], it was emphasized that there must be a stage of inflation

* Author to whom any correspondence should be addressed.

Modern Physics Letters A
 2150130 (17 pages)
 © World Scientific Publishing Company
 DOI: 10.1142/S0217732321501303



On the reformulation of the Thomas–Fermi model to make it compatible with the Planck-scale

Himangshu Barman and Anisur Rahaman*

Hooghly Mohsin College, Chinsurah, Hooghly – 712101, West Bengal, India
 *anisur.rahman@saha.ac.in; manisurn@gmail.com

Sohan Kumar Jha

Chandernagore College, Chandernagore, Hooghly, West Bengal, India

Received 27 January 2021

Revised 23 April 2021

Accepted 5 May 2021

Published 18 June 2021

Thomas–Fermi model is considered here to make it cogent to capture the Planck-scale effect with the use of a generalization of uncertainty relation. Here generalization contains both linear and quadratic terms of momentum. We first reformulate the Thomas–Fermi model for the non-relativistic case. We have shown that it can also be reformulated for taking into account the relativistic effect. We study the dialectic screening for both the non-relativistic and relativistic cases and find out the Fermi length for both the cases explicitly.

Keywords: Thomas–Fermi model; generalized uncertainty relation; Planck-scale effect.

1. Introduction

Over the decades, there has been a huge interest in the study of predicting the expected behavior of the physical system in the vicinity of Planck-scale. Three are different ways of studying the expected behavior of physical systems in the vicinity of Planck-scale through some well-designed formulation which has a very close link with the well-developed theory (string theory) believed to be suitable for the Planck-scale regime. The generalization of uncertainty relation is one of the most important and well-accepted frameworks in this respect. It acquired a great deal of attention when it has been found to be concomitant with the string theory, loop quantum gravity, and non-commutativity of space-time as well, at the conceptual level.^{1,3–5} The generalization of uncertainty relation is made in various ways however the generalization associated with minimum length and minimum length along with

*Corresponding author.

Study of black holes in standard and modified gravity

Thesis submitted for the award of
Doctor of Philosophy in Science (Physics)
of
The University of Burdwan



Submitted by

SOHAN KUMAR JHA

(R-Ph.D./Regn./sc/physics/43) dated 24.06.2022

Under the Supervision of Dr. Anisur Rahaman (WBES)

Durgapur Govt. College, Durgapur, Burdwan

Work done in

Hooghly Mohsin College, Chinsurah, Hooghly

And

Durgapur Govt. College, Durgapur, Burdwan

Chapter 9

Summary and Conclusions

General theory of relativity is without a doubt a tremendously successful theory and is accepted as a standard theory of gravity. However, modified theories of gravity are becoming a subject of study for several reasons. The discovery of the accelerated expansion of the universe is perhaps the major reason for this end. This motivation is becoming increasingly important indeed after the detection of gravitational waves. So, even if general relativity turns out to be accurate (low-energy effective) description of gravity, the modified theory of gravity is still worthwhile to research. This motivation has gained momentum as a result of recent observations of EHT collaboration concerning the captured shadows of $M87^*$ and $SgrA^*$. In addition to phenomenology, the modified theories of gravity are beneficial for a deeper understanding of different aspects of gravity. It has to be kept in mind that the general theory of relativity requires modification in the UV because it is insufficient as a quantum theory in any case. Unfortunately, the quantum theory of gravity has not yet been developed, nonetheless, various methods of quantum correction have been introduced through different indirect means. In this perspective, the amendment of the Lorentz violation effect and the non-commutative spacetime within the standard theory is noteworthy. Another derived kind of modification is the amendment of the combined effects of Lorentz violation and non-commutative spacetime. Besides, modification by encapsulating the medium effect, such as considering the existence of scalar hair has also attracted attention. This thesis is primarily a description of modifications of the standard theory of gravity through the amendment of Lorentz violation due to the bumblebee field and non-commutative character of spacetime. The free parameters involved in the resulting modification are then constrained from the recent observations of the EHT collaboration concerning the captured shadow of $M87^*$. Besides, a modification through scalar hair is also considered to study the strong lensing effect by the supermassive black hole.

After giving a brief discussion of the general theory of relativity and its consequences in Chapter I, we have considered the Einstein-bumblebee gravity model where LV scenario gets involved through a bumblebee field vector field B_μ . A spontaneous symmetry breaking allows the field to acquire a vacuum expectation value that generates LV into the system. We have described a few classical tests related to Einstein-bumblebee gravity in Chapter II. We have seen that although the redshift scenario remains unaltered, the surface gravity acquires a LV correction in this background. When we study the motion of a particle confined in a circular orbit we notice that it also remains unaltered whereas the motion in a generalized non-circular orbit does not remain so. The precise investigation of the circular orbit extracts this surprising exposition. Our main endeavour in the article [118] was to study the motion of a particle in the bumblebee background that contains a LV parameter with a non-commutative but Lorentz invariant setting formulated by Snyder. The way we have formulated our investigation is capable of providing corrections on the perihelion shift of a particle likely to appear in the vicinity of the Planck scale for two different means in a unified manner. The replacement of the Schwarzschild background by the bumblebee-inspired background renders a correction through the LV parameter ℓ whereas the non-commutative setting of Snyder renders a correction through the parameter λ_s in the same energy scale. Our result shows that the correction in the perihelion shift contains two pure terms that depend on ℓ and λ_s respectively along with some interfering terms containing both parameters ℓ and λ_s . One of the pure terms comes from the use of a bumblebee background and the other

appears because of the use of non-commutative spacetime proposed by Snyder. The interfering terms that appear are very very small since the term contains the product of two very small factors λ_s and ℓ . Although the interfering term is negligibly small, it has some theoretical consequence, e.g., symmetric contribution may get disturbed by an asymmetric term - the reverse perhaps does not get so. It is true that both the parameters λ_s and ℓ are small. A physical result containing some arbitrary parameter would be physically sensitive if the parameters can be constrained from experimental observation. Both the parameters can be put under constraints using the same arguments available in [45] and [44]. The conjecture used there is that the correction would be of the order of general relativistic correction. Here, we can, indeed, put a restriction on the parameters λ_s and ℓ following the same argument. The upper bound of the predicted values of the parameters is given in Table (2.1). Note that the predicted values of ℓ are identical to the values obtained in the article [44]. It is indeed the expected result. Our study enables us to put another constraint on the parameter λ_s when the constrain on ℓ is known if it is taken into consideration that the correction that appeared in the form of interference which is proportional to $\lambda_s \ell$ would be of the same order of magnitude of the pure terms. Note that the first-order correction term is proportional to $\lambda_s \ell$. So if we are intended to constrain the interfering term it will provide new information that the parameters may have reciprocal out-turn between each other. When the contribution through one parameter dominates, the contribution from the other will get suppressed automatically.

Chapter III contains a description to establish that Kerr-Sen-like spacetime is a viable solution of Einstein-bumblebee gravity model [76] where LV scenario gets involved through the said bumblebee field vector B_μ . Then, it has been extended to study the properties of the shadow it is supposed to cast. To this end, the effective potential that results from the null geodesics in the bumblebee rotating black hole spacetime is computed that in turn helps to get the tentative nature of the motion of photon predicted for different choices of the parameters a , b , and ℓ . Then the nature of shadow is studied and how does the shadow gets deformed has also been studied for different variations of a , b , and ℓ . We observe that the shadow gets shifted towards the right for positive ℓ and shifted towards left for negative ℓ when a and b remain fixed. However, shifting is always towards the right when b increases whatever the set of values of ℓ and a are taken. We have also studied the rate of emission of energy for this type of black hole. The emission rate decreases when b increases for any set of fixed values of a and ℓ . It also decreases when ℓ increases for an arbitrary set of fixed values of a and b . A crucial difference however in the situation is noticed when ℓ increases. The emission rate although decreases with the increase of ℓ like the case when b increases, the pick of the curve gets shifted towards lower ω in the situation when ℓ increases. The deformation of the shadow for the Kerr-Sen-like black hole in the Einstein-bumblebee gravity model with the variation of ℓ observed here is a theoretical prediction. It shows that it enhances the distortion of shadow, and it would be detected by the new generation gravitational antennas.

Chapter IV deals basically with the in-medium effect on the Kerr-Sen-like spacetime which has been found as a solution to the equations developed from Einstein-bumblebee gravity in [76] which has a LV parameter ℓ . This modified spacetime is used to study the propagation of light in a non-magnetized pressure-less plasma in [119]. We have considered the plasma as a medium with dispersive properties given by a frequency-dependent index of refraction. The gravitational field is determined by the mass, the spin, and the bumblebee parameter. The Gravitational field due to plasma is neglected here. We have studied how the nature of shadows gets affected by the LV effect associated with the bumblebee field in the pressure-less nonmagnetic plasma. We have also studied the energy emission scenario and the weak field lensing in the Kerr-Sen-like spacetime due to Einstein-bumblebee gravity background when it is veiled in a plasma medium. The results for Kerr, Kerr-like, and Schwarzschild black holes can, as well, be obtained from this result with a suitable limit. We have investigated in detail the impact of the charge ($Q^2 \propto b$), plasma parameter k , and the Lorentz violating bumblebee parameter ℓ on the structure of shadow, on the lensing effect of light, and on the energy emission due to black hole radiation. It has been found that the new parameters quantitatively influence the structure of the event horizon by altering the radius significantly. It is observed that the size of the shadow viewed by a distant observer reduces with an increase in the charge Q and the size of the shadow appears to be larger with the increase in the plasma parameter k . Therefore, the

bumblebee field maintains its action of deforming the shadow in presence of plasma as well. Since the energy liberated from the black hole depends on the area of the shadow, the rate of energy emission from the black hole is higher when the black hole is surrounded by plasma. As far as the angle of deflection is concerned, the photons are observed to experience an increase in the deviation as the plasma factor k increases. While on the other hand, the angle of deflection reduces sufficiently when the amount of charge parameter increases. It is also observed that the deflection angle increases with an increase in the value of the LV parameter ℓ . Sufficient negative ℓ may cease the lensing effect too!

Chapter V is devoted to constraining the free parameters that have entered into the modified models adopted here. The idea behind this is as follows. The theory of general relativity predicts that the Kerr metric is capable of describing astrophysical black holes. However, such black holes may not exist in a perfect vacuum due to the presence of surrounding matter, like plasma, dark matter, etc. The accretion disks may also alter the black hole, which may not fit with the Kerr metric. The bumblebee-inspired Kerr spacetime enables the incorporation of potential deviations from the Kerr metric through the additional deviation parameters. The advantage of this type of modified gravity is that it is a generic one and it has the ability to cover the prediction of the Kerr metric since the introduced parameters can be chosen in such a way that it makes the null deviation of the shadow from Kerr spacetime. There is a theoretical motivation for modified theories of gravity indeed however the constraining of the free parameter from the experimental observation allows us to examine the viability of the model. In this context the information of the captured image by the EHT collaboration became instrumental.

The EHT collaboration has captured the image of supermassive black hole M87* exhibiting a deviation from circularity $\Delta C \leq 0.10$. The observation did not say anything about modified theories of gravity or suggest any alternatives to the Kerr black hole. Motivated by this, we considered Kerr-Sen-like modified black holes, which have additional deviation parameters ℓ and b to the Kerr black hole. The presence of Plasma adds an additional parameter. We use the deviation from circularity $\Delta C \leq 0.10$ as deduced by the EHT collaboration to constrain the Kerr-Sen-like black hole parameters. We have observed that the bound $\Delta C \leq 0.10$ is satisfied by black hole shadows over a finite parameter space both in the presence of plasma and in the absence of it. Besides, the information available from the article [117] allows us to put constrain on the value of ℓ . We have found that the value of the parameter $\ell > -1$ and the upper bound of it is 0.621031. So ℓ can take both positive and negative values. We would like to mention that in the calculation of the rate of energy emission, we did not consider the greybody factor. The mathematical formulation of it is much involved for any black hole. Moreover, it is important when quantitative estimation is brought under consideration. Unfortunately, there is no available data to compare it with the real situation. A fascinating and involved extension of this work would be to evaluate it theoretically.

We have described the superradiance phenomena of the scalar field scattered off Kerr-Sen-like black holes in detail in Chapter VI. The contents of this chapter have been studied in [120]. We have already mentioned that this is a black hole solution to Einstein-bumblebee gravity model. A Lorentz violating parameter is there in the spacetime metric of this modified gravity. Here, Lorentz violation takes place via a spontaneous symmetry breaking when the pseudovector field of the Einstein-bumble model receives a vacuum expectation value. We have also studied superradiance instability. We have studied here how the superradiance phenomena and related instability scenario gets influenced by the Lorentz violation effect through the Kerr-Sen-like background which is the outcome of the Einstein-bumblebee gravity model. Employing asymptotic matching of the scalar wave, it has been established that in the low-frequency limit, i.e., for $\omega < m\hat{\Omega}_{eh}$, the scalar waves become superradiant amplified. The numerical computation, however, shows that for $m \leq 0$ the massive scalar field has a non-superradiant mode. For $m \geq 0$ it is superradiant. The superradiant process enhances with the decrease of the Lorentz violation parameter and the reverse is the case when the Lorentz violation parameter increases irrespective of the sign of the value of this parameter. We have also demonstrated how the superradiant process gets influenced by the parameter b . From Fig. (6.10) it is clear that superradiance enhances with the decrease of the positive value of the parameter b . Note that $b = \frac{Q^2}{M}$. So it cannot be negative. Moreover, extending the issue of the black hole bomb, the analytical study of superradiant instability is made. The plots in Fig. (6.11) related to the study reveal

that the LV parameter remarkably affects the instability regime. In the background with the negative LV parameters, the scalar field has more chances to acquire unstable dynamics and for the positive values of the LV parameter, it is less. Therefore, the Lorentz violation has a significant influence on the superradiance scattering phenomena and the corresponding instability linked with it.

As an extension, we describe in Chapter VII how a framework is developed where quantum correction due to the Lorentz violation and non-commutative character of spacetime has been taken into account on the same footing [121]. The spacetime background renders a non-commutative Kerr-like Lorentz symmetry violating black hole. We have extensively studied different aspects of the non-commutative and Lorentz violating Kerr-like black hole. The spin, the mass, the Lorentz violation parameter, and the non-commutative parameter involved in it determine the gravitational field of this black hole. First of all, we study geometry in detail concerning its horizon structure and ergosphere. The article [121] contains the study of two important optical phenomena in the vicinity of this black hole. In this respect, we have considered the superradiance phenomena and find that it crucially depends on the parameter ℓ and ϑ_n apart from its dependence on a which is linked with the spin of the black hole. The superradiance process enhances with the decrease in the value of the Lorentz violation parameter and it diminishes when we increase the value of the Lorentz violation parameter. We also observe that with the increase in the value of the parameter ϑ_n the superradiance process gets diminished. However, with the increase in the value of a the superradiance process increases. Next, we have brought into our investigation the effect of Lorentz violating parameter ℓ and non-commutative parameter ϑ_n on the size of the black hole shadow. We have observed that the size of the black hole shadow increases with an increase in the value of the parameter ℓ and it decreases with an increase in the value of the parameter ϑ_n . Thus, it can be safely concluded that Lorentz violation and non-commutativity, both, have significant impacts on black hole shadow. We have also studied energy emission rates. These results have clearly established the influence of the Lorentz violation parameter and non-commutative parameter on emission rate. We observe that the energy emission rate decreases with an increase in the value of b for any set of fixed values of a and ℓ . It also decreases with an increase in the value of ℓ , when a and b are held fixed, and with an increase in the value of a , if ℓ and b are kept fixed.

We have been able to constrain the parameters even in the modified theories augmented with the combined effect of Lorentz violation and the non-commutative character of spacetime using the observations of EHT collaboration. For inclination angle $\theta = 90^\circ$, the deviation from circularity $\Delta C \leq 0.1$ and angular diameter $\theta_d = 42 \pm 3 \mu\text{as}$ within 1σ region are satisfied for finite parameter space $(\frac{\vartheta_n}{M^2} - \frac{\hat{a}}{M})$. For inclination angle $\theta = 17^\circ$, the circularity deviation $\Delta C \leq 0.1$ is satisfied for the entire parameter space $(\frac{\vartheta_n}{M^2} - \frac{\hat{a}}{M})$. The angular diameter $\theta_d = 42 \pm 3 \mu\text{as}$ within 1σ is satisfied for finite parameter space $(\frac{\vartheta_n}{M^2} - \frac{\hat{a}}{M})$. The axis ratio D_X satisfies the constraint $1 < D_X \lesssim 4/3$ for the entire parameter space at both the inclination angles $\theta = 90^\circ$ as well as $\theta = 17^\circ$. Therefore our study enables us to establish the fact that non-commutative Kerr-like black holes are remarkably consistent with EHT images of $M87^*$. It demands that ruling out non-commutative Kerr-like black holes from the observational data of black hole shadow would be illogical. Thus, non-commutative Kerr-like black hole may be considered a suitable candidate for the astrophysical black hole. It has also been shown that the possible upper bound of ϑ_n , which is associated with the non-commutativity, is $0.000505973M^2$. It is intriguing and indeed a novel way to constrain the parameter associated with the non-commutativity from the shadow of an astronomical black hole. Till now we do not have any available data to constrain the parameter ℓ and ϑ_n from the superradiance effect and from the energy emission process. So, the parameter cannot be constrained by knowledge of the superradiance phenomena and the energy emission process. We have made all the plots for the superradiance and the energy emission process maintaining the constraint obtained from the EHT data concerning the shadow of the $M87^*$.

Chapter VIII is devoted to study the strong as well as weak lensing due to the black hole modified with scalar hair. Black holes have been considered more than bare fantastic results of the Einstein equations for quite some time now. Nonetheless, it is only recently that their direct existence was detected substantially due to the report of the results of the Event Horizon Telescope Collaborations. So, the study of aspects of black holes and the consequences of their presence have now surfaced with new alleviation. In this environment, we study strong as well as weak lensing in the background of a

modified black hole. Hence, modification due to scalar hair is considered in [241] and an attempt has been made to study lensing scenarios and how the presence of hair influence the lensing property. The rationale adopted here evades the no-hair theorem since the hair is conceived in this situation by fresh sources from the surroundings, such as dark matter, which is considered to have a constant energy-momentum tensor. This modification permitted us to unfasten parameters α_h and ℓ_0 . The former refers back hole to the deformation because of the presence of outside supply and the ℓ_0 is associated with alteration in thermodynamical parcels because of the presence of hair. We observe that the lensing coefficient \bar{a} increases with α_h but the lensing coefficient \bar{b} and the impact parameter b_m decrease with the increase of α_h . However, with the increase of ℓ_0 , although \bar{a} decrease \bar{b} gets enhanced. The impact parameter b_m increases with the increase of ℓ_0 . The values of the parameters resemble Schwarzschild black hole whenever we put $\alpha_h = 0$.

The modified models that we have examined so far each have their own advantages in order to understand supermassive black holes through the windows that the observations of the EHT collaboration has opened recently. However, it is still too early to say which model fits the experiment the best or performs better than another models. As a result, numerous investigations in this regard could be pursued. While conducting our research, we focused on the information pertaining to $M87^*$. What further insight does the information from $SgrA^*$ provide about these modifications that are still being investigated?